THESE DE DOCTORAT DE L'ETABLISSEMENT UNIVERSITE BOURGOGNE FRANCHE-COMTE

PREPAREE A l'UNIVERSITE DE FRANCHE-COMTE (BESANCON, FR) ET

L'UNIVERSITA DEGLI STUDI DI NAPOLI "FEDERICO II" (NAPOLI, IT)

École doctorale Sciences physiques pour l'ingénieur et microtechniques

Doctorat de Mécanique

Par

Magliacano Dario

Vibro-acoustique des matériaux poreux avec des inclusions périodiques

Thèse présentée et soutenue à Napoli (IT), le 20/02/2020

Composition du Jury :

Pr Pezerat Charles	Université du Maine (Le Mans, FR)	Président
Pr Cinefra Maria	Politecnico di Torino (Torino, IT)	Examinatrice
Pr Lopez Arteaga Ines	Eindhoven University of Technology (Eindhoven, NL)	Examinatrice
Pr Arfaoui Makrem	University of Tunis El Manar (Tunis, TN)	Examinateur

Rapporteurs :

Pr Deü Jean-François	Conservatoire National des Arts et Métiers (Paris, FR)	Rapporteur
Pr Goransson Peter	KTH Royal Institute of Technology (Stockholm, SE)	Rapporteur

Cette thèse a été co-encadrée par :

Pr Ouisse Morvan	ENSMM (Besançon, France)	Directeur de thèse
Pr De Rosa Sergio	Università degli Studi di Napoli "Federico II" (Napoli, IT)	Directeur de thèse
Pr Franco Francesco	Università degli Studi di Napoli "Federico II" (Napoli, IT)	Codirecteur de thèse
Pr Khelif Abdlekrim	Université de Franche-Comté (Besançon, France)	Codirecteur de thèse

H2020-MSCA-ITN-EJD EU Project 675441

ESR5 / *double degree*

DARIO MAGLIACANO

VIBROACOUSTICS OF POROUS MEDIA WITH PERIODIC INCLUSIONS

A thesis submitted in 2020 to the faculties at

Université de Franche-Comté (France)

and

Università degli Studi di Napoli "Federico II" (Italy)

in partial fulfillment of the requirements for the degree of

Doctor of Philosophy.

Approved by:

Université de Franche-Comté	Università degli Studi di Napoli "Federico II"
Prof. M. Ouisse	Prof. S. De Rosa
Prof. A. Khelif	Prof. F. Franco

ABSTRACT

The design based on periodic elements is a powerful strategy for the achievement of lightweight sound packages and represents a convenient solution for manufacturing aspects.

Several theoretical models exist to study the physical behavior of porous and poro-elastic media, and the most complex ones are based on the definition of more than ten parameters. For example, the theory of poro-elasticity formulated by Maurice Biot allows to take into account the mechanical properties of the foam, simultaneously to its acoustical characteristics. In addition, some of these parameters are very complicated to measure; therefore, while the estimation of all the necessary parameters usually represents the starting point in the construction of a reliable model, in this case it constitutes by itself a specific difficulty. This is one of the reasons why, although poro-elastic media are extensively used for several industrial applications in order to fulfill strictly-regulated requirements of noise reduction, their modeling still represents a non-trivial issue. Numerical simulation techniques, like Finite Element Methods (FEM), may be problematic in case of real complex geometries, especially in terms of computational times and mesh convergence. On the other hand, analytical models, although being partially limited by approximating assumption, constitute a powerful tool to quickly understand physics and general trends of the problem.

Even if porous and poro-elastic media are widely used for vibroacoustic applications, they suffer from a lack of performances at low frequencies compared to their efficiency at higher ones. This issue is generally overcome by multi-layering; anyway, the efficiency of such systems depends on the allowable thickness. A more efficient technique to improve the low frequency performances of sound packages consists in including a periodic pattern in a foam, in order to create wave interferences or resonance effects that may be advantageous for the system dynamics. In this context, numerical tools to properly design sound packages are more and more studied. An interesting research target is the inclusion of vibroacoustic treatments at early stage of product development through the use of porous media with periodic inclusions, which exhibit proper dynamic filtering effects; this addresses different applications in transportation (aerospace, automotive, railway), energy and civil engineering sectors, where both weight and space, as well as vibroacoustic comfort, still remain as critical issues.

The main numerical tool that is developed in this work is the shift cell operator approach, which allows the description of the propagation of all existing waves from the definition of the unit cell, through the resolution of a quadratic eigenvalue problem that can handle any frequency-dependent parameters. It belongs to the class of the $k(\omega)$ (wave number as a function of the angular frequency) techniques, instead of using the classical $\omega(k)$ (angular frequency as a function of wave number) that leads to non-linear eigenvalue problems. This method has been already successfully used for the description of the mechanical behavior of periodic visco-elastic or piezoelectric structures. Here it is proposed an extension to equivalent fluid and diphasic models of porous materials, which makes possible to overcome the limits of existing approaches in order to obtain a device whose frequency efficiency outperforms existing designs.

The aim of this manuscript, therefore, is to introduce some enhancements to the state of the art of the shift cell approach applied to equivalent fluid and diphasic models embedding a periodic pattern.

ACKNOWLEDGEMENTS

Thinking about my journey, I cannot help but realize about how many people have taken me under their wings, in the same way that a cyclist, tending every fiber of his body to reach the summit that separates him from the finish line, finds strength and support from the cheering that people offer along the way. This similarity comes directly from the acknowledgements of my first degree in Aerospace Engineering and, almost seven years and two thesis later, I could not devise a different one that described the concept so effectively. The achievement of this goal is not exclusively because of me, but also of all those who surround me and who have collaborated with me, each in its own way.

To my parents, without whom I could never have reached this point. Despite the physical distance, you didn't make me feel alone, not even for a single moment. You are the definition of Family, in its most intimate meaning, and this goal is as much a part of my life as of yours. I love you.

To nonna Maria, zia Franca, zia Bianca, zio Leo, zia Rosi, Carmine and Piero, for having always been by my side. And to nonna Lina, who has seen me growing up from a privileged perspective.

To Andrea, Tony, Christian, Faby, il Loco, Nanni, Bob, il Taca, Stefano, to be constantly by my side for more than 15 years. I will never forget the path we've gone along all together.

To Vittorio, Max and Checco, the best brothers I could meet. Our bond will never be countered.

To Genny and Gaetano. The cult lives!

To Iaia, for having shared with me the beginning of this adventure.

To the comrades of the Crous (in random order): Eleonora "grande", Eleonora "petite", Simone, Enrico, Luca, Zoila, Agatino, Costanza, Danilo, Fatima, Matteo, Piero, Sabina, Giorgia, Marta, Micaela, Miriam, Yaakoub, Elena, Evelin. "Well, here at last, dear friends, on the shores of the Doubs comes the end of our fellowship in Franche-Comté. Go in peace! I will not say: do not weep; for not all tears are an evil." (semicit.).

To Kenza, the perfect synthesis between a confidant and an interior designer.

To Giulia, who has shown me the meaning of a German romantic term, which is also the title of the 2nd Rammstein album. Quack.

To Andrea, Simone and Nicolò. Without you, my experience in Besançon could not have been even remotely comparable to what it actually was. I miss every single moment I've spent with you.

To Fabrizio and Giovanni, pack companions in the savanna of research.

To Roberta, for showing me a world full of colors (yellow, mostly). Pri!

A special thank goes to my supervisors, Professors Morvan Ouisse, Sergio De Rosa, Francesco Franco and Abdelkrim Khelif, for their constant availability and courtesy, for the trust that they have always shown to me, as well as for their advices and encouragements.

Thanks also to Prof. Noureddine Atalla, for welcoming me to the Université de Sherbrooke (CA), and to Hugo Siwiak, for giving me the opportunity to experience an industrial secondment in Vibratec (Lyon, FR). In conclusions, thanks to Prof. Peter Göransson and Prof. Jean-François Deü, for their precious contributions to the final version of this manuscript.

This project has received funding from the European Union's Horizon 2020 research and innovation program under the Marie Skłodowska-Curie grant agreement No. 675441.

INDEX

ABSTRACT 1
ACKNOWLEDGEMENTS 3
INDEX 5
1. INTRODUCTION 7
1.1. Definition of porous medium 9
1.2. Propagation models 10
1.2.1. Motionless skeleton ("equivalent fluid") models 11
1.2.1.1. Delany-Bazley model (1970) 11
1.2.1.2. Delany-Bazley-Miki model (1990) 12
1.2.1.3. Johnson-Champoux-Allard model (1987 – 1991) 13
1.2.1.4. Johnson-Champoux-Allard-Lafarge model (1993) 15
1.2.1.5. Johnson-Champoux-Allard-Pride-Lafarge model (1997) 15
1.2.2. Diphasic models (Biot theory) 16
1.3. Preliminary definitions about periodic conditions 20
1.3.1. Brillouin zones 20
1.3.2. Bloch waves 21
1.3.3. Floquet-Bloch theory 21
1.3.4. Dispersion relations 22
2. EQUIVALENT FLUID MODEL ANALYSES 25
2.1. Shift cell operator technique 26
2.1.1. Introduction 26
2.1.2. Weak formulation 27
2.1.3. Right and left eigenvalue problems 29
2.1.4. Group velocity 30
2.1.5. Classifying criteria to distinguish propagative and evanescent waves 32
2.1.6. Validation of the method 33
2.1.7. Meaning and behavior of band gaps for inclusions of increasing size 34
2.1.8. Comparison of computational cost 35
2.2. Numerical results 36
2.2.1. Dispersion curves 36
2.2.2. Absorption coefficient 39
2.2.3. Transmission loss 41
2.3. Branch tracking and computation of equivalent absorption coefficient and TL 42
2.3.1. Transfer Matrix Method formulation 43

2.3.2. Results 44
2.4. Non-rigid inclusion test campaign 48
2.5. Design guidelines 53
2.6. Comparison of acoustic performances between a homogeneous unit cell and an unit cell with inclusion with fixed mass 56
2.7. Computation of TL and dispersion curves for a unit cell with Helmholtz resonators 58
2.8. Conclusions 60
3. BIOT MODEL ANALYSES 63
3.1. Shift cell operator technique 64
3.1.1. Introduction 64
3.1.2. Weak formulation 64
3.1.3. Finite element implementation 67
3.1.4. Validation of the method 70
3.1.5. Branch tracking 72
3.2. Absorption coefficient and transmission loss comparisons between JCA and Biot models 74
3.2.1. Computational cost comparison between JCA and Biot models 77
3.3. Non-rigid inclusion test campaign 78
3.3.1. Design of absorption coefficient low frequency improvement 81
3.4. Design guidelines 81
3.5. Conclusions 88
4. GLOBAL CONCLUSIONS AND PERSPECTIVES 89
APPENDICES 91
A. EQUIVALENT FLUID NUMERICAL TEST CAMPAIGN 92
A.1. Dispersion curves 92
A.1.1. Non-rigid inclusions 108
A.2. Absorption coefficient 124
A.2.1. Unit cell dimensions design guidelines 132
A.2.2. Foam airflow resistivity design guidelines 135
A.3. Transmission loss 138
BIBLIOGRAPHY 141
LIST OF FIGURES 151
LIST OF TABLES 159
LIST OF PUBLICATIONS 161
International journals (peer-reviewed) 161
International conferences 161

1. INTRODUCTION

“If we knew what it was we were doing, it would not be called research, would it?”

(Albert Einstein)

A metamaterial is an arrangement of artificial structural elements designed to achieve unusual properties, whose main advantage, over their conventional counterparts, comes from their designability. With their customized and tunable responses, metamaterials offer excellent flexibility in material design and bring a new perspective in understanding materials. Once metamaterial researchers understood the basics, subsequent years saw a transition into potential and actual applications. Consequently, commercialized software introduced specific modules for metamaterial simulation. With the advancement of software and hardware in parallel computing and clusters, nowadays the simulation of metamaterial-inspired devices and equipment is viable and cost-effective [1]. Indeed, the metamaterial market is expected to have a high growth during the next years: the overall market is expected to be valued at USD 4635 Million by 2025 from USD 30 Million in 2016 [2].

Fast urbanization and transport development cause serious noise-induced health risks, such as annoyance, sleep disturbance, or even ischemic heart disease [3]. Therefore, nowadays, environment noise control is becoming a subject of great interest. Generally, common sound absorbing materials could be divided into two categories: resonant and porous materials [4]. Resonant materials for sound absorption mainly involve Helmholtz resonators [5] and/or perforated panels [6]. They are based on the principle of internal resonance effect; these materials shows good performances at low frequencies, but they often have the disadvantage of narrow frequency stop-bands [7]. Porous materials for acoustic applications are composed of channels, cracks or cavities that allow the sound waves entering the materials. Sound energy is dissipated by thermal and viscous losses; these energy consumption principles assure sound absorption over broader frequency ranges [8], [9].

The design based on periodic elements is a powerful strategy for the achievement of lightweight sound packages and represents a convenient solution for manufacturing aspects [10]. An interesting research target is the inclusion of vibroacoustic treatments at early stage of product development through the use of porous media with periodic inclusions [11], which exhibit proper dynamic filtering effects [12]–[16]; this addresses different applications in transportation (aerospace [17], [18], automotive [19]–[23], railway), energy and civil engineering sectors, where both weight and space, as well as vibroacoustic comfort, still remain as critical issues [24].

As described by Horoshenkov [25], there is growing interest in innovative solutions concerning materials for acoustic applications. Moreover, inhomogeneous materials have been considered in the relevant literature [26], [27]. In order to enhance the acoustic properties of these materials, several studies have investigated the case of double porosity [28]–[31]. The double porosity configuration consists in a set of periodical perforations, in the thickness direction. Under certain conditions, the perforated material can be considered as an equivalent homogeneous porous material. Double porosity materials have proven to be very effective for the enhancement of acoustic properties [32].

To this aim, the Wave Finite Element Method (WFEM) is widely used in the relevant literature in order to study wave propagation in periodic structures [33], [34], combining the advantages of the Finite Element Method (FEM) and spectral techniques [35]. This method has been formulated mainly for acoustic [36] and piezoelectric [37] problems. However, almost all the current approaches are based on harmonic response computations, hence they depend on the excitation.

The added value of the main numerical tool which is developed in this work, the shift cell technique, is that it provides information (dispersion diagrams) that are independent from the excitation, and therefore it constitutes a valuable tool for the design of original solutions that will be efficient regardless of the excitation. The shift cell operator approach allows the description of the propagation of all existing waves from the description of the unit cell through the resolution of a quadratic eigenvalue problem, which can handle any frequency-dependency of parameters [38]–[43].

It belongs to the class of the $k(\omega)$ (wave number as a function of the angular frequency) methods, which allow computing dispersion curves for frequency-dependent problems, instead of using the classical $\omega(k)$ (angular frequency as a function of wave number) that leads to non-linear eigenvalue problems. This technique has been successfully applied for describing the mechanical behavior of periodic structures embedding visco-elastic materials [44]–[48] or piezoelectric materials [49].

Here we propose an extension to equivalent fluid and diphasic models of porous materials, which makes possible to overcome the limits of existing approaches in order to obtain a device whose frequency efficiency outperforms existing designs [50]–[53].

In particular, compared to the research performed by Wang *et al.* [54], [55], in the present work the $k(\omega)$ problem (herein addressed as "shift cell") is specifically derived for porous and poro-elastic materials, respectively modeled as equivalent fluids and Biot foams. In this manuscript, these models precisely describe the physical behavior for rigid-framed and elastic-framed foams; in addition, the formulation developed here is not restricted to 1D, and it is provided in details for FE implementation.

In this context, the aim of this manuscript is to introduce some enhancements to the state of the art of the shift cell technique applied to equivalent fluid and diphasic models.

1.1. Definition of porous medium

A porous medium is a material containing pores (voids). The skeleton of the material is usually referred to as "matrix" or "frame". The pores are generally filled with a fluid (liquid or gas). Several natural materials, such as rocks and soil (e.g., aquifers, petroleum reservoirs), zeolites, biological tissues (e.g. bones, wood, cork) and artificial substances, such as cements and ceramics, can be considered as porous materials [56]. Indeed, the most part of their fundamental properties can only be rationalized by considering them to be porous materials [57]. The concept of porous material is used in different fields of applied science and engineering [58]:

- filtration;
- mechanics (acoustics, geomechanics, soil mechanics, rock mechanics);
- engineering (petroleum engineering, bio-remediation, construction engineering);
- geosciences (hydrogeology, petroleum geology, geophysics);
- biology and biophysics;
- material science.

A foam is a porous medium that is formed by trapping pockets of gas in a liquid or solid. A bath sponge and the head on a glass of beer are examples of foams. An important division of solid foams is into closed-cell foams and open-cell foams [59], [60]:

- in a closed-cell foam, the gas forms discrete pockets, each completely surrounded by the solid material;
- in an open-cell foam, the gas pockets connect with each other.

A bath sponge is an example of an open-cell foam: water can easily flow through the entire structure, displacing the air. A camping mat is an example of a closed-cell foam: the gas pockets are sealed from each other so the mat cannot soak up water. The term foam may also refer to anything that is analogous to such a foam, such as quantum foam, polyurethane foam (foam rubber), XPS foam, polystyrene, phenolic, or many other manufactured foams [61].

In particular, polyurethane (PUR and PU) is a polymer composed of organic units joined by carbamate (urethane) links. While most PUs are thermosetting polymers that do not melt when heated, thermoplastic polyurethanes are also available. Nowadays, PUs are used in the manufacture of:

- high-resilience foam seating;
- rigid foam insulation panels;
- microcellular foam seals and gaskets;
- durable elastomeric wheels and tires (such as roller coaster, escalator, shopping cart, elevator, and skateboard wheels);
- automotive suspension bushings;
- electrical potting compounds;
- high performance adhesives;
- surface coatings and surface sealants;
- synthetic fibers;
- carpet underlay;
- hard-plastic parts (e.g., for electronic instruments).

A porous medium is most often characterized by its porosity [62]. Both the solid matrix and the pore space may be continuous, so as to form two interpenetrating continua such as in a sponge [56]. Porosity or void fraction is a measure of the void (i.e. "empty") spaces in a material, and is a fraction of the volume of voids over the total volume, between 0 and 1, or as a percentage between 0 and 100%. Porosity is defined by the ratio:

$$\phi = \frac{V_V}{V_T} \tag{1}$$

where $V_V$is the volume of void-space (such as fluids) and V_T is the total or bulk volume of material, including the solid and void components. Effective porosity is most commonly considered to represent the porosity of a structure available to contribute to fluid flow through it. The acoustic performance of poro-elastic materials used in sound packages is controlled by dissipative effects in the fluid filling the porous space and by the deformation of the porous skeleton [63]. On this basis, Biot proposed a system of coupled displacement equations, one for the porous frame and one for the interstitial fluid [64].

1.2. Propagation models

Many theoretical models are available to predict the physical behavior of porous materials. The most complex models require the definition of more than ten parameters to model the physical system of a porous absorbing material. It is the case, for example, of the theory of poro-elasticity developed by Maurice Biot [65], which allows to take into account the mechanical properties of the material, simultaneously to its acoustical behavior [66]. Moreover, some of the parameters that are present in the different theoretical models are very difficult to measure. In general, the measurements of all the necessary parameters, that usually constitute the first step in the construction of a reliable model, represent by themselves a specific issue. Therefore, even if porous materials are widely used in many fields of industrial applications to achieve the requirements of noise reduction, that nowadays derive from strict regulations, the modeling of porous materials is still a problematic issue. Numerical simulations, like FEM, are often problematic in case of real complex geometries, especially in terms of computational times and convergence. At the same time, analytical models, even if partly limited by restrictive approximating hypotheses, represent a powerful instrument to capture quickly the physics of the problem and general trends [32].

1.2.1. Motionless skeleton ("equivalent fluid") models

The phase decoupling frequency is defined as the frequency for which the inertial effects of the solid phase are equal, in magnitude, to the viscous effects of the fluid part [67]. The expression of the phase decoupling frequency is given by Zwikker and Kosten as $f_d = \frac{\sigma\phi^2}{2\pi\rho}$.

If one considers a foam, excited by an acoustic load at a frequency much higher than the phase decoupling one, with a stiffness (or a weight) much greater than the one of the air, the material frame can be considered as rigid and motionless [68]. Therefore, the porous medium with motionless skeleton can be replaced by the homogeneous fluid layer without modifying the reflected field in the external medium [10]. Two classes of equivalent fluid models (i.e. expressions of complex ρ and K as functions of the frequency and of the pore shape) can be listed [68]:

- Empirical models, which generally require the knowledge of a small number of parameters (or information); even if they are based on approximating assumptions, they are still very popular and very used.
- Semi-phenomenological models, which have been formulated for more complex pore morphologies; for this class of models, only the asymptotic behaviors are known, while a behavior between these asymptotes is assumed without being mathematically proven.

Some of the models reported above are further described:

1. Delany-Bazley (1970) – 1 parameter empirical model;
2. Delany-Bazley-Miki (1990) – 1 parameter empirical model;
3. Johnson-Champoux-Allard (1987 – 1991) – 5 parameters semi-phenomenological model;
4. Johnson-Champoux-Allard-Lafarge (1993) – 6 parameters semi-phenomenological model;
5. Johnson-Champoux-Allard-Pride-Lafarge (1997) – 8 parameters semi-phenomenological model.

1.2.1.1. Delany-Bazley model (1970)

From a large number of measurements on fibrous materials with porosities close to 1, Delany and Bazley [69] have proposed empirical expressions for the values of the complex wave number k and characteristic impedance Z_c for such materials:

$$Z_c = \rho_0 c_0 \left[1 + 9.08\left(10^3 \frac{f}{\sigma}\right)^{-0.75} - j11.9\left(10^3 \frac{f}{\sigma}\right)^{-0.73}\right], \tag{2}$$

$$k = \frac{\omega}{c_0}\left[1 + 10.8\left(10^3 \frac{f}{\sigma}\right)^{-0.70} - j10.3\left(10^3 \frac{f}{\sigma}\right)^{-0.59}\right]. \tag{3}$$

Boundaries, proposed by the authors, for the validity of these power law expressions are:

$$0.01 < \frac{f}{\sigma} < 1.00. \tag{4}$$

This empirical model, which can provide reasonable estimations of k and Z_c in the approximative frequency range defined above, is still widely used for its simplicity: only one parameter, σ, is needed to describe the acoustic behavior of a material.

1.2.1.2. Delany-Bazley-Miki model (1990)

The model by Delany-Bazley-Miki [70] presents revised expressions for the complex wave number k and characteristic impedance Z_c of Delany-Bazley model [69]. In the case of multi-layers, Miki noticed that the real part of the surface impedance, when estimated with the classical Delany-Bazley model, may turn negative at low frequencies, thus leading to a non-physical result. In this context, Miki suggests the usage of the following expressions:

$$Z_c = \rho_0 c_0 \left[1 + 5.50\left(10^3 \frac{f}{\sigma}\right)^{-0.632} - j8.43\left(10^3 \frac{f}{\sigma}\right)^{-0.632}\right], \tag{5}$$

$$k = \frac{\omega}{c_0}\left[1 + 7.81\left(10^3 \frac{f}{\sigma}\right)^{-0.618} - j11.41\left(10^3 \frac{f}{\sigma}\right)^{-0.618}\right]. \tag{6}$$

The elapsed time (20 years) between the formulation of the original Delany-Bazley model and Miki corrections may explain, partially, the wide usage of the first expressions although the second ones should be preferred. The validity of Miki model is the same of that related to the original formulation, even if his revised expressions behaves well in a larger frequency range, in particular for $\frac{f}{\sigma} < 0.01$.

Figure 1 shows the normalized surface impedance computed from the original models (thin lines) and the new models (thick lines) with flow resistivity $\sigma = 100{,}000$ N*s*m^{-4} and thickness $d = 10$ mm. It is seen that these results show a distinct difference at frequencies below 1 kHz and that the real part of the former becomes negative with decreasing frequency. Such an impedance cannot be realized. This frequency range is found to be coincident with the range $f/\sigma < 0.01$ to which Delany and Bazley gave a warning not to extrapolate their models. At least the Delany-Bazley-Miki model is well behaved in this frequency range, although this does not necessary means that it provides a good prediction of the acoustic behavior in this range.

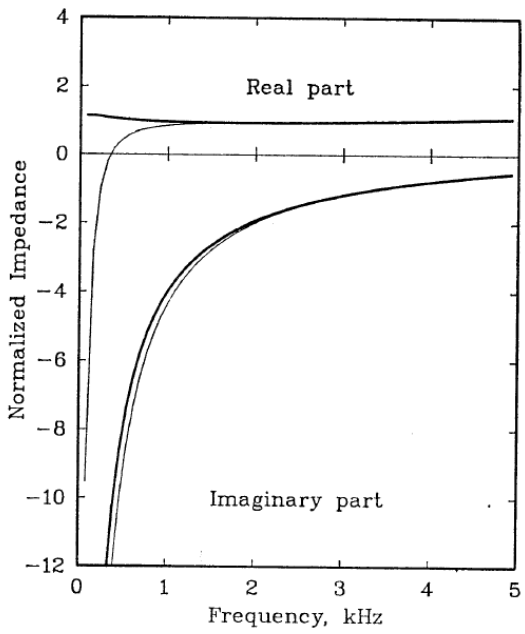

*Figure 1: Comparison between the surface impedance predicted from the new model and that from the original model with $\sigma = 100{,}000$ N*s*m^{-4} and $d = 10$ mm* [70].

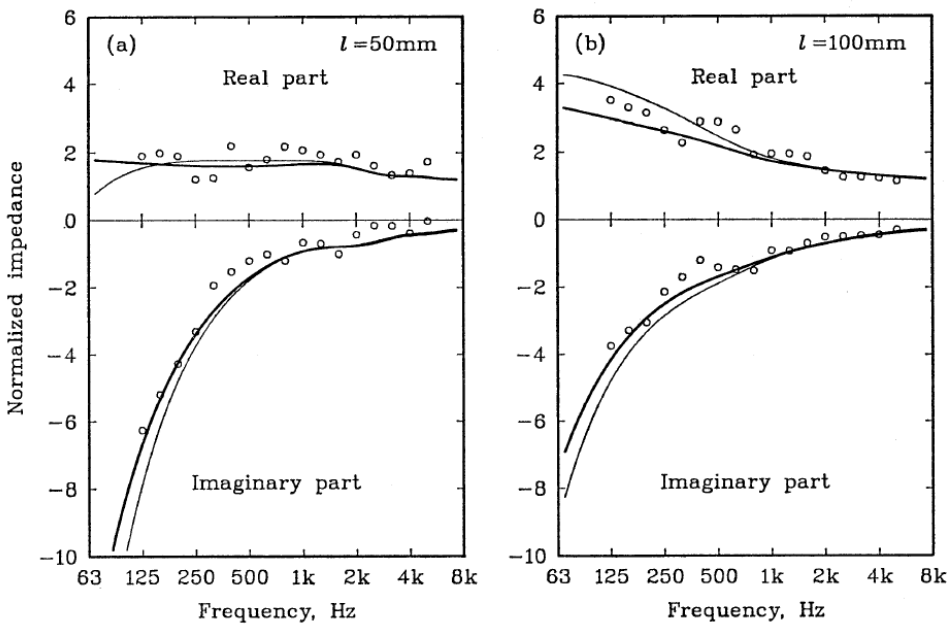

*Figure 2: Comparison between measured and predicted surface impedance. Dots are the measured data by Nakajima et al.. Thick curves and thin curves show the predictions from the new model and the original, respectively, with $\sigma = 41{,}000$ N*S*M⁻⁴ and (a) $d = 50$ mm, (b) $d = 100$ mm* [70].

Figure 2 shows the normalized surface impedance data obtained by T. Nakajima and T. Kawai for a rigidly backed rock wool of 50 (on the left) and 100 (on the right) mm thickness with 150 kg/m^3 density. The thick curves in Figure 1 and Figure 2 show the impedance computed from the new models with $\sigma = 41{,}000$ N*S*M^{-4}. The thin curves show the impedance computed from the original models with the same σ-value. In this example, it may be said that the prediction from the new models is superior to that from the original over the whole frequency range, especially in the range $f < 400$ Hz, which is out of the validity range of the original model [70].

1.2.1.3. Johnson-Champoux-Allard model (1987 – 1991)

The Johnson-Champoux-Allard model is based on the work by Johnson, Koplik & Dashen [71] to describe visco-inertial dissipative effects inside the porous media. The work by Champoux & Allard [72] is used to describe the thermal dissipative effects. In 1987, Johnson Koplik and Dashen proposed a semi-phenomenological model to describe the complex density of an acoustical porous material with a motionless skeleton having arbitrary pore shapes. This expression is:

$$\rho(\omega) = \frac{\alpha_\infty \rho_0}{\phi}\left[1 + \frac{\sigma\phi}{j\omega\rho_0\alpha_\infty}\sqrt{1 + j\frac{4\alpha_\infty^2\eta\rho_0\omega}{\sigma^2\Lambda^2\phi^2}}\right]. \tag{7}$$

In 1991, Champoux and Allard formulated an expression for the equivalent bulk modulus for the same kind of foams, based on the previous research by Johnson *et al.*:

$$K(\omega) = \frac{\frac{\gamma P_0}{\phi}}{\gamma - (\gamma-1)\left[1 - j\frac{8\kappa}{\Lambda'^2 c_p \rho_0 \omega}\sqrt{1 + j\frac{\Lambda'^2 c_p \rho_0 \omega}{16\kappa}}\right]^{-1}}, \tag{8}$$

where:

- P_0 [kg/(m*s^2)] is the fluid equilibrium pressure;

- κ is the thermal conductivity of the air (≈0.0257 kg*m/(s^3*K) for air at 20°C).

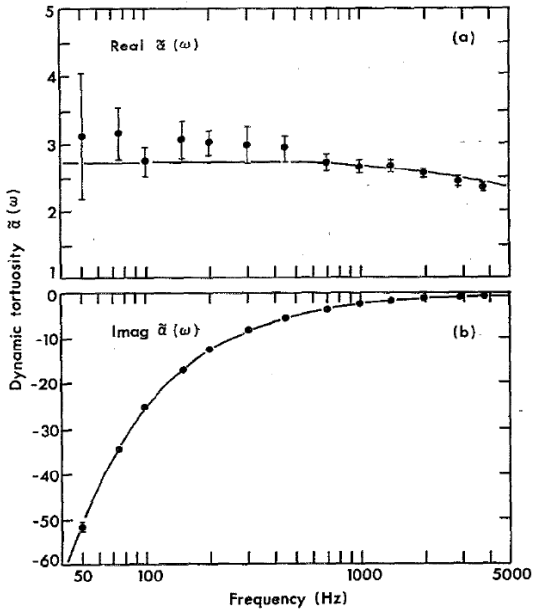

Figure 3: Dynamic tortuosity of air for a porous ceramic media: (a) real part, (b) imaginary part. Solid line and dots respectively represent theoretical prediction and experimental results [72].

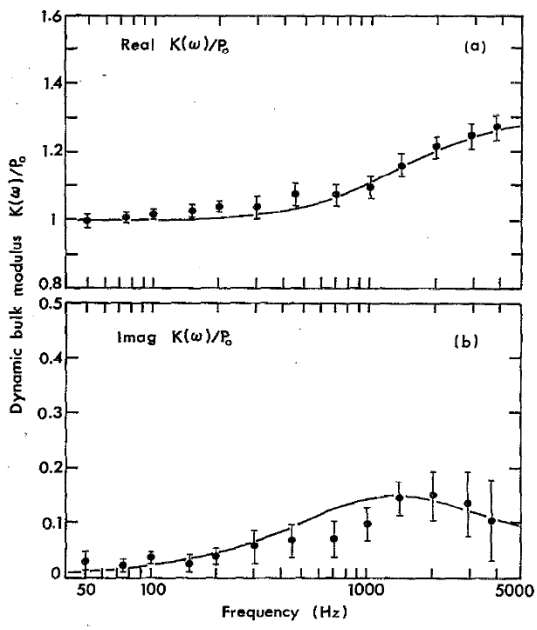

Figure 4: Dynamic bulk modulus (in units of P_0) of air for a porous ceramic: (a) real part, (b) imaginary part. Solid line and dots respectively represent theoretical prediction and experimental results [72].

The expression of ρ found by Johnson, Koplik & Dashen does not represent the exact behavior of the equivalent mass density when ω approaches low values; in this case, its real part (or the imaginary part of the dynamic permeability) is not correct. The ame happens for the expression of the equivalent bulk modulus given by Champoux & Allard.

The porous medium used in the experimental investigation is a Filtros porous ceramic QF-130. The values of the measured physical parameters are $\phi = 0.432$, $\alpha_\infty = 1.70$, and $\sigma = 44{,}500$ N*S*M^{-4}.

The dynamic bulk modulus, after having been normalized by the fluid equilibrium pressure P_0, has been evaluated for the range of 50-5000 Hz.

At low frequencies, the real part of the dynamic bulk modulus approaches asymptotically a numerical value equal to 1, clearly indicating an isothermal process, while at high frequencies it approaches a value of 1.4, indicating an adiabatic process. The imaginary part approaches zero at both low and high frequencies. It appears that the prediction of the real part of dynamic tortuosity becomes very good around $f > 450$ Hz, while both real and imaginary part of dynamic bulk modulus lightly deviates from experimental data in the range between 300 and 1500 Hz [72].

1.2.1.4. Johnson-Champoux-Allard-Lafarge model (1993)

The Johnson-Champoux-Allard-Lafarge model is based on the research by Johnson, Koplik & Dashen [71] to estimate visco-inertial dissipation inside porous materials, while the works by Champoux & Allard [9] and Lafarge, Lemarinier, Allard & Tarnow [73] are used to define the thermal dissipation. The description of ρ remains the same of the JCA model, while that of K is modified in 1993 by Lafarge *et al.*, which highlight a lack of information at low frequencies due to thermal effects. Indeed, in the JCA model, four parameters are used to calculate ρ and the visco-inertial effects, while only two parameters are required to estimate K and the thermal effects. This observation leads Lafarge *et al.* to the introduction of a new parameter, the static thermal permeability $k_0' = \frac{\phi \Lambda'^2}{8}$ [m^2], in order to describe the low frequency behavior taking into account also thermal effects. The new expression of K, introduced by Lafarge *et al.*, is:

$$K(\omega) = \frac{\frac{\gamma P_0}{\phi}}{\gamma - (\gamma - 1)\left[1 - j\frac{\phi\kappa}{k_0' c_p \rho_0 \omega}\sqrt{1 + j\frac{4k_0' c_p \rho_0 \omega}{\kappa \Lambda'^2 \phi^2}}\right]^{-1}}. \tag{9}$$

In any case, this expression is still not correct at low frequencies.

1.2.1.5. Johnson-Champoux-Allard-Pride-Lafarge model (1997)

The Johnson-Champoux-Allard-Pride-Lafarge model [73] is further refined by Pride, Morgan & Gangi (and corrected by D. Lafarge) in 1997, in order to account for pores with possible constrictions between them. The final expression obtained for ρ is:

$$\rho = \frac{\rho_0 \alpha(\omega)}{\phi}, \tag{10}$$

with:

$$\alpha(\omega) = \alpha_\infty \left[1 + \frac{1}{j\overline{\omega}} F(\omega)\right], \tag{11}$$

$$\overline{\omega} = \frac{\omega \rho_0 k_0 \alpha_\infty}{\eta \phi}, \tag{12}$$

$$F(\omega) = 1 - P + P\sqrt{1 + \frac{M}{2P^2}\, j\overline{\omega}}, \tag{13}$$

$$P = \frac{M}{4\left(\frac{\alpha_0}{\alpha_\infty} - 1\right)}, \tag{14}$$

$$M = \frac{8k_0\alpha_\infty}{\phi\Lambda^2}, \tag{15}$$

and where α_0 is the static viscous tortuosity. The final expression obtained for K is:

$$K = \frac{\gamma P_0}{\phi\beta(\omega)}, \tag{16}$$

with:

$$\beta(\omega) = \gamma - (\gamma - 1)\left[1 + \frac{1}{j\overline{\omega}'}F'(\omega)\right]^{-1}, \tag{17}$$

$$\overline{\omega}' = \frac{k_0' c_p \rho_0 \omega}{\kappa\phi}, \tag{18}$$

$$F'^{(\omega)} = 1 - P' + P'\sqrt{1 + \frac{M'}{2P'^2}j\overline{\omega}'}, \tag{19}$$

$$P' = \frac{M'}{4(\alpha_0' - 1)}, \tag{20}$$

$$M' = \frac{8k_0'}{\phi\Lambda'^2}. \tag{21}$$

1.2.2. Diphasic models (Biot theory)

For many materials having an elastic frame and set on a rigid floor, the frame can be almost motionless for large ranges of acoustical frequencies, thus allowing the use of models worked out for rigid framed materials. Nevertheless, this is not generally true for the entire range of acoustical frequencies. Moreover, for a material set between two elastic plates and for many other similar situations, frame vibration is induced by the vibrations of the plates. The transmission of sound through such a sandwich can be predicted only in the context of a model where both the fluid and solid parts move [10]. Such a model is provided by the Biot theory [64] of sound propagation in poro-elastic materials. Only the case of isotropic porous structures is herein considered. According to the Biot theory, the deformations of the structure related to wave propagation are supposed to be similar to those in an elastic solid [74].

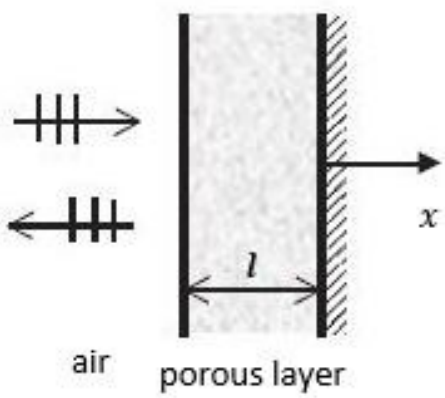

Figure 5: A layer of porous material bonded on to a rigid wall, in a normal acoustic field [10].

In order to obtain simple boundary conditions at the interface, the material is glued to the wall. Under a normal acoustic load, the shear wave is not excited and only the compressional waves propagate in the medium. The description of the acoustic field is easier for this case than for oblique incidence.

Thus, the Biot theory is used to study the behavior, represented by the surface impedance, of the foam in a normal acoustic field. Two incident and two reflected compressional waves propagate in directions parallel to the x axis. The velocity of the solid and fluid parts are respectively defined as [10]:

$$\dot{u}^s(x) = V_I^1 e^{-j\delta_1 x} + V_R^1 e^{j\delta_1 x} + V_I^2 e^{-j\delta_2 x} + V_R^2 e^{j\delta_2 x}, \tag{22}$$

$$\dot{u}^f(x) = \mu_1\left[V_I^1 e^{-j\delta_1 x} + V_R^1 e^{j\delta_1 x}\right] + \mu_2\left[V_I^2 e^{-j\delta_2 x} + V_R^2 e^{j\delta_2 x}\right], \tag{23}$$

where:

- the time dependence $e^{j\omega t}$ has been removed;
- the quantities $V_I^1, V_R^1, V_I^2, V_R^2$ are the velocities of the frame at $x = 0$ associated with the incident and the reflected first and second Biot compressional waves;
- the eigenvalues δ_1 and δ_2 are the complex wave numbers of the two compressional waves $\delta_1 = \sqrt{\frac{A_1}{2} - \sqrt{\frac{{A_1}^2}{4} - A_2}}$ and $\delta_2 = \sqrt{\frac{A_1}{2} + \sqrt{\frac{{A_1}^2}{4} - A_2}}$.

The parameters that characterize the poro-elastic material are:

- ϕ is the open porosity;
- σ is the static flow resistivity;
- α_∞ is the tortuosity;
- Λ is the viscous characteristic length;
- η_{visc} is the viscosity;
- $q_0 = \frac{\eta_{visc}}{\sigma}$ is the static viscous permeability;
- $\nu_{visc} = \frac{\eta_{visc}}{\rho_0}$;
- $\nu_{therm} = \frac{\nu_{visc}}{Pr}$;
- Pr is the Prandtl number.

Furthermore, the following quantities are defined [75]:

- $A_1 = \omega^2 \frac{\tilde{\rho}_{11}R - 2\tilde{\rho}_{12}Q + \tilde{\rho}_{22}P}{RP - Q^2}$;
- $A_2 = \omega^4 \frac{\tilde{\rho}_{11}\tilde{\rho}_{22} - {\tilde{\rho}_{12}}^2}{RP - Q^2}$;
- $\tilde{\rho}_{11}$, $\tilde{\rho}_{12}$ and $\tilde{\rho}_{22}$ are parameters depending on the nature and the geometry of the porous medium and the density of the fluid; in particular:
  - $\tilde{\rho}_{11} = \rho_1 + \rho_a + \frac{b}{j\omega}$;
  - $\tilde{\rho}_{12} = -\rho_a - \frac{b}{j\omega}$;
  - $\tilde{\rho}_{22} = \phi\rho_0 + \rho_a + \frac{b}{j\omega}$.
- ρ_0 is the bulk density of the fluid phase;
- ρ_1 is the bulk density of the solid phase;
- $\rho_a = \phi\rho_0(\alpha_\infty - 1)$ is an inertial coupling term;
- $b = \sigma\phi^2 G(\omega)$ is the viscous drag;
- $G(\omega) = \sqrt{1 + \frac{4j{\alpha_\infty}^2\eta_{visc}\rho_0\omega}{(\sigma\Lambda\phi)^2}}$ is the relaxation function, as predicted by Johnson-Champoux-Allard model [71], [72];
- $\tilde{\rho} = \left(\tilde{\rho}_{11} - \frac{\tilde{\rho}_{12}^2}{\tilde{\rho}_{22}}\right)$;
- P, Q, R are elasticity coefficients to be determined by "gedanken experiments" [10]; in particular [62]:

- $P = \frac{(1-\phi)\left(1-\phi-\frac{KB}{KS}\right)KS+\phi\frac{KB*KS}{KF}}{1-\phi-\frac{KB}{KS}+\phi\frac{KS}{KF}} - \frac{2}{3}N \cong \left(1+\frac{\nu}{1-2\nu}\right)2N + \frac{1-\phi^2}{\phi}KF;$
- $Q = \frac{\left(1-\phi-\frac{KB}{KS}\right)\phi KS}{1-\phi-\frac{KB}{KS}+\phi\frac{KS}{KF}} \cong (1-\phi)KF;$
- $R = \frac{\phi^2 KS}{1-\phi-\frac{KB}{KS}+\phi\frac{KS}{KF}} \cong \phi KF.$

- $N = |N|(1+j\eta) = \frac{Y}{2(1+\nu)}$ is the complex shear modulus of the frame;
- $Y = |Y|(1+j\eta)$ is the complex Young modulus of the frame;
- η is the loss factor of the frame;
- ν is the Poisson's ratio of the frame;
- $KB = \frac{2N(\nu+1)}{3(1-2\nu)}$ is the bulk modulus of the frame in vacuum;
- $KS = \frac{KB}{1-\phi}$ is the bulk modulus of the elastic solid from which the frame is made;
- KF is the bulk modulus of the fluid phase, computed starting from the equivalent one (e.g.: $KF = \phi K_{JCA}$);
- $\tilde{\gamma} = \phi\left(\frac{\tilde{\rho}_{12}}{\tilde{\rho}_{22}} - \frac{Q}{R}\right);$
- $\mu_i = \frac{P\delta_i^2 - \omega^2\tilde{\rho}_{11}}{\omega^2\tilde{\rho}_{12} - Q\delta_i^2}, i = 1,2$ is the ratio of the velocity of the air over the velocity of the frame for the two compressional waves and indicates in what medium the waves propagate preferentially.

The stresses in the material are given by:

$$\sigma_{xx}^s(x) = -Z_1^s\left[V_I^1 e^{-j\delta_1 x} - V_R^1 e^{j\delta_1 x}\right] - Z_2^s\left[V_I^2 e^{-j\delta_2 x} - V_R^2 e^{j\delta_2 x}\right], \tag{24}$$

$$\sigma_{xx}^f(x) = -\phi Z_1^f \mu_1\left[V_I^1 e^{-j\delta_1 x} - V_R^1 e^{j\delta_1 x}\right] - \phi Z_2^f \mu_2\left[V_I^2 e^{-j\delta_2 x} - V_R^2 e^{j\delta_2 x}\right], \tag{25}$$

where:

- the quantities $Z_{1,2}^{s,f}$ are the characteristic impedances related to the propagation of the wave in the solid and in the air associated with first and second Biot compressional waves;
- $Z_{1,2}^s = \left(P + Q\mu_{1,2}\right)\frac{\delta_{1,2}}{\omega};$
- $Z_{1,2}^f = \left(R + \frac{Q}{\mu_{1,2}}\right)\frac{\delta_{1,2}}{\phi\omega}.$

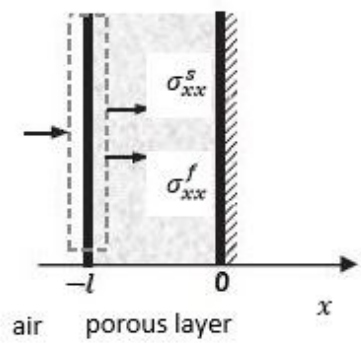

Figure 6: A thin layer of air and porous material including the boundary [10].

At $x = 0$, where the wall and the material are in contact, the velocities are equal to zero:

$$\dot{u}^s(0) = \dot{u}^f(0) = 0. \tag{26}$$

At $x = -l$, the porous material is in contact with the free air. Let us consider a thin layer of air and porous material, including this boundary.

Let us denote by $p(-l - \varepsilon)$ the pressure in the air on the left-hand side of the thin layer, while $\sigma_{xx}^{s}(-l + \varepsilon)$ and $\sigma_{xx}^{f}(-l + \varepsilon)$ are the stresses acting on the air and on the frame on the right-hand side. The resulting force ΔF acting on the thin layer is:

$$\Delta F = p(-l - \varepsilon) + \sigma_{xx}^{s}(-l + \varepsilon) + \sigma_{xx}^{f}(-l + \varepsilon). \tag{27}$$

This force tends to zero with ε, and a boundary condition for the stress at $x = -l$ is:

$$p(-l) + \sigma_{xx}^{s}(-l) + \sigma_{xx}^{f}(-l) = 0. \tag{28}$$

Another boundary condition is derived from the continuity of pressure and can be expressed as:

$$\sigma_{xx}^{f}(-l) = -\phi p(-l), \tag{29}$$

ϕ being the porosity of the material. The use of Equation (28) and Equation (29) yields:

$$\sigma_{xx}^{s}(-l) = -(1-\phi)p(-l). \tag{30}$$

The conservation of the volume of air and frame through the plane $x = -l$ yields:

$$\phi \dot{u}^{f}(-l) + (1-\phi)\dot{u}^{f}(-l) = \dot{u}^{a}(-l), \tag{31}$$

$\dot{u}^{a}(-l)$ being the velocity of the free air at the boundary. The surface impedance Z_s (simply indicated as Z in the following equations) of the material is given by:

$$Z = \frac{p(-l)}{\dot{u}^{a}(-l)}. \tag{32}$$

This surface impedance can be evaluated in the following way. At first, it can easily be shown that the definitions of $\dot{u}^{s}(x)$ and $\dot{u}^{f}(x)$, together with the boundary condition at $x = 0$, yield:

$$V_I^1 = -V_R^1, \tag{33}$$

$$V_I^2 = -V_R^2. \tag{34}$$

Therefore, considering the boundary condition derived from the continuity of pressure and all subsequent equations:

$$\begin{cases} -(1-\phi)\dot{u}^{a}(-l)Z = -Z_1^s V_I^1\left(e^{j\delta_1 x} + e^{-j\delta_1 x}\right) - Z_2^s V_I^2\left(e^{j\delta_2 x} + e^{-j\delta_2 x}\right) \\ -\phi\dot{u}^{a}(-l)Z = -Z_1^f \phi\mu_1 V_I^1\left(e^{j\delta_1 x} + e^{-j\delta_1 x}\right) - Z_2^f \phi\mu_2 V_I^2\left(e^{j\delta_2 x} + e^{-j\delta_2 x}\right) \\ \left[\phi\mu_1 + (1-\phi)V_I^1\left(e^{j\delta_1 x} - e^{-j\delta_1 x}\right)\right] + \left[\phi\mu_2 + (1-\phi)V_I^2\left(e^{j\delta_2 x} - e^{-j\delta_2 x}\right)\right] = \dot{u}^{a}(-l) \end{cases}. \tag{35}$$

This system of three equations has a solution (V_I^1, V_I^2) if:

$$\begin{vmatrix} -(1-\phi)Z & -2Z_1^s\cos(\delta_1 l) & -2Z_2^s\cos(\delta_2 l) \\ -Z & -2Z_1^f\mu_1\cos(\delta_1 l) & -2Z_2^f\mu_2\cos(\delta_2 l) \\ 1 & 2j\sin(\delta_1 l)\,(\phi\mu_1 + 1 - \phi) & 2j\sin(\delta_2 l)\,(\phi\mu_2 + 1 - \phi) \end{vmatrix} = 0, \tag{36}$$

and Z is given by:

$$Z = -j\frac{Z_1^s Z_2^f \mu_2 - Z_2^s Z_1^f \mu_1}{(\phi\mu_2 + 1 - \phi)\left[Z_1^s - (1-\phi)Z_1^f\mu_1\right]\tan(\delta_2 l) + (\phi\mu_1 + 1 - \phi)\left[Z_2^f - (1-\phi)Z_2^s\mu_2\right]\tan(\delta_1 l)}. \tag{37}$$

A systematic method of calculating the surface impedance at oblique incidence, based on transfer matrices, is presented in Allard *et al.* [10].

1.3. Preliminary definitions about periodic conditions

Although porous materials are commonly used for vibroacoustic applications, they suffer from a lack of absorption at low frequencies compared to their efficiency at higher ones. This difficulty is usually overcome by multi-layering [76], [77]. However, while reducing the impedance mismatch at the air-material interface, the efficiency of such devices relies on the allowable thickness [78], [79].

A more efficient way to enhance the low frequency performances of sound packages consists in embedding periodic inclusions in a porous layer [80], [81] in order to create wave interferences or resonance effects that may play a positive role in the dynamics of the system. Therefore, numerical tools to properly design sound packages are more and more useful. In the work by Groby *et al.* [80], the influence of the periodic inclusions on the absorption coefficient was explained by excitation of additional acoustic modes which dissipate acoustic energy. Indeed, periodic patterns of surface irregularities or volume heterogeneities usually lead to energy entrapment either at the surface or inside the structure, this being strongly linked to mode excitation: in other words, the excitation of something similar to a structural mode of the initial macroscopically-homogeneous medium is enabled by the presence of a periodic set of inclusions. This phenomenon was first noticed by Wood [82]. The particular properties of such structures have been studied in mechanics, with application to composite materials [83], [84], in optics (initially motivated by the collection of solar energy) [85], [86], and in geophysics for the study of the “city-site” effect [87]. The properties of such structures are now studied to create band-gaps for elastic or acoustic waves [88], [89], and have been used for the design of porous materials for acoustic applications [80]. Although this procedure still relies on the dimension of the inclusions, it can provide an acoustical performance enhancement that is widely more efficient than just increasing the thickness.

1.3.1. Brillouin zones

Léon Brillouin (1889–1969), a French physicist, developed the concept of a Brillouin zone. In mathematics and solid-state physics, the first Brillouin zone is a uniquely defined primitive cell in reciprocal space. Planes related to points on the reciprocal lattice represent the boundaries of this cell. The importance of the Brillouin zone comes from the Bloch wave description of waves in a periodic system, in which it is derived that the solutions can be completely characterized by their behavior in a single Brillouin zone.

The first Brillouin zone is defined as the locus of points in reciprocal space that are closer to the origin of the reciprocal lattice than they are to any other reciprocal lattice points. They exist also the second, third, etc., Brillouin zones, corresponding to a sequence of disjoint regions (all with the same volume) at increasing distances from the origin, but these are used less frequently; as a consequence, the first Brillouin zone is often simply referred to as the Brillouin zone. A related concept is that of the irreducible Brillouin zone, which is defined as the first Brillouin zone reduced by all of the symmetries in the point group of the lattice [90].

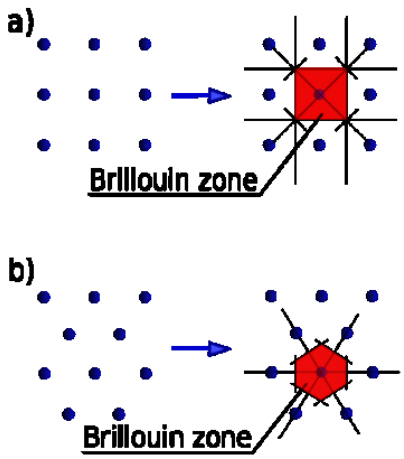

Figure 7: The reciprocal lattices (dots) and corresponding first Brillouin zones of (a) square lattice and (b) hexagonal lattice.

1.3.2. Bloch waves

The concept of Bloch wave (also known as Bloch state or Bloch function or Bloch wave function), formulated by the Swiss physicist Felix Bloch, defines a type of wave function for a particle in a periodically repeating environment, most commonly an electron in a crystal. A wave function ψ is a Bloch wave if it has the form:

$$\psi(\boldsymbol{r}) = e^{j\boldsymbol{kr}} u(\boldsymbol{r}), \tag{38}$$

where

- $\boldsymbol{r}$ is the position;
- ψ is the Bloch wave;
- u is a periodic function with the same periodicity as the lattice;
- $\boldsymbol{k}$ is a vector of real numbers called the crystal wave vector;
- e is Euler's number;
- j is the imaginary unit.

This means that one should multiply a plane wave by a periodic function in order to get a Bloch wave. These Bloch wave eigenstates are indicated with subscripts as $\psi_{n,\boldsymbol{k}}$, where n is a discrete index, called the band index, which is present because there are many distinct Bloch waves with the same $\boldsymbol{k}$ (each has a different periodic component u). Within a band (i.e., for fixed n), $\psi_{n,\boldsymbol{k}}$ varies continuously with $\boldsymbol{k}$, together with its energy. Also, for any reciprocal lattice vector $\boldsymbol{K}$, one has that $\psi_{n,\boldsymbol{k}} = \psi_{n,\boldsymbol{k}+\boldsymbol{K}}$. Therefore, all different Bloch waves occur for $\boldsymbol{k}$-values within the first Brillouin zone of the lattice [91].

1.3.3. Floquet-Bloch theory

The classical approach, known as Floquet-Bloch (F-B) theory, belongs to the class of solutions to 1D periodic linear differential equations of the form $\dot{x} = A(t)x$, with $A(t)$ a piecewise continuous periodic function with period T. Floquet's theorem, due to Gaston Floquet [92], gives a canonical form for each fundamental matrix solution of this common linear system, through a coordinate change that transforms the periodic system to a traditional linear system with constant real coefficients.

In solid-state physics, the extension of this result to 3D systems is known as Bloch's theorem. In the literature dealing with wave propagation problems in mechanical systems [55], [93], the theory is generally referred to as Floquet-Bloch theory [92].

In physics and engineering, dispersion diagrams represent the effect of dispersion on the properties of a wave traveling within a material, and thus they offer a good perspective to explain the wave field behavior inside bodies, relating the wave length or wave number to the wave frequency. Dispersion may be caused either by geometric boundary conditions or by interaction of the waves with the transmitting system and, in its presence, wave velocity is no longer uniquely defined, leading to the distinction between the concepts of phase velocity and group velocity.

The Helmholtz equation is a known example of equation describing the spatial behavior, where the physical periodic structure of the studied object translates into spatial periodicity of its coefficients. In this context, the F-B theory can be applied to obtain the dispersion characteristics of different periodic systems. The F-B theory reduces the problem to the calculations performed in the so-called unit cell, under certain specific boundary conditions derived accordingly [94]. Thus, it provides a strategy to obtain a set of solutions of a linear ordinary equations system of the form:

$$\boldsymbol{f}'(x) = \boldsymbol{M}(x)\boldsymbol{f}(x), \tag{39}$$

where $\boldsymbol{f}(x)$ is the solution vector and the matrix $\boldsymbol{M}$ is periodic such that $\boldsymbol{M}(x+L) = \boldsymbol{M}(x)$ for a given period L. If $\boldsymbol{F}$ is a fundamental matrix of solutions, then a matrix $\boldsymbol{B}$ can be found such that:

$$\boldsymbol{F}(x+L) = \boldsymbol{B}\boldsymbol{F}(x). \tag{40}$$

$\boldsymbol{B}$ can be constructed by setting $x = 0$ in Equation (40) such that $\boldsymbol{B} = \boldsymbol{F}^{-1}(0)\boldsymbol{F}(L)$. The simplest case is obtained using $\boldsymbol{F}(0) = \boldsymbol{I}$, so that $\boldsymbol{B} = \boldsymbol{F}(L)$. There is not a unique choice for the fundamental matrix $\boldsymbol{F}$, therefore $\boldsymbol{B}$ is also not unique. However, its eigenvalues are intrinsic to the problem and, under the right transformation, it can be used as a propagator or evolution factor, relating the value of the solution at a point inside the period with its value at a point outside of it. Only the solution inside a period is therefore needed, verifying that:

$$\hat{\boldsymbol{f}}(x+L) = \beta_F \hat{\boldsymbol{f}}(x). \tag{41}$$

According to the classical nomenclature, $\beta_F = e^{k_F L}$ is called Floquet multiplier, while k_F is the complex Floquet exponent. Furthermore, Floquet found that the solution at any point can be factorized in two terms:

$$\hat{\boldsymbol{f}}(x) = \boldsymbol{f}(x)e^{k_F x}, \tag{42}$$

where $\boldsymbol{f}(x)$ is a periodic function, that represents the eigenvectors if $\boldsymbol{M}$ is a constant matrix and carries the periodicity L of the coefficients of the problem [94].

1.3.4. Dispersion relations

In physics and engineering, dispersion relations represent the effect of dispersion in a medium on the properties of a wave traveling within it [95]. A dispersion relation relates the wave length (or wave number) of a wave to its frequency. Dispersion may be caused either by geometric boundary conditions or by interaction of the waves with the transmitting material; it happens when pure plane waves, with distinct wave lengths, have distinct propagation velocities, so that a wave packet of different wave lengths tends to spread out in space.

The speed of a plane wave, v, is a function of the wave length λ. The wave speed, length, and frequency are related by the identity [96]:

$$v(\lambda) = \lambda f(\lambda). \tag{43}$$

The function $f(\lambda)$ constitutes the dispersion relation of the given medium. Dispersion relations are more commonly expressed as functions of the wavenumber $k = \frac{2\pi}{\lambda}$ [96]:

$$f(k) = \frac{k}{2\pi} v(k), \tag{44}$$

2. EQUIVALENT FLUID MODEL ANALYSES

"Science is the captain, and practice the soldiers."

(Leonardo da Vinci)

2.1. Shift cell operator technique

2.1.1. Introduction

The main advantage of designing sound packages with periodic patterns [76], [97] is that they can provide a combination of absorption, resonance and wave interferences effects [12]–[15]. This leads to several applications in transportation (aeronautics [17], [18], space, automotive [19]–[23], railway), energy and civil engineering fields, where both weight and space, as well as vibroacoustic comfort, still constitute critical issues [24].

Of course, one of the most important necessities is to develop efficient numerical techniques in order to handle the problem. In the classical approach, the displacement field is modeled exactly in the direction of wave propagation, by using a harmonic function, and in an approximated way in the perpendicular directions, by using finite elements. Then, an eigenvalue problem is formulated by introducing the displacement field into the governing equations. The solution of the eigenvalue problem at a specific frequency, gives the wave numbers of all the propagating modes [44]. The two most popular numerical approaches that can be distinguished for computing dispersion curves are the Semi-Analytical Finite Element method (SAFE) and the Wave Finite Element (WFE) method [44].

The main disadvantage of the SAFE method is that the finite elements used are not standard, and therefore they should be defined for each particular application. Nevertheless, many specific FE for different types of structures have been developed since 1975 [44]. Gavric used this technique to calculate the dispersion relationship in a free rail by using triangular and quadrilateral elements, with those elements obtained from Hamilton's principle [98]. Hayashi *et al.* derived the SAFE formulation for the wave guides of complex cross-sectional shape through virtual work principles [99]. By using Lagrange's equations, Damljanovic and Weaver developed the linear triangular elements for SAFE method to investigate the elastic waves in wave guides of arbitrary cross-section [100]. The wave mode characteristics in damped wave guides were examined by Bartoli *et al.*, with the elements derived also from Hamilton's principle [101]. The SAFE technique has also been adopted to investigate the wave propagation characteristics for thin-walled structures by Finnveden [102].

In order to avoid development of specific finite elements, the Wave Finite Element Method considers the structures as periodic in order to model, with standard FE, a period of the structure. Through the use of the Periodic Structure Theory (PST), an eigenvalue problem can be formulated from the stiffness and mass matrices of the finite element model, in order to find the wave numbers of all propagating waves [44]. By using WFE technique, one can introduce structural or viscous damping, as indicated by Duhamel [103]. This approach involves the resolution of a complex polynomial or transcendental eigenvalue problem, as underlined by Mace and Manconi [104]. Contrary to SAFE method, the displacement field is approximated in the direction of propagation. Thus, some numerical issues can arise when the size of the finite element mesh is too coarse. As recommended by Mace and Manconi, a minimum of six elements per wave length is a good rule of thumb to ensure a reliable analysis [104].

One of the main problems of these two approaches is the difficulty to deal with complex mechanical wave propagation specifically of multi-modal nature. Indeed, the existence at each frequency step of a number of wavemodes that potentially exchange energy make the computation and characterization of wave attenuation a delicate task.

To this aim, Collet *at al.* introduced a new numerical formulation, the so-called shift cell, in order to compute the multi-modal damped wave numbers in the whole first Brillouin zone of periodic visco-elastic media, with non-homogeneous and generic frequency-dependent damping characteristics [44].

Herein, the shift cell operator technique is re-formulated for porous materials, providing details on its implementation [105]. Essentially, the shift cell technique consists in a reformulation of Floquet-Bloch periodic conditions, whose added value is that it provides information (dispersion curves) that are independent from the excitation, and thus it represents a valuable tool for the design of original solutions that will be efficient regardless of the excitation. In particular, its major advantage stands in allowing the introduction of a generic frequency dependence of visco-elastic material behavior [44]; this is essential, if one needs to compute the dispersion curves of a porous material modeled as an equivalent fluid. Indeed, even if the usage of F-B periodic conditions actually allows it, a very powerful non-linear solver is required in that case. The shift cell operator, instead, leads to a quadratic eigenvalue problem even in the presence of frequency-dependences and/or damping. The main reason why the shift cell method differs from the classical F-B approach is that it consists in a reformulation of classical F-B conditions, in which the phase shift of the boundary conditions and the exponential amplitude decrease, related to wave propagation, are integrated into the partial derivative operator. Consequently, the periodicity is included in the overall behavior of the structure while the continuity conditions are imposed at the edges of the unit cell [38]–[43].

2.1.2. Weak formulation

Considering a porous layer modeled as an equivalent fluid, using either Delany-Bazley or Johnson-Champoux-Allard model, the starting point is the classical Helmholtz equation:

$$\rho \frac{\omega^2}{K} p + \Delta p = 0, \tag{45}$$

where $p = p(\boldsymbol{x}, \omega)$ is the acoustic pressure, $\boldsymbol{x} = (x, y, z)$ is the coordinate vector, ω is the angular frequency, $\rho = \rho(\omega)$ is the equivalent fluid density and $K = K(\omega)$ is the bulk modulus [97]. The periodicity is described by $\rho(\boldsymbol{x} - \boldsymbol{r}\boldsymbol{n}) - \rho(\boldsymbol{x}) = 0$ and $K(\boldsymbol{x} - \boldsymbol{r}\boldsymbol{n}) - K(\boldsymbol{x}) = 0, \forall \boldsymbol{x} \in \Omega$, where $\boldsymbol{n}$ is a vector of integers normal to the face considered, $\boldsymbol{r} = (\boldsymbol{r}_1; \boldsymbol{r}_2; \boldsymbol{r}_3)$ is a matrix containing the three vectors defining the cell periodicity directions and lengths, and Ω is the domain of interest.

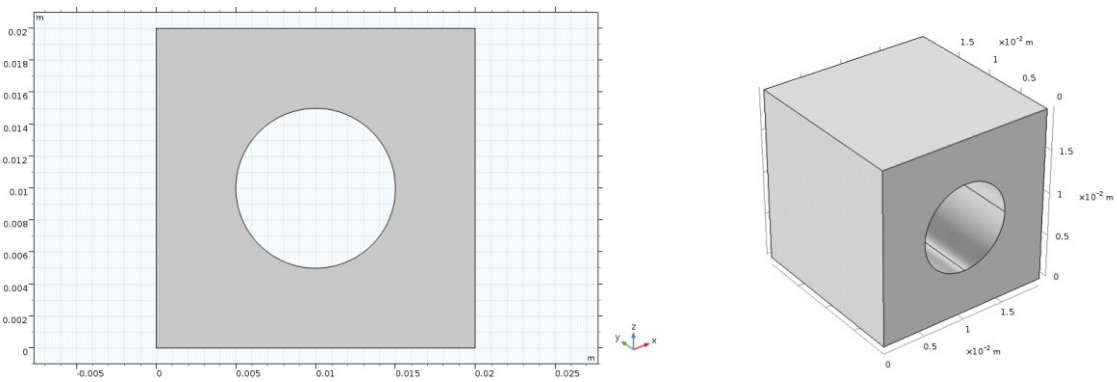

Figure 8: 2D and 3D unit cells used in COMSOL implementation of shift cell technique. The 2D geometry (on the left) is a 2 cm square with a 5 mm radius circular hole, while the 3D one (on the right) is a 2 cm cube with a 5 mm radius cylindrical hole.

This applies everywhere except on the discontinuity surfaces, where appropriate boundary conditions apply. When inclusions with finite densities and bulk moduli are used, these are the continuity conditions stated on pressure and normal velocity; instead, when perfectly rigid inclusions are considered, the normal velocity on the inclusion surfaces vanishes.

By further developing Equation (45) and applying the Bloch theorem, which generalizes Floquet's results to 3D systems, such as $p(\boldsymbol{x},\omega) = p(\boldsymbol{x})e^{j\boldsymbol{k}\boldsymbol{x}}$, where $\boldsymbol{k}$, for a 3D application with real angles, is:

$$\boldsymbol{k} = k\boldsymbol{\theta} = k\begin{bmatrix} cos\theta cos\phi \\ cos\theta sin\phi \\ sin\theta \end{bmatrix}, \tag{46}$$

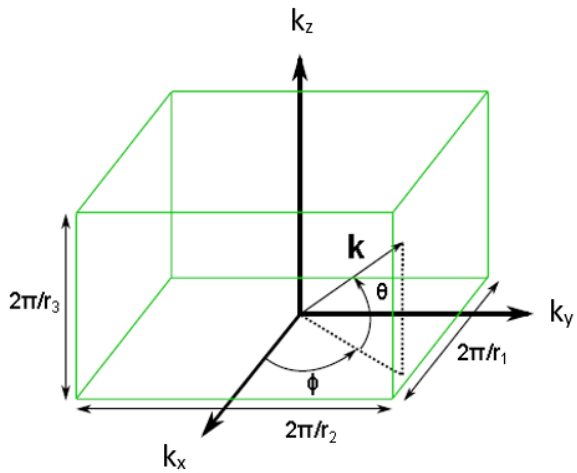

Figure 9: Reciprocal lattice vector in a 3D unitary cell [105].

one can obtain:

$$\rho\frac{\omega^2}{K}p + (\boldsymbol{\nabla} + j\boldsymbol{k})^T \cdot (\boldsymbol{\nabla} + j\boldsymbol{k})p = 0. \tag{47}$$

$p(x)$ being periodic, the Dirichlet boundary conditions imply continuity along the periodic directions. A weak formulation consists in finding p such that $\forall\tilde{p}$, which obeys to the periodic boundary conditions, one has:

$$\omega^2 \int_\Omega \frac{1}{K}\tilde{p}p\, d\Omega + \int_\Omega \frac{1}{\rho}\tilde{p}\boldsymbol{\nabla}^T \cdot \boldsymbol{\nabla}p\, d\Omega +$$

$$+j\boldsymbol{k} \cdot \int_\Omega \frac{1}{\rho}\tilde{p}\boldsymbol{\nabla}^T p\, d\Omega + j\boldsymbol{k}^T \cdot \int_\Omega \frac{1}{\rho}\tilde{p}\boldsymbol{\nabla}p\, d\Omega - (\boldsymbol{k}^T \cdot \boldsymbol{k}) \int_\Omega \frac{1}{\rho}\tilde{p}p\, d\Omega = 0. \tag{48}$$

The solution approach follows a common weak formulation of a differential problem in a discrete coordinate scheme. After rewriting the second term through the use of an integration by parts, for which the considerations on classical weighted residual methods [106] are valid, and considering that Γ is the boundary domain, one obtains:

$$\omega^2 \int_\Omega \frac{1}{K}\tilde{p}p\, d\Omega + \int_\Gamma \frac{1}{\rho}\tilde{p}\boldsymbol{\nabla}^T p\, d\Gamma - \int_\Omega \frac{1}{\rho}\boldsymbol{\nabla}\tilde{p} \cdot \boldsymbol{\nabla}^T p\, d\Omega +$$

$$+2j\boldsymbol{k} \cdot \int_\Omega \frac{1}{\rho}\tilde{p}\boldsymbol{\nabla}^T p\, d\Omega - (\boldsymbol{k}^T \cdot \boldsymbol{k}) \int_\Omega \frac{1}{\rho}\tilde{p}p\, d\Omega = 0. \tag{49}$$

The boundary condition causes the integral on the boundary to vanish:

$$\omega^2 \int_\Omega \frac{1}{K}\tilde{p}p\, d\Omega - \int_\Omega \frac{1}{\rho}\boldsymbol{\nabla}\tilde{p}\cdot\boldsymbol{\nabla}^T p\, d\Omega + 2j\boldsymbol{k}\cdot\int_\Omega \frac{1}{\rho}\tilde{p}\boldsymbol{\nabla}^T p\, d\Omega - (\boldsymbol{k}^T\cdot\boldsymbol{k})\int_\Omega \frac{1}{\rho}\tilde{p}p\, d\Omega = 0. \quad (50)$$

$$\omega^2 \int_\Omega \frac{1}{K}\tilde{p}p\, d\Omega - \int_\Omega \frac{1}{\rho}\boldsymbol{\nabla}\tilde{p}\cdot\boldsymbol{\nabla}^T p\, d\Omega +$$

$$+j\boldsymbol{k}\cdot\int_\Omega \frac{1}{\rho}(\tilde{p}\boldsymbol{\nabla}^T p - \boldsymbol{\nabla}^T\tilde{p}p)\, d\Omega - (\boldsymbol{k}^T\cdot\boldsymbol{k})\int_\Omega \frac{1}{\rho}\tilde{p}p\, d\Omega = 0. \quad (51)$$

Finally, one can discretize the weak formulation through the Finite Element Method: considering that $\boldsymbol{\varphi}$ is the eigenvector, Equation (51) can be written in its matrix form:

$$\left(\underline{\underline{K}} + jk\underline{\underline{L}} + k^2\underline{\underline{H}} - \omega^2\underline{\underline{M}}\right)\boldsymbol{\varphi} = 0, \quad (52)$$

with the following matrices:

- $\underline{\underline{K}} \propto \int_\Omega \frac{1}{\rho}\boldsymbol{\nabla}\tilde{p}\cdot\boldsymbol{\nabla}p\, d\Omega$;
- $\underline{\underline{L}} \propto \int_\Omega \frac{1}{\rho}(\boldsymbol{\nabla}\tilde{p}p - \tilde{p}\boldsymbol{\nabla}p)\cdot\boldsymbol{\theta}\, d\Omega$;
- $\underline{\underline{H}} \propto \int_\Omega \frac{1}{\rho}\tilde{p}p\, d\Omega$;
- $\underline{\underline{M}} \propto \int_\Omega \frac{1}{K}\tilde{p}p\, d\Omega$.

Here, $\underline{\underline{M}}$ and $\underline{\underline{K}}$ are respectively the symmetric mass and symmetric stiffness matrices, $\underline{\underline{L}}$ is a skew-symmetric matrix and $\underline{\underline{H}}$ is a symmetric matrix; all of them are complex and frequency-dependent.

2.1.3. Right and left eigenvalue problems

In this section, the link between left and right eigenvectors is derived. A left eigenvector of a matrix is the same as the right eigenvector of the same real transposed matrix. Equation (52) leads to the following right eigenvalue problem:

$$\left[\left(\underline{\underline{K}} - \omega^2\underline{\underline{M}}\right) + \lambda_i\underline{\underline{L}} - \lambda_i^2\underline{\underline{H}}\right]\boldsymbol{\varphi}_i^r = 0, \quad (53)$$

where $\lambda_i = jk_i$ is the i-th eigenvalue and $\boldsymbol{\varphi}_i^r$ denotes the right eigenvector associated to λ_i. Equation (53) can be rewritten as

$$\underline{\underline{A_1}}(\omega)\boldsymbol{\psi}_i^r = \lambda_i\underline{\underline{A_2}}(\omega)\boldsymbol{\psi}_i^r, \quad (54)$$

with

- $\underline{\underline{A_1}}(\omega) = \begin{pmatrix} 0 & \underline{\underline{I_d}} \\ \underline{\underline{K}} - \omega^2\underline{\underline{M}} & \underline{\underline{L}} \end{pmatrix}$;
- $\underline{\underline{A_2}}(\omega) = \begin{pmatrix} \underline{\underline{I_d}} & 0 \\ 0 & \underline{\underline{H}} \end{pmatrix}$;
- $\boldsymbol{\psi}_i^r = \begin{pmatrix} \boldsymbol{\varphi}_i^r \\ \lambda_i\boldsymbol{\varphi}_i^r \end{pmatrix}$.

where $\underline{\underline{I_d}}$ is the identity matrix. Conversely, a left-eigenvector for the same eigenvalue satisfies:

$$\boldsymbol{\psi}_i^{l^T} \underline{\underline{A_1}}(\omega) = \lambda_i \boldsymbol{\psi}_i^{l^T} \underline{\underline{A_2}}(\omega), \text{ with } \boldsymbol{\psi}_i^l = \begin{pmatrix} \underline{\underline{A}} \\ \underline{\underline{B}} \end{pmatrix}. \tag{55}$$

$$\begin{pmatrix} \underline{\underline{A}}^T & \underline{\underline{B}}^T \end{pmatrix} \begin{pmatrix} 0 & \underline{\underline{I_d}} \\ \underline{\underline{K}} - \omega^2 \underline{\underline{M}} & \underline{\underline{L}} \end{pmatrix} = \lambda_i \begin{pmatrix} \underline{\underline{A}}^T & \underline{\underline{B}}^T \end{pmatrix} \begin{pmatrix} \underline{\underline{I_d}} & 0 \\ 0 & \underline{\underline{H}} \end{pmatrix}, \tag{56}$$

$$\begin{pmatrix} \underline{\underline{B}}^T (\underline{\underline{K}} - \omega^2 \underline{\underline{M}}) & \underline{\underline{A}}^T \underline{\underline{I_d}} + \underline{\underline{B}}^T \underline{\underline{L}} \end{pmatrix} = \lambda_i \begin{pmatrix} \underline{\underline{A}}^T \underline{\underline{I_d}} & \underline{\underline{B}}^T \underline{\underline{H}} \end{pmatrix}, \tag{57}$$

$$\begin{cases} \underline{\underline{B}}^T \left(\underline{\underline{K}} - \omega^2 \underline{\underline{M}} \right) = \lambda_i \left(\underline{\underline{A}}^T \underline{\underline{I_d}} \right) \\ \underline{\underline{A}}^T \underline{\underline{I_d}} + \underline{\underline{B}}^T \underline{\underline{L}} = \lambda_i (\underline{\underline{B}}^T \underline{\underline{H}}) \end{cases}, \tag{58}$$

$$\begin{cases} \underline{\underline{B}}^T \left(\underline{\underline{K}} - \omega^2 \underline{\underline{M}} \right) - \lambda_i \left(\underline{\underline{A}}^T \underline{\underline{I_d}} \right) = 0 \\ \underline{\underline{A}}^T \underline{\underline{I_d}} + \underline{\underline{B}}^T \underline{\underline{L}} - \lambda_i (\underline{\underline{B}}^T \underline{\underline{H}}) = 0 \end{cases}, \tag{59}$$

$$\underline{\underline{B}}^T \left(\underline{\underline{K}} - \omega^2 \underline{\underline{M}} \right) + \lambda_i \left(\underline{\underline{A}}^T \underline{\underline{I_d}} + \underline{\underline{B}}^T \underline{\underline{L}} \right) - \lambda_i \left(\underline{\underline{A}}^T \underline{\underline{I_d}} \right) - \lambda_i^2 (\underline{\underline{B}}^T \underline{\underline{H}}) = 0, \tag{60}$$

$$\underline{\underline{B}}^T \left[\left(\underline{\underline{K}} - \omega^2 \underline{\underline{M}} \right) + \lambda_i \underline{\underline{L}} - \lambda_i^2 \underline{\underline{H}} \right] = 0, \tag{61}$$

$$\left[\left(\underline{\underline{K}} - \omega^2 \underline{\underline{M}} \right) + \lambda_i \underline{\underline{L}} - \lambda_i^2 \underline{\underline{H}} \right]^T \underline{\underline{B}} = 0, \tag{62}$$

$$\left[\left(\underline{\underline{K}} - \omega^2 \underline{\underline{M}} \right) - \lambda_i \underline{\underline{L}} - \lambda_i^2 \underline{\underline{H}} \right] \underline{\underline{B}} = 0, \tag{63}$$

$$\left[\left(\underline{\underline{K}} - \omega^2 \underline{\underline{M}} \right) + \lambda_{-i} \underline{\underline{L}} - \lambda_{-i}^2 \underline{\underline{H}} \right] \boldsymbol{\varphi}_{-i}^r = 0, \tag{64}$$

$$\begin{cases} \underline{\underline{B}} = \boldsymbol{\varphi}_{-i}^r = \boldsymbol{\varphi}_i^l \\ \underline{\underline{A}}^T = \lambda_i \boldsymbol{\varphi}_{-i}^{r^T} \underline{\underline{H}} - \boldsymbol{\varphi}_{-i}^{r^T} \underline{\underline{L}} = \lambda_i \boldsymbol{\varphi}_i^{l^T} \underline{\underline{H}} - \boldsymbol{\varphi}_i^{l^T} \underline{\underline{L}} \end{cases}. \tag{65}$$

In the resolution of the right eigenvalue problem, the i-th mode ($i \in N^+$) is defined by its λ_i and its eigenvector $\boldsymbol{\varphi}_i^r$. For each mode i, a mode $-i$ is associated with λ_{-i} such that $\lambda_{-i} = -\lambda_i$ and $\boldsymbol{\varphi}_{-i}^r = \boldsymbol{\varphi}_i^l$. Therefore, by solving the right eigenvalue problem, the left solution is found too [105].

2.1.4. Group velocity

For frequency-dependent systems, the estimation of the group velocity is not trivial [107]. In order to find its expression, Equation (54) is now differentiated with respect to ω:

$$\frac{\partial \underline{\underline{A_1}}(\omega)}{\partial \omega} \boldsymbol{\psi}_i^r + \underline{\underline{A_1}}(\omega) \frac{\partial \boldsymbol{\psi}_i^r}{\partial \omega} = \frac{\partial \lambda_i}{\partial \omega} \underline{\underline{A_2}}(\omega) \boldsymbol{\psi}_i^r + \lambda_i \frac{\partial \underline{\underline{A_2}}(\omega)}{\partial \omega} \boldsymbol{\psi}_i^r + \lambda_i \underline{\underline{A_2}}(\omega) \frac{\partial \boldsymbol{\psi}_i^r}{\partial \omega}, \tag{66}$$

and multiplied by the left eigenvector such that:

$$\boldsymbol{\psi}_i^{l^T} \frac{\partial \underline{\underline{A_1}}(\omega)}{\partial \omega} \boldsymbol{\psi}_i^r + \boldsymbol{\psi}_i^{l^T} \underline{\underline{A_1}}(\omega) \frac{\partial \boldsymbol{\psi}_i^r}{\partial \omega} =$$

$$= \boldsymbol{\psi}_i^{l^T} \frac{\partial \lambda_i}{\partial \omega} \underline{\underline{A_2}}(\omega) \boldsymbol{\psi}_i^r + \boldsymbol{\psi}_i^{l^T} \lambda_i \frac{\partial \underline{\underline{A_2}}(\omega)}{\partial \omega} \boldsymbol{\psi}_i^r + \boldsymbol{\psi}_i^{l^T} \lambda_i \underline{\underline{A_2}}(\omega) \frac{\partial \boldsymbol{\psi}_i^r}{\partial \omega}. \tag{67}$$

Considering that:

$$\boldsymbol{\psi}_i^{l^T} \underline{\underline{A_1}}(\omega) = \lambda_i \boldsymbol{\psi}_i^{l^T} \underline{\underline{A_2}}(\omega), \tag{68}$$

one obtains:

$$\boldsymbol{\psi}_i^{l^T} \frac{\partial \underline{\underline{A_1}}(\omega)}{\partial \omega} \boldsymbol{\psi}_i^r = \boldsymbol{\psi}_i^{l^T} \frac{\partial \lambda_i}{\partial \omega} \underline{\underline{A_2}}(\omega) \boldsymbol{\psi}_i^r + \boldsymbol{\psi}_i^{l^T} \lambda_i \frac{\partial \underline{\underline{A_2}}(\omega)}{\partial \omega} \boldsymbol{\psi}_i^r, \tag{69}$$

$$\boldsymbol{\psi}_i^{l^T} \frac{\partial \lambda_i}{\partial \omega} \underline{\underline{A_2}}(\omega) \boldsymbol{\psi}_i^r = \boldsymbol{\psi}_i^{l^T} \frac{\partial \underline{\underline{A_1}}(\omega)}{\partial \omega} \boldsymbol{\psi}_i^r - \boldsymbol{\psi}_i^{l^T} \lambda_i \frac{\partial \underline{\underline{A_2}}(\omega)}{\partial \omega} \boldsymbol{\psi}_i^r, \tag{70}$$

$$\frac{\partial \lambda_i}{\partial \omega} \boldsymbol{\psi}_i^{l^T} \underline{\underline{A_2}}(\omega) \boldsymbol{\psi}_i^r = \boldsymbol{\psi}_i^{l^T} \left[\frac{\partial \underline{\underline{A_1}}(\omega)}{\partial \omega} - \lambda_i \frac{\partial \underline{\underline{A_2}}(\omega)}{\partial \omega} \right] \boldsymbol{\psi}_i^r, \tag{71}$$

$$\frac{\partial \lambda_i}{\partial \omega} = \frac{\boldsymbol{\psi}_i^{l^T} \left[\frac{\partial \underline{\underline{A_1}}(\omega)}{\partial \omega} - \lambda_i \frac{\partial \underline{\underline{A_2}}(\omega)}{\partial \omega} \right] \boldsymbol{\psi}_i^r}{\boldsymbol{\psi}_i^{l^T} \underline{\underline{A_2}}(\omega) \boldsymbol{\psi}_i^r}, \tag{72}$$

which gives the expression of the group slowness using $\lambda_i = jk_i$:

$$\frac{\partial k_i}{\partial \omega} = -j \frac{\boldsymbol{\psi}_i^{l^T} \left[\frac{\partial \underline{\underline{A_1}}(\omega)}{\partial \omega} - \lambda_i \frac{\partial \underline{\underline{A_2}}(\omega)}{\partial \omega} \right] \boldsymbol{\psi}_i^r}{\boldsymbol{\psi}_i^{l^T} \underline{\underline{A_2}}(\omega) \boldsymbol{\psi}_i^r}, \tag{73}$$

$$\frac{\partial k_i}{\partial \omega} = -j \frac{\boldsymbol{\psi}_i^{l^T} \begin{pmatrix} 0 & 0 \\ \frac{\partial (\underline{\underline{K}} - \omega^2 \underline{\underline{M}})}{\partial \omega} & \frac{\partial \underline{\underline{L}}}{\partial \omega} - \lambda_i \frac{\partial \underline{\underline{H}}}{\partial \omega} \end{pmatrix} \boldsymbol{\psi}_i^r}{\boldsymbol{\psi}_i^{l^T} \begin{pmatrix} \underline{\underline{I_d}} & 0 \\ 0 & \underline{\underline{H}} \end{pmatrix} \boldsymbol{\psi}_i^r}, \tag{74}$$

$$\frac{\partial k_i}{\partial \omega} = -j \frac{\begin{pmatrix} \lambda_i \boldsymbol{\varphi}_i^{l^T} \underline{\underline{H}} - \boldsymbol{\varphi}_i^{l^T} \underline{\underline{L}} & \boldsymbol{\varphi}_i^{l^T} \end{pmatrix} \begin{pmatrix} 0 & 0 \\ \frac{\partial (\underline{\underline{K}} - \omega^2 \underline{\underline{M}})}{\partial \omega} & \frac{\partial \underline{\underline{L}}}{\partial \omega} - \lambda_i \frac{\partial \underline{\underline{H}}}{\partial \omega} \end{pmatrix} \begin{pmatrix} \boldsymbol{\varphi}_i^r \\ \lambda_i \boldsymbol{\varphi}_i^r \end{pmatrix}}{\begin{pmatrix} \lambda_i \boldsymbol{\varphi}_i^{l^T} \underline{\underline{H}} - \boldsymbol{\varphi}_i^{l^T} \underline{\underline{L}} & \boldsymbol{\varphi}_i^{l^T} \end{pmatrix} \begin{pmatrix} \underline{\underline{I_d}} & 0 \\ 0 & \underline{\underline{H}} \end{pmatrix} \begin{pmatrix} \boldsymbol{\varphi}_i^r \\ \lambda_i \boldsymbol{\varphi}_i^r \end{pmatrix}}, \tag{75}$$

$$\frac{\partial k_i}{\partial \omega} = -j \frac{\begin{pmatrix} \lambda_i \boldsymbol{\varphi}_i^{l^T} \underline{\underline{H}} - \boldsymbol{\varphi}_i^{l^T} \underline{\underline{L}} & \boldsymbol{\varphi}_i^{l^T} \end{pmatrix} \begin{pmatrix} 0 \\ \frac{\partial (\underline{\underline{K}} - \omega^2 \underline{\underline{M}})}{\partial \omega} \boldsymbol{\varphi}_i^r + \lambda_i \left(\frac{\partial \underline{\underline{L}}}{\partial \omega} - \lambda_i \frac{\partial \underline{\underline{H}}}{\partial \omega} \right) \boldsymbol{\varphi}_i^r \end{pmatrix}}{\begin{pmatrix} \lambda_i \boldsymbol{\varphi}_i^{l^T} \underline{\underline{H}} - \boldsymbol{\varphi}_i^{l^T} \underline{\underline{L}} & \boldsymbol{\varphi}_i^{l^T} \end{pmatrix} \begin{pmatrix} \underline{\underline{I_d}} \boldsymbol{\varphi}_i^r \\ \lambda_i \underline{\underline{H}} \boldsymbol{\varphi}_i^r \end{pmatrix}}, \tag{76}$$

$$\frac{\partial k_i}{\partial \omega} = -j \frac{\boldsymbol{\varphi}_i^{l^T} \left[\frac{\partial (\underline{\underline{K}} - \omega^2 \underline{\underline{M}})}{\partial \omega} + \lambda_i \left(\frac{\partial \underline{\underline{L}}}{\partial \omega} - \lambda_i \frac{\partial \underline{\underline{H}}}{\partial \omega} \right) \right] \boldsymbol{\varphi}_i^r}{\left[\lambda_i \boldsymbol{\varphi}_i^{l^T} \underline{\underline{H}} - \boldsymbol{\varphi}_i^{l^T} \underline{\underline{L}} \right] \underline{\underline{I_d}} \boldsymbol{\varphi}_i^r + \boldsymbol{\varphi}_i^{l^T} \lambda_i \underline{\underline{H}} \boldsymbol{\varphi}_i^r}, \tag{77}$$

$$\frac{\partial k_i}{\partial \omega} = -j \frac{\boldsymbol{\varphi}_i^{l^T} \left[-2\omega \underline{\underline{M}} + \frac{\partial \underline{\underline{K}}}{\partial \omega} + \lambda_i \frac{\partial \underline{\underline{L}}}{\partial \omega} - \lambda_i^2 \frac{\partial \underline{\underline{H}}}{\partial \omega} \right] \boldsymbol{\varphi}_i^r}{\boldsymbol{\varphi}_i^{l^T} \left[-\underline{\underline{L}} + 2\lambda_i \underline{\underline{H}} \right] \boldsymbol{\varphi}_i^r}. \tag{78}$$

Finally, the complex group velocity is the inverse of the complex group slowness:

$$C_g = \frac{\partial \omega}{\partial k_i} = \frac{j \boldsymbol{\varphi}_i^{l^T} \left[-\underline{\underline{L}} + 2\lambda_i \underline{\underline{H}} \right] \boldsymbol{\varphi}_i^r}{\boldsymbol{\varphi}_i^{l^T} \left[-2\omega \underline{\underline{M}} + \frac{\partial \underline{\underline{K}}}{\partial \omega} + \lambda_i \frac{\partial \underline{\underline{L}}}{\partial \omega} - \lambda_i^2 \frac{\partial \underline{\underline{H}}}{\partial \omega} \right] \boldsymbol{\varphi}_i^r}. \tag{79}$$

It should be pointed out that the frequency dependence of equivalent fluid models is generally known analytically; therefore, the computation of C_g is fast due to the fact that the derivatives of the matrices with respect to ω can be expressed analytically:

$$\frac{\partial \underline{\underline{K}}}{\partial \omega} = -\frac{1}{\rho^2}\frac{\partial \rho}{\partial \omega}\underline{\underline{K}}, \frac{\partial \underline{\underline{L}}}{\partial \omega} = -\frac{1}{\rho^2}\frac{\partial \rho}{\partial \omega}\underline{\underline{L}}, \frac{\partial \underline{\underline{H}}}{\partial \omega} = -\frac{1}{\rho^2}\frac{\partial \rho}{\partial \omega}\underline{\underline{H}}, \tag{80}$$

with $\frac{\partial \rho}{\partial \omega}$ to be derived from the specific equivalent fluid model chosen. This is without doubts the most efficient way to perform the C_g computation, but one could also opt to numerically estimate the matrix derivatives, or even directly the $\frac{\Delta\omega}{\Delta k_i}$ values.

2.1.5. Classifying criteria to distinguish propagative and evanescent waves

For undamped systems, waves are sorted according to their propagative (k purely real) or evanescent (k purely imaginary) behavior. When dissipation occurs, such as it happens for a porous material modeled as an equivalent fluid, all wave numbers are complex; as a consequence, there is no purely propagative solution and all waves are damped, with a decay rate that may be used to distinguish the branches in two categories: those that are rapidly damped and those that are slowly damped in space. Hence, the latter could be classified as propagative ones.

In general, the distinction between them is difficult and thus some classifying criteria are proposed:

I. The ratio between the real and the imaginary parts of every wavenumber [105]: $C_I = real(k)/imag(k)$. The physical meaning of C_I is related to the fact that the real part of a wave number represents the propagative behavior, while its imaginary part is linked to the dissipation and therefore should be smaller than the real part in order to be able to consider a wave as propagative. It should be noted that, since the real part of k is periodic while the imaginary one is not, in order to correctly apply this criterion, the real part of k must be turned into non-periodic, by mirroring it in correspondence to each period; in particular, starting with $a = 2$ and for each frequency f_i with $i > 0$ of a specific dispersion branch, the procedure is as it follows:

$$\text{if } \frac{\mathrm{d}f_{i-1}}{\mathrm{d}real(k_{i-1})} > 0 \text{ and if } \frac{\mathrm{d}f_i}{\mathrm{d}real(k_i)} < 0 \rightarrow real(k_{1:end}) = a\frac{\pi}{r} - real(k_{1:end}), a = a + 1. \tag{81}$$

II. The ratio between the real parts of the energy transport speed, defined as $v_E = \frac{I}{E}$ for undamped waves, and the group velocity C_g: $C_{II} = \frac{real(v_E)}{real(C_g)}$, where I is the flow of energy and $E = E_k + E_p = \int_\Omega \frac{1}{2}(\rho v^2 + \frac{p^2}{\rho c^2})d\Omega$ is the total energy. Waves may be qualified as propagative if the energy is transported at a velocity which is at least close to the order of C_g.

Only the waves corresponding to $C_I > \tau_I$ and $C_{II} > \tau_{II}$ are classified as propagative. In practice, in the context of the following analysis, the thresholds τ are chosen such as $\tau_I = 1$ and $\tau_{II} = 0.7$; these values may be chosen differently according to the problem of interest. The choice of k, C_g and v_E as indicators of the "propagativeness" nature of a wave at a specific frequency has been originally proposed by Billon [105], who defined criteria similar to the ones above; in the present work, they have been re-formulated, in order to specifically adapt them for the application on porous materials modeled as equivalent fluids.

Since there is no strict distinction between “propagative” and “evanescent” waves, an alternative approach would be to define an indicator of the propagativeness nature for each ω value of the dispersion relation, as it is shown in Section 2.3.2..

2.1.6. Validation of the method

In order to validate the shift cell technique implementation for a porous material modeled as an equivalent fluid, in the studied configuration and for propagation along the x-axis, a first calculation is made to compare shift cell results with those obtained using classical F-B periodic conditions, using (non-dissipative) air as material and a perfectly rigid cylindrical inclusion located at the center of the unit cell [108].

The validation analysis is performed in the frequency range 0 – 17000 Hz: this is an interesting range for acoustic applications and it assures that the wave length is much larger than the pore size (≈100 µm), which is a necessary condition in order to use equivalent fluid models. The size of the perfectly rigid cylindrical inclusion is also large, compared to the typical characteristic lengths that may be observed on a representative unit cell describing the macroscopic behavior of the foam [109].

The 2D and 3D unit cells are respectively constituted by a 2 cm square with a 0.5 cm radius circular rigid inclusion and by a 2 cm cube with a 0.5 cm radius cylindrical rigid inclusion. For analogous cases, some results are available in literature in terms of absorption coefficient [110]. In particular, one can observe that this arrangement exhibits a band gap between 6000 Hz and 10000 Hz for waves propagating along x direction.

It should be noted that, in this work, the 3D cases are in fact 2D ones solved with 3D meshing, not exploiting the possibility, from the geometrical point of view, of doing a 2D meshing. This choice is motivated by the fact that a 3D mesh actually captures the behavior along an additional direction respect to the 2D one, thus allowing to carry out analyses for any combination of angles ϕ and θ [111].

Dashed red lines in Figure 10 correspond to the results obtained with the Floquet-Bloch method, while blue points represent the results obtained through the shift cell approach. The comparison shows a perfect agreement between the results of the two techniques.

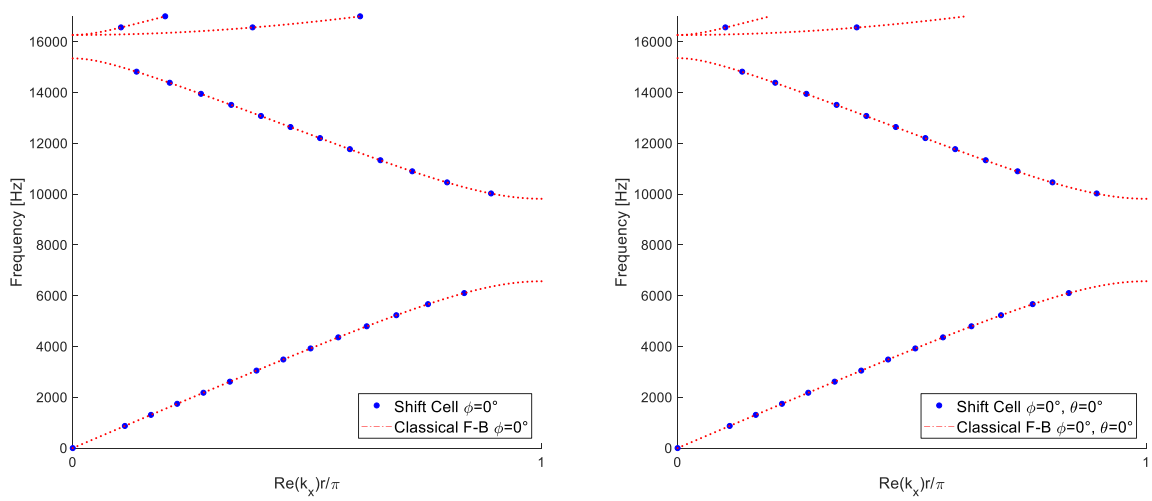

Figure 10: Comparison between dispersion curves obtained with classical Floquet-Bloch and shift cell techniques on a 2D (on the left) and 3D (on the right) unit cell made of air.

2.1.7. Meaning and behavior of band gaps for inclusions of increasing size

In this section, it is shown what happens to the band gap, in the previously defined 2D unit cell, when the size of the inclusion (that has perfectly rigid walls) changes. Now both real and imaginary parts are shown, the latter being actually positive but shown as negative in the plots due to axis consistence. If no damping is included in the model, k is either purely real, the wave is then propagative, or purely imaginary, the wave being then evanescent. The radius of the inclusion for the three cases represented in Figure 11 are respectively equal to $\frac{s}{32}$, $\frac{s}{4}$ and $\frac{s}{2.1}$, where s is the side length: the opening frequency of the Bragg band gap decreases when the radius is increased, and at the same time the width of the gap increases. On the contrary, instead of using the adiabatic value (142 kPa) for the bulk modulus of air, one can artificially add a frequency-constant imaginary part to it (142+j12 kPa is used here for illustration), so that one can simulate a band gap behavior in presence of dissipation, similar to that obtained when using equivalent fluids, as shown later.

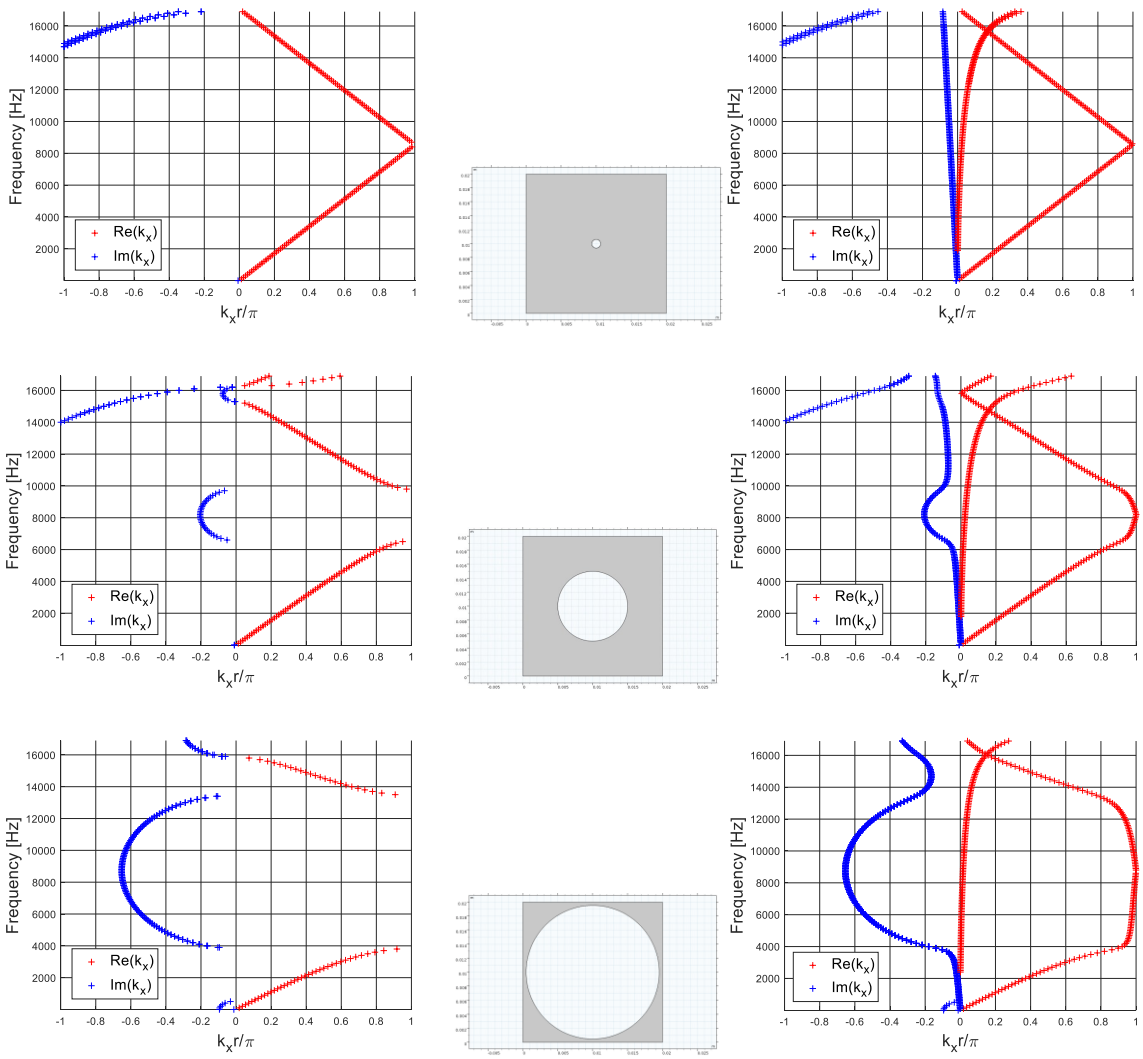

Figure 11: Dispersion curves for a 2D cell made of air, with increasing inclusion radius (from top to bottom: $s/32$, $s/4$ and $s/2.1$, with adiabatic (left column) and complex (right column) bulk modulus.

Indeed, a complex bulk modulus prevents the presence of ideal band gaps in dispersion curves; one can clearly see that the gap is opening but, because of the damping, k_x is no longer purely imaginary around the band gap, the slow branch with undamped material becomes a fast wave when damping is added and allows rapid and damped energy transportation inside the band gap. So, the real part of k_x (being mirrored and turned into non-periodic as explained in the 1st classifying criterion introduced in Section 2.1.5) is not equal to $\frac{\pi}{r}$ anymore, but remains low (compared to the imaginary one), which means that the wave will be strongly spatially attenuated, and this is exactly the expected behavior for band gaps in dissipative media. Also, a very fast branch, for which the imaginary part goes out of the plot bound, can be observed in the right column of Figure 11.

2.1.8. Comparison of computational cost

Figure 12 and Figure 13 show a comparison of the computational cost, in terms of time and as a function of the number of elements in the finite element model, between the shift cell and the F-B techniques. In particular, both eigenproblems are solved using 100 frequency steps. The 2D unit cell is meshed using triangular elements while, for the 3D geometry, tetrahedral elements are used. Both 2D and 3D geometries correspond to those shown in Figure 8 and these results, in terms of computational times, are related to an undamped case. Raw data are also approximated through a piecewise cubic Hermite interpolating polynomial technique.

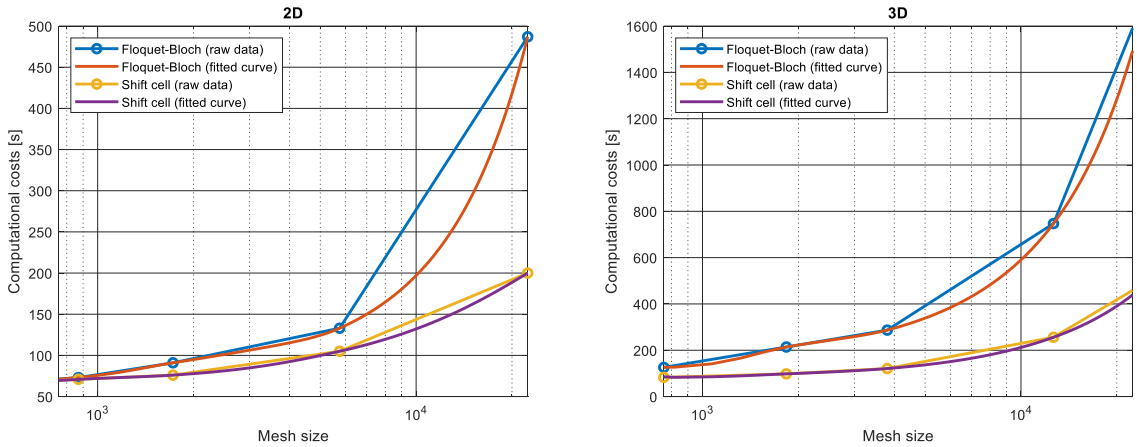

Figure 12: Computational times [s] in the 2D (left) and 3D (right) cases, for increasing number of elements.

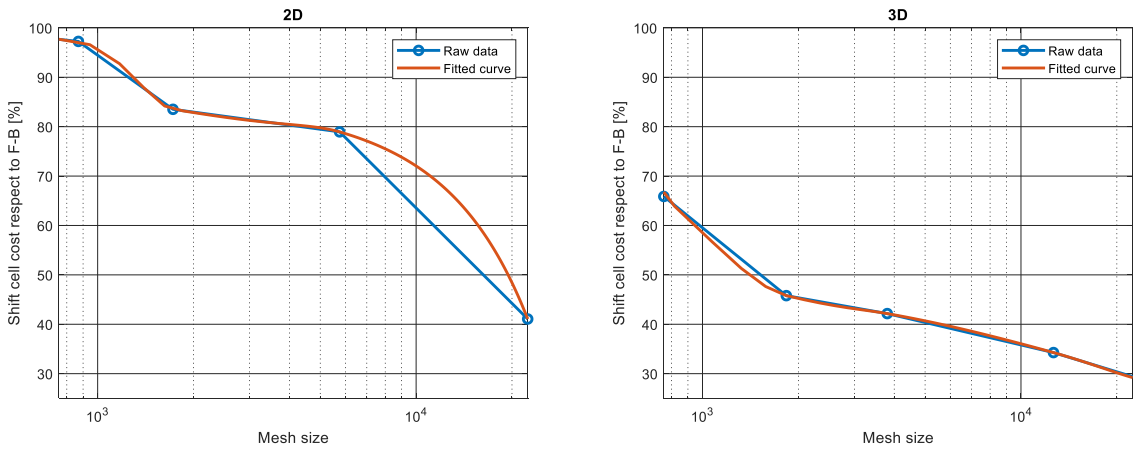

Figure 13: Computational time percentage in the 2D (left) and 3D (right) cases, for increasing number of elements.

As a conclusion, for the case of interest, the calculation cost is always lower with the proposed approach than the one required by the classical technique. The gain becomes more advantageous when the number of elements of the finite element mesh increases, which makes the technique even more attractive. The lower cost is attributed to the handling of the boundary conditions, which is much simpler in the proposed approach, where continuity instead of classical F-B periodic conditions are imposed.

2.2. Numerical results

Dispersion curves (calculated with the shift cell technique) and acoustical characteristics (computed using classical Floquet-Bloch periodic conditions) for different numerical test cases are shown in Appendix A. In particular, they are obtained for each possible combination between two geometries (with and without inclusion), two models (2D and 3D), two equivalent fluids (Delany-Bazley and Johnson-Champoux-Allard models) and two materials (melamine and "black" polyurethane foams). While dispersion curves are computed for an infinite repetition of unit cells, absorption coefficient and transmission loss are calculated for a finite repetition of five unit cells, using the same domain and boundary conditions of the infinite periodic system. This, in a first approximation, allows the comparison between dispersion and acoustical characteristics of the equivalent finite system. Indeed, it has been noted that a further increase in the number of repeated unit cells would lead to a change in the mean value of absorption coefficient and transmission loss respectively below 2% and 20%, respect to the usage of a repetition of five unit cells. It should be also highlighted that a homogeneous 3D unit cell with a 2D periodicity essentially represents an infinite layer with a given thickness; however, in the context of this manuscript, in order to keep a consistent nomenclature, this configuration is still addressed as "homogeneous case" or "homogeneous unit cell". In particular, continuity conditions are applied along x-axis and z-axis, while sound hard wall boundary conditions are used on the surfaces orthogonal to the y-axis. It is well known that the parameters of the equivalent fluid models can have a strong impact on the performances of the acoustic device [112], hence they should be obtained in a precise way. In the current case, they have been experimentally determined in GAUS laboratory at University of Sherbrooke (Canada) and are reported in Table 1.

Table 1: Acoustical parameters for two porous materials modeled as equivalent fluids: black PU and melamine.

	Black PU	**Melamine**
Porosity	0.96	0.99
Tortuosity	1.075	1.02
Resistivity [Pa*s/m^2]	5815	8430
Viscous characteristic length [mm]	0.102	0.138
Thermal characteristic length [mm]	0.269	0.154
Density [kg/m^3]	29.5	5.73

2.2.1. Dispersion curves

For each dispersion curve plot, three eigenvectors are reported. They are all extracted at the frequency of 8500 Hz (half of the range) and along the direction that conventionally corresponds to $\phi = \theta = 0°$ in the first Brillouin zone. Their branches are ordered as: at increasing frequencies, "1st" is represented by the first real part that reaches the unitary value, "2nd" is the second one and so on.

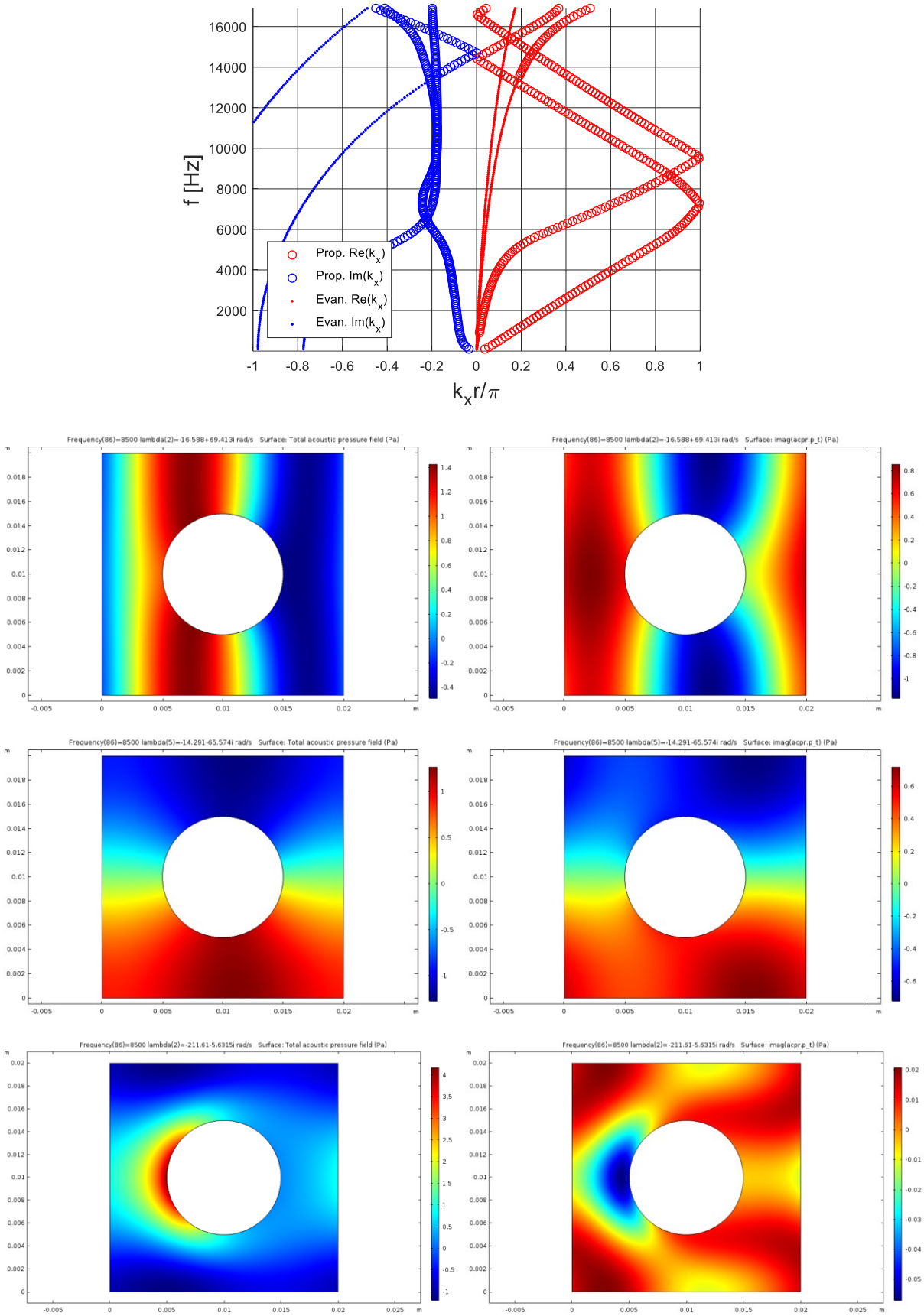

Figure 14: Dispersion curves for a JCA-modeled melamine 2D unit cell with a perfectly rigid inclusion; from top to bottom, the 1st, 2nd and 3rd branch eigenvectors are shown in terms of real (on the left) and imaginary (on the right) parts.

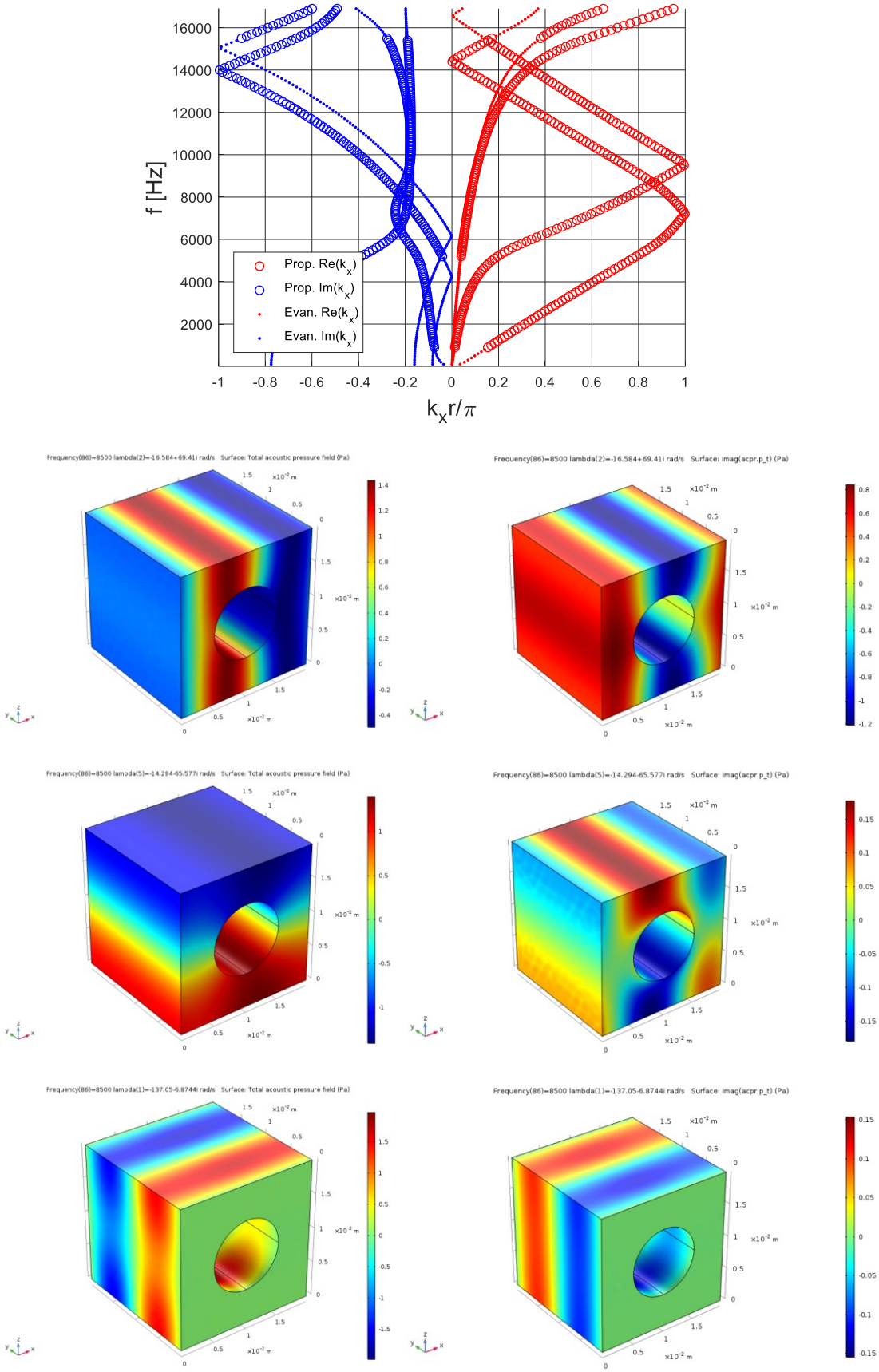

Figure 15: Dispersion curves for a JCA-modeled melamine 3D unit cell with a perfectly rigid inclusion; from top to bottom, the 1st, 2nd and 3rd branch eigenvectors are shown in terms of real (on the left) and imaginary (on the right) parts.

One may notice that there could be some discontinuous curves where the wave propagates, then becomes evanescent, then propagates again (or vice-versa): this is not an expected configuration, and it is probably due to the fact that all waves are evanescent with different rates and so a non-perfect tuning of the sorting criteria could lead to lines that disappears and reappears on the plots.

In conclusion, from the comparison between the models in Figure 14 and Figure 15, it can be derived that the 2D model captures in an efficient way the general physics of the system, except for an additional fast compressional wave, which is taken into account only through the use of the correspondent 3D model. Therefore, as explained in Section 2.1.6, a 3D meshing is necessary in order to carry out dispersion analyses for each combination of angles ϕ and θ.

2.2.2. Absorption coefficient

The absorption coefficient is usually computed starting from the surface impedance [113]. This technique is only valid for plane waves impinging upon homogeneous materials, and just at low frequencies for non-homogeneous ones. In a more general way, that is always correct, the absorption coefficient can be determined as [114]:

$$\alpha = \frac{\Pi_{dissipated}}{\Pi_{incident}}, \text{ where } \Pi_{dissipated} = \Pi_{thermal} + \Pi_{viscous}. \tag{82}$$

The terms can be expressed as [114]:

$$\Pi_{incident} = \frac{S|p_0|^2}{2\rho_0 c_0}, \tag{83}$$

$$\Pi_{thermal} = \frac{1}{2}\Im\left(-\omega \int_{\Omega_p} \frac{\phi^2}{K} pp^* d\Omega\right), \Pi_{viscous} = \frac{1}{2}\Im\left(\int_{\Omega_p} \frac{\phi^2}{\omega\tilde{\rho}_{22}} \underline{\boldsymbol{\nabla}} p . \underline{\boldsymbol{\nabla}} p^* d\Omega\right), \tag{84}$$

where

- $S =$ surface interested by incident pressure;
- $p_0 =$ amplitude of the excitation mode (incident pressure);
- $\rho_0 =$ density of the interstitial fluid (air);
- $c_0 =$ sound speed in the interstitial fluid (air);
- $\Omega =$ poro-elastic volume;
- $p^* = conj(p)$;
- $\underline{\boldsymbol{\nabla}}\ operator =$ gradient.

In order to check the correct implementation of power calculations, one can perform these two checks:

- $p_{surface} = (1 + R)p_0$;
- $\Pi_{dissipated} = \Pi_{input} = \frac{1}{2}\Re \int_S pv^* dS$, where v is the velocity.

Note that the second equation is valid only if there are no other dissipating sources in addition to the material itself [115]. For the cases with inclusion, some differences between curves can be observed at high frequencies. As expected, the curve computed through the averaged impedance is different from (and less correct than) the two computed using power ratios; the small gap between these two, instead, can be explicated as a FE error due to the numerical integrations that are required in order to estimate the specific power contributions.

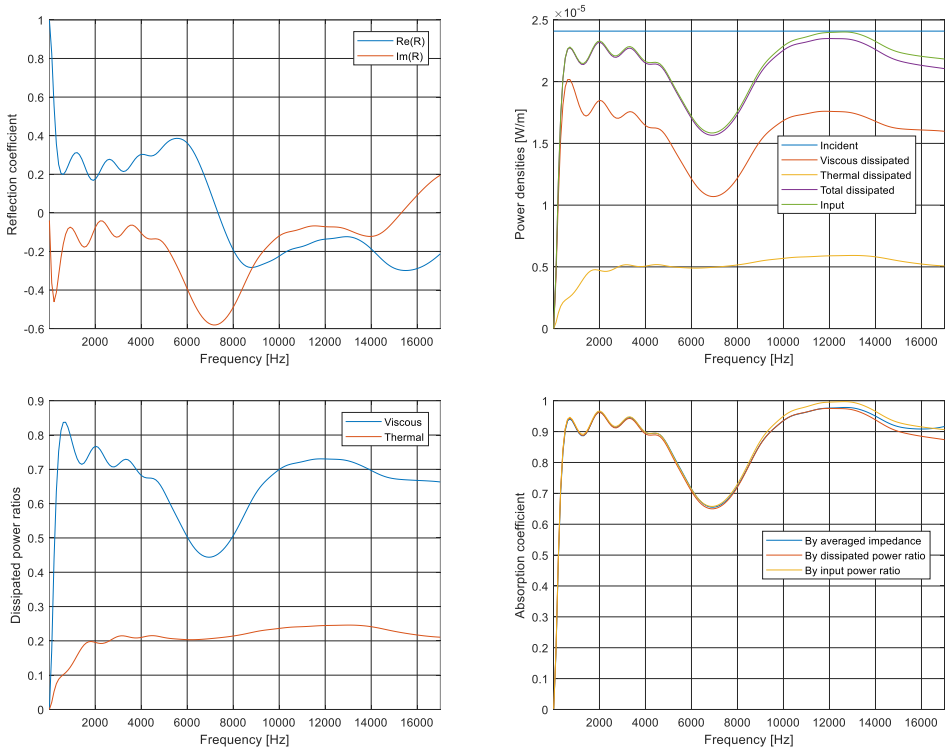

Figure 16: Reflection coefficient, power densities, dissipated power ratios and absorption coefficient computed for a 2D JCA-modeled melamine foam with a perfectly rigid inclusion.

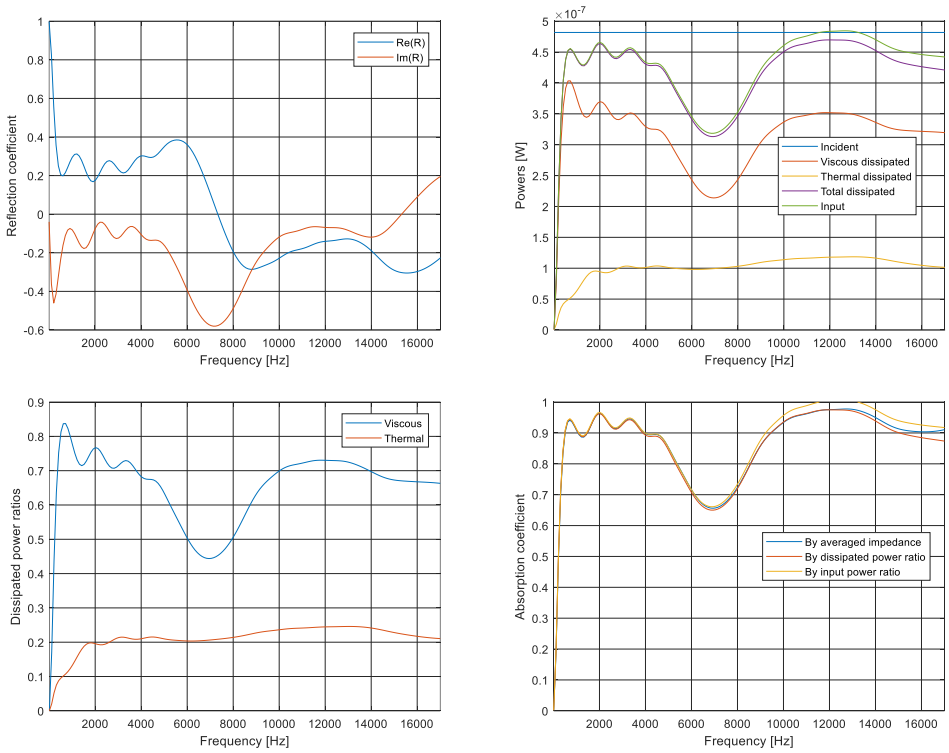

Figure 17: Reflection coefficient, powers, dissipated power ratios and absorption coefficient computed for a 3D JCA-modeled melamine foam with a perfectly rigid inclusion.

2.2.3. Transmission loss

In order to obtain the following plots, transmission losses are numerically calculated as:

$$TL = 10\log_{10}\frac{\Pi_{incident}}{\Pi_{transmitted}}, \tag{85}$$

where $\Pi_{incident}$ and $\Pi_{transmitted}$ represent the incident and transmitted power, respectively [116]. For a plane wave configuration, the value computed for homogeneous flat configurations is equivalent to the one obtained with the Transfer Matrix Method [10], [117]:

$$TL = 10\log\left(\frac{1}{4}\left|T_{11} + \frac{T_{12}}{\rho_0 c_0} + \rho_0 c_0 T_{21} + T_{22}\right|^2\right), \tag{86}$$

$$\text{with } \begin{bmatrix} T_{11} & T_{12} \\ T_{21} & T_{22} \end{bmatrix} = \begin{bmatrix} \cos(k_m d) & j\sin(k_m d)\, Z_c \\ \frac{j\sin(k_m d)}{Z_c} & \cos(k_m d) \end{bmatrix}, \tag{87}$$

and the formula provided by Doutres *et al.* [118]. Both of these two formulas are valid only for a finite depth layer and homogeneous isotropic material; therefore, while in the homogeneous cases the comparison between these methods represents a validation of the numerical results, for the cases with inclusion it has the purpose to show the differences respect to the homogeneous curves.

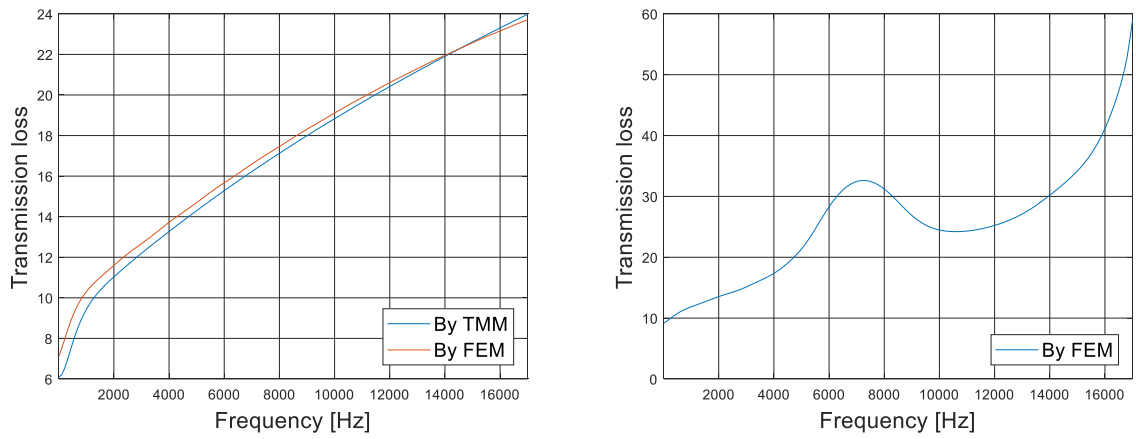

Figure 18: Transmission loss computed for a 2D JCA-modeled melamine foam; homogeneous (on the left) and with a perfectly rigid inclusion (on the right).

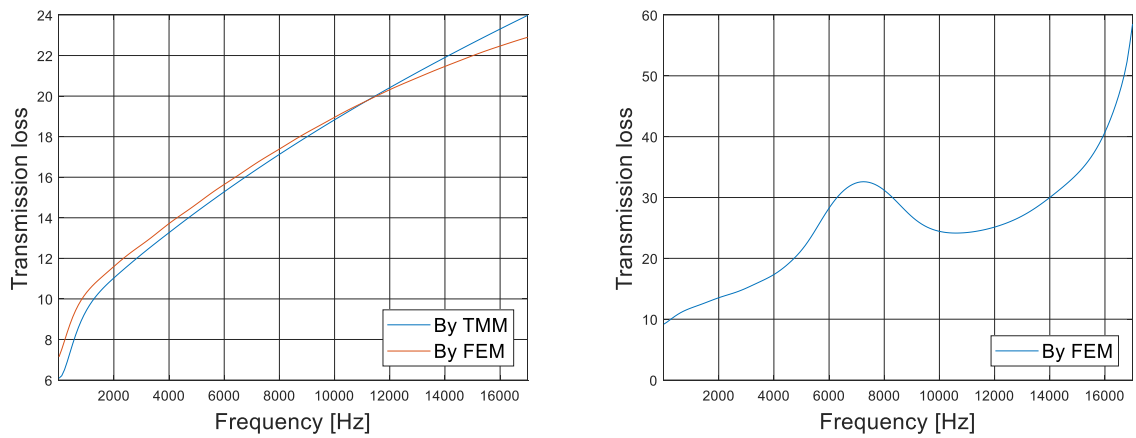

Figure 19: Transmission loss computed for a 3D JCA-modeled melamine foam; homogeneous (on the left) and with a perfectly rigid inclusion (on the right).

Concerning the cases with the inclusion, one can notice that an improvement of transmission loss properties is shown at all frequencies [119], in particular in correspondence of a peak at a frequency around 7 kHz, in which it is equal to about 15 dB, and at high frequencies.

2.3. Branch tracking and computation of equivalent absorption coefficient and TL

In the shift cell approach, the pulsation ω and the direction of the wave propagation (ϕ, θ) are imposed. The solutions of the quadratic eigenvalue problem are the waveguides $\lambda_i = jk_i$. There is a set of points, forming branches, which one may wish to connect and follow, according to the nature of each specific branch. Some solutions are proposed in literature, such as a MAC sorting criterion [44], but these methods generally require to store many data at each iteration. Instead, the group velocity constitutes a relevant indicator in order to follow the branches, from a point of calculation to the next one [105]. Thus, this quantity allows to be sure of the correctness of the dispersion relation, in particular in the case of branch crossing.

The proposed approach consists in comparing a single group velocity value at a specific frequency $C_{g_i}(f)$ and $\boldsymbol{C_g}(f + \Delta f)$: from the value associated to a starting point, the routine compares the initial C_{g_i} with all the group velocities at the next frequency step $f + \Delta f$, and a minimization is performed in order to identify the point at $f + \Delta f$ to which is associated the closest value of C_g. Then, this point is defined as the new starting one and so on, step by step, the branch is tracked.

Dispersion curves help designers to understand the nature of the waves that can propagate in a sound package, and the way they are attenuated on the basis of an infinite periodic arrangement of the unit cell. It should be pointed out that the great advantage of this technique is that it allows the designing and the performance estimation of acoustic systems regardless of the number of repeated unit cells along the thickness and of the eventual the mismatch between numerical and real boundary conditions. In particular, in this section, it is shown how these results can be used to compute the transmission loss at normal incidence for an acoustic package composed by a finite arrangement of 5 cells. This, in a first approximation, allows comparing dispersion and acoustical characteristics of the equivalent finite system. For more complex cases, advanced homogenization techniques may be used [120]–[122]. For a plane wave configuration, the transmission loss is computed in three different ways.

I. Transfer matrix method [109], [112] (homogeneous case):

$$TL = 10 \log\left(\frac{1}{4}\left|T_{11} + \frac{T_{12}}{\rho_0 c_0} + \rho_0 c_0 T_{21} + T_{22}\right|^2\right), \tag{88}$$

$$\text{with} \begin{bmatrix} T_{11} & T_{12} \\ T_{21} & T_{22} \end{bmatrix} = \begin{bmatrix} \cos(k_m d) & j\sin(k_m d)\, Z_c \\ \frac{j\sin(k_m d)}{Z_c} & \cos(k_m d) \end{bmatrix}; \tag{89}$$

II. Full FEM with 5 cells (case with inclusion):

$$TL = 10 \log_{10} \frac{\Pi_{incident}}{\Pi_{transmitted}}; \tag{90}$$

III. Transfer matrix method with 5 cells, where k and Z_c are provided by the dispersion curves (proposed approach); in order to perform this estimation, only the 1st branch of the diagram is taken into account, since it is the only one to which corresponds an eigenvector along the direction of the plane wave excitation, the others being orthogonal to it. This assumption is

valid as long as, in the frequency range of interest, there are no other propagative dispersion branches to which is associated a mode that acts along the plane wave direction in the TL analysis. For a plane wave that acts along an arbitrary direction, a more complex formulation is required. While k is a direct output of the dispersion relation, the equivalent characteristic impedance is computed as $Z_c = \sqrt{K\rho}$, where the density ρ is obtained from the JCA model and the bulk modulus is calculated as $K = \rho\left(\frac{\omega}{k}\right)^2$.

The 3rd way of computation actually consists in a homogenization and many works that deal with the relation between this kind of approaches and Bloch waves can be found in literature.

It should be noted that, for the sake of comparison with the corresponding dispersion diagram, only the 1st branch (tracked through the previously defined algorithm) is meaningful, due to the fact that the related mode is the only one, between those considered here (which are the lowest order and therefore the least attenuated modes), that is actually excited during these transmission loss analysis. It should be also pointed out that the dispersion branch taken into account is actually propagative, according to the previously defined classifying criteria, in the whole frequency range considered.

For the inhomogeneous configuration, the validation is obtained using an implementation of the plane wave forced response of the periodic cell accounting for fluid loading [123].

2.3.1. Transfer Matrix Method formulation

In the following plots, the Transfer Matrix Method is used to estimate both the equivalent absorption coefficient and the equivalent transmission loss, also for a wave with non-zero incidence.

In order to do this, the formulations are modified as follows: for example, supposing that the thickness d of the sample develops along the x direction, starting from the classical transfer matrix expression:

$$\begin{bmatrix} T_{11} & T_{12} \\ T_{21} & T_{22} \end{bmatrix} = \begin{bmatrix} \cos(k_m d) & j\sin(k_m d)\, Z_c \\ \frac{j\sin(k_m d)}{Z_c} & \cos(k_m d) \end{bmatrix}, \tag{91}$$

one needs to substitute k_m with $k_{tmm} = \sqrt{{k_m}^2 - \left({k_0}^2\left({k_y}^2 + {k_z}^2\right)\right)}$, where:

$$\begin{pmatrix} k_x \\ k_y \\ k_z \end{pmatrix} = \begin{pmatrix} cos\theta cos\phi \\ cos\theta sin\phi \\ sin\theta \end{pmatrix}, \begin{bmatrix} T_{11} & T_{12} \\ T_{21} & T_{22} \end{bmatrix} = \begin{bmatrix} \cos(k_{tmm} d) & j\sin(k_{tmm} d)\, Z_c \\ \frac{j\sin(k_{tmm} d)}{Z_c} & \cos(k_{tmm} d) \end{bmatrix}. \tag{92}$$

The absorption coefficient can then be computed as:

$$Z_{tmm} = \frac{T_{11}}{T_{21}} \rightarrow R_{tmm} = \frac{Z_{tmm}k_x - Z_0}{Z_{tmm}k_x + Z_0} \rightarrow \alpha_{tmm} = 1 - |R_{tmm}|^2, \tag{93}$$

while the transmission loss formula remains unchanged:

$$TL_{tmm} = 10\log\left(\frac{1}{4}\left|T_{11} + \frac{T_{12}}{\rho_0 c_0} + \rho_0 c_0 T_{21} + T_{22}\right|^2\right). \tag{94}$$

In synthesis, the techniques used to estimate the acoustic properties of the unit cell, according to each case, are reported in the following Table 2 and Table 3.

Table 2: Techniques used to estimate the transmission loss, according to the angles of incidence.

	Homogeneous	**Inclusion**
0°, 0°	FEM TMM Equivalent TMM	FEM Equivalent TMM
45°, 45°	TMM Equivalent TMM	Equivalent TMM

Table 3: Techniques used to estimate the absorption coefficient, according to the angles of incidence.

	Homogeneous	**Inclusion**
0°, 0°	Averaged Z_s Dissipated power ratio Input power ratio TMM Equivalent TMM	Averaged Z_s Dissipated power ratio Input power ratio
45°, 45°	TMM Equivalent TMM	*No estimation*

2.3.2. Results

In order to better appreciate the behavior of each branch in the studied frequency range, dispersion and group velocity diagrams are also colorized with a scale of colors that indicates the level of "propagativeness": the value 0 means that the wave at that specific frequency is totally spatially attenuated, while the value 1 represents a properly propagative behavior. In particular, considering the classifying criteria previously defined, if all of them are satisfied then the propagativeness value is equal to 1, otherwise it is computed as the product between the results of the two classifying ratios divided by the correspondent thresholds. It should be noted that, if a specific criterion is satisfied, its contribution to the estimation of the level of propagativeness is always equal to 1, even if its related ratio is larger.

$$\text{if } C_I > \tau_I \rightarrow \ prop_I = 1, \text{ else } prop_I = \frac{C_I}{\tau_I} \tag{95}$$

$$\text{if } C_{II} > \tau_{II} \rightarrow \ prop_{II} = 1, \text{ else } prop_{II} = \frac{C_{II}}{\tau_{II}} \tag{96}$$

$$level\ of\ propagativeness = prop_I prop_{II} \tag{97}$$

For a 3D melamine unit cell, with the previously mentioned properties, the following results are produced: the evanescent – propagative dispersion (Figure 20 and Figure 25) and group velocity (Figure 21 and Figure 26) curves, the branch-tracked dispersion and group velocity curves (Figure 22 and Figure 27) and the comparison of the absorption coefficient (Figure 23) and transmission loss (Figure 24 and Figure 28) curves with the equivalent ones, that are those computed starting from the wave numbers obtained from the dispersion relations. These curves are obtained for both a homogeneous and a heterogeneous (with perfectly rigid inclusion) 3D unit cell, whose foam is modeled as a JCA equivalent fluid. For all studied configurations, the branch-tracking algorithm is able to correctly classify the solutions, even in the presence of band gaps, branch-crossing or branch-veering phenomena. While the equivalent TL computations are almost perfect, those related to the absorption coefficient in the case of the presence of an inclusion are not able to properly reproduce the behavior of the unit cell.

This is due to the fact that the adopted procedure, based on the calculation of Z_c, Z_s, R and α, is valid only for the case of a homogeneous medium interested by incident plane waves.

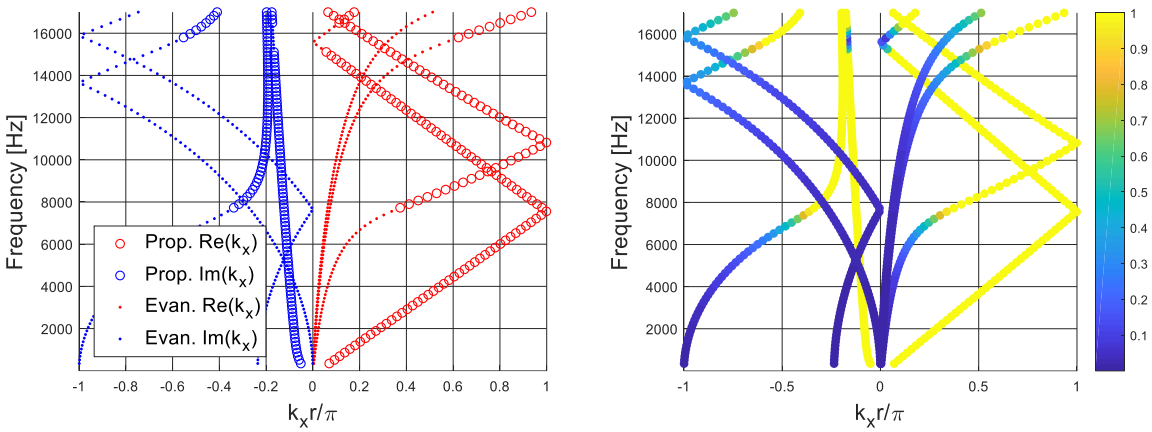

Figure 20: Evanescent and propagative parts of dispersion curves computed for a 3D JCA-modeled melamine unit cell; homogeneous case. The color scale (on the right) indicates the level of propagativeness.

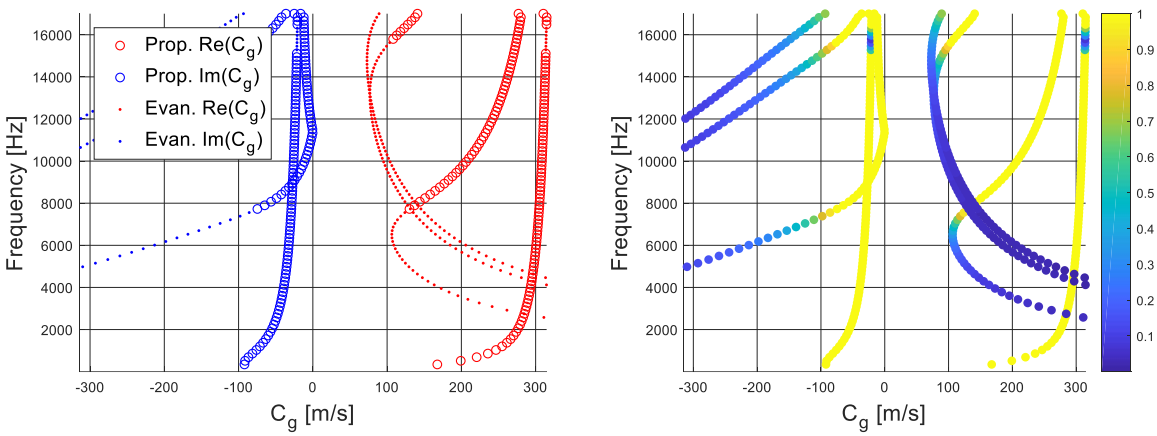

Figure 21: Evanescent and propagative parts of group velocities computed for a 3D JCA-modeled melamine unit cell; homogeneous case. The color scale (on the right) indicates the level of propagativeness.

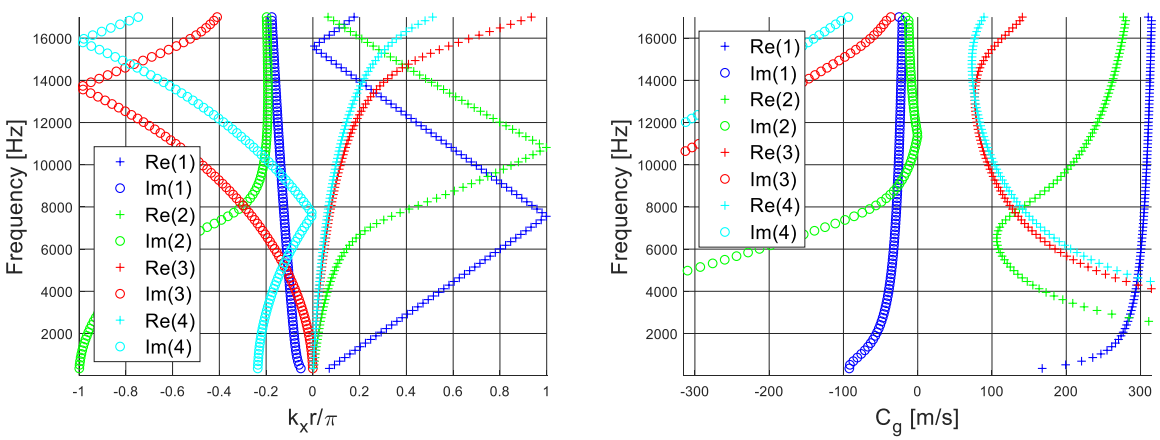

Figure 22: Branch-tracked dispersion curves (on the left) and group velocities (on the right) computed for a 3D JCA-modeled melamine unit cell; homogeneous case.

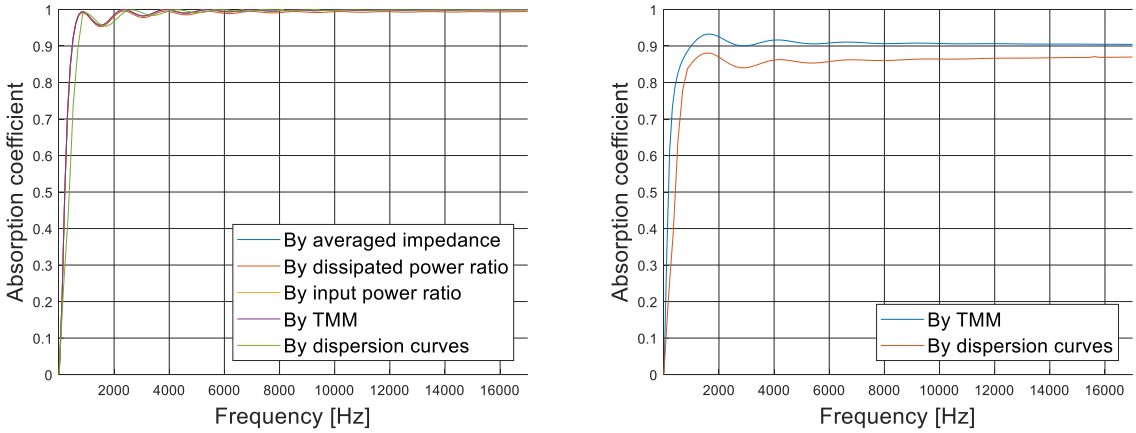

Figure 23: Comparison of absorption coefficient between the equivalent curve and those previously obtained for wave incidence angles $\phi = 0°, \theta = 0°$ (on the left) and $\phi = 45°, \theta = 45°$ (on the right), computed for a 3D JCA-modeled melamine foam; homogeneous case.

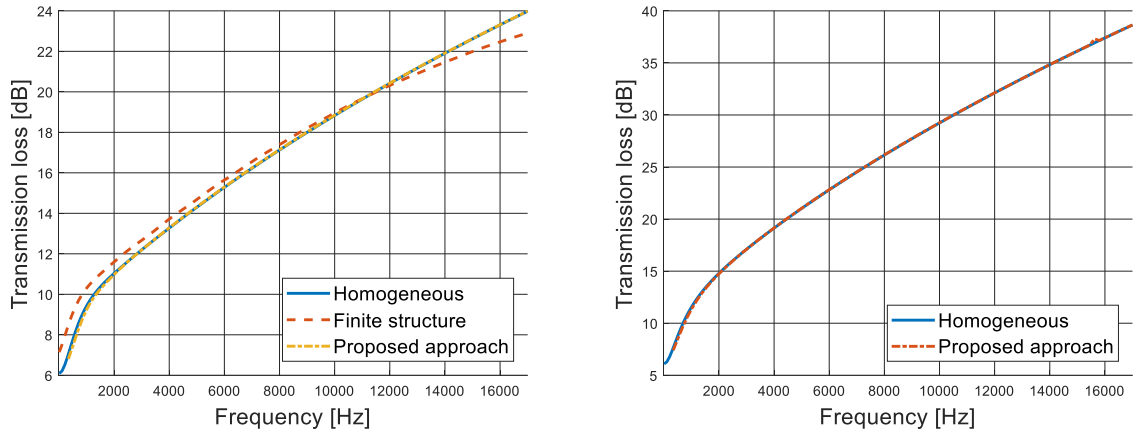

Figure 24: Comparison of transmission loss between the equivalent curve and those previously obtained for wave incidence angles $\phi = 0°, \theta = 0°$ (on the left) and $\phi = 45°, \theta = 45°$ (on the right), computed for a 3D JCA-modeled melamine foam; homogeneous case.

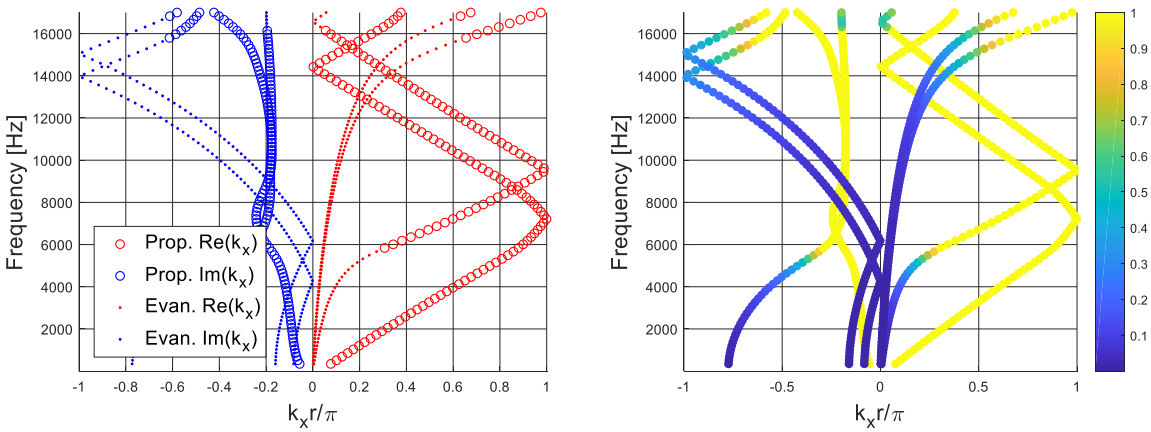

Figure 25: Evanescent and propagative parts of dispersion curves computed for a 3D JCA-modeled melamine unit cell; case with inclusion. The color scale (on the right) indicates the level of propagativeness.

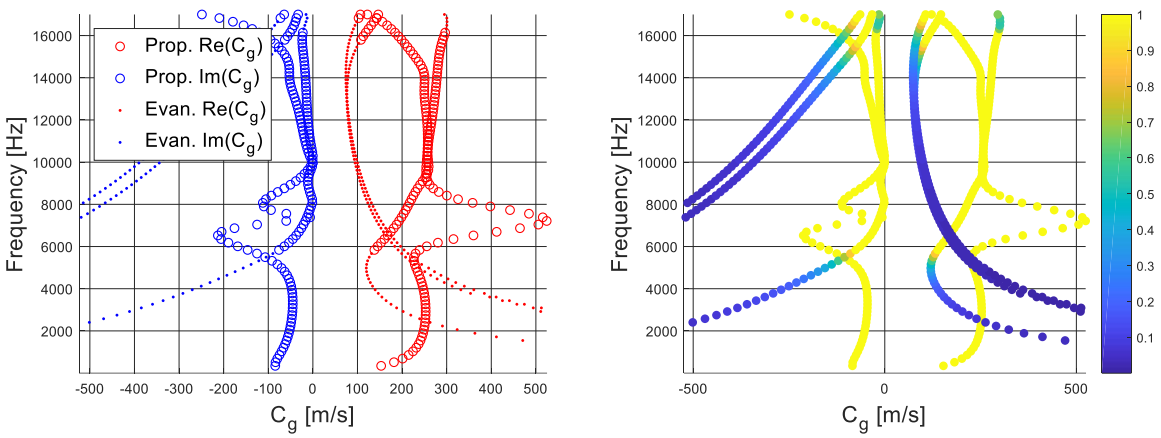

Figure 26: Evanescent and propagative parts of group velocities computed for a 3D JCA-modeled melamine unit cell; case with inclusion. The color scale (on the right) indicates the level of propagativeness.

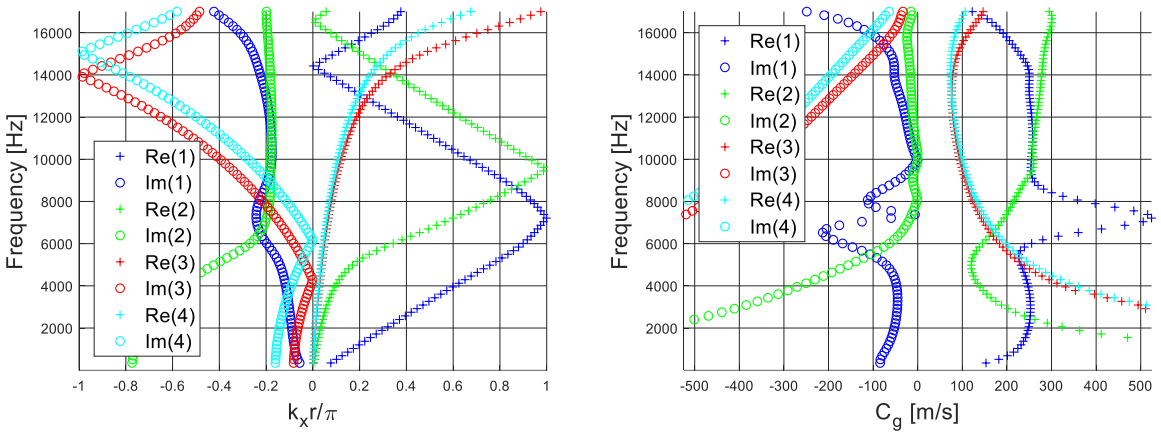

Figure 27: Branch-tracked dispersion curves (on the left) and group velocities (on the right) computed for a 3D JCA-modeled melamine unit cell; case with inclusion.

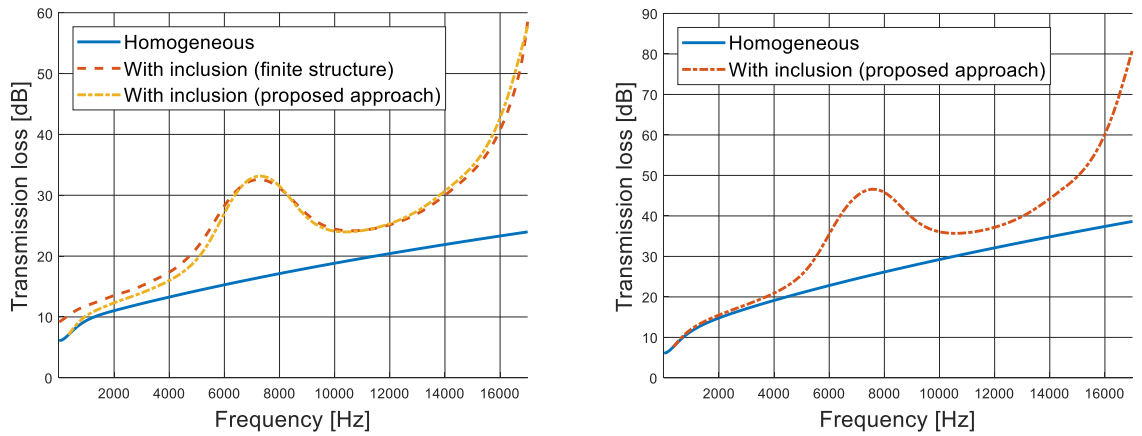

Figure 28: Comparison of transmission loss between the equivalent curve and those previously obtained for wave incidence angles $\phi = 0°, \theta = 0°$ (on the left) and $\phi = 45°, \theta = 45°$ (on the right), computed for a 3D JCA-modeled melamine foam; case with inclusion.

For what concerns the propagative – evanescent plots, one can notice that the first mode is propagative at almost all frequencies, the second one appears to propagate starting from middle frequencies, while the third and fourth ones are relevant only at high frequencies.

2.4. Non-rigid inclusion test campaign

Table 4: Combinations of foams and inclusions used for the non-rigid inclusion test campaign, performed on a 3D JCA-modeled unit cell.

Configuration	Foam	Inclusion	Configuration	Foam	Inclusion
1	Melamine	none	25	M10	none
2		rigid	26		rigid
3		air	27		air
4		PU 1	28		PU 1
5		PU black	29		Melamine
6		M10	30		PU black
7		Mel. 173	31		Mel. 173
8		PU 60	32		PU 60
9	P1	none	33	Melamine 173	none
10		rigid	34		rigid
11		air	35		air
12		Melamine	36		PU 1
13		PU black	37		Melamine
14		M10	38		PU black
15		Mel. 173	39		M10
16		PU 60	40		PU 60
17	PU black	none	41	PU 60	none
18		rigid	42		rigid
19		air	43		air
20		PU 1	44		PU 1
21		Melamine	45		Melamine
22		M10	46		PU black
23		Mel. 173	47		M10
24		PU 60	48		Mel. 173

The same JCA-modeled 3D unit cell can also be tested with some non-rigid inclusions [124]. In particular, 48 setups are discussed here, whose fundamental parameters are reported in Table 4 and Table 5 (air properties are shown in Table 6). In the current case, the characteristics of the materials called “Melamine” and “Black PU” are experimentally determined, while those of the materials called “P1” and “M10” are taken from the work performed by Doutres *et al.* [125] and those related to “Melamine 173” and “PU 60” from a paper by Deckers *et al.* [62]. Except for the “Melamine” and “Melamine 173” materials, all the others are polyurethane foams.

From Figure 109 to Figure 156 in Appendix A.1.1, dispersion curves are computed for each of the 48 cases of study.

Also, some comparative absorption coefficient and transmission loss plots are shown from Figure 29 to Figure 40: in particular, each of the foams is tested using eight different inclusions, according to the combinations reported in Table 4.

Table 5: Non-acoustic parameters of the foams used for the non-rigid inclusion test campaign, performed on a 3D JCA-modeled unit cell.

	Porosity	Tortuosity	Resistivity [Pa*s/m^2]	Viscous characteristic length [mm]	Thermal characteristic length [mm]
Melamine	0.99	1.02	8430	0.138	0.154
P1	0.956	1.06	3490	0.187	0.250
Black PU	0.96	1.075	5815	0.102	0.269
M10	0.982	1.25	3670	0.240	0.310
Mel. 173	0.98	1.01	9500	0.166	0.249
PU 60	0.98	1.17	3750	0.110	0.742

Table 6: Air properties.

Density [kg/m^3]	1.205
Prandtl number	0.713
Dynamic viscosity [kg/(m*s)]	$1.983*10^{-5}$
Adiabatic bulk modulus [kg/(m*s^2)]	$1.42*10^{5}$
Specific heat ratio	1.401

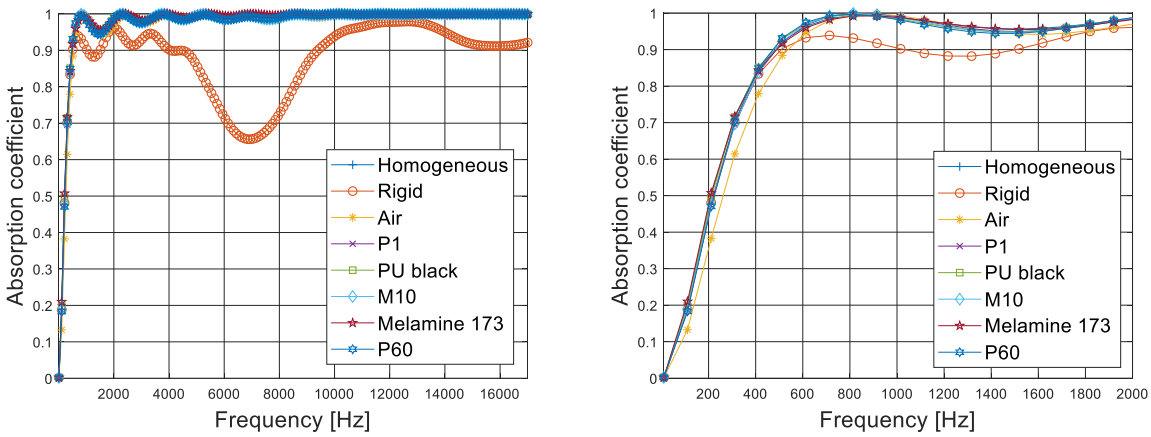

Figure 29: Comparison between the absorption coefficient curves for cases 1-8 of Table 4.

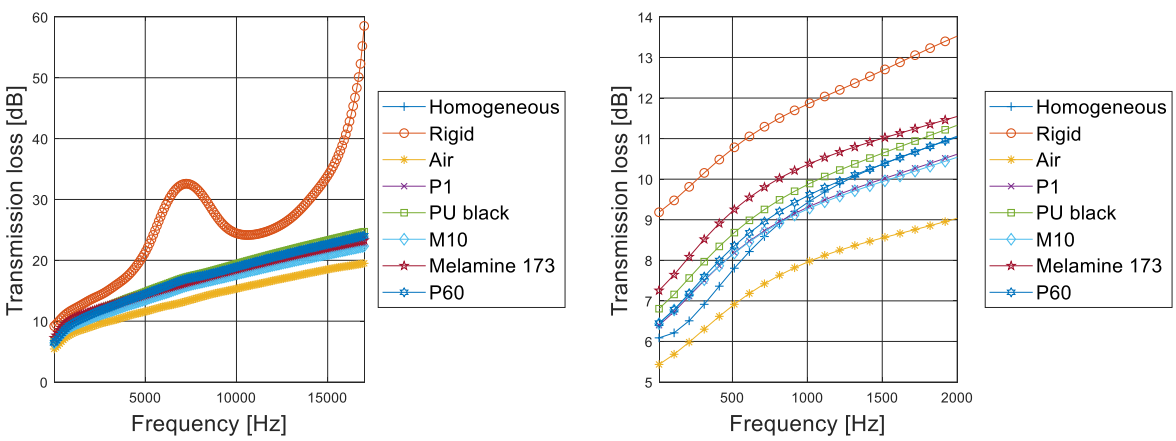

Figure 30: Comparison between the transmission loss curves for cases 1-8 of Table 4.

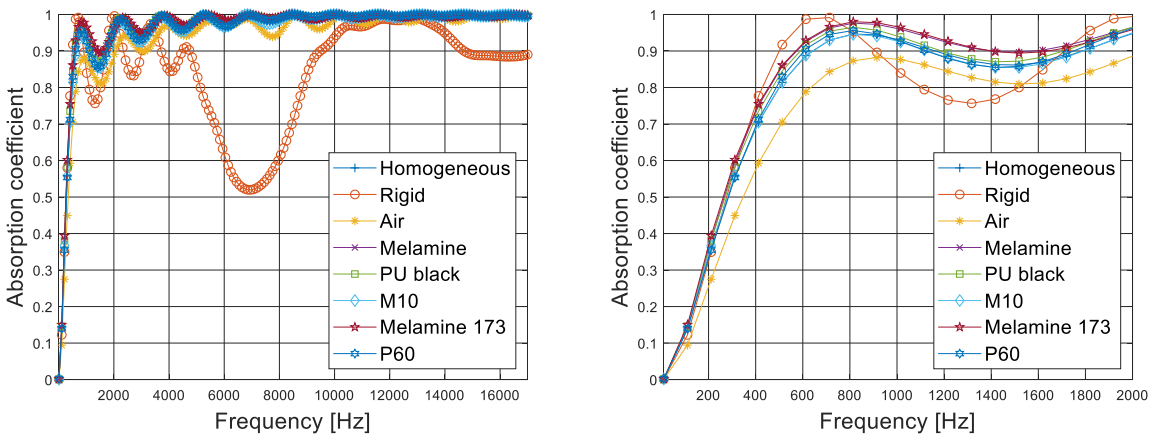

Figure 31: Comparison between the absorption coefficient curves for cases 9-16 of Table 4.

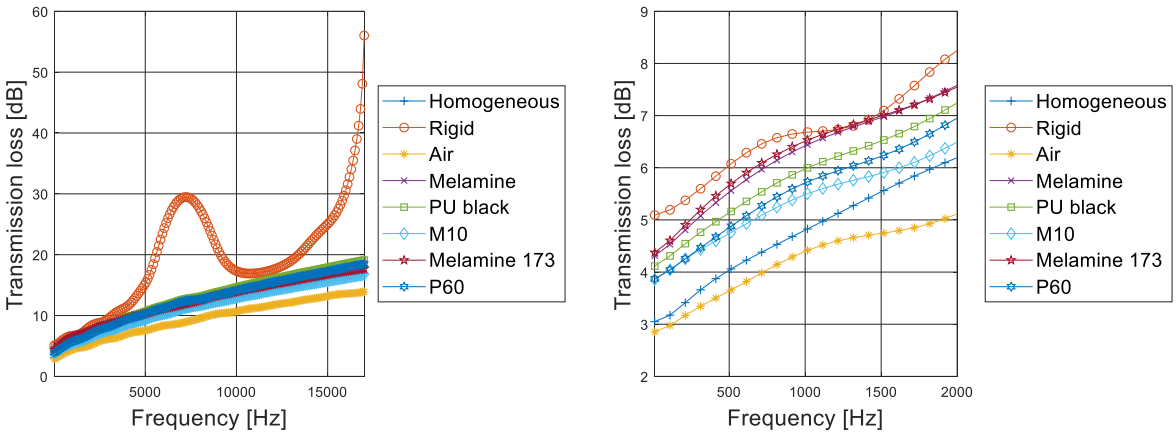

Figure 32: Comparison between the transmission loss curves for cases 9-16 of Table 4.

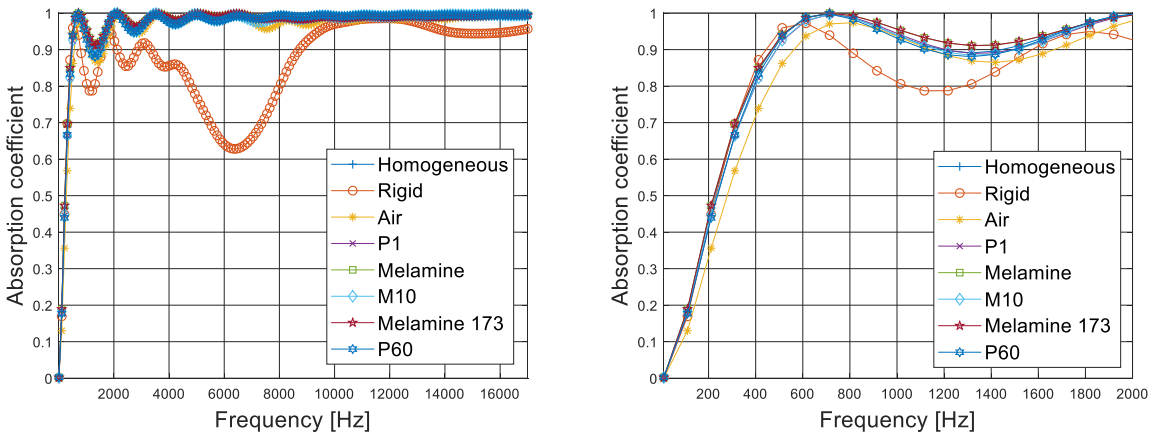

Figure 33: Comparison between the absorption coefficient curves for cases 17-24 of Table 4.

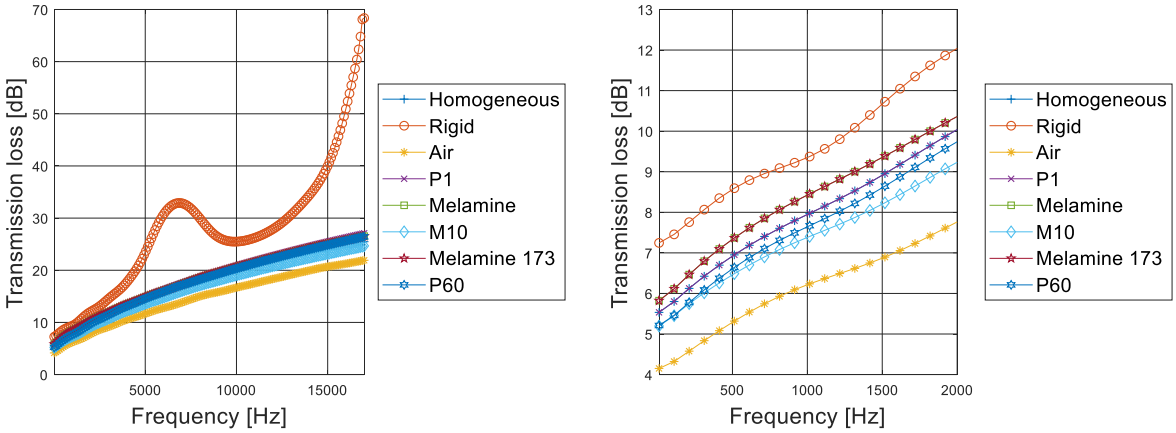

Figure 34: Comparison between the transmission loss curves for cases 17-24 of Table 4.

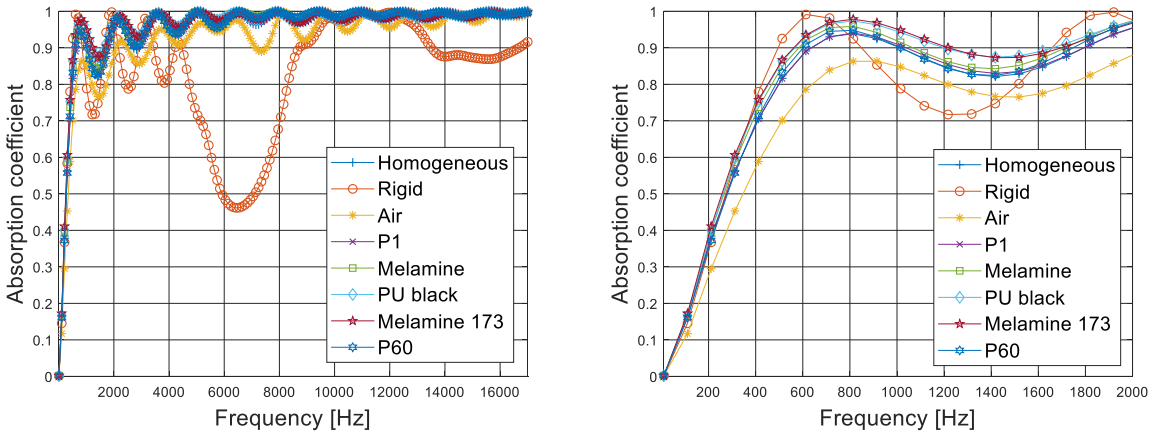

Figure 35: Comparison between the absorption coefficient curves for cases 25-32 of Table 4.

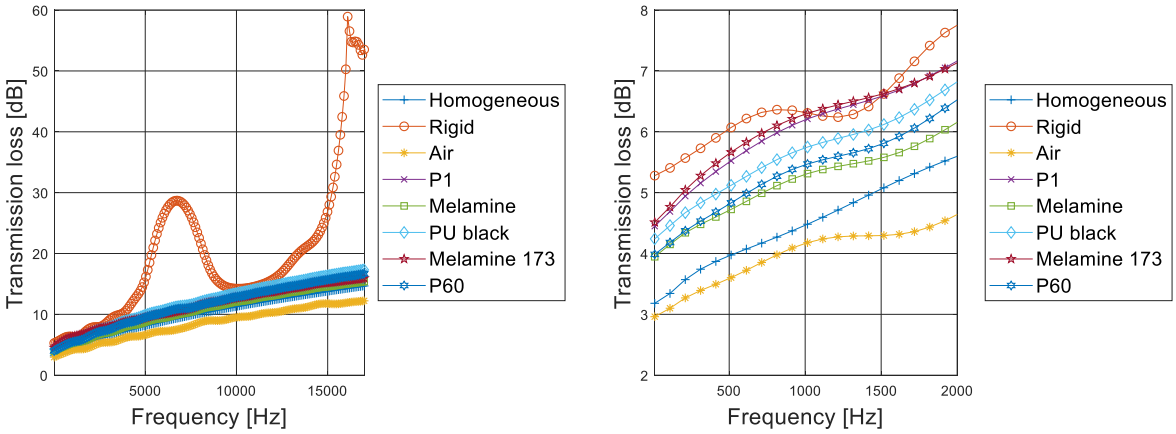

Figure 36: Comparison between the transmission loss curves for cases 25-32 of Table 4.

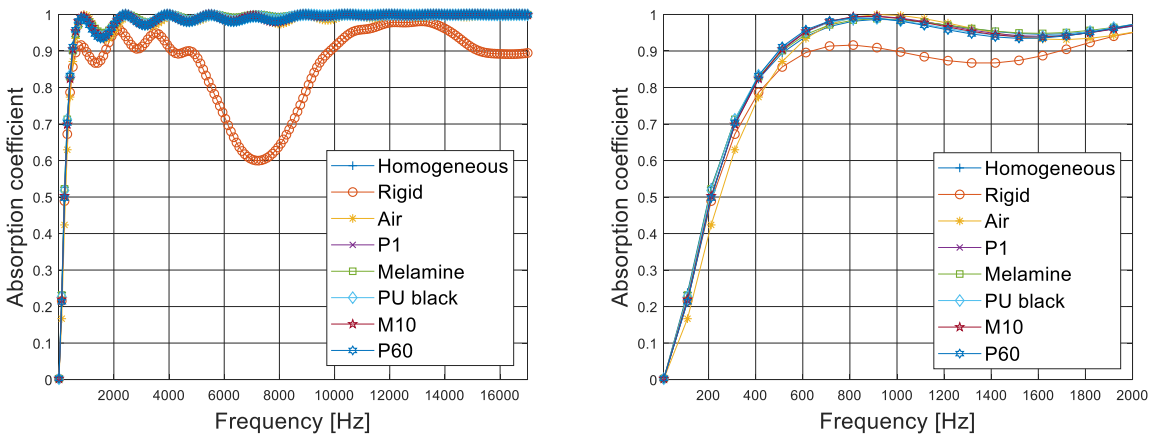

Figure 37: Comparison between the absorption coefficient curves for cases 33-40 of Table 4.

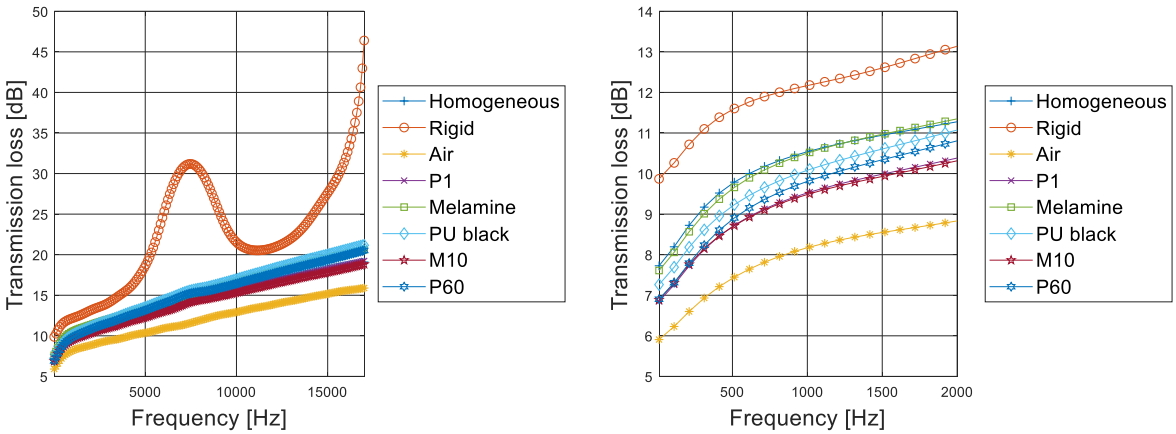

Figure 38: Comparison between the transmission loss curves for cases 33-40 of Table 4.

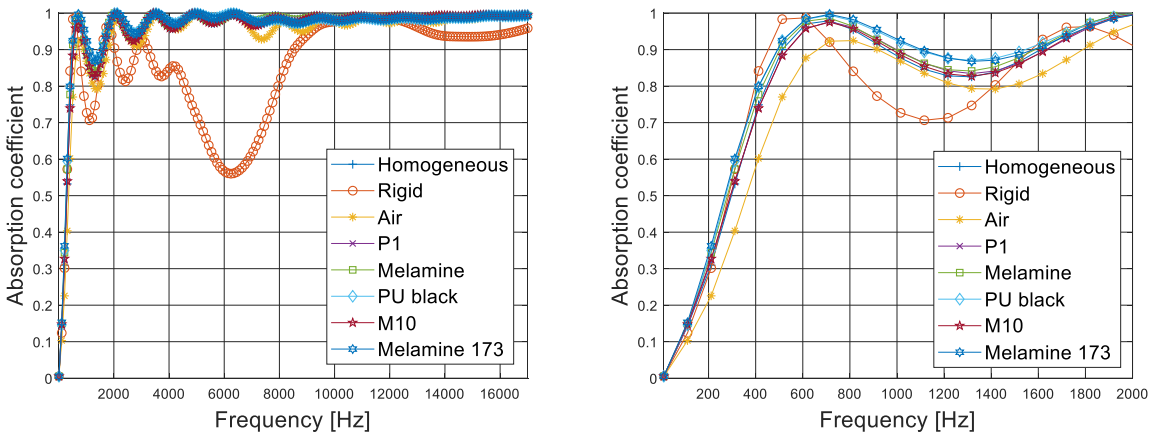

Figure 39: Comparison between the absorption coefficient curves for cases 41-48 of Table 4.

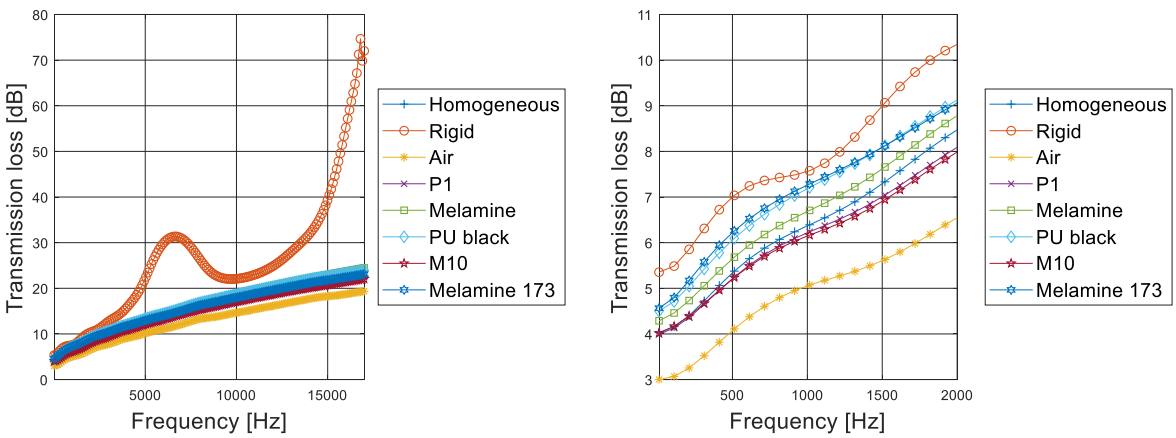

Figure 40: Comparison between the transmission loss curves for cases 41-48 of Table 4.

It can be noticed that, with reference to the dispersion diagrams, those that are obtained in the case of a foam inclusion show very few differences respect to their homogeneous case. In addition, for what concerns the transmission loss, the effect of the inclusion is not particularly advantageous in these situations: in the case of the air, indeed, there is a drop of performances at all frequencies while, in the case of a foam inclusion, only a slight change of the values can be seen, as well as a very small effect of the periodicity when this is equal to half of the wave length (around 7000 Hz).

Anyway, some different cases, that may be more interesting from the practical point of view, can be studied by modelling the foam unit cell through the use of the Biot model, instead that as an equivalent fluid; doing so, indeed, allows to take into account the elasticity of the skeleton and the entire problem formulation depends not anymore only on the pressure, but on the skeleton displacements too: this means that it is possible to properly write the coupling conditions between the foam and an eventual (non-perfectly rigid) solid inclusion.

2.5. Design guidelines

In this section, some guidelines are provided in order to predict at which frequency the 1st performance peak (related to periodicity effects: half of the wave length = periodicity dimension) appears, together with its amplitude, as functions of the unit cell dimensions. Conversely, also the link between the unit cell dimensions and the 1st performance peak amplitude as functions of the design frequency is shown. The test campaign is carried out in the 0 – 15000 Hz frequency range, by comparing a repetition of five unit cells described by Configurations 1 and 2 of Table 4, where the dimension of the inclusion changes accordingly to those of the unit cell (the ratio between the unit cell and the inclusion dimensions is kept constant). Raw data are reported in Table 7, and results are shown in Figure 41 and Figure 42. Surface impedance and reflection coefficient plots can be found in Appendix A.2.1.

According to the results obtained, and considering that a typical acoustic excitation in aeronautics lays in the range of 20 – 2000 Hz [126], one should choose a unit cell dimension between 0.065 m and 0.1 m in order to obtain a transmission loss improvement of averagely 25% respect to the use of a simple foam layer of the same thickness. Considering an automotive application, instead, the typical acoustic excitation lays in the range of 20 – 4000 Hz [127], and therefore one should choose a unit cell dimension between 0.035 m and 0.1 m in order to obtain a transmission loss improvement of averagely 35%, always respect to the use of a simple foam layer of the same thickness. These quantitative considerations are valid for the material and the geometry described above.

Table 7: Raw data for unit cell dimension design guidelines, in the case of a 3D JCA-modeled melamine unit cell.

Unit cell dimension [m]	1st alpha peak [Hz]	α variation	1st TL peak [Hz]	TL variation
0.0200	6870	-34%	7248	94%
0.0350	3795	-25%	4150	48%
0.0425	3085	-22%	3322	44%
0.0500	2523	-19%	2825	41%
0.0650	1903	-17%	2257	30%
0.0800	1417	-14%	1920	23%
0.0950	1075	-13%	1429	21%

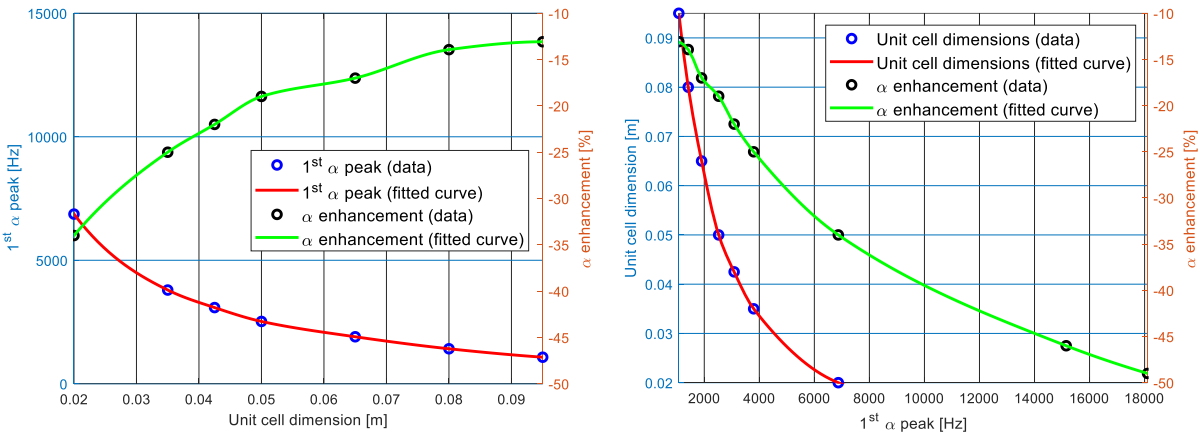

Figure 41: Absorption coefficient design curves as functions of the unit cell dimension (on the left) and the frequency of the 1st peak (on the right), in the case of a 3D JCA-modeled melamine foam.

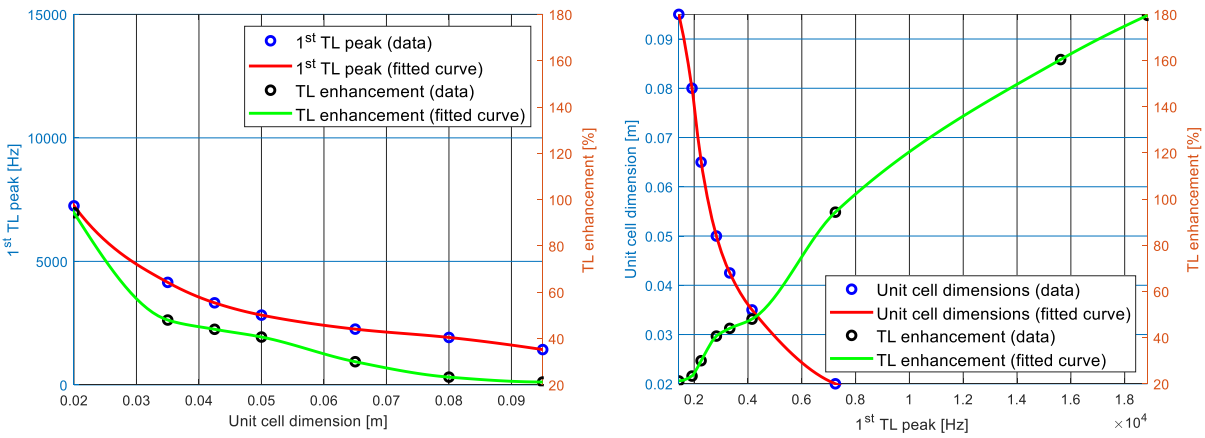

Figure 42: Transmission loss design curves as functions of the unit cell dimension (on the left) and the frequency of the 1st peak (on the right), in the case of a 3D JCA-modeled melamine foam.

Furthermore, some additional guidelines are also provided in order to predict at which frequency the 1st performance peak appears, together with its amplitude, as functions of the airflow resistivity value of the foam. The test campaign is carried out in the 0 – 15000 Hz frequency range, by comparing a repetition of five unit cells described by Configurations 1 and 2 of Table 4, where the airflow resistivity value is artificially changed.

Raw data are reported in Table 8, and results are shown from Figure 43 to Figure 45. Surface impedance and reflection coefficient plots can be found in Appendix A.2.2.

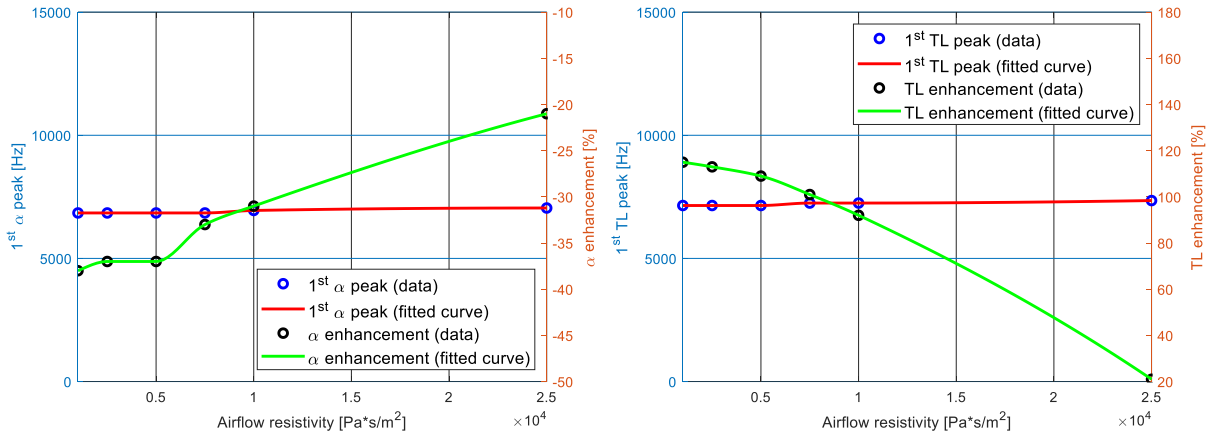

Figure 43: Absorption coefficient (on the left) and transmission loss (on the right) design curves as functions of the foam airflow resistivity, in the case of a 3D JCA-modeled melamine foam.

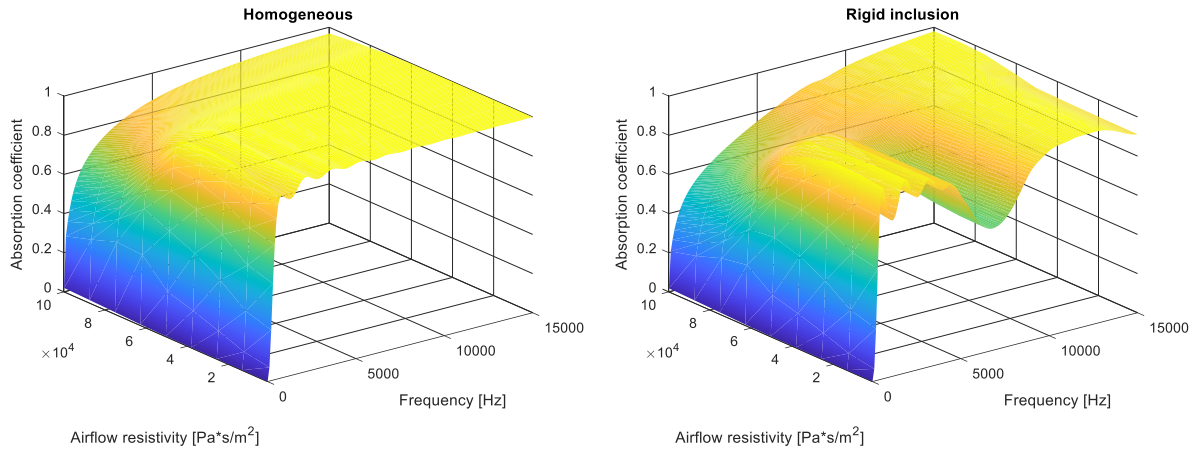

Figure 44: Absorption coefficient value as a function of frequency and foam airflow resistivity; homogeneous case (on the left) and case with a cylindrical perfectly rigid inclusion (on the right), computed for a 3D JCA-modeled melamine foam.

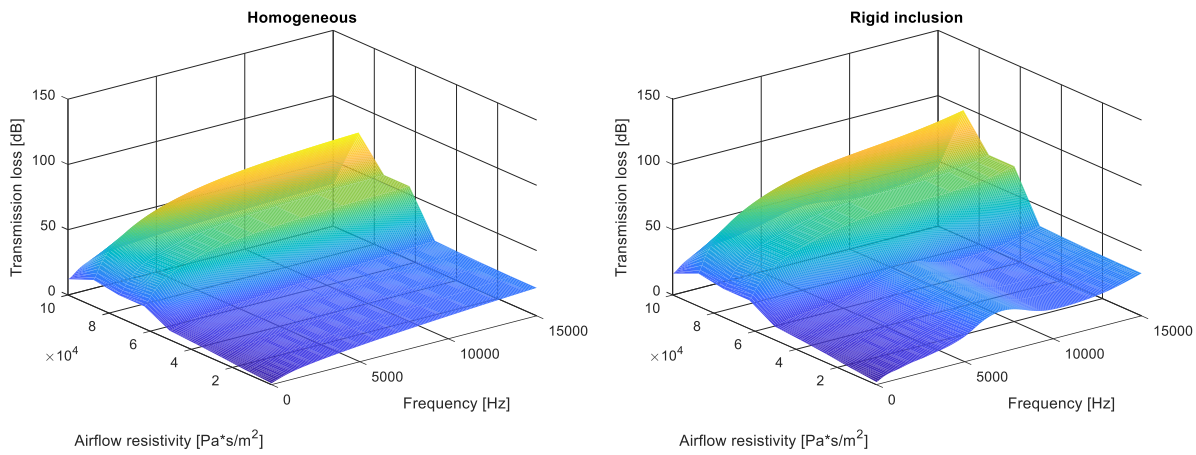

Figure 45: Transmission loss value as a function of frequency and foam airflow resistivity; homogeneous case (on the left) and case with a cylindrical perfectly rigid inclusion (on the right), computed for a 3D JCA-modeled melamine foam.

Table 8: Raw data for airflow resistivity design guidelines, in the case of a 3D JCA-modeled melamine unit cell.

Airflow resistivity [Pa*s/m^2]	1st alpha peak [Hz]	α variation	1st TL peak [Hz]	TL variation
1000	6846	-38%	7148	115%
2500	6846	-37%	7148	113%
5000	6846	-37%	7148	109%
7500	6846	-33%	7248	101%
10000	6947	-31%	7248	92%
25000	7047	-21%	7349	21%

Looking at Figure 43, it is clear that the static airflow resistivity has no meaningful impact on the position of the periodicity peak in the frequency range, since the related curves remain almost constant both for absorption coefficient and transmission loss plots. Instead, one may notice that σ has a non-negligible effect on the variation of the non-homogeneous values, compared to the homogeneous ones, in correspondence of the periodicity peak: in particular, this variation reduces its amplitude at increasing airflow resistivity values, both for absorption coefficient and transmission loss performances. This is probably due to the fact that, as shown in Figure 44 and, in an even more evident manner, in Figure 45, for a homogeneous layer of foam, when σ increases absorption coefficient performances decrease, while transmission loss ones gets better. This is an expected phenomenon, since the airflow resistivity parameter may be considered as an "acoustical hardness" indicator of a foam, in the sense that, the higher it is, the less air permeability there is. Therefore, sound waves cannot enter materials, and so absorption coefficient is reduced and transmission loss increases. It is evident, then, that the general effect of the presence of any external inclusion in the foam reduces at increasing σ, and the non-homogeneous curves tend to assume the same behavior of the homogeneous ones, still maintaining a bias difference in the average value (as it can be clearly seen from Figure 45). Indeed, already starting from $\sigma = 50000\ \frac{\mathrm{Pa*s}}{\mathrm{m}^2}$, periodicity peaks are no more precisely identifiable, neither in absorption coefficient nor in transmission loss curves.

2.6. Comparison of acoustic performances between a homogeneous unit cell and an unit cell with inclusion with fixed mass

In the previous sections, all the comparisons between homogeneous cases and cases with inclusions are made considering unit cells with the same dimensions; in other words, it means that the performances of a layer with periodic inclusions are estimated assuming that is has the same thickness of the related homogeneous one.

One may want also to compare absorption coefficient and transmission loss plots for the case in which the unit cell with inclusion has the same mass (and therefore different dimensions) respect to the homogeneous one [128]. For example, considering an unit cell made of Melamine and with a perfectly rigid inclusion (case 2 of Table 4), when comparing it to the homogeneous case with fixed dimensions, it obviously has a slower mass (75.56% of the homogeneous unit cell value); therefore, in order to perform a comparison with fixed mass respect to the homogeneous case, one should increase each dimension of the unit cell with inclusion of a certain quantity that, for the specific case, is equal to the 7.56%.

At this point, making some considerations based on the results shown in Figure 46 and Figure 47, one may notice that the curve with fixed mass, respect to the one with fixed dimensions, has a performance peak caused by periodicity effect that is shifted at lower frequencies (this is due to the different dimensions between the two cases with inclusion) and also of different amplitude (due to the different mass of the compared unit cells).

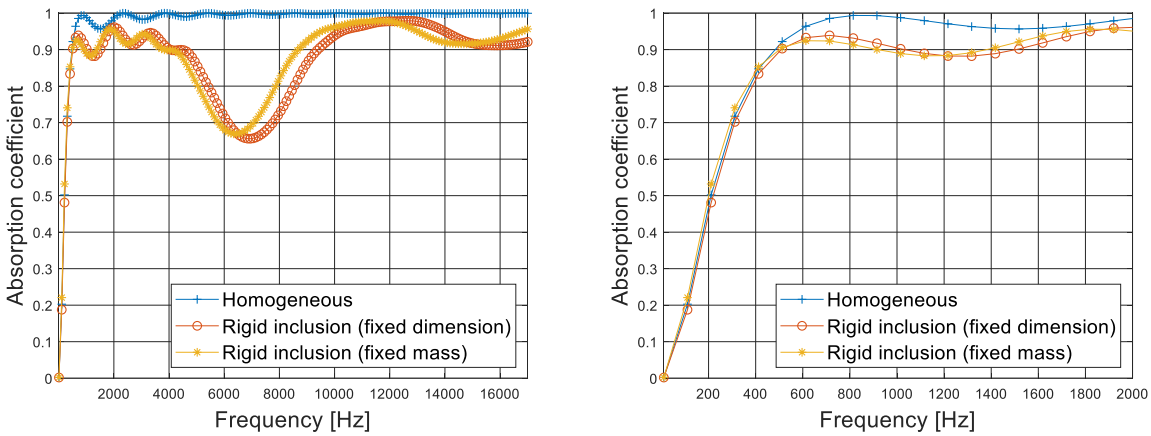

Figure 46: Comparison of absorption coefficient curves between the homogeneous case, the case with inclusion with fixed dimensions and the case with inclusion with fixed mass, computed for a 3D JCA-modeled melamine foam.

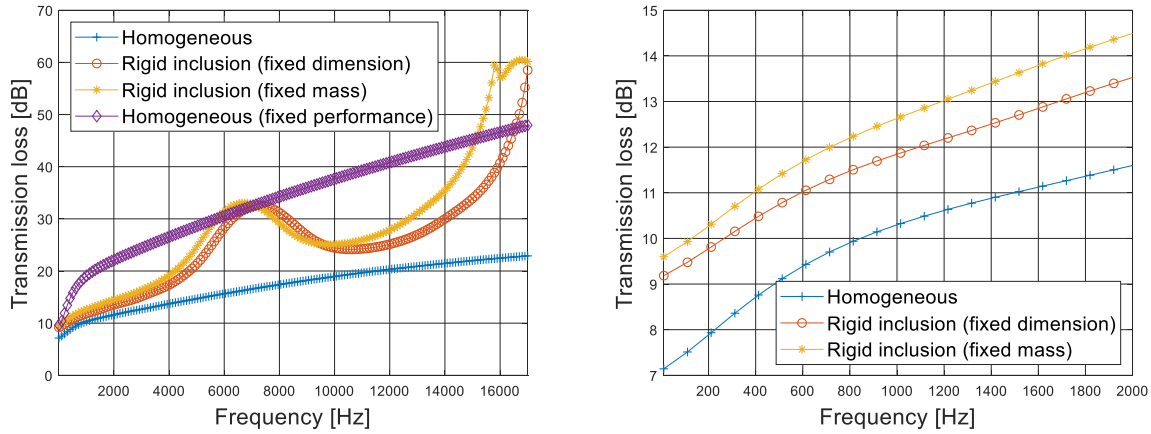

Figure 47: Comparison of transmission loss curves between the homogeneous case, the case with inclusion with fixed dimensions, the case with inclusion with fixed mass and the homogeneous case with fixed performance in the 6000-8000 Hz frequency range, computed for a 3D JCA-modeled melamine foam.

Furthermore, in order to obtain the same transmission loss performances in the periodicity peak range (between 6000 and 8000 Hz, for the specific cases considered) by the use of a simple homogeneous layer made of the same foam, one should use a thickness that is around twice the one required for the cases with inclusion, therefore leading to an increment of the mass of about 100%. This clearly points out the advantage of designing foam layer with periodic inclusion patterns in order to improve the performances in a specific range of frequencies, allowing a save both in terms of thickness and, most of all, mass, respect to a classical homogeneous foam layer.

2.7. Computation of TL and dispersion curves for a unit cell with Helmholtz resonators

In this section, the paper from Lagarrigue *et al.* [129] is used as reference; in this work, absorption coefficient curves for different configurations of porous unit cells with embedded Helmholtz resonators are computed. A Helmholtz resonator consists of a known volume (of any shape) with rigid walls and a small hole in one side. An outside variation in air pressure causes the plug of air in the hole to oscillate in and out, producing adiabatic compressions and rarefactions of the enclosed air. The system is similar to a spring-mass system, with the enclosed volume of air acting as the spring, and the plug of air acting as the mass [130]–[132].

Basically, the advantage of using a Helmholtz resonator rather than a classical rigid inclusion is that it can provide a performance improvement in terms of both absorption coefficient and transmission loss. Indeed, there are mainly two ways of reducing the transmitted power: by reflecting it, or by absorbing it; a simple rigid inclusion essentially reflects the power back, causing a transmission loss increase and an absorption coefficient decrease, while a Helmholtz resonator traps and dissipate the energy inside it, leading to an improvement of both characteristics [133], [134].

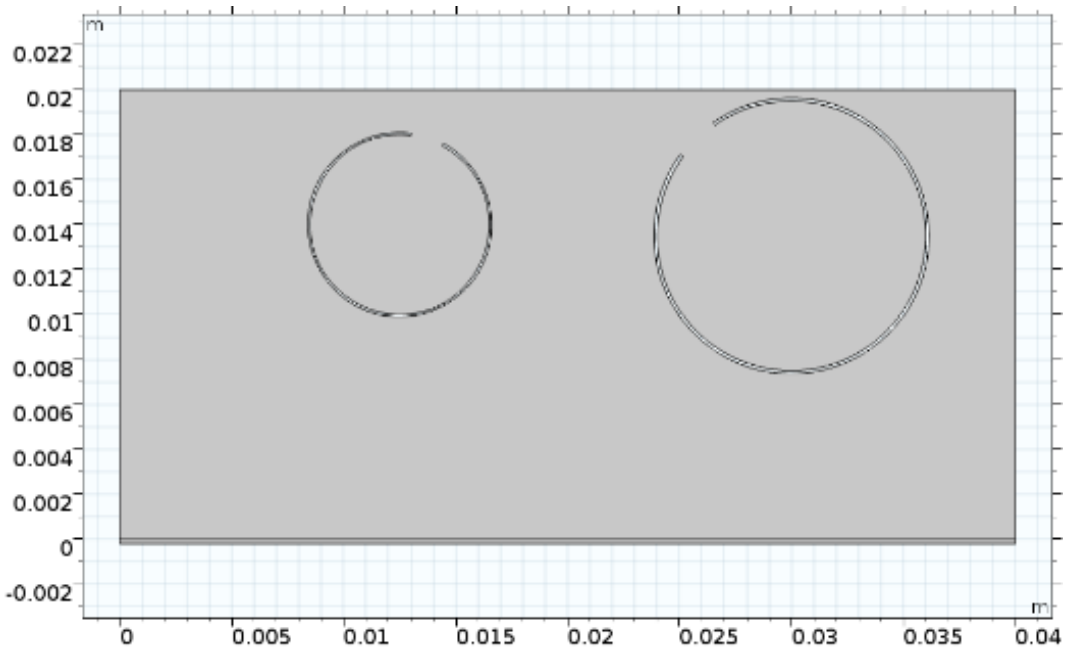

Figure 48: Unit cell with Helmholtz resonators [129].

Table 9: Acoustical parameters of the reference porous material used in the study of an Helmholtz resonating system.

Open porosity	0.95
Tortuosity	1.42
Static airflow resistivity [kg/(s*m^3)]	8900
Viscous characteristic length [m]	180e-6
Thermal characteristic length [m]	360e-6

In particular, the configuration presented in Figure 3 of [129] is here considered. Respect to the reference work performed by Lagarrigue et al., here the analysis on this unit cell with embedded Helmholtz resonators also includes a transmission loss and a dispersion relation computation.

These curves are also presented with zooms up to 2 kHz, since this is clearly the most challenging frequency range in which the periodicity and resonance effects could bring new solutions: above 4 kHz, indeed, single layers of foam are already very efficient without the need for a periodic arrangement [135]. The data of the foam used in this analysis are reported in Table 9.

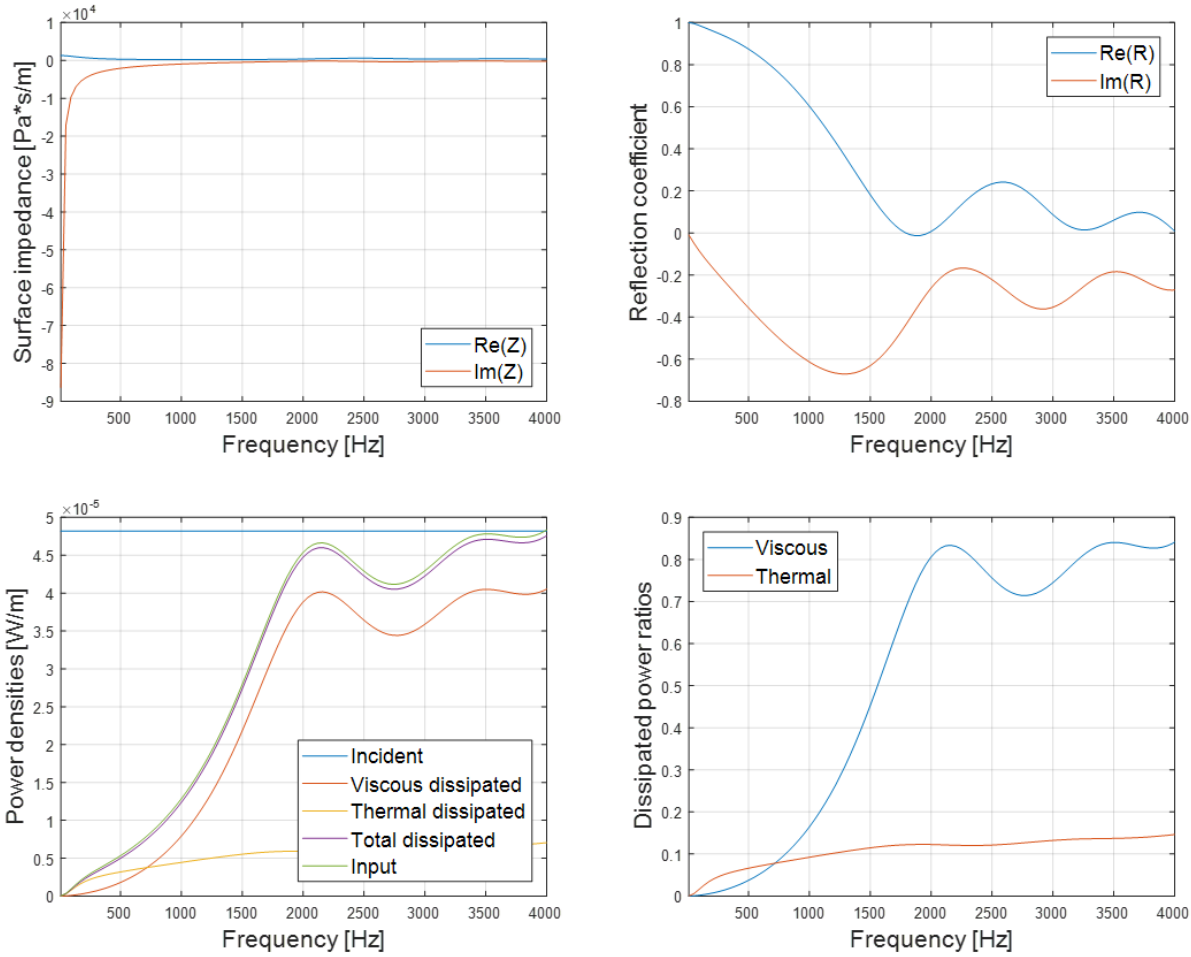

Figure 49: Acoustic characteristics of the unit cell with Helmholtz resonators.

In order to reproduce the absorption coefficient curve in the frequency range of 0 - 4000 Hz, different techniques are used for its computation.

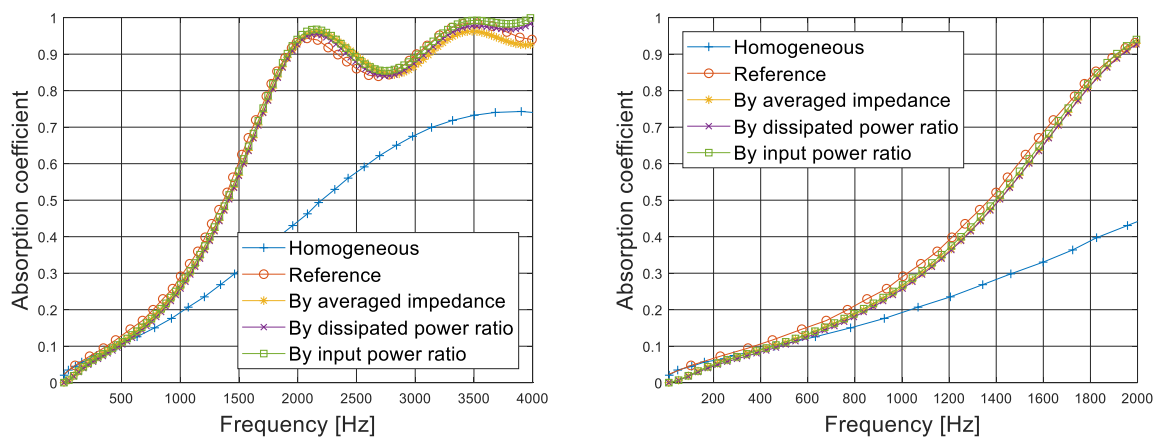

Figure 50: Comparison of absorption coefficient curves with the reference one for the unit cell with Helmholtz resonators.

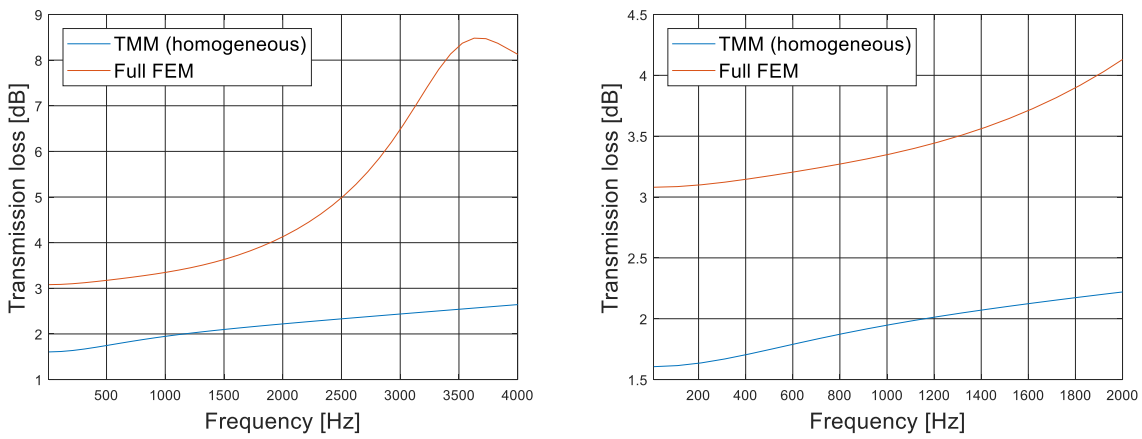

Figure 51: Transmission loss curve for the unit cell with Helmholtz resonators.

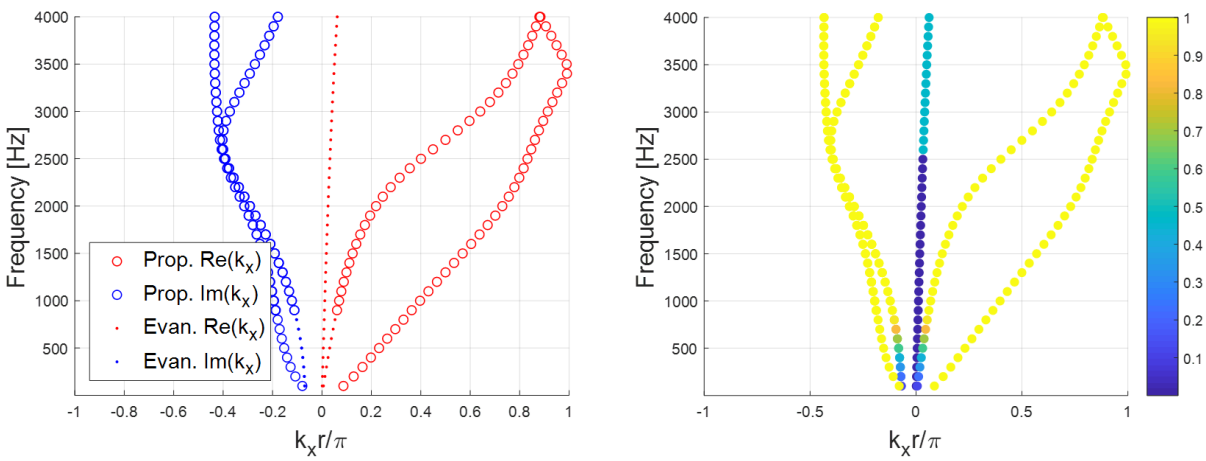

Figure 52: Dispersion curves for the unit cell with Helmholtz resonators.

2.8. Conclusions

In this section, the shift cell operator technique has been re-formulated for porous materials, providing details on its implementation [61]. This approach provides information (dispersion diagrams) that are independent from the excitation, and thus it represents a valuable tool for the design of original solutions that will be efficient regardless of the excitation. Its major advantage stands in allowing the introduction of a generic frequency dependence of visco-elastic material behavior [44]; this is fundamental, if one needs to compute the dispersion diagram of a porous material modeled as an equivalent fluid. Indeed, even if the usage of F-B periodic conditions actually allows it, a very powerful non-linear solver is required in that case. The shift cell operator, instead, leads to a quadratic eigenvalue problem even in the presence of frequency-dependences and/or damping.

The link between left and right eigenvectors has been derived in order to determine an analytical expression for the group velocity. Some classifying criteria have been proposed, in order to distinguish between evanescent and propagative waves. In order to validate the shift cell technique implementation for foams modeled as equivalent fluids, a first calculation has been made to compare shift cell results with those obtained using classical F-B periodic conditions, using (non-dissipative) air as material and a perfectly rigid cylindrical inclusion located at the center of the unit cell [65].

Figure 11 shows what happens to the band gap, when the size of the inclusion (that has perfectly rigid walls) changes. Figure 12 and Figure 13 show a comparison of the computational cost, in terms of time and as a function of the number of elements in the finite element model, between the shift cell and the F-B techniques.

Dispersion curves (calculated with the shift cell technique) and acoustical characteristics (computed using Floquet-Bloch periodic conditions) for different numerical test cases have been obtained for each possible combination between two geometries (with and without inclusion), two models (2D and 3D), two equivalent fluids (Delany-Bazley and Johnson-Champoux-Allard models) and two materials (melamine and "black" polyurethane foams).

A branch-tracking technique has been proposed, and it has been shown how its results can be used to estimate the transmission loss at normal incidence for an acoustic package composed by a finite arrangement of 5 cells. This, in a first approximation, allows the comparison between dispersion and acoustical characteristics of the equivalent finite system. The same JCA-modeled 3D unit cell has also been tested with some non-rigid inclusions [124].

Some guidelines have been provided in order to predict at which frequency the 1st performance peak (related to periodicity effects: half of the wave length = periodicity dimension) appears, together with its amplitude, as functions of the unit cell dimensions. Conversely, also the link between the unit cell dimensions and the 1st performance peak amplitude as functions of the design frequency has been shown. According to the results obtained, and considering that a typical acoustic excitation in aeronautics lays in the range of 20 – 2000 Hz [126], one should choose a unit cell dimension between 0.065 m and 0.1 m in order to obtain a transmission loss improvement of averagely 25% respect to the use of a simple foam layer of the same thickness. Considering an automotive application, instead, the typical acoustic excitation lays in the range of 20 – 4000 Hz [127], and therefore one should choose a unit cell dimension between 0.035 m and 0.1 m in order to obtain a transmission loss improvement of averagely 35%, always respect to the use of a simple foam layer of the same thickness. Furthermore, some additional guidelines are also provided in order to predict at which frequency the 1st performance peak appears, together with its amplitude, as functions of the airflow resistivity value of the foam. As shown in Figure 44 and, in an even more evident manner, in Figure 45, for a homogeneous layer of foam, when σ increases absorption coefficient performances decrease, while transmission loss ones gets better. This is an expected phenomenon, since the airflow resistivity parameter may be considered as an "acoustical hardness" indicator of a foam, in the sense that, the higher it is, the less air permeability there is. Therefore, sound waves cannot enter materials, and so absorption coefficient is reduced and transmission loss increases. It is evident, then, that the general effect of the presence of any external inclusion in the foam reduces at increasing σ, and the non-homogeneous curves tends to assume the same behavior of the homogeneous one, still maintaining a bias difference in the average value (as it can be clearly seen from Figure 45).

A comparison between absorption coefficient and transmission loss plots has also been made for the case in which the unit cell with inclusion has the same mass (and therefore different dimensions) respect to the homogeneous one [128]. In order to obtain the same transmission loss performances in the periodicity peak range (between 6000 and 8000 Hz, for the specific cases considered) by the use of a simple homogeneous layer made of the same foam, one should use a thickness that is around twice the one required for the cases with inclusion, therefore leading to an increment of the mass of about 100%. This clearly highlights the advantage of designing a porous sound package embedding periodic inclusions in order to improve the performances in a specific range of frequencies, allowing a save both in terms of thickness and, most of all, mass, respect to a classical homogeneous foam layer.

The paper from Lagarrigue *et al.* [129] is used as reference in order to study a porous unit cell with embedded Helmholtz resonators. Respect to the reference work, here the analysis on this unit cell with embedded Helmholtz resonators also included a transmission loss and a dispersion relation computation.

3. BIOT MODEL ANALYSES

"Nothing in life is to be feared, it is only to be understood.
Now is the time to understand more, so that we may fear less."

(Marie Curie)

3.1. Shift cell operator technique

3.1.1. Introduction

Under specific boundary and/or load conditions, and at specific frequencies, the solid phase (also called frame or skeleton) of a porous material can be considered as motionless [69]–[73]. For example, above the phase decoupling frequency (defined in Section 1.2.1), a displacement of the fluid phase does not induce a displacement of the solid phase; in such cases, no wave propagates in the solid phase, and thus a motionless skeleton model can be used in order to describe the acoustic behavior of the medium [68]. This is the main hypothesis at the base of Section 2, and the complete vibroacoustic behavior of the medium can be simplified, compared to poro-elastic models.

Indeed, these models take into account the wave propagations (and interactions) in both fluid and solid phases of a foam. Biot model [64] is the most comprehensive one to describe the vibroacoustics of a poro-elastic material, but it requires several parameters (and high computational costs) to be used: a set of parameters for each of the two phases.

In case of low-frequencies acoustic loads, or in case of mechanical excitations, waves can propagate in both phases; therefore, motionless skeleton models cannot be used and a diphasic model is required [68].

In this section, the shift cell operator technique is re-formulated for poro-elastic materials, providing details on its FEM implementation too.

3.1.2. Weak formulation

Considering a porous layer modeled through Biot's theory [64], the coupled starting system is constituted by the equation of motion of the solid part and the classical Helmholtz equation, respectively:

$$\begin{cases} \boldsymbol{\nabla} \cdot \underline{\underline{\hat{\sigma}}}(\boldsymbol{u}) + \omega^2 \tilde{\rho} \boldsymbol{u} + \tilde{\gamma} \boldsymbol{\nabla} p = 0 \\ \Delta p + \omega^2 \frac{\tilde{\rho}_{22}}{R} p - \omega^2 \frac{\tilde{\rho}_{22}}{\phi^2} \tilde{\gamma} \boldsymbol{\nabla} \cdot \boldsymbol{u} = 0 \end{cases}, \tag{98}$$

where $\boldsymbol{u} = (u, v, w)$ is the solid phase displacement vector and $p = p(\boldsymbol{x}, \omega)$ is the acoustic pressure [97]. The following quantities are introduced [75], together with those defined in Section 1.2.2:

- ω is the angular frequency;
- $\underline{\underline{\sigma_T}}(\boldsymbol{u}, p)$ is the total stress tensor;
- $\underline{\underline{\hat{\sigma}}}(\boldsymbol{u}) = \underline{\underline{C}}\,\underline{\underline{\varepsilon}}(\boldsymbol{u})$ is the stress tensor of the frame in vacuum, whose generic element can be written as $\hat{\sigma}_{ij} = \left(\mu_1 - \frac{Q^2}{R}\right) \delta_{ij} \varepsilon_{kk} + 2\mu_2 \varepsilon_{ij}$, where δ_{ij} is the Kronecker delta and $\varepsilon_{kk} = tr(\boldsymbol{\varepsilon}) = \varepsilon_{ux} + \varepsilon_{vy} + \varepsilon_{wz}$;
- $\underline{\underline{C}}$ is the Hooke elasticity tensor, with $C_{11} = \mu_1 - \frac{Q^2}{R} + 2\mu_2$ and $C_{12} = \mu_1 - \frac{Q^2}{R}$;
- $\underline{\underline{\varepsilon}}(\boldsymbol{u}) = \frac{1}{2}(\boldsymbol{\nabla u} + \boldsymbol{\nabla u}^T)$ is the symmetric strain tensor;
- $\mu_1 = \frac{2\nu}{1-2\nu} N$ and $\mu_2 = N$ are respectively the first and second Lamé parameters.

For each physical property of the system, the periodicity is described by $\alpha\left(\boldsymbol{x}-\underline{\underline{r}}\boldsymbol{n}\right)-\alpha(\boldsymbol{x})=0$, where α is a generic physical property, $\boldsymbol{n}$ is a vector of integers normal to the face considered, $\underline{\underline{r}}=(\boldsymbol{r}_1;\ \boldsymbol{r}_2;\ \boldsymbol{r}_3)$ is a matrix containing the three vectors defining the cell periodicity directions and lengths, and Ω is the domain of interest. This applies everywhere except on the discontinuity surfaces, where appropriate boundary conditions apply.

By further developing Equation (98) and applying the Bloch theorem, which generalizes Floquet's results to 3D systems, one can obtain:

$$\begin{cases}(\boldsymbol{\nabla}+j\boldsymbol{k})\cdot\underline{\underline{C}}\frac{1}{2}\left((\boldsymbol{\nabla}+j\boldsymbol{k})\boldsymbol{u}+(\boldsymbol{\nabla}+j\boldsymbol{k})\boldsymbol{u}^T\right)+\omega^2\tilde{\rho}\boldsymbol{u}+\tilde{\gamma}(\boldsymbol{\nabla}+j\boldsymbol{k})p=\boldsymbol{0}\\ (\boldsymbol{\nabla}+j\boldsymbol{k})^T\cdot(\boldsymbol{\nabla}+j\boldsymbol{k})p+\omega^2\frac{\tilde{\rho}_{22}}{R}p-\omega^2\frac{\tilde{\rho}_{22}}{\phi^2}\tilde{\gamma}(\boldsymbol{\nabla}+j\boldsymbol{k})\cdot\boldsymbol{u}=0\end{cases}. \tag{99}$$

The solution approach follows a common weak formulation of a differential problem in a discrete coordinate scheme. A $(\boldsymbol{u},p)$ formulation, in its classical form, can be found in literature [136]:

$$\begin{cases}\int_{\boldsymbol{\Omega}}\underline{\underline{\hat{\sigma}}}(\boldsymbol{u}):\underline{\underline{\varepsilon}}(\delta\boldsymbol{u})\,d\Omega-\omega^2\int_{\Omega}\tilde{\rho}\boldsymbol{u}\cdot\delta\boldsymbol{u}\,d\Omega-\int_{\Omega}\left(\tilde{\gamma}+\phi\left(1+\frac{Q}{R}\right)\right)\boldsymbol{\nabla}p\cdot\delta\boldsymbol{u}\,d\Omega+\\ \qquad-\int_{\Omega}\phi\left(1+\frac{Q}{R}\right)p\boldsymbol{\nabla}\cdot\delta\boldsymbol{u}\,d\Omega-\int_{\Gamma}(\boldsymbol{\sigma_T}(\boldsymbol{u},p)\cdot\boldsymbol{n})\cdot\delta\boldsymbol{u}\,d\Gamma=0\\ \int_{\boldsymbol{\Omega}}\frac{\phi^2}{\omega^2\tilde{\rho}_{22}}\boldsymbol{\nabla}p\cdot\boldsymbol{\nabla}\delta p\,d\Omega-\int_{\boldsymbol{\Omega}}\frac{\phi^2}{R}p\delta p\,d\Omega-\int_{\Omega}\left(\tilde{\gamma}+\phi\left(1+\frac{Q}{R}\right)\right)\boldsymbol{\nabla}\delta p\cdot\boldsymbol{u}\,d\Omega+\\ \qquad-\int_{\Omega}\phi\left(1+\frac{Q}{R}\right)\delta p\boldsymbol{\nabla}\cdot\boldsymbol{u}\,d\Omega-\int_{\Gamma}\phi(U_n-u_n)\delta p\,d\Gamma=0\end{cases}, \tag{100}$$

where $\delta\boldsymbol{u}$ and δp are admissible variations of the solid phase displacement vector and the interstitial fluid pressure of the poro-elastic medium, respectively. Considering that $\underline{\underline{\hat{\sigma}}}(\boldsymbol{u})=\underline{\underline{C}}\underline{\underline{\varepsilon}}(\boldsymbol{u})=\underline{\underline{C}}\frac{1}{2}(\boldsymbol{\nabla}\boldsymbol{u}+\boldsymbol{\nabla}\boldsymbol{u}^T)$, and introducing the shift cell operator as explained above, one obtains:

$$\begin{cases}\int_{\boldsymbol{\Omega}}\left(\underline{\underline{C}}\frac{1}{2}\left((\boldsymbol{\nabla}+j\boldsymbol{k})\boldsymbol{u}+(\boldsymbol{\nabla}+j\boldsymbol{k})\boldsymbol{u}^T\right)\right):\left((\boldsymbol{\nabla}-j\boldsymbol{k})\delta\boldsymbol{u}+(\boldsymbol{\nabla}-j\boldsymbol{k})\delta\boldsymbol{u}^T\right)d\Omega+\\ \qquad-\omega^2\int_{\Omega}\tilde{\rho}\boldsymbol{u}\cdot\delta\boldsymbol{u}\,d\Omega-\int_{\Omega}\left(\tilde{\gamma}+\phi\left(1+\frac{Q}{R}\right)\right)(\boldsymbol{\nabla}+j\boldsymbol{k})p\cdot\delta\boldsymbol{u}\,d\Omega+\\ \qquad-\int_{\Omega}\phi\left(1+\frac{Q}{R}\right)p(\boldsymbol{\nabla}-j\boldsymbol{k})\cdot\delta\boldsymbol{u}\,d\Omega=0\\ \int_{\boldsymbol{\Omega}}\frac{\phi^2}{\omega^2\tilde{\rho}_{22}}(\boldsymbol{\nabla}+j\boldsymbol{k})p\cdot(\boldsymbol{\nabla}-j\boldsymbol{k})\delta p\,d\Omega-\int_{\boldsymbol{\Omega}}\frac{\phi^2}{R}p\delta p\,d\Omega+\\ -\int_{\Omega}\left(\tilde{\gamma}+\phi\left(1+\frac{Q}{R}\right)\right)(\boldsymbol{\nabla}-j\boldsymbol{k})\delta p\cdot\boldsymbol{u}\,d\Omega-\int_{\Omega}\phi\left(1+\frac{Q}{R}\right)\delta p(\boldsymbol{\nabla}+j\boldsymbol{k})\cdot\boldsymbol{u}\,d\Omega=0\end{cases}, \tag{101}$$

where the boundary condition caused the integral on the boundary to vanish. Recalling that:

$$\boldsymbol{k}=k\boldsymbol{\theta}=k\begin{bmatrix}\theta_x\\ \theta_y\\ \theta_z\end{bmatrix}=k\begin{bmatrix}cos\theta cos\phi\\ cos\theta sin\phi\\ sin\theta\end{bmatrix}, \tag{102}$$

one can define the following quantities:

- $\underline{\underline{\hat{\sigma}_\theta}}(\boldsymbol{u})=\underline{\underline{C}}\underline{\underline{\varepsilon_\theta}}(\boldsymbol{u})$, whose generic term is $\hat{\sigma}_{\theta\,ij}=\left(\mu_1-\frac{Q^2}{R}\right)\delta_{ij}\varepsilon_{\theta\,kk}+2\mu_2\varepsilon_{\theta\,ij}$;
- $\underline{\underline{\varepsilon_\theta}}(\boldsymbol{u})=\frac{1}{2}(\boldsymbol{\theta}\boldsymbol{u}+\boldsymbol{\theta}\boldsymbol{u}^T)$.

Therefore:

$$\begin{cases} \int_{\boldsymbol{\Omega}} \underline{\underline{\hat{\sigma}}}(\boldsymbol{u}):\underline{\underline{\varepsilon}}(\delta\boldsymbol{u})\, d\Omega + jk\int_{\boldsymbol{\Omega}} \underline{\underline{\hat{\sigma}_\theta}}(\boldsymbol{u}):\underline{\underline{\varepsilon}}(\delta\boldsymbol{u})\, d\Omega - jk\int_{\boldsymbol{\Omega}} \underline{\underline{\hat{\sigma}}}(\boldsymbol{u}):\underline{\underline{\varepsilon_\theta}}(\delta\boldsymbol{u})\, d\Omega + \\ +k^2\int_{\boldsymbol{\Omega}} \underline{\underline{\hat{\sigma}_\theta}}(\boldsymbol{u}):\underline{\underline{\varepsilon_\theta}}(\delta\boldsymbol{u})\, d\Omega - \omega^2\int_{\Omega} \tilde{\rho}\boldsymbol{u}\cdot\delta\boldsymbol{u}\, d\Omega + \\ -\int_{\Omega}\left(\tilde{\gamma}+\phi\left(1+\frac{Q}{R}\right)\right)(\boldsymbol{\nabla}+j\boldsymbol{k})p\cdot\delta\boldsymbol{u}\, d\Omega - \int_{\Omega}\phi\left(1+\frac{Q}{R}\right)p(\boldsymbol{\nabla}-j\boldsymbol{k})\cdot\delta\boldsymbol{u}\, d\Omega = 0 \\ \int_{\boldsymbol{\Omega}}\frac{\phi^2}{\omega^2\tilde{\rho}_{22}}\boldsymbol{\nabla}p\cdot\boldsymbol{\nabla}\delta p\, d\Omega + jk\int_{\boldsymbol{\Omega}}\frac{\phi^2}{\omega^2\tilde{\rho}_{22}}\boldsymbol{\theta}\cdot p\boldsymbol{\nabla}\delta p\, d\Omega - jk\int_{\boldsymbol{\Omega}}\frac{\phi^2}{\omega^2\tilde{\rho}_{22}}\boldsymbol{\theta}\cdot\boldsymbol{\nabla}p\delta p\, d\Omega + \\ +k^2\int_{\boldsymbol{\Omega}}\frac{\phi^2}{\omega^2\tilde{\rho}_{22}}p\delta p\, d\Omega - \int_{\boldsymbol{\Omega}}\frac{\phi^2}{R}p\delta p\, d\Omega - \int_{\Omega}\left(\tilde{\gamma}+\phi\left(1+\frac{Q}{R}\right)\right)\boldsymbol{\nabla}\delta p\cdot\boldsymbol{u}\, d\Omega + \\ +jk\int_{\Omega}\left(\tilde{\gamma}+\phi\left(1+\frac{Q}{R}\right)\right)\boldsymbol{\theta}\cdot\delta p\boldsymbol{u}\, d\Omega - \int_{\Omega}\phi\left(1+\frac{Q}{R}\right)\delta p\boldsymbol{\nabla}\cdot\boldsymbol{u}\, d\Omega + \\ -jk\int_{\Omega}\phi\left(1+\frac{Q}{R}\right)\boldsymbol{\theta}\cdot\delta p\boldsymbol{u}\, d\Omega = 0 \end{cases}, \tag{103}$$

$$\begin{cases} \int_{\boldsymbol{\Omega}} \underline{\underline{\hat{\sigma}}}(\boldsymbol{u}):\underline{\underline{\varepsilon}}(\delta\boldsymbol{u})\, d\Omega + jk\int_{\boldsymbol{\Omega}}\left(\underline{\underline{\hat{\sigma}_\theta}}(\boldsymbol{u}):\underline{\underline{\varepsilon}}(\delta\boldsymbol{u}) - \underline{\underline{\hat{\sigma}}}(\boldsymbol{u}):\underline{\underline{\varepsilon_\theta}}(\delta\boldsymbol{u})\right) d\Omega + \\ +k^2\int_{\boldsymbol{\Omega}} \underline{\underline{\hat{\sigma}_\theta}}(\boldsymbol{u}):\underline{\underline{\varepsilon_\theta}}(\delta\boldsymbol{u})\, d\Omega - \omega^2\int_{\Omega}\tilde{\rho}\boldsymbol{u}\cdot\delta\boldsymbol{u}\, d\Omega - \int_{\Omega}\tilde{\gamma}\boldsymbol{\nabla}p\cdot\delta\boldsymbol{u}\, d\Omega + \\ -jk\int_{\Omega}\tilde{\gamma}\boldsymbol{\theta}\cdot p\delta\boldsymbol{u}\, d\Omega - \int_{\Omega}\phi\left(1+\frac{Q}{R}\right)(\boldsymbol{\nabla}p\cdot\delta\boldsymbol{u} + p\boldsymbol{\nabla}\cdot\delta\boldsymbol{u})\, d\Omega = 0 \\ \int_{\boldsymbol{\Omega}}\frac{\phi^2}{\omega^2\tilde{\rho}_{22}}\boldsymbol{\nabla}p\cdot\boldsymbol{\nabla}\delta p\, d\Omega + jk\int_{\boldsymbol{\Omega}}\frac{\phi^2}{\omega^2\tilde{\rho}_{22}}(\boldsymbol{\theta}\cdot p\boldsymbol{\nabla}\delta p - \boldsymbol{\theta}\cdot\boldsymbol{\nabla}p\delta p)\, d\Omega + \\ +k^2\int_{\boldsymbol{\Omega}}\frac{\phi^2}{\omega^2\tilde{\rho}_{22}}p\delta p\, d\Omega - \int_{\boldsymbol{\Omega}}\frac{\phi^2}{R}p\delta p\, d\Omega - \int_{\Omega}\tilde{\gamma}\boldsymbol{\nabla}\delta p\cdot\boldsymbol{u}\, d\Omega + \\ +jk\int_{\Omega}\tilde{\gamma}\boldsymbol{\theta}\cdot\delta p\boldsymbol{u}\, d\Omega - \int_{\Omega}\phi\left(1+\frac{Q}{R}\right)(\boldsymbol{\nabla}\delta p\cdot\boldsymbol{u} + \delta p\boldsymbol{\nabla}\cdot\boldsymbol{u})\, d\Omega = 0 \end{cases}. \tag{104}$$

Finally, one can discretize the weak formulation through the Finite Element Method: considering that $\boldsymbol{\varphi_s}$ and $\boldsymbol{\varphi_f}$ are the eigenvectors of the solid and fluid parts respectively, the system of equations can be written in its matrix form:

$$\begin{cases} \left(\underline{\underline{K_s}} + jk\underline{\underline{L_s}} + k^2\underline{\underline{H_s}} - \omega^2\underline{\underline{M_s}}\right)\boldsymbol{\varphi_s} - \left(\underline{\underline{N_s}} + jk\underline{\underline{O_s}} + \underline{\underline{T_s}}\right)\boldsymbol{\varphi_f} = 0 \\ \left(\underline{\underline{K_f}} + jk\underline{\underline{L_f}} + k^2\underline{\underline{H_f}} - \omega^2\underline{\underline{M_f}}\right)\boldsymbol{\varphi_f} - \omega^2\left(\underline{\underline{N_f}} - jk\underline{\underline{O_f}} + \underline{\underline{T_f}}\right)\boldsymbol{\varphi_s} = 0 \end{cases}, \tag{105}$$

with the following matrices:

- $\underline{\underline{K_s}} \propto \int_{\boldsymbol{\Omega}} \underline{\underline{\hat{\sigma}}}(\boldsymbol{u}):\underline{\underline{\varepsilon}}(\delta\boldsymbol{u})\, d\Omega$;
- $\underline{\underline{L_s}} \propto \int_{\boldsymbol{\Omega}} \left(\underline{\underline{\hat{\sigma}_\theta}}(\boldsymbol{u}):\underline{\underline{\varepsilon}}(\delta\boldsymbol{u}) - \underline{\underline{\hat{\sigma}}}(\boldsymbol{u}):\underline{\underline{\varepsilon_\theta}}(\delta\boldsymbol{u})\right) d\Omega$;
- $\underline{\underline{H_s}} \propto \int_{\boldsymbol{\Omega}} \underline{\underline{\hat{\sigma}_\theta}}(\boldsymbol{u}):\underline{\underline{\varepsilon_\theta}}(\delta\boldsymbol{u})\, d\Omega$;
- $\underline{\underline{M_s}} \propto \int_{\Omega} \tilde{\rho}\boldsymbol{u}\cdot\delta\boldsymbol{u}\, d\Omega$;
- $\underline{\underline{N_s}} \propto \int_{\Omega} \tilde{\gamma}\boldsymbol{\nabla}p\cdot\delta\boldsymbol{u}\, d\Omega$;
- $\underline{\underline{O_s}} \propto \int_{\Omega} \tilde{\gamma}\boldsymbol{\theta}\cdot p\delta\boldsymbol{u}\, d\Omega$;
- $\underline{\underline{T_s}} \propto \int_{\Omega} \phi\left(1+\frac{Q}{R}\right)(\boldsymbol{\nabla}p\cdot\delta\boldsymbol{u} + p\boldsymbol{\nabla}\cdot\delta\boldsymbol{u})\, d\Omega$;

- $\underline{\underline{K_f}} \propto \int_{\boldsymbol{\Omega}} \frac{\phi^2}{\tilde{\rho}_{22}} \boldsymbol{\nabla} p \cdot \boldsymbol{\nabla} \delta p \, d\Omega;$
- $\underline{\underline{L_f}} \propto \int_{\boldsymbol{\Omega}} \frac{\phi^2}{\tilde{\rho}_{22}} (\boldsymbol{\theta} \cdot p \boldsymbol{\nabla} \delta p - \boldsymbol{\theta} \cdot \boldsymbol{\nabla} p \delta p) \, d\Omega;$
- $\underline{\underline{H_f}} \propto \int_{\boldsymbol{\Omega}} \frac{\phi^2}{\tilde{\rho}_{22}} p \delta p \, d\Omega;$
- $\underline{\underline{M_f}} \propto \int_{\boldsymbol{\Omega}} \frac{\phi^2}{R} p \delta p \, d\Omega;$
- $\underline{\underline{N_f}} \propto \int_{\Omega} \tilde{\gamma} \boldsymbol{\nabla} \delta p \cdot \boldsymbol{u} \, d\Omega;$
- $\underline{\underline{O_f}} \propto \int_{\Omega} \tilde{\gamma} \boldsymbol{\theta} \cdot \delta p \boldsymbol{u} \, d\Omega;$
- $\underline{\underline{T_f}} \propto \int_{\Omega} \phi \left(1 + \frac{Q}{R}\right) (\boldsymbol{\nabla} \delta p \cdot \boldsymbol{u} + \delta p \boldsymbol{\nabla} \cdot \boldsymbol{u}) \, d\Omega.$

Here, $\underline{\underline{M_{s,f}}}$ and $\underline{\underline{K_{s,f}}}$ are respectively the symmetric mass and symmetric stiffness matrices, $\underline{\underline{L_{s,f}}}$ are skew-symmetric matrices, $\underline{\underline{H_{s,f}}}$ are symmetric matrices and $\underline{\underline{N_s}} = \underline{\underline{N_f}}^T$, $\underline{\underline{O_s}} = \underline{\underline{O_f}}^T$ and $\underline{\underline{T_s}} = \underline{\underline{T_f}}^T$ are the matrices that couple the solid and fluid behaviors; all of them are complex and frequency-dependent. Therefore, the coupled system can be written as it follows:

$$\begin{bmatrix} \left(\underline{\underline{K_s}} + jk\underline{\underline{L_s}} + k^2\underline{\underline{H_s}} - \omega^2\underline{\underline{M_s}}\right) & -(\underline{\underline{N_s}} + jk\underline{\underline{O_s}} + \underline{\underline{T_s}}) \\ -(\underline{\underline{N_f}} - jk\underline{\underline{O_f}} + \underline{\underline{T_f}}) & \frac{1}{\omega^2}(\underline{\underline{K_f}} + jk\underline{\underline{L_f}} + k^2\underline{\underline{H_f}} - \omega^2\underline{\underline{M_f}}) \end{bmatrix} \begin{Bmatrix} \boldsymbol{\varphi_s} \\ \boldsymbol{\varphi_f} \end{Bmatrix} = \begin{Bmatrix} 0 \\ 0 \end{Bmatrix}. \tag{106}$$

3.1.3. Finite element implementation

In order to numerically implement the shift cell technique for Biot-modeled foams, the vector equation related to the motion of the solid part is split into three scalar equations. The following matrices are defined accordingly:

$$\boldsymbol{u} = \begin{bmatrix} u \\ v \\ w \end{bmatrix}, \boldsymbol{\nabla u} = \begin{bmatrix} \frac{\partial u}{\partial x} & \frac{\partial v}{\partial x} & \frac{\partial w}{\partial x} \\ \frac{\partial u}{\partial y} & \frac{\partial v}{\partial y} & \frac{\partial w}{\partial y} \\ \frac{\partial u}{\partial z} & \frac{\partial v}{\partial z} & \frac{\partial w}{\partial z} \end{bmatrix}, \boldsymbol{\theta u} = \begin{bmatrix} \theta_x u & \theta_x v & \theta_x w \\ \theta_y u & \theta_y v & \theta_y w \\ \theta_z u & \theta_z v & \theta_z w \end{bmatrix}, \tag{107}$$

$$\underline{\underline{\varepsilon}}(\boldsymbol{u}) = \begin{bmatrix} \frac{\partial u}{\partial x} & \frac{1}{2}\left(\frac{\partial u}{\partial y} + \frac{\partial v}{\partial x}\right) & \frac{1}{2}\left(\frac{\partial u}{\partial z} + \frac{\partial w}{\partial x}\right) \\ \frac{1}{2}\left(\frac{\partial u}{\partial y} + \frac{\partial v}{\partial x}\right) & \frac{\partial v}{\partial y} & \frac{1}{2}\left(\frac{\partial v}{\partial z} + \frac{\partial w}{\partial y}\right) \\ \frac{1}{2}\left(\frac{\partial u}{\partial z} + \frac{\partial w}{\partial x}\right) & \frac{1}{2}\left(\frac{\partial v}{\partial z} + \frac{\partial w}{\partial y}\right) & \frac{\partial w}{\partial z} \end{bmatrix}, \tag{108}$$

$$\underline{\underline{\varepsilon_\theta}}(\boldsymbol{u}) = \begin{bmatrix} \theta_x u & \frac{1}{2}\left(\theta_y u + \theta_x v\right) & \frac{1}{2}(\theta_z u + \theta_x w) \\ \frac{1}{2}\left(\theta_y u + \theta_x v\right) & \theta_y v & \frac{1}{2}\left(\theta_z v + \theta_y w\right) \\ \frac{1}{2}(\theta_z u + \theta_x w) & \frac{1}{2}\left(\theta_z v + \theta_y w\right) & \theta_z w \end{bmatrix}, \tag{109}$$

$$\underline{\underline{\hat{\sigma}}}(\boldsymbol{u}) = \begin{bmatrix} C_{11}\frac{\partial u}{\partial x} + C_{12}\left(\frac{\partial v}{\partial y} + \frac{\partial w}{\partial z}\right) & (C_{11} - C_{12})\frac{1}{2}\left(\frac{\partial u}{\partial y} + \frac{\partial v}{\partial x}\right) & (C_{11} - C_{12})\frac{1}{2}\left(\frac{\partial u}{\partial z} + \frac{\partial w}{\partial x}\right) \\ (C_{11} - C_{12})\frac{1}{2}\left(\frac{\partial u}{\partial y} + \frac{\partial v}{\partial x}\right) & C_{11}\frac{\partial v}{\partial y} + C_{12}\left(\frac{\partial u}{\partial x} + \frac{\partial w}{\partial z}\right) & (C_{11} - C_{12})\frac{1}{2}\left(\frac{\partial v}{\partial z} + \frac{\partial w}{\partial y}\right) \\ (C_{11} - C_{12})\frac{1}{2}\left(\frac{\partial u}{\partial z} + \frac{\partial w}{\partial x}\right) & (C_{11} - C_{12})\frac{1}{2}\left(\frac{\partial v}{\partial z} + \frac{\partial w}{\partial y}\right) & C_{11}\frac{\partial w}{\partial z} + C_{12}\left(\frac{\partial u}{\partial x} + \frac{\partial v}{\partial y}\right) \end{bmatrix}, \quad (110)$$

$$\underline{\underline{\hat{\sigma}_\theta}}(\boldsymbol{u}) =$$

$$\begin{bmatrix} C_{11}\theta_x u + C_{12}(\theta_y v + \theta_z w) & (C_{11} - C_{12})\frac{1}{2}(\theta_y u + \theta_x v) & (C_{11} - C_{12})\frac{1}{2}(\theta_z u + \theta_x w) \\ (C_{11} - C_{12})\frac{1}{2}(\theta_y u + \theta_x v) & C_{11}\theta_y v + C_{12}(\theta_x u + \theta_z w) & (C_{11} - C_{12})\frac{1}{2}(\theta_z v + \theta_y w) \\ (C_{11} - C_{12})\frac{1}{2}(\theta_z u + \theta_x w) & (C_{11} - C_{12})\frac{1}{2}(\theta_z v + \theta_y w) & C_{11}\theta_z w + C_{12}(\theta_x u + \theta_y v) \end{bmatrix}. \quad (111)$$

The numerical model is therefore based on the following matrix weak formulation:

- $\underline{\underline{K_{s,u}}} \propto \int_{\boldsymbol{\Omega}} \begin{pmatrix} \left(C_{11}\frac{\partial u}{\partial x} + C_{12}\left(\frac{\partial v}{\partial y} + \frac{\partial w}{\partial z}\right)\right)\frac{\partial \delta u}{\partial x} + \\ +(C_{11} - C_{12})\frac{1}{4}\left(\left(\frac{\partial u}{\partial y} + \frac{\partial v}{\partial x}\right)\left(\frac{\partial \delta u}{\partial y} + \frac{\partial \delta v}{\partial x}\right) + \left(\frac{\partial u}{\partial z} + \frac{\partial w}{\partial x}\right)\left(\frac{\partial \delta u}{\partial z} + \frac{\partial \delta w}{\partial x}\right)\right) \end{pmatrix} d\Omega;$
- $\underline{\underline{L_{s,u}}} \propto$
$$\int_{\boldsymbol{\Omega}} \begin{pmatrix} \left(C_{11}\theta_x u + C_{12}(\theta_y v + \theta_z w)\right)\frac{\partial \delta u}{\partial x} + \\ +(C_{11} - C_{12})\frac{1}{4}\left(\left(\theta_y u + \theta_x v\right)\left(\frac{\partial \delta u}{\partial y} + \frac{\partial \delta v}{\partial x}\right) + (\theta_z u + \theta_x w)\left(\frac{\partial \delta u}{\partial z} + \frac{\partial \delta w}{\partial x}\right)\right) + \\ -\left(C_{11}\frac{\partial u}{\partial x} + C_{12}\left(\frac{\partial v}{\partial y} + \frac{\partial w}{\partial z}\right)\right)\theta_x \delta u + \\ -(C_{11} - C_{12})\frac{1}{4}\left(\left(\frac{\partial u}{\partial y} + \frac{\partial v}{\partial x}\right)(\theta_y \delta u + \theta_x \delta v) + \left(\frac{\partial u}{\partial z} + \frac{\partial w}{\partial x}\right)(\theta_z \delta u + \theta_x \delta w)\right) \end{pmatrix} d\Omega;$
- $\underline{\underline{H_{s,u}}} \propto$
$$\int_{\boldsymbol{\Omega}} \begin{pmatrix} \left(C_{11}\theta_x u + C_{12}(\theta_y v + \theta_z w)\right)\theta_x \delta u + \\ +(C_{11} - C_{12})\frac{1}{4}\left((\theta_y u + \theta_x v)(\theta_y \delta u + \theta_x \delta v) + (\theta_z u + \theta_x w)(\theta_z \delta u + \theta_x \delta w)\right) \end{pmatrix} d\Omega;$
- $\underline{\underline{M_{s,u}}} \propto \int_{\Omega} \tilde{\rho} u \delta u \, d\Omega;$
- $\underline{\underline{N_{s,u}}} \propto \int_{\Omega} \tilde{\gamma}\frac{\partial p}{\partial x}\delta u \, d\Omega;$
- $\underline{\underline{O_{s,u}}} \propto \int_{\Omega} \tilde{\gamma}\theta_1 p \delta u \, d\Omega;$
- $\underline{\underline{T_{s,u}}} \propto \int_{\Omega} \phi\left(1 + \frac{Q}{R}\right)\left(\frac{\partial p}{\partial x}\delta u + p\frac{\partial \delta u}{\partial x}\right) d\Omega;$
- $\underline{\underline{K_{s,v}}} \propto \int_{\boldsymbol{\Omega}} \begin{pmatrix} \left(C_{11}\frac{\partial v}{\partial y} + C_{12}\left(\frac{\partial u}{\partial x} + \frac{\partial w}{\partial z}\right)\right)\frac{\partial \delta v}{\partial y} + \\ +(C_{11} - C_{12})\frac{1}{4}\left(\left(\frac{\partial u}{\partial y} + \frac{\partial v}{\partial x}\right)\left(\frac{\partial \delta u}{\partial y} + \frac{\partial \delta v}{\partial x}\right) + \left(\frac{\partial v}{\partial z} + \frac{\partial w}{\partial y}\right)\left(\frac{\partial \delta v}{\partial z} + \frac{\partial \delta w}{\partial y}\right)\right) \end{pmatrix} d\Omega;$

- $\underline{\underline{L_{s,v}}} \propto$

$$\int_{\boldsymbol{\Omega}} \begin{pmatrix} \left(C_{11}\theta_y v + C_{12}(\theta_x u + \theta_z w)\right)\frac{\partial \delta v}{\partial y} + \\ +(C_{11}-C_{12})\frac{1}{4}\left(\left(\theta_y u + \theta_x v\right)\left(\frac{\partial \delta u}{\partial y}+\frac{\partial \delta v}{\partial x}\right) + \left(\theta_z v + \theta_y w\right)\left(\frac{\partial \delta v}{\partial z}+\frac{\partial \delta w}{\partial y}\right)\right) + \\ -\left(C_{11}\frac{\partial v}{\partial y} + C_{12}\left(\frac{\partial u}{\partial x}+\frac{\partial w}{\partial z}\right)\right)\theta_y \delta v + \\ -(C_{11}-C_{12})\frac{1}{4}\left(\left(\frac{\partial u}{\partial y}+\frac{\partial v}{\partial x}\right)\left(\theta_y \delta u + \theta_x \delta v\right) + \left(\frac{\partial v}{\partial z}+\frac{\partial w}{\partial y}\right)\left(\theta_z \delta v + \theta_y \delta w\right)\right) \end{pmatrix} d\Omega;$$

- $\underline{\underline{H_{s,v}}} \propto$

$$\int_{\boldsymbol{\Omega}} \begin{pmatrix} \left(C_{11}\theta_y v + C_{12}(\theta_x u + \theta_z w)\right)\theta_y \delta v + \\ +(C_{11}-C_{12})\frac{1}{4}\left(\left(\theta_y u + \theta_x v\right)\left(\theta_y \delta u + \theta_x \delta v\right) + \left(\theta_z v + \theta_y w\right)\left(\theta_z \delta v + \theta_y \delta w\right)\right) \end{pmatrix} d\Omega;$$

- $\underline{\underline{M_{s,v}}} \propto \int_{\Omega} \tilde{\rho} v \delta v \, d\Omega;$
- $\underline{\underline{N_{s,v}}} \propto \int_{\Omega} \tilde{\gamma}\frac{\partial p}{\partial y}\delta v \, d\Omega;$
- $\underline{\underline{O_{s,v}}} \propto \int_{\Omega} \tilde{\gamma}\theta_2 p \delta v \, d\Omega;$
- $\underline{\underline{T_{s,v}}} \propto \int_{\Omega} \phi\left(1+\frac{Q}{R}\right)\left(\frac{\partial p}{\partial y}\delta v + p\frac{\partial \delta v}{\partial y}\right) d\Omega;$
- $\underline{\underline{K_{s,w}}} \propto \int_{\boldsymbol{\Omega}} \begin{pmatrix} \left(C_{11}\frac{\partial w}{\partial z} + C_{12}\left(\frac{\partial u}{\partial x}+\frac{\partial v}{\partial y}\right)\right)\frac{\partial \delta w}{\partial z} + \\ +(C_{11}-C_{12})\frac{1}{4}\left(\left(\frac{\partial v}{\partial z}+\frac{\partial w}{\partial y}\right)\left(\frac{\partial \delta v}{\partial z}+\frac{\partial \delta w}{\partial y}\right) + \left(\frac{\partial u}{\partial z}+\frac{\partial w}{\partial x}\right)\left(\frac{\partial \delta u}{\partial z}+\frac{\partial \delta w}{\partial x}\right)\right) \end{pmatrix} d\Omega;$
- $\underline{\underline{L_{s,w}}} \propto$

$$\int_{\boldsymbol{\Omega}} \begin{pmatrix} \left(C_{11}\theta_z w + C_{12}\left(\theta_x u + \theta_y v\right)\right)\frac{\partial \delta w}{\partial z} + \\ +(C_{11}-C_{12})\frac{1}{4}\left(\left(\theta_y w + \theta_z v\right)\left(\frac{\partial \delta w}{\partial y}+\frac{\partial \delta v}{\partial z}\right) + \left(\theta_z u + \theta_x w\right)\left(\frac{\partial \delta u}{\partial z}+\frac{\partial \delta w}{\partial x}\right)\right) + \\ -\left(C_{11}\frac{\partial w}{\partial z} + C_{12}\left(\frac{\partial u}{\partial x}+\frac{\partial v}{\partial y}\right)\right)\theta_z \delta w + \\ -(C_{11}-C_{12})\frac{1}{4}\left(\left(\frac{\partial w}{\partial y}+\frac{\partial v}{\partial z}\right)\left(\theta_y \delta w + \theta_z \delta v\right) + \left(\frac{\partial u}{\partial z}+\frac{\partial w}{\partial x}\right)\left(\theta_z \delta u + \theta_x \delta w\right)\right) \end{pmatrix} d\Omega;$$

- $\underline{\underline{H_{s,w}}} \propto$

$$\int_{\boldsymbol{\Omega}} \begin{pmatrix} \left(C_{11}\theta_z w + C_{12}\left(\theta_x u + \theta_y v\right)\right)\theta_z \delta w + \\ +(C_{11}-C_{12})\frac{1}{4}\left(\left(\theta_y w + \theta_z v\right)\left(\theta_y \delta w + \theta_z \delta v\right) + \left(\theta_z u + \theta_x w\right)\left(\theta_z \delta u + \theta_x \delta w\right)\right) \end{pmatrix} d\Omega;$$

- $\underline{\underline{M_{s,w}}} \propto \int_{\Omega} \tilde{\rho} w \delta w \, d\Omega;$
- $\underline{\underline{N_{s,w}}} \propto \int_{\Omega} \tilde{\gamma}\frac{\partial p}{\partial z}\delta w \, d\Omega;$

- $\underline{\underline{O_{s,w}}} \propto \int_{\Omega} \tilde{\gamma}\theta_3 p\delta w \, d\Omega;$
- $\underline{\underline{T_{s,w}}} \propto \int_{\Omega} \phi\left(1+\frac{Q}{R}\right)\left(\frac{\partial p}{\partial z}\delta w + p\frac{\partial \delta w}{\partial z}\right) d\Omega;$
- $\underline{\underline{K_f}} \propto \int_{\boldsymbol{\Omega}} \frac{\phi^2}{\tilde{\rho}_{22}}\left(\frac{\partial p}{\partial x}\frac{\partial \delta p}{\partial x} + \frac{\partial p}{\partial y}\frac{\partial \delta p}{\partial y} + \frac{\partial p}{\partial z}\frac{\partial \delta p}{\partial z}\right) d\Omega;$
- $\underline{\underline{L_f}} \propto \int_{\boldsymbol{\Omega}} \frac{\phi^2}{\tilde{\rho}_{22}}\left(p\left(\frac{\partial \delta p}{\partial x}\theta_1 + \frac{\partial \delta p}{\partial y}\theta_2 + \frac{\partial \delta p}{\partial z}\theta_3\right) - \left(\frac{\partial p}{\partial x}\theta_1 + \frac{\partial p}{\partial y}\theta_2 + \frac{\partial p}{\partial z}\theta_3\right)\delta p\right) d\Omega;$
- $\underline{\underline{H_f}} \propto \int_{\boldsymbol{\Omega}} \frac{\phi^2}{\tilde{\rho}_{22}} p\delta p \, d\Omega;$
- $\underline{\underline{M_f}} \propto \int_{\boldsymbol{\Omega}} \frac{\phi^2}{R} p\delta p \, d\Omega;$
- $\underline{\underline{N_f}} \propto \int_{\Omega} \tilde{\gamma}\left(u\frac{\partial \delta p}{\partial x} + v\frac{\partial \delta p}{\partial y} + w\frac{\partial \delta p}{\partial z}\right) d\Omega;$
- $\underline{\underline{O_f}} \propto \int_{\Omega} \tilde{\gamma}(\theta_1 u + \theta_2 v + \theta_3 w)\delta p \, d\Omega;$
- $\underline{\underline{T_f}} \propto \int_{\Omega} \phi\left(1+\frac{Q}{R}\right)\left(\left(\frac{\partial \delta p}{\partial x}u + \frac{\partial \delta p}{\partial y}v + \frac{\partial \delta p}{\partial z}w\right) + \delta p\left(\frac{\partial u}{\partial x} + \frac{\partial v}{\partial y} + \frac{\partial w}{\partial z}\right)\right) d\Omega.$

3.1.4. Validation of the method

In order to validate the shift cell technique implementation for Biot-modeled foams, in the studied configuration and for propagation along the x-axis, a first calculation (Figure 53) is made to compare shift cell results with those obtained by Serra *et al.* [36] using the Wave Finite Element Method [137] and with those computed through an analytical model, which is valid for infinite homogeneous isotropic porous media, where three waves propagate (two compressional waves and one shear wave):

$$k_{shear} = \omega\sqrt{\frac{\tilde{\rho}_{11}\tilde{\rho}_{22} - \tilde{\rho}_{12}{}^2}{N\tilde{\rho}_{22}}}, \tag{112}$$

$$k_{fast,slow} = \sqrt{\frac{A_1}{2} \pm \sqrt{\frac{A_1{}^2}{4} - A_2}}, \text{ with} \tag{113}$$

$$A_1 = \omega^2 \frac{\tilde{\rho}_{11}R - 2\tilde{\rho}_{12}Q + \tilde{\rho}_{22}P}{RP - Q^2} \text{ and } A_2 = \omega^4 \frac{\tilde{\rho}_{11}\tilde{\rho}_{22} - \tilde{\rho}_{12}{}^2}{RP - Q^2}. \tag{114}$$

Parameters of foam and air used in the validation shown in Figure 53 and Figure 54 can be found in Appendix B of Serra *et al.* [36]. The two phases present in a poro-elastic material behave differently: the main difference with the pure elastic case lies in the existence of a second compressional wave, which is highly attenuated in the low frequency range. Each of the three waves propagates in the solid as well as in the fluid phase of the poro-elastic material. The ratios of the fluid over the solid velocities of the different wave types are given by [62]:

$$\mu_{shear} = -\frac{\tilde{\rho}_{12}}{\tilde{\rho}_{22}}, \tag{115}$$

$$\mu_{fast,slow} = \frac{Pk_{fast,slow}^2 - \omega^2\tilde{\rho}_{11}}{\omega^2\tilde{\rho}_{12} - Qk_{fast,slow}^2}. \tag{116}$$

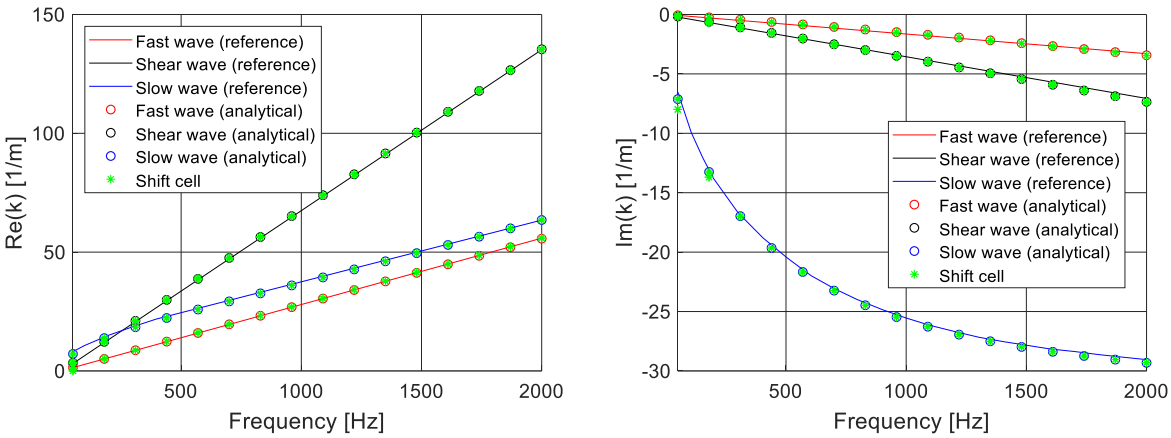

Figure 53: Dispersion curves for a 3D Biot-modeled unit cell, validation with Serra plots [36]*; real (left) and imaginary (right) parts.*

The shift cell approach has several advantages compared to the WFEM one. Indeed, as described by Serra *et al.* [36], the WFEM approach applied to Biot-modeled foams leads to a transcendental eigenvalue problem that can be solved by using a nonlinear solver, such as MatLab *fsolve* function. However, a lot of numerical difficulties exist and robust solutions have yet to be developed. Under the hypotheses of plane wave, this can be turned into a quadratic eigenvalue problem, whose accuracy is very sensitive to the choice of the length and of the meshing of the periodic substructure. Instead, the use of the shift cell approach leads directly to a quadratic eigenvalue problem, with no assumption on the nature of the waves, whose accuracy only depends on the meshing of the periodic structure. In particular, poro-elastic elements have slow convergence rates and the criterion of 6 elements per wave length may not be sufficient in the general case [138], thus the use of 10 elements per wave length in the three directions is recommended as a rule of the thumb [36].

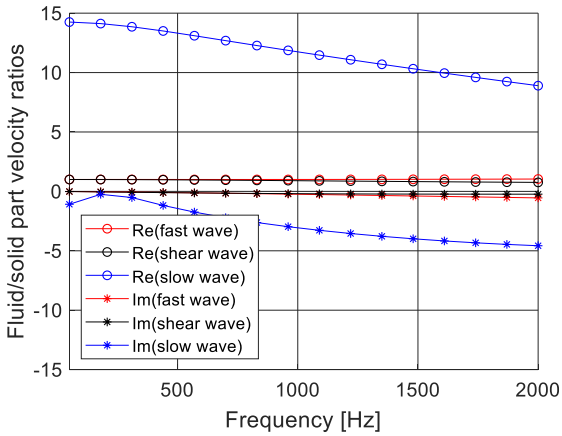

Figure 54: Ratios of the fluid over the solid velocities of the different wave types for a 3D Biot-modeled unit cell.

An additional validation (Figure 55 and Figure 56) is then carried out through a comparison with the results obtained on a JCA-modeled 3D unit cell (Figure 8), both in a homogeneous configuration (Table 10) and with a perfectly rigid cylindrical inclusion; in this case, a 3D periodicity is considered.

For the sake of comparison with the equivalent fluid case, here the properties of the foam are modified in order to simulate a rigid frame behavior; in particular, the Young modulus is set to $E = 10^{15}$ Pa and the loss factor is nullified.

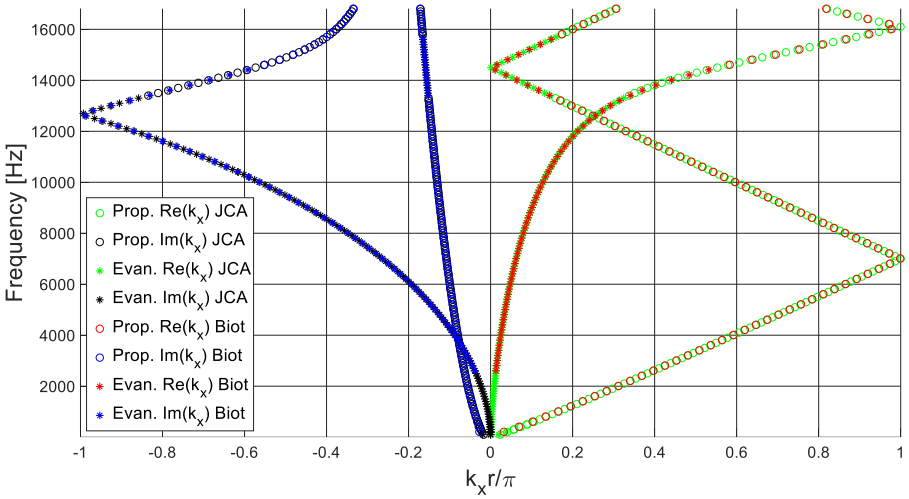

Figure 55: Dispersion curves validation with JCA plots; here, the Biot curves are computed for a 3D homogeneous PU 60 unit cell, with $E = 10^{15}$ Pa and structural loss factor $= 0$.

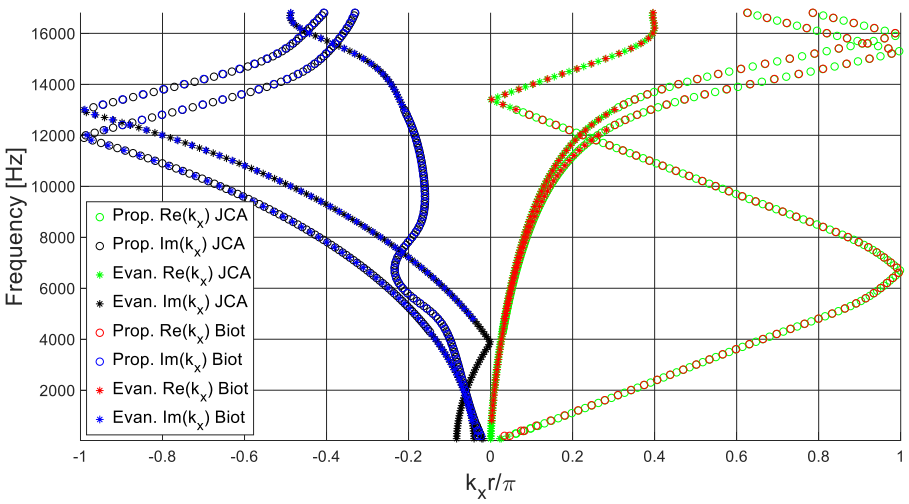

Figure 56: Dispersion curves validation with JCA plots; here, the Biot curves are computed for a 3D PU 60 unit cell with a perfectly rigid cylindrical inclusion, with $E = 10^{15}$ Pa and structural loss factor $= 0$.

Again, one may notice that there could be some discontinuous curves where the wave propagates, then becomes evanescent, then propagates again (or vice-versa): this is not an expected configuration, and it is probably due to the fact that, as said in Section 2.2.1, all waves are evanescent with different rates and so a non-perfect tuning of the classifying criteria could lead to lines that disappears and reappears on the plots.

3.1.5. Branch tracking

In this section, a branch tracking algorithm is introduced for Biot-modeled foams. In this case, due to the higher number of parameters and matrices compared to those associated to an equivalent fluid problem, it would be much more complex to formulate and solve a coupled eigenvalue problem in order to obtain an analytical expression for the group velocity. Therefore, here the proposed approach is more simple, with respect to the one explained in Section 2.3, and consists in comparing a single wave number value at a specific frequency $k_i(f)$ and $\boldsymbol{k}(f + \Delta f)$.

From the wave number associated to a starting point, the routine compares the initial k_i with all the group velocities at the next frequency step $f + \Delta f$ and a minimization is made in order to identify the point at $f + \Delta f$ to which is associated the closest value of k. Then, this point is defined as the new starting one and so on, step by step, the branch is identified.

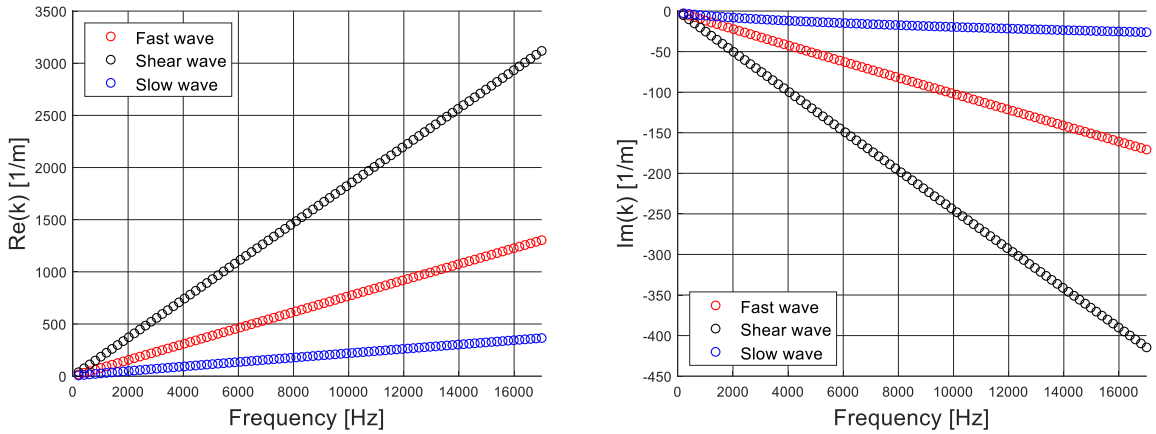

Figure 57: Real (left) and imaginary (right) parts of analytically estimated dispersion curves for a 3D Biot-modeled homogeneous PU 60 foam.

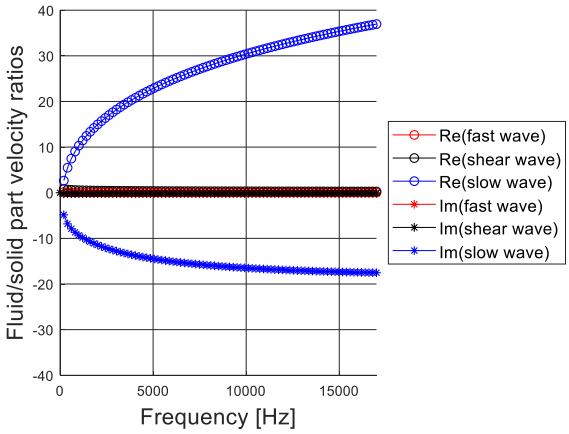

Figure 58: Ratios of the fluid over the solid velocities of the different wave types in a 3D Biot-modeled homogeneous PU 60 foam.

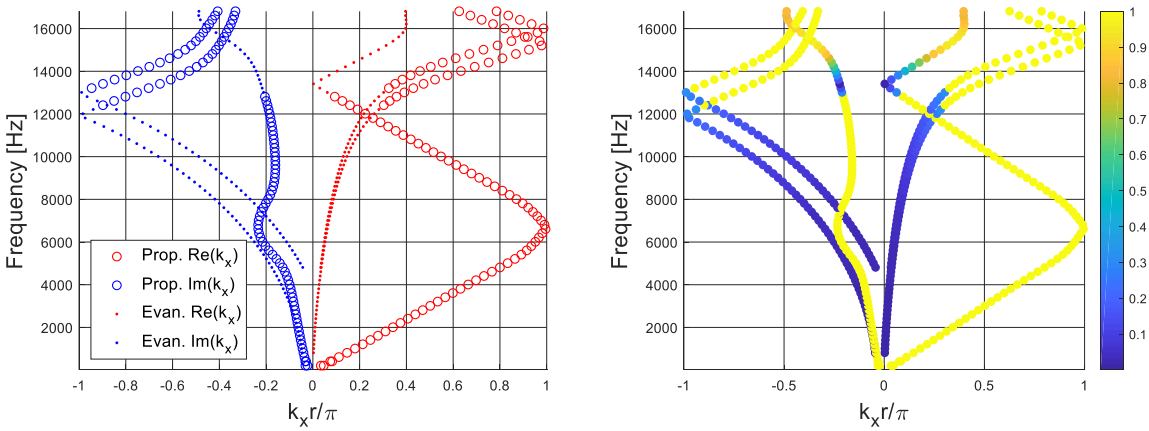

Figure 59: Evanescent and propagative parts of dispersion curves for a 3D Biot-modeled PU 60 unit cell, with a perfectly rigid cylindrical inclusion. The color scale (on the right) indicates the level of propagativeness.

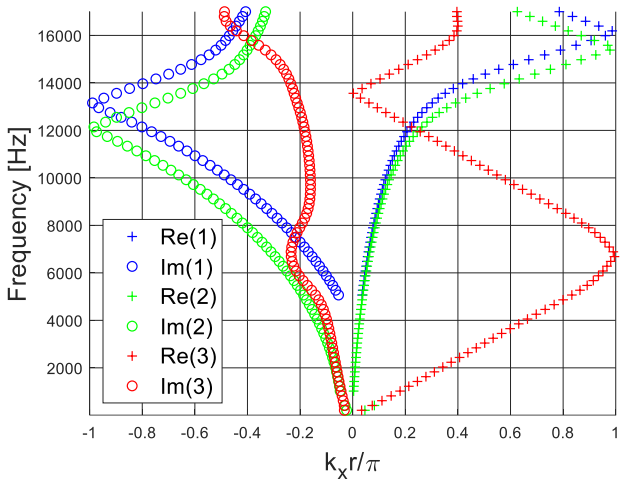

Figure 60: Branch-tracked dispersion curves for a 3D Biot-modeled PU 60 unit cell, with a perfectly rigid cylindrical inclusion.

For all tested configurations, which involve the computation of 20 eigenvalues, the branch-tracking algorithm, through the use of a proper frequency step in the eigenproblem definition, is able to correctly classify the solutions, even in the presence of band gaps, branch-crossing or branch-veering.

3.2. Absorption coefficient and transmission loss comparisons between JCA and Biot models

The following results are related to the same finite element model configuration described in Section 2.3; the unit cell configuration is the 3D one described in Figure 8, and the poro-elastic properties of the foams are reported in Table 10. With reference to the following plots, one can notice that, In the case of PU 60 foam (Figure 61 and Figure 62), no meaningful differences are shown between JCA and Biot results. The same happens for Test foam 1 absorption coefficient curve (Figure 63), while a non-negligible transmission loss performance increase can be seen at high frequencies, when the Biot model is used (Figure 64): this is due to the structural response of the foam skeleton, whose elasticity is neglected when using an equivalent fluid model instead. This phenomenon is even more evident in the case of Test foam 2, probably due to its high airflow resistivity value, where some clear differences between JCA and Biot results are shown at low-middle frequencies, both for absorption coefficient (Figure 65) and transmission loss curves (Figure 66).

Table 10: Poro-elastic properties of the tested foams.

	PU 60	**Test foam 1**	**Test foam 2**
Porosity	0.98	0.96	0.97
Tortuosity	1.17	1.7	2.52
Airflow resistivity [Pa*s/m^2]	3750	32000	87000
Viscous characteristic length [mm]	0.11	0.09	0.037
Thermal characteristic length [mm]	0.742	0.165	0.119
Density [kg/m^3]	22.1	30	31
Young modulus [kPa]	70 + j19	733+j73	143+j8
Shear modulus [kPa]	25 + j7	264+j*26	55+j3
Loss factor	0.265	0.1	0.055
Poisson ratio	0.39	0.387	0.3

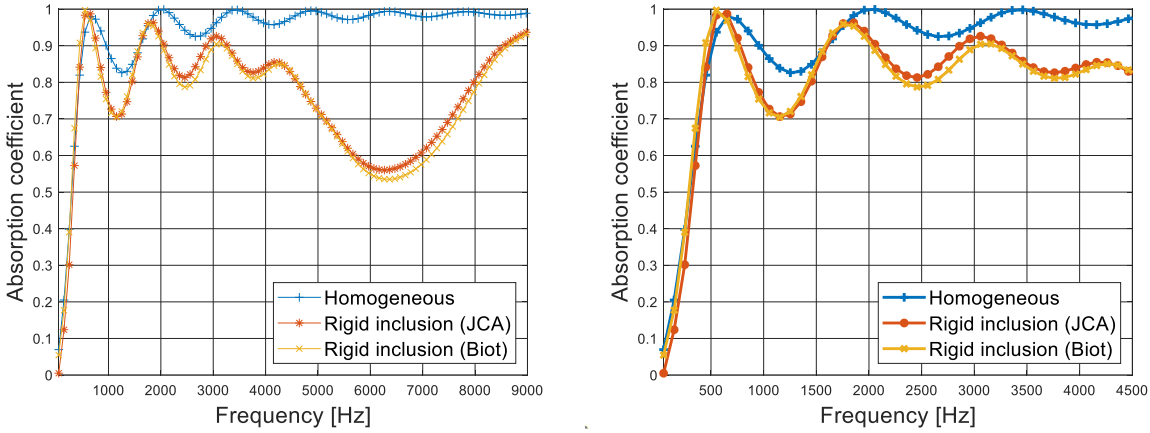

Figure 61: Absorption coefficient comparisons between JCA and Biot models for PU 60 foam.

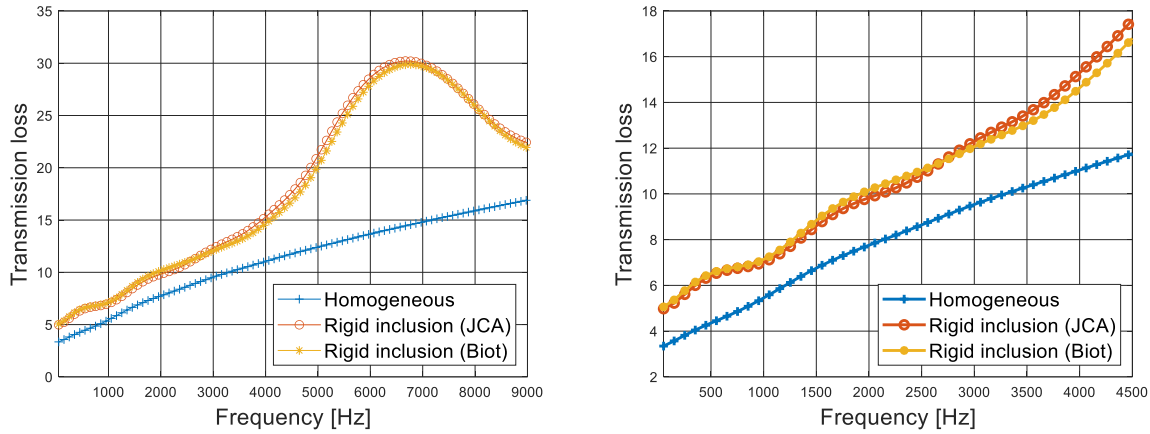

Figure 62: Transmission loss comparisons between JCA and Biot models for PU 60 foam.

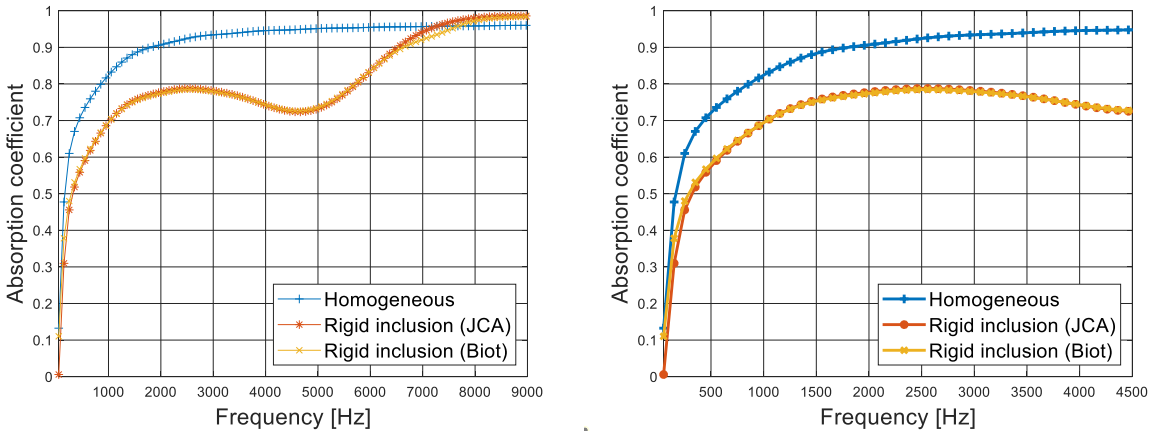

Figure 63: Absorption coefficient comparisons between JCA and Biot models for Test foam 1.

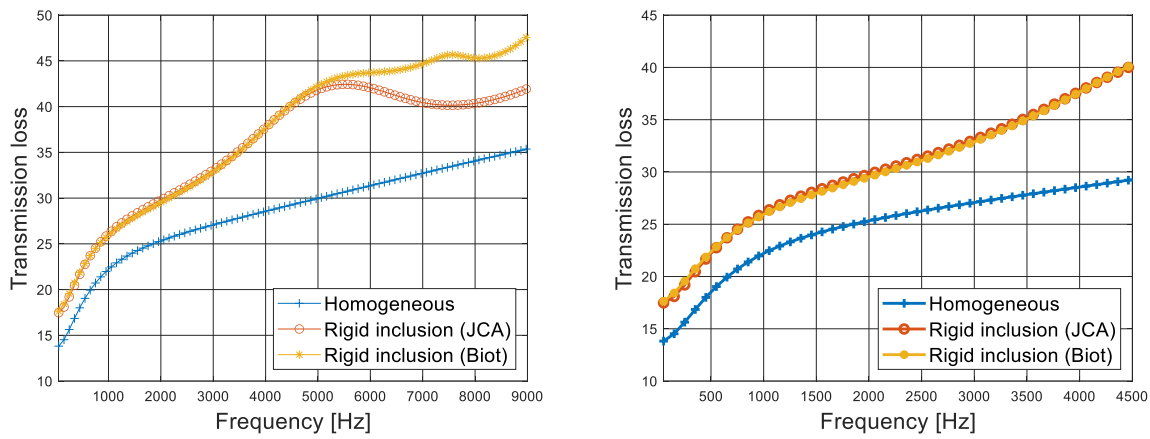

Figure 64: Transmission loss comparisons between JCA and Biot models for Test foam 1.

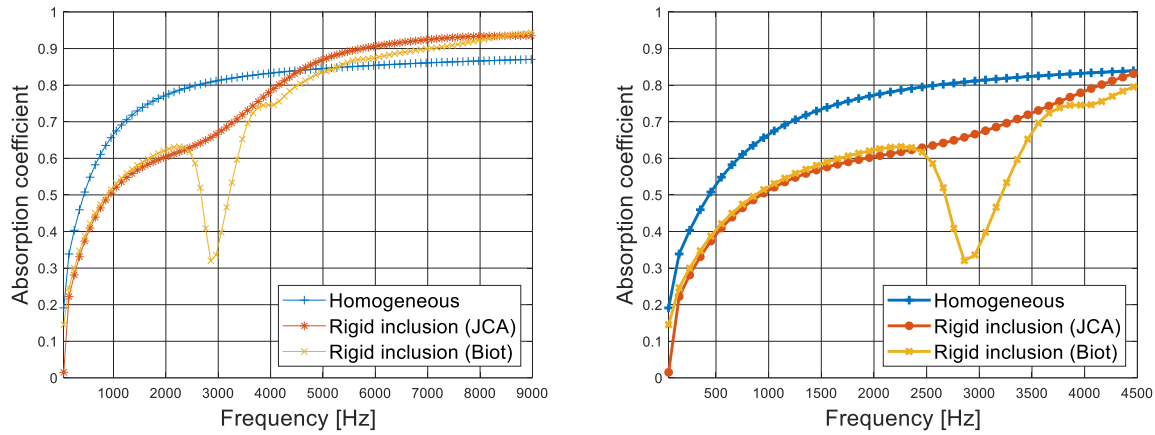

Figure 65: Absorption coefficient comparisons between JCA and Biot models for Test foam 2.

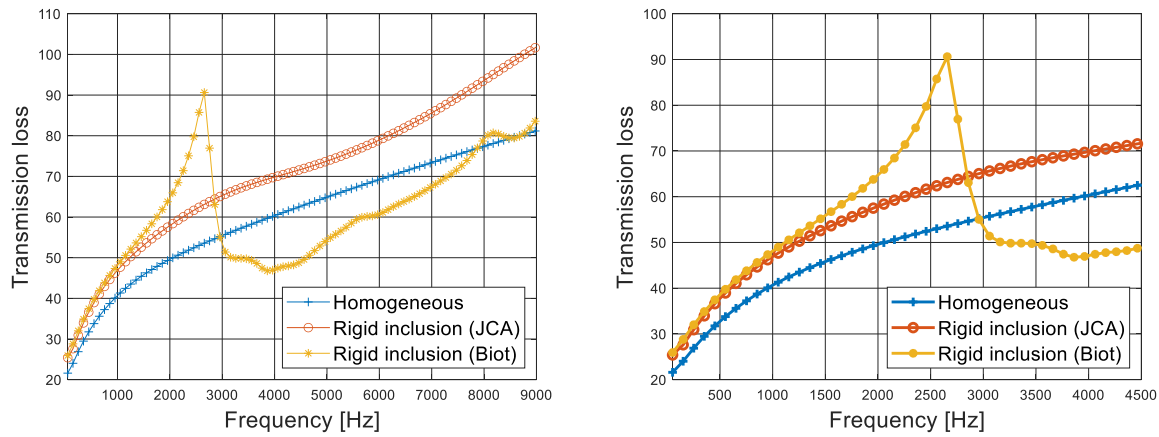

Figure 66: Transmission loss comparisons between JCA and Biot models for Test foam 2.

3.2.1. Computational cost comparison between JCA and Biot models

Figure 67 and Figure 68 show a comparison of the computational cost, in terms of time and as a function of the number of elements in the finite element model, between JCA and Biot models for the computation of the values of absorption coefficient and transmission loss at a single frequency.The 3D geometry is meshed using tetrahedral elements are used, and the configuration considered is the one described by case 42 of Table 4. Raw data are also approximated through a piecewise cubic Hermite interpolating polynomial technique. As expected, the calculation cost is always higher with the Biot model than the one required by the JCA one. However, this difference decreases with an almost logarithmic behavior when the number of elements of the finite element model is increasing.

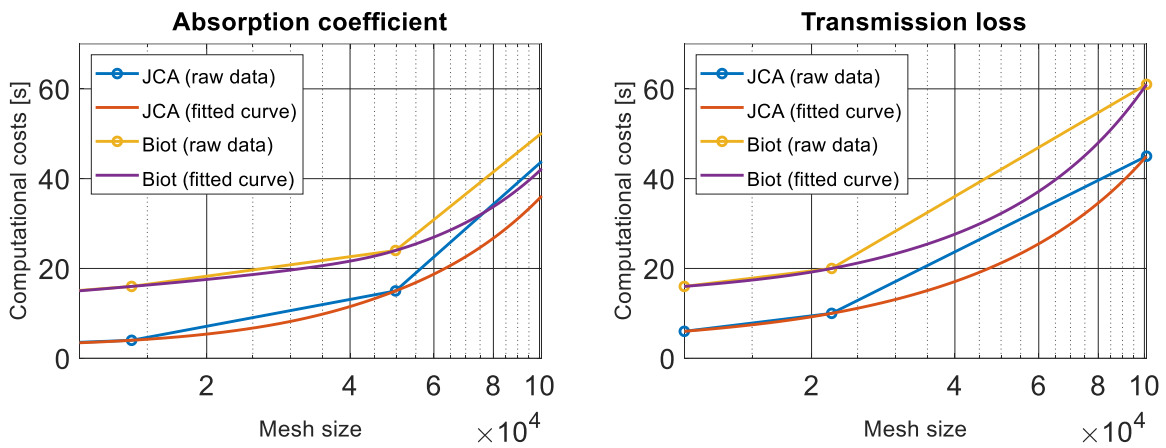

Figure 67: Computational times [s] for a single value of absorption coefficient (left) and transmission loss (right), for increasing number of elements.

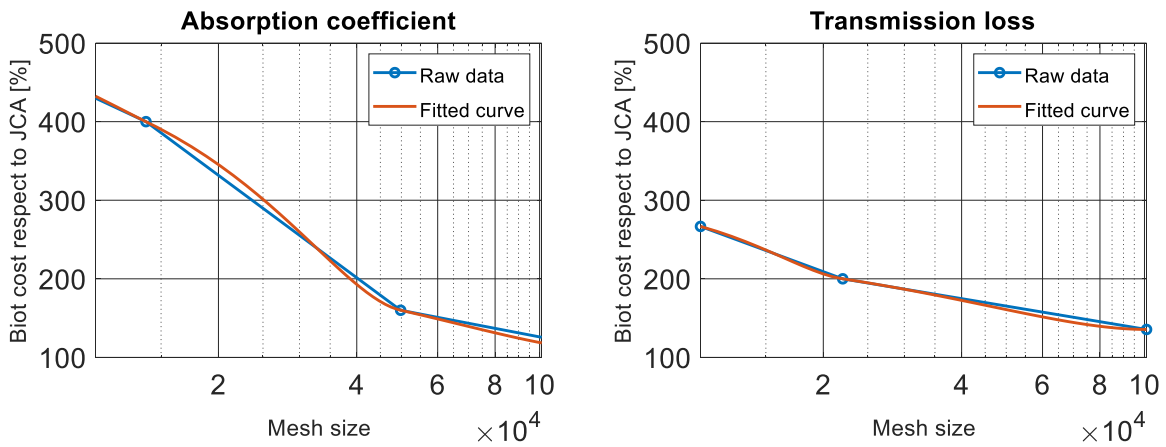

Figure 68: Computational time percentage for a single value of absorption coefficient (left) and transmission loss (right), for increasing number of elements.

Considering the very few differences between JCA and Biot models highlighted in Figure 61, the usage of the latter is recommended only in presence of a foam whose frame elasticity clearly plays a relevant role in its acoustic performance. Furthermore, this choice becomes more justified for finite element models that require a very fine mesh, since the difference between the two approaches, in terms of computational time, reduces with increasing mesh size.

3.3. Non-rigid inclusion test campaign

Through the use of the acoustic-structure coupling that comes from the implementation of Biot model, the previous non-rigid inclusion test campaign (Section 2.4) can be extended by considering some solid (but still non-perfectly-rigid) inclusions in the 3D-modeled unit cell described in Figure 8. In particular, 6 setups are discussed here, whose fundamental parameters are reported in Table 11. However, only results related to Configurations 1, 2 and 6 of Table 12 are shown, since those related to Configurations 3, 4, and 5 have negligible differences respect to Configuration 2.

Table 11: Elastic properties of the materials used in the non-rigid inclusions test campaign, with a Biot-modeled PU 60 foam.

Material	Density [kg/m^3]	Young modulus [kPa]	Poisson ratio
PU 60	22.1	70 + j19	0.39
Aluminum 3003-H18	2730	69e6	0.33
Steel AISI 4340	7850	205e6	0.28
Titanium beta-21S	4940	105e6	0.33
Silicon rubber	1100	1e6*(1 + j0.4)	0.47

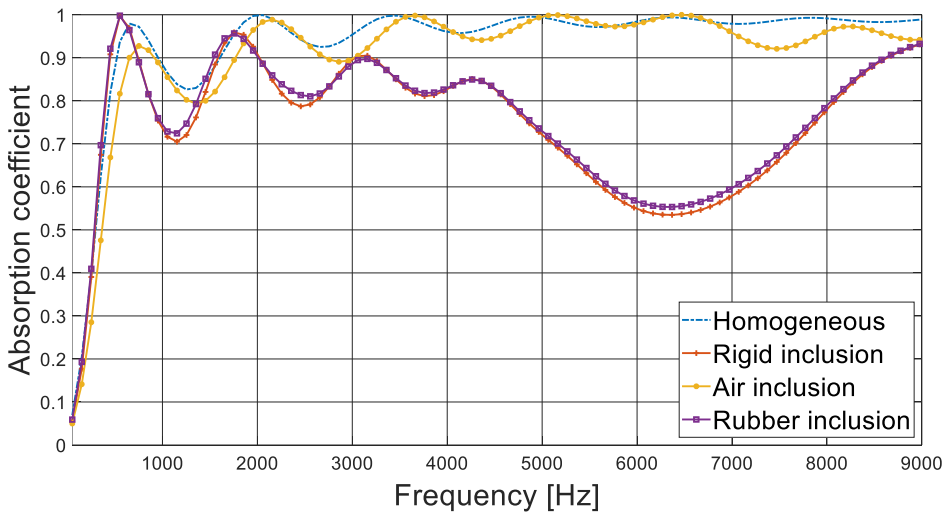

Figure 69: Absorption coefficient computations for Configurations 1, 2 and 6.

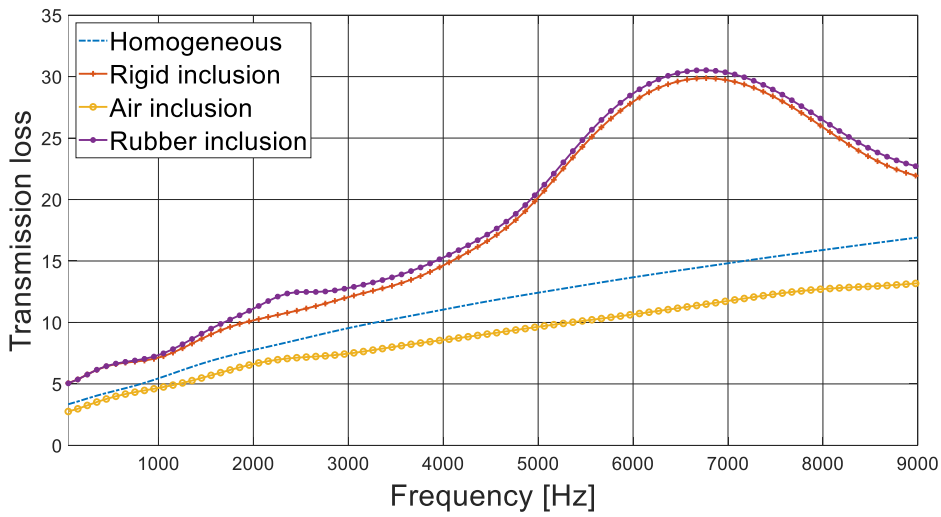

Figure 70: Transmission loss computations for Configurations 1, 2 and 6.

Table 12: Combinations of inclusions used in the non-rigid inclusions test campaign, with a Biot-modeled PU 60 foam, and mass variations respect to the homogeneous case.

Configuration	Inclusion	Mass variation [%]
1	Homogeneous	0
2	Perfectly rigid	-19.63495408
3	Aluminum 3003-H18	2405.859374
4	Steel AISI 4340	6954.771814
5	Titanium beta-21S	4369.354783
6	Silicon rubber	957.6704529

Additional results are provided from Figure 71 to Figure 74, obtained by carrying out the non-rigid inclusion test campaign also using Test foam 1 and Test foam 2, described in Table 10.

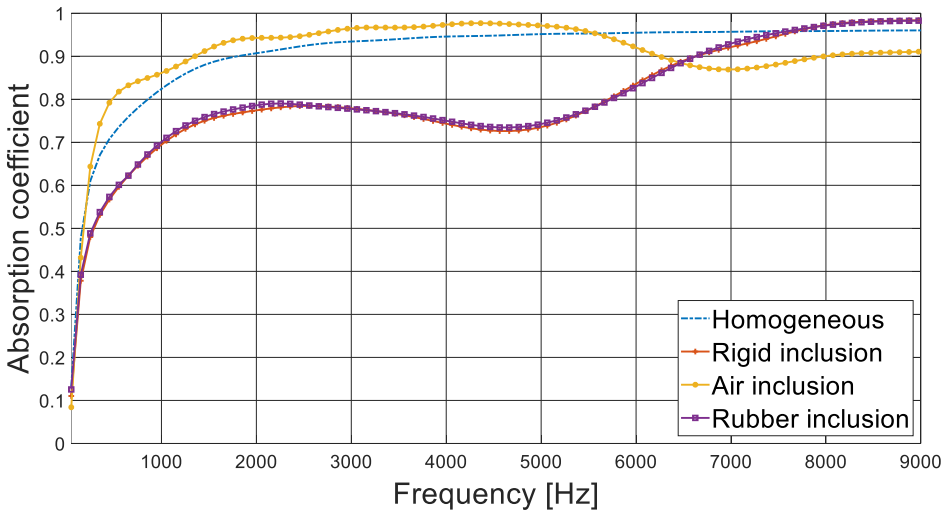

Figure 71: Non-rigid inclusion test campaign for Test foam 1 absorption coefficient.

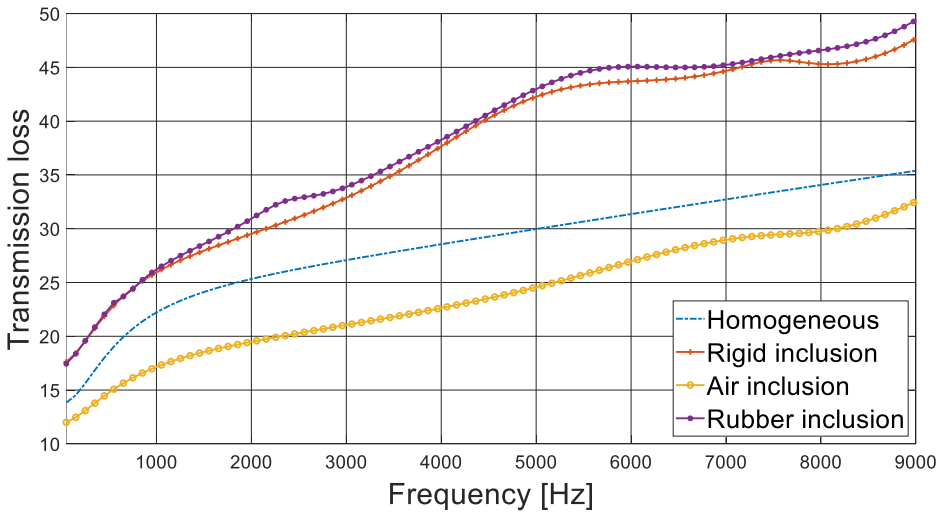

Figure 72: Non-rigid inclusion test campaign for Test foam 1 transmission loss.

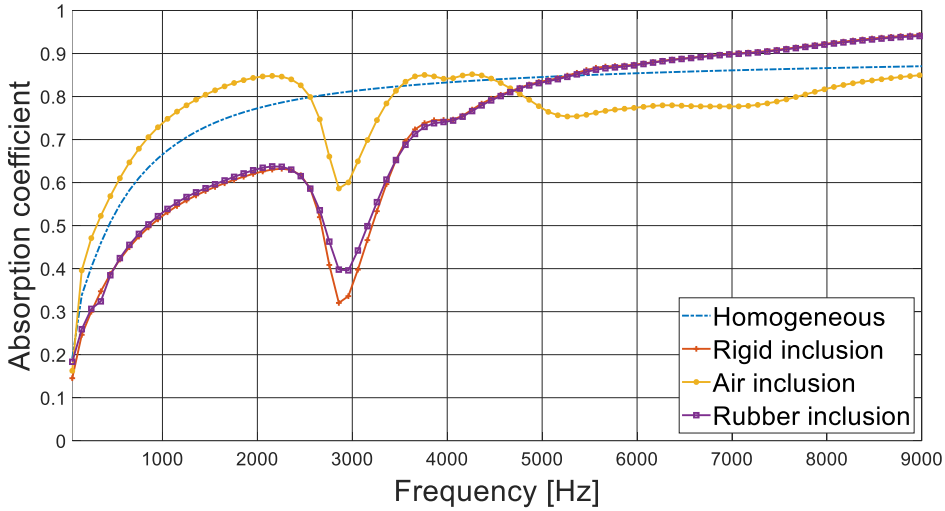

Figure 73: Non-rigid inclusion test campaign for Test foam 2 absorption coefficient.

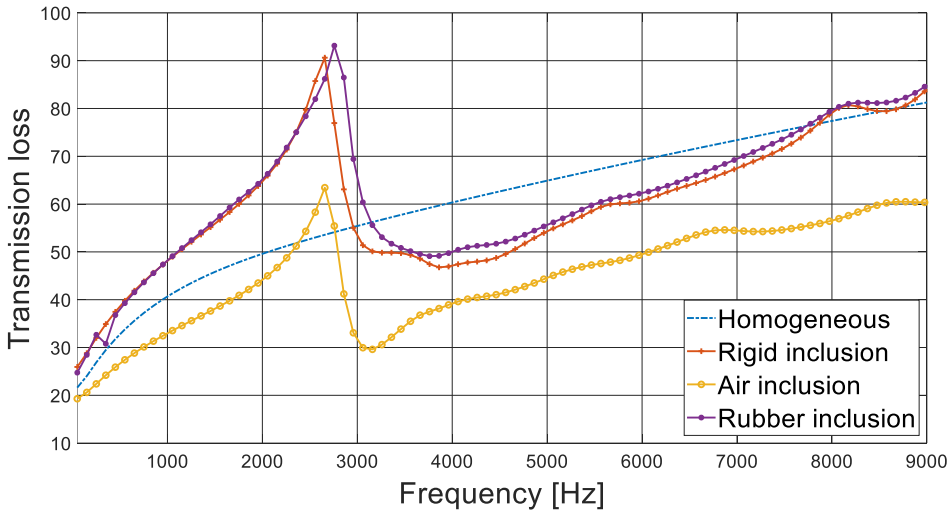

Figure 74: Non-rigid inclusion test campaign for Test foam 2 transmission loss.

Some interesting considerations may be formulated, based on the results provided herein. In the context of the studied systems, after appropriate checks, the cause of all the macroscopic resonances has been addressed to the effect of periodicity (half of the wavelength = periodicity dimension), except from the case related to Test foam 2, where the main visible peak is caused by a spring-mass effect (as already highlighted in Section 3.2, Figure 65 and Figure 66). In this case, this is also confirmed by the fact that, looking at the "Air inclusion" curves from Figure 69 to Figure 72, they do not seem to "sense" the effect of the inclusion, probably due to the low impedance mismatch between the contact surfaces; instead, in Figure 73 and Figure 74, the peaks are visible also in case of an inclusion filled by air, this being a further clue leading to a spring-mass resonance.

As expected, it should be noted how the sharpness of the performance peaks rises when the structural loss factor of the foam decreases. Moreover, the fact that the periodicity peak shifts backward in frequency from PU 60 case to Test foam 1 case, could be explained through the higher tortuosity value of the latter. This behavior is better explained in Section 3.4, which provides a more detailed discussion and additional results about design guidelines.

3.3.1. Design of absorption coefficient low frequency improvement

The aim of this section is to show that, even if apparently the insertion of a periodic inclusion pattern in a layer of foam always leads to an absorption coefficient performance decay for the cases of study (Figure 69), instead there is an actual way to improve it without necessarily exploiting the use of Helmholtz resonators (Section 2.7). In particular, if one uses a repetition of sufficiently small unit cells, some oscillations of the periodic absorption coefficient values can be observed at low frequencies, respect to the homogeneous case. Results in Figure 75 are related to Configurations 1, 2 and 6 of Table 12, where the setup is constituted by a repetition of five 3D unit cells described in Figure 8; the length of the side of each unit cell is 0.01 m. In this situation, the differences between the perfectly rigid inclusion and the rubber inclusion cases are negligible at low frequencies. It can be noticed that the effect described above lays in the range of 550 – 1450 Hz, very interesting for acoustic applications, where the average improvement is of about 16 %.

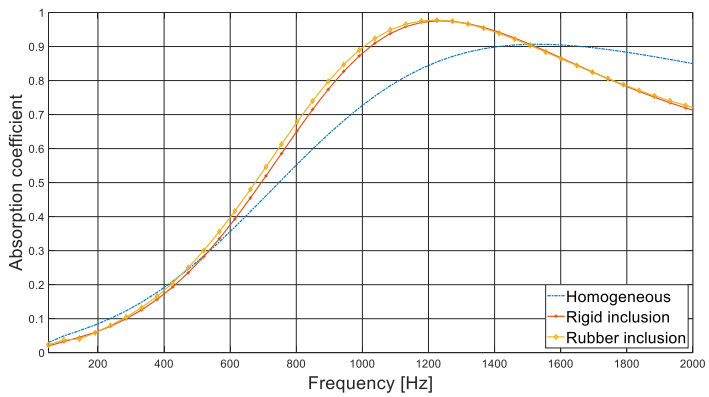

Figure 75: Absorption coefficient low frequency improvement for a repetition of five 3D PU 60 unit cells.

3.4. Design guidelines

In this section, with reference to a Biot-modeled PU 60 foam, as already done in Section 2.5 for a JCA-modeled melamine foam, some design guidelines are investigated. Firstly, they are provided in order to predict at which frequency the 1st performance peak (related to periodicity effects: half of the wavelength = periodicity dimension) appears, together with its amplitude, as functions of the unit cell dimensions. Conversely, also the link between the unit cell dimensions and the 1st performance peak amplitude as functions of the design frequency is shown. The test campaign is carried out in the 0 – 10000 Hz frequency range, through the use of a repetition of five 3D unitary cells constituted by a 2 cm cube with a 0.5 cm radius perfectly rigid cylindrical inclusion, where the dimension of the inclusion changes accordingly to those of the unit cell (the ratio between the unit cell and the inclusion dimensions is kept constant). According to the results obtained in Figure 76 and Figure 77, and considering that a typical acoustic excitation in aeronautics lays in the range of 20 – 2000 Hz [126], one should choose a unit cell dimension between 0.065 m and 0.1 m in order to obtain a transmission loss improvement of averagely 25% respect to the use of a simple foam layer of the same thickness. Considering an automotive application, instead, the typical acoustic excitation lays in the range of 20 – 4000 Hz [127], and therefore one should choose a unit cell dimension between 0.035 m and 0.1 m in order to obtain a transmission loss improvement of averagely 35% respect to the use of a simple foam layer of the same thickness.

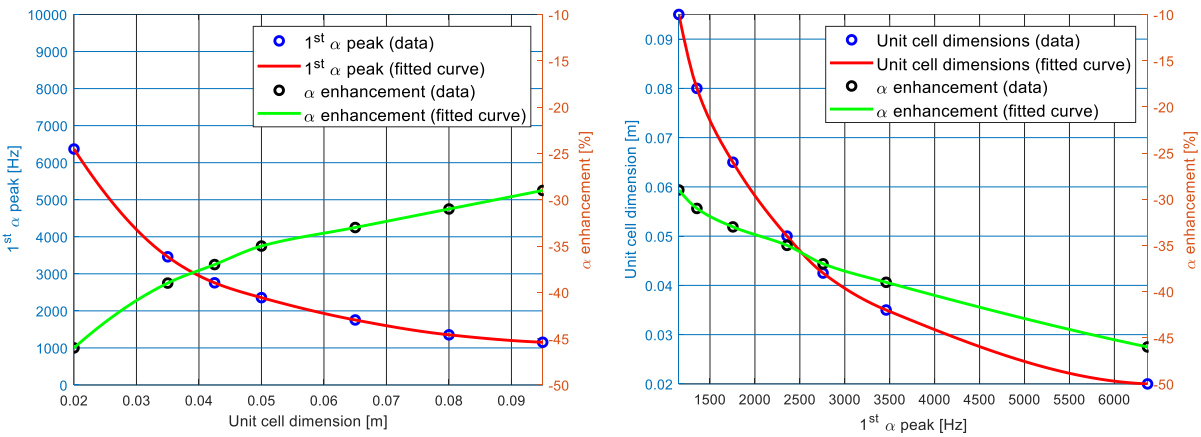

Figure 76: Absorption coefficient design curves as a function of the unit cell dimension (on the left) and the frequency of the 1st peak (on the right).

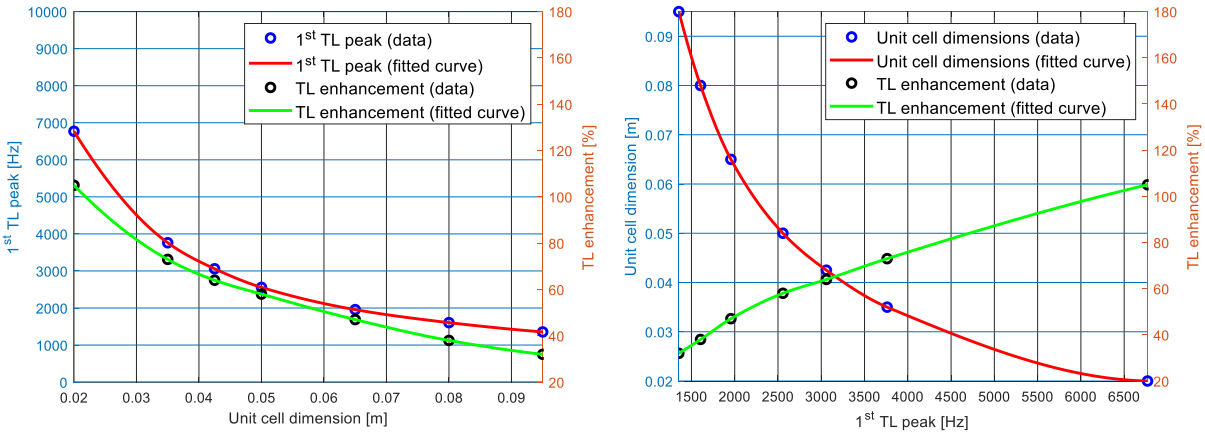

Figure 77: Transmission loss design curves as a function of the unit cell dimension (on the left) and the frequency of the 1st peak (on the right).

Furthermore, some guidelines are also provided in order to predict at which frequency the 1st performance peak appears, together with its amplitude, as functions of the foam airflow resistivity (Figure 78 – Figure 80), tortuosity (Figure 81 – Figure 83), viscous and thermal characteristic lengths (Figure 84 – Figure 86, Figure 87 – Figure 89). The test campaign is carried out in the 0 – 10000 Hz frequency range, by comparing a repetition of five PU 60 unit cells, whose geometry is described in Figure 8 and where the value of the studied parameter is artificially changed. This kind of analysis has not been extended also to porosity, since it typically assumes values that oscillate around 0.96 – 0.98.

Looking at Figure 78, it is clear that the static airflow resistivity has no meaningful impact on the position of the periodicity peak in the frequency range. Instead, one may notice that σ has a non-negligible effect on the variation of the non-homogeneous values, compared to the homogeneous ones, in correspondence of the periodicity peak. In particular, this variation reduces its amplitude at increasing airflow resistivity values, both for absorption coefficient and transmission loss performances. This is probably due to the fact that, as shown in Figure 79 and, in an even more evident manner, in Figure 80, for a homogeneous layer of foam, when σ increases absorption coefficient performances decrease, while transmission loss ones gets better. This is an expected phenomenon, since the airflow resistivity parameter may be considered as an “acoustical hardness” indicator of a foam, in the sense that, the higher it is, the less air permeability there is.

It is evident, then, that the general effect of any external inclusion in the foam reduces at increasing σ, and the non-homogeneous curves tend to assume the same behavior of the homogeneous ones. Indeed, starting from $\sigma = 60000\ \frac{\mathrm{Pa*s}}{\mathrm{m}^2}$, periodicity peaks are no more precisely identifiable.

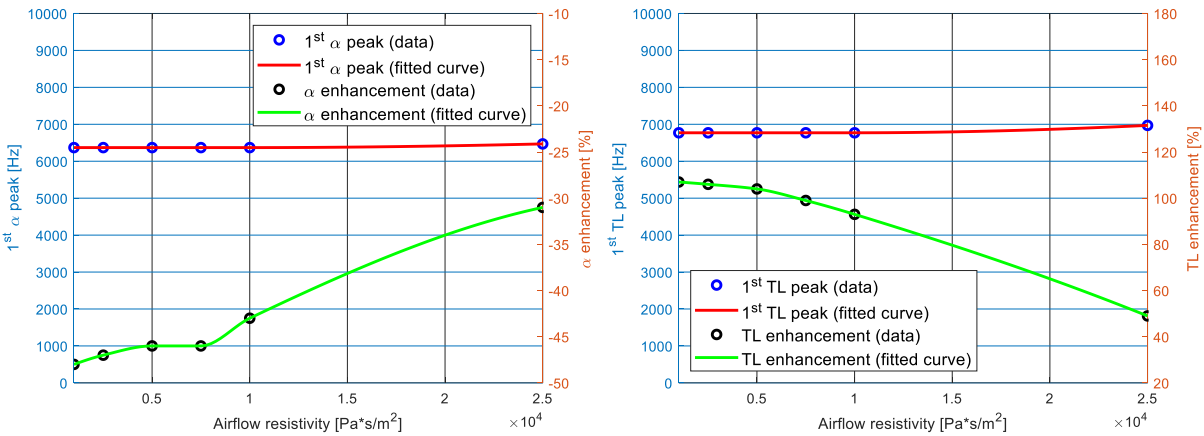

Figure 78: Absorption coefficient (on the left) and transmission loss (on the right) design curves as functions of the foam airflow resistivity.

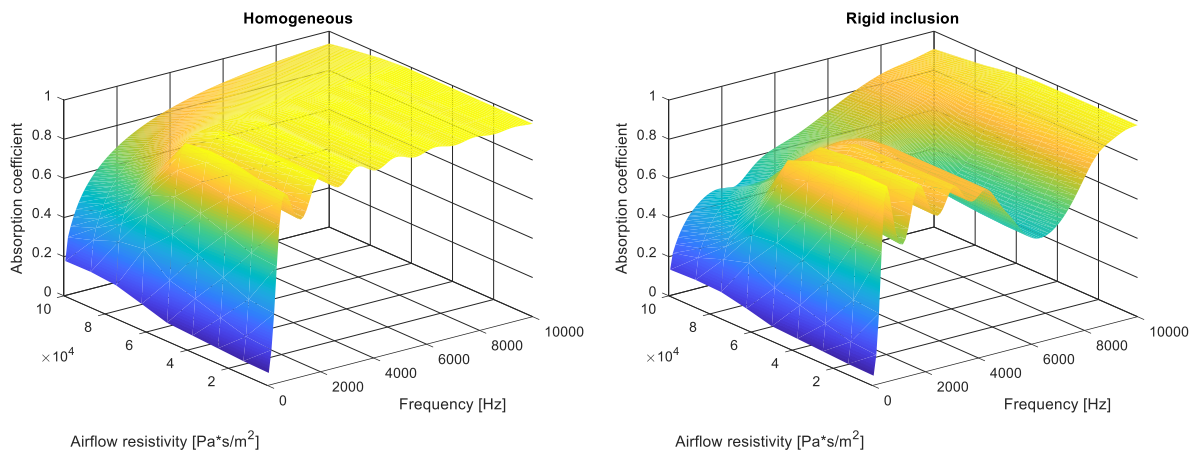

Figure 79: Absorption coefficient value as a function of frequency and foam airflow resistivity; homogeneous case (on the left) and case with a cylindrical perfectly rigid inclusion (on the right).

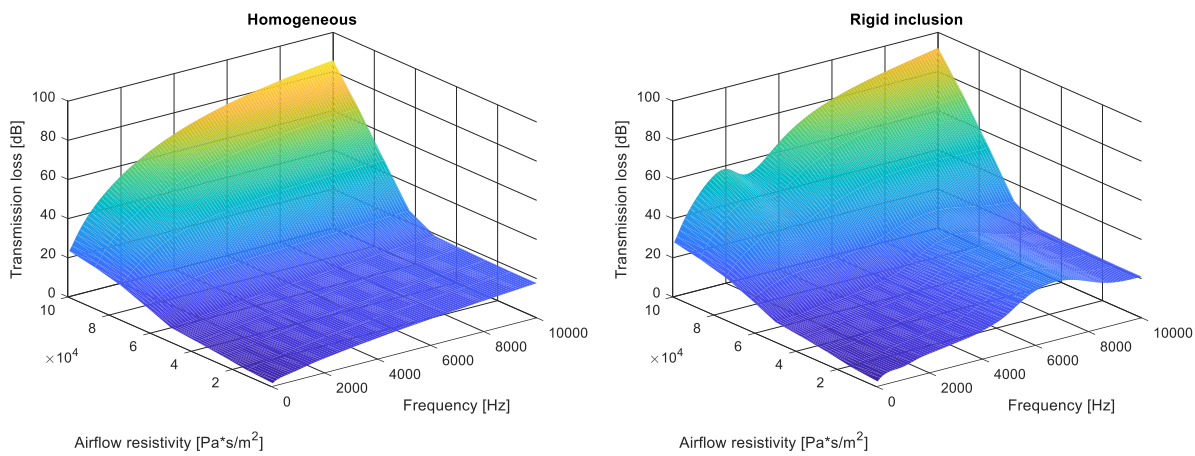

Figure 80: Transmission loss value as a function of frequency and foam airflow resistivity; homogeneous case (on the left) and case with a cylindrical perfectly rigid inclusion (on the right).

For what concerns the tortuosity of the foam, from Figure 81 to Figure 83 it is evident that it has a strong impact on the acoustic performances of the system. In particular, at increasing tortuosity, the periodicity peak shifts backward in frequency, while also weakly reducing its amplitude.

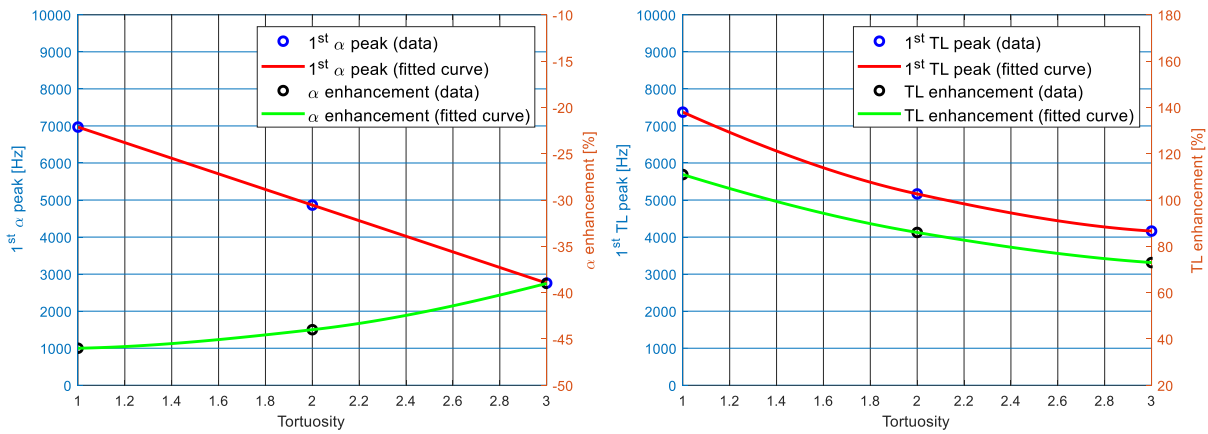

Figure 81: Absorption coefficient (on the left) and transmission loss (on the right) design curves as functions of the foam tortuosity.

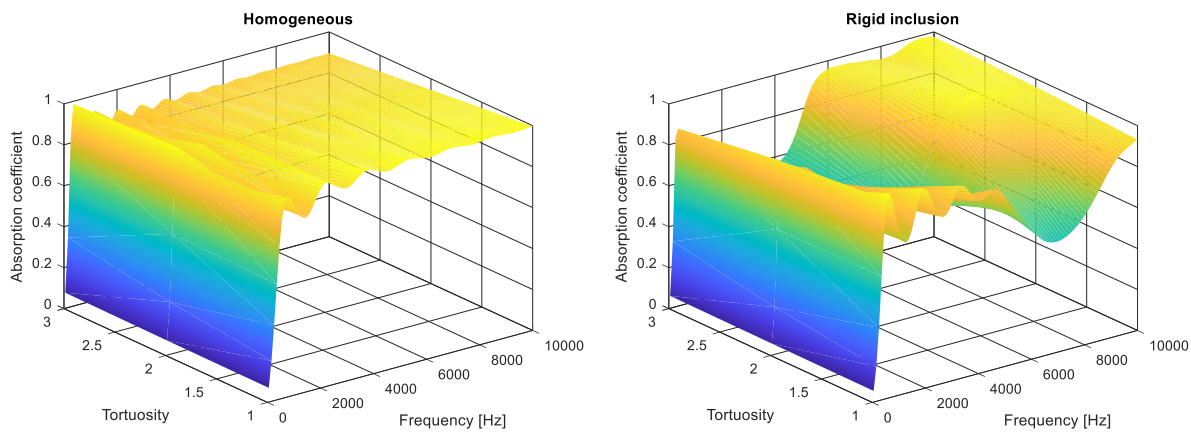

Figure 82: Absorption coefficient value as a function of frequency and foam tortuosity; homogeneous case (on the left) and case with a cylindrical perfectly rigid inclusion (on the right).

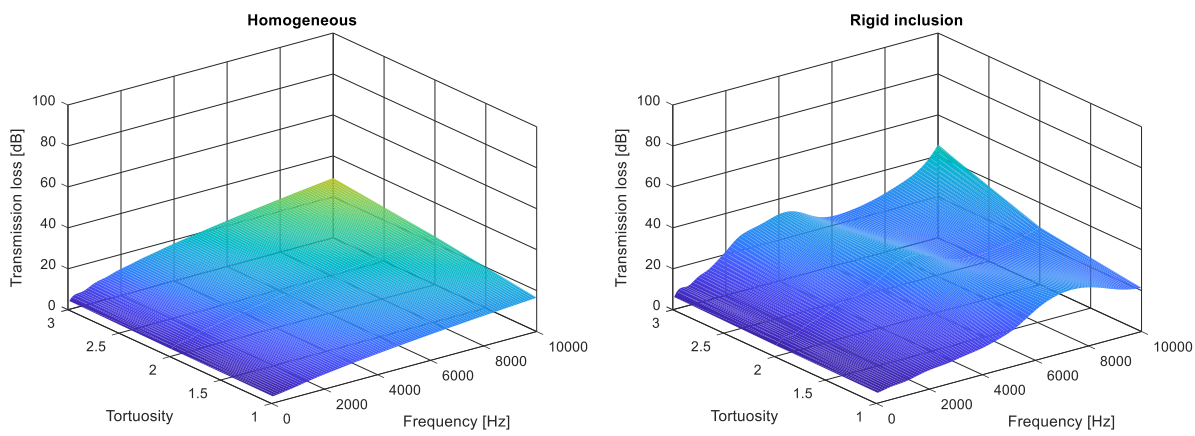

Figure 83: Transmission loss value as a function of frequency and foam tortuosity; homogeneous case (on the left) and case with a cylindrical perfectly rigid inclusion (on the right).

Figure 84 show that also the viscous characteristic length has a meaningful impact, in this context.

The behavior is the inverse of the one related to tortuosity: at increasing viscous characteristic length, the periodicity peak shifts forward in frequency, while also weakly increasing its amplitude. In addition, a higher value of viscous characteristic length means a less reflecting foam: absorption increases (Figure 85), while transmission loss decreases (Figure 86).

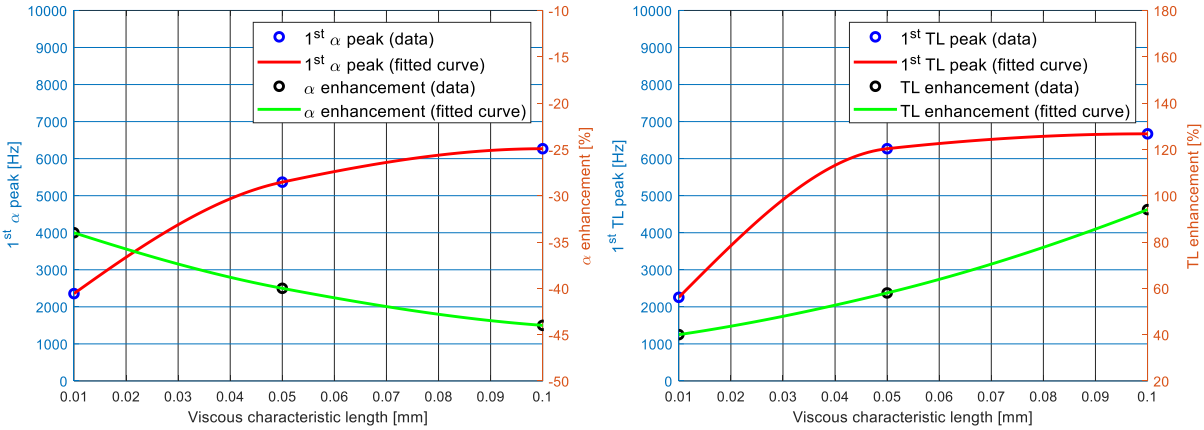

Figure 84: Absorption coefficient (on the left) and transmission loss (on the right) design curves as functions of the foam viscous characteristic length.

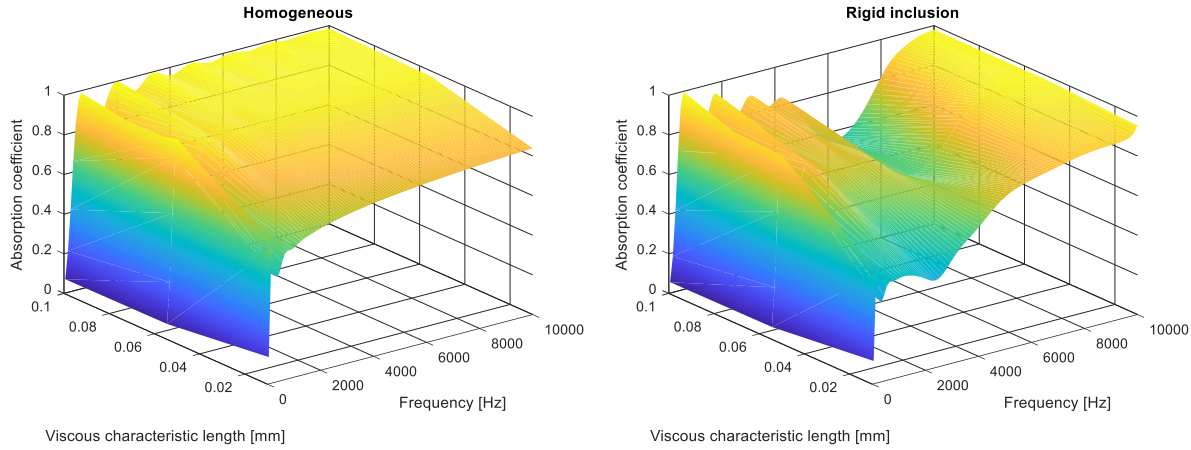

Figure 85: Absorption coefficient value as a function of frequency and foam viscous characteristic length; homogeneous case (on the left) and case with a cylindrical perfectly rigid inclusion (on the right).

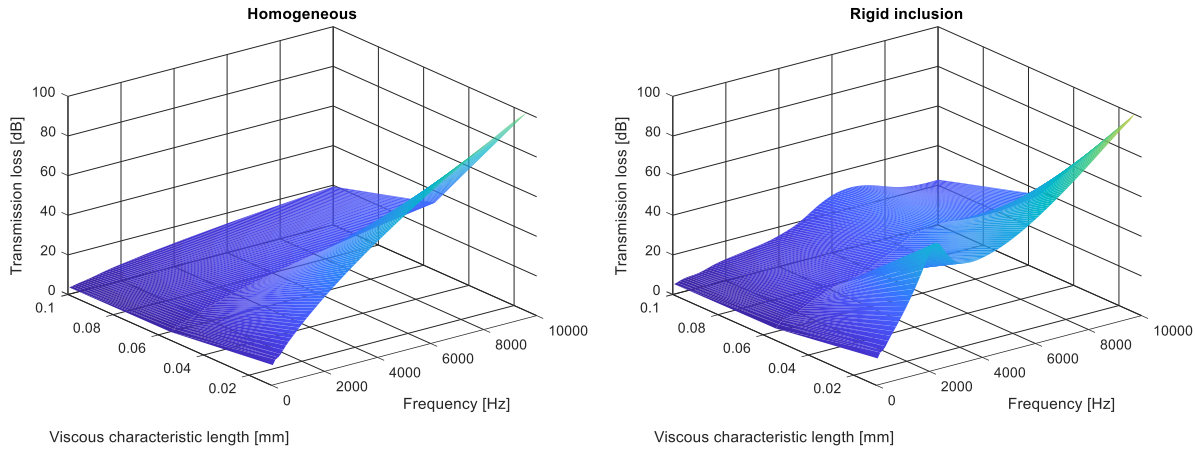

Figure 86: Transmission loss value as a function of frequency and foam viscous characteristic length; homogeneous case (on the left) and case with a cylindrical perfectly rigid inclusion (on the right).

Differently from the viscous one, from Figure 87 it can be stated that the thermal characteristic length has no evident impact on the frequency position of the periodicity peaks, but it has a more intense effect on their amplitude: at increasing thermal characteristic length, the periodicity peak do not shift in frequency, but increases its amplitude.

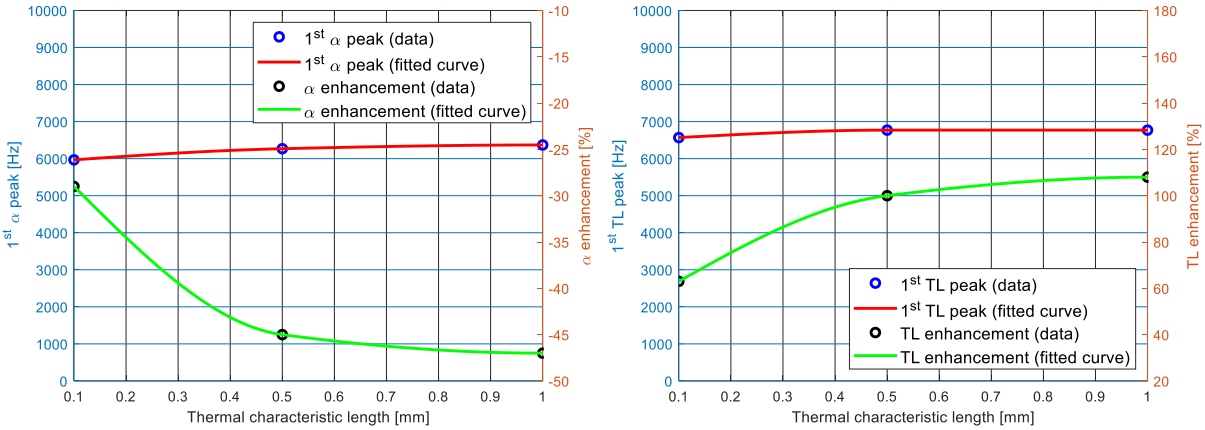

Figure 87: Absorption coefficient (on the left) and transmission loss (on the right) design curves as functions of the foam thermal characteristic length.

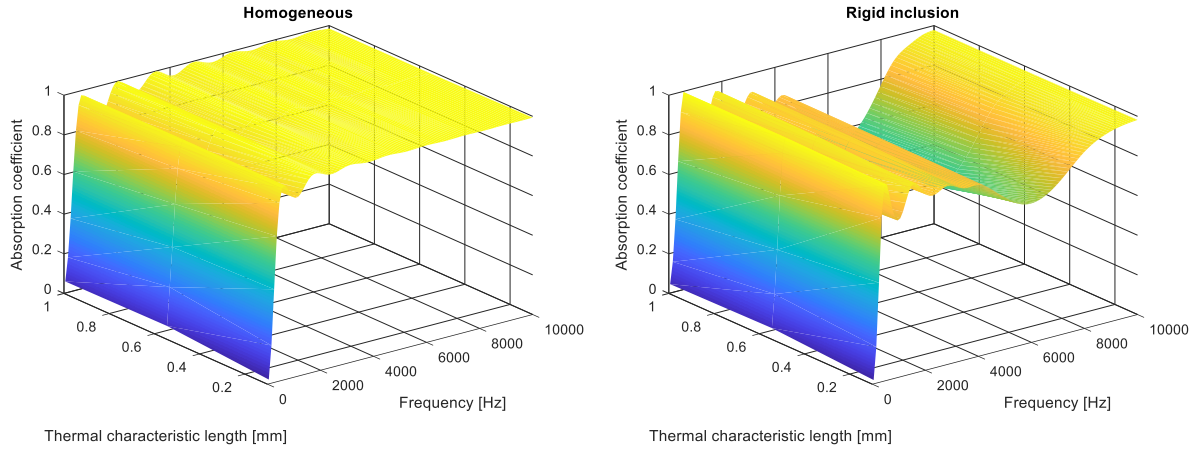

Figure 88: Absorption coefficient value as a function of frequency and foam thermal characteristic length; homogeneous case (on the left) and case with a cylindrical perfectly rigid inclusion (on the right).

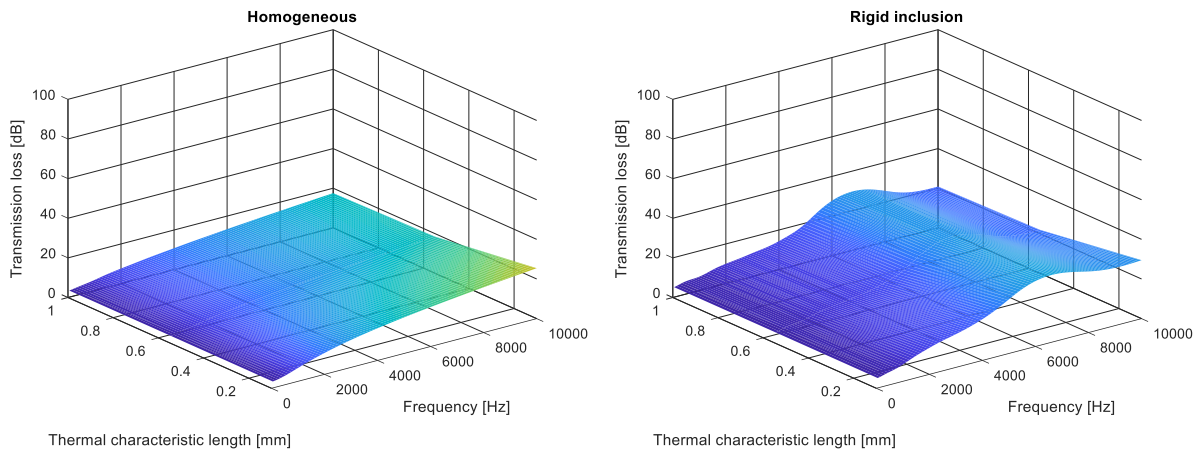

Figure 89: Transmission loss value as a function of frequency and foam thermal characteristic length; homogeneous case (on the left) and case with a cylindrical perfectly rigid inclusion (on the right).

Moreover, as it can be stated from Figure 90, Figure 91 and Figure 92, frame density, Young modulus and loss factor parametric analyses do not provide any evident shifts in terms of absorption coefficient and transmission loss.

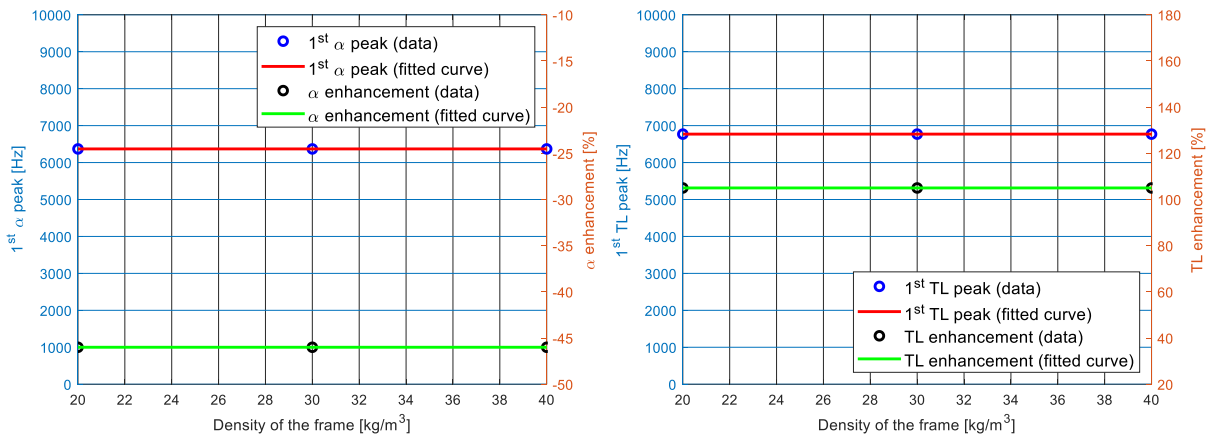

Figure 90: Absorption coefficient (on the left) and transmission loss (on the right) design curves as functions of the foam skeleton density.

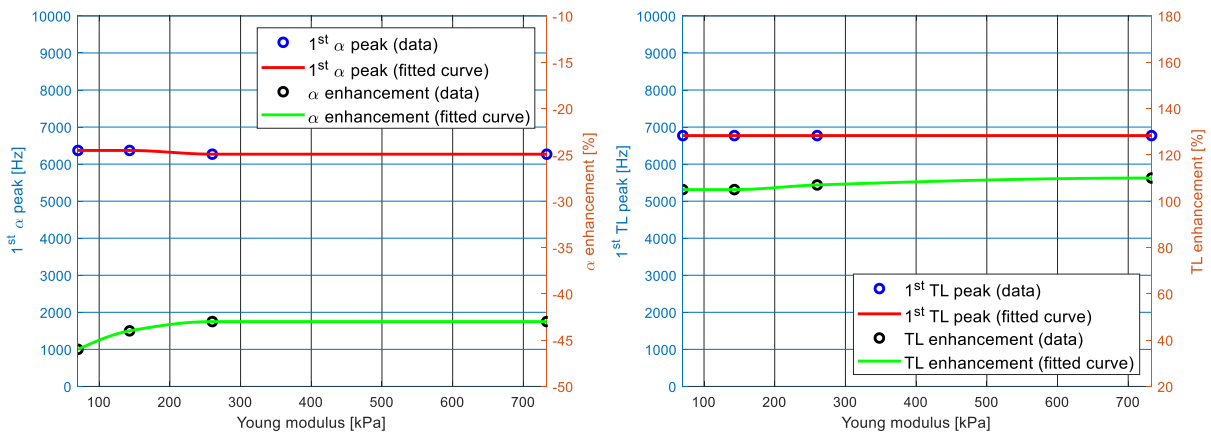

Figure 91: Absorption coefficient (on the left) and transmission loss (on the right) design curves as functions of the foam Young modulus.

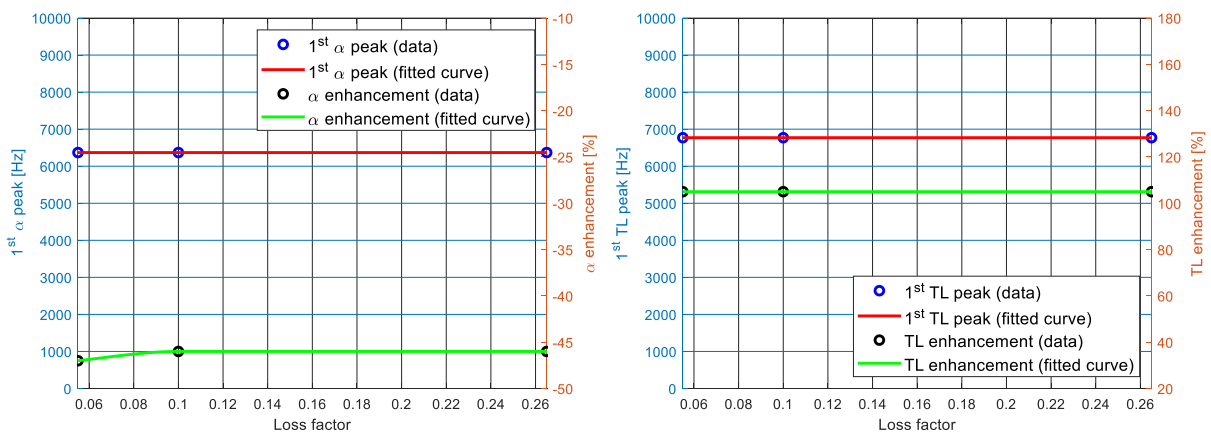

Figure 92: Absorption coefficient (on the left) and transmission loss (on the right) design curves as functions of the foam loss factor.

Therefore it can be concluded that, in general, the elastic characteristics of a foam represent parameters that are less meaningful, compared to the ones related to its porous nature, in order to tune the acoustic performances of a periodic arrangement of unit cells.

Summarizing, in order to tune the frequency position of an acoustic performance peak caused by periodicity effects, one should act on the unit cell dimension (discordant trend), the tortuosity (discordant trend) and the viscous characteristic length (concordant trend); instead, to the aim of properly designing its amplitude, one could change the unit cell dimension (discordant trend), the airflow resistivity (discordant trend), the tortuosity (discordant trend) the viscous characteristic length (concordant trend) and/or the thermal characteristic length (concordant trend).

3.5. Conclusions

In this section, the shift cell operator technique has been re-formulated for poro-elastic materials, providing details on its FEM implementation too.

In order to validate the shift cell technique implementation for Biot-modeled foams, a first calculation has been made to compare shift cell results with those obtained by Serra [36] using the Wave Finite Element Method [137] and with those computed through an analytical model, which is valid for infinite homogeneous isotropic porous media, where three waves propagate (two compressional waves and one shear wave). An additional validation (Figure 55 and Figure 56) has then been carried out through a comparison with the results obtained on a JCA-modeled 3D unit cell (Figure 8), both in a homogeneous configuration (Table 10) and with a perfectly rigid cylindrical inclusion.

For all tested configurations, which involve the computation of 20 eigenvalues with 200 Hz frequency steps, a branch-tracking algorithm has been identified. Through the use of a proper frequency step in the eigenproblem definition, it is able to correctly classify the solutions, even in the presence of band gaps, branch-crossing or branch-veering phenomena.

Figure 67 and Figure 68 show a comparison of the computational cost, in terms of time and as a function of the number of elements in the finite element model, between JCA and Biot models for the computation of the values of absorption coefficient and transmission loss at a single frequency. Considering the very few differences between JCA and Biot models highlighted in Figure 61, the usage of the latter is recommended only in presence of a foam whose frame elasticity clearly plays a relevant role in its acoustic performance. Furthermore, this choice becomes more justified for finite element models that require a very fine mesh, since the difference between the two approaches, in terms of computational time, reduces with increasing mesh size.

Through the use of the acoustic-structure coupling that comes from the implementation of Biot model, the previous non-rigid inclusion test campaign (Section 2.4) has been extended by considering some solid (but still non-perfectly-rigid) inclusions in the 3D-modeled unit cell described in Figure 8. In particular, 6 setups have been discussed, whose fundamental parameters are reported in Table 11.

In conclusion, some guidelines are provided in order to predict at which frequency the 1st performance peak appears, together with its amplitude, as functions of unit cell dimensions, airflow resistivity, tortuosity, characteristic lengths, frame density, Young modulus and loss factor; conversely, it is shown also the link between the unit cell dimensions and the 1st performance peak amplitude as functions of the design frequency.

4. GLOBAL CONCLUSIONS AND PERSPECTIVES

"We're still pioneers, we've barely begun.
Our greatest accomplishments cannot be behind us, 'cause our destiny lies above us."

(Matthew McConaughey / Cooper - Interstellar)

The inclusion of vibroacoustic treatments at early stage of product development through the use of porous media with periodic inclusions [11], which exhibit proper dynamic filtering effects [12]–[16], is a powerful strategy for the achievement of lightweight sound packages and represents a convenient solution for manufacturing aspects [10], [76].

This can have different applications in transportation (aerospace [17], [18], automotive [19]–[23], railway), energy and civil engineering fields, where weight, space and vibroacoustic comfort are still critical challenges [24].

The present research aims at the study of a specific numerical method for the vibroacoustic modelling of porous and poro-elastic media embedding periodic inclusions.

Section 1 presents the state of art of the subject, and gives some preliminary definitions about porous media. Some preliminary definitions about periodic conditions, which are necessary in order to face the rest of the manuscript, are given too.

Section 2 considers the shift cell operator technique, providing details on its implementation [105]. Essentially, the shift cell technique provides a reformulation of Floquet-Bloch periodic conditions and its major advantage stands in allowing the introduction of a generic frequency dependence of visco-elastic material behavior [44]; this is essential, if one needs to compute the dispersion curves of a porous material modeled as an equivalent fluid. Indeed, even if the usage of F-B periodic conditions actually allows it, a very powerful non-linear solver is required in that case. The shift cell operator, instead, leads to a quadratic eigenvalue problem even in the presence of frequency-dependences and/or damping. The main reason why the shift cell method differs from the classical F-B approach is that it consists in a reformulation of classical F-B conditions, in which the phase shift of the boundary conditions and the exponential amplitude decrease, related to wave propagation, are integrated into the partial derivative operator. Consequently, the periodicity is included in the overall behavior of the structure while the continuity conditions are imposed at the edges of the unit cell [38]–[43].

Section 3 reproduces the analyses carried out in Section 2, but through the use of Biot model. Many results, in terms of dispersion curves, absorption coefficient and transmission loss are presented, together with some interesting comparisons with those obtained using equivalent fluid models.

The outcome of this research is very promising, since the methodological basis and its validations are given in order to trace future characterizations and applications of periodic porous media in acoustics. In this context, an interesting study that has been partially planned will involve processes of optimization concerning the geometry of the unit cell, the foam material and the inclusion material and shape, in order to design and obtain outstanding configurations for low frequency noise control and, in general, for each specific application of interest. Future works can also focus on embedding resonant inclusions in a porous layer, which offer an alternative to multi-layering and double porosity materials in the design of sound absorption and insulation packages for low frequency applications. In conclusion, another interesting possibility could be the integration of the metamaterial obtained by embedding periodic inclusions in a foam as a sandwich core: this would allow to stiffen the system, while taking advantage of the structural properties of the sandwich plates. These perspectives could be realized through numerical and/or experimental research studies.

APPENDICES

"Not all those who wander are lost."

(John Ronald Reuel Tolkien - The Lord of the Rings)

A. EQUIVALENT FLUID NUMERICAL TEST CAMPAIGN

A.1. Dispersion curves

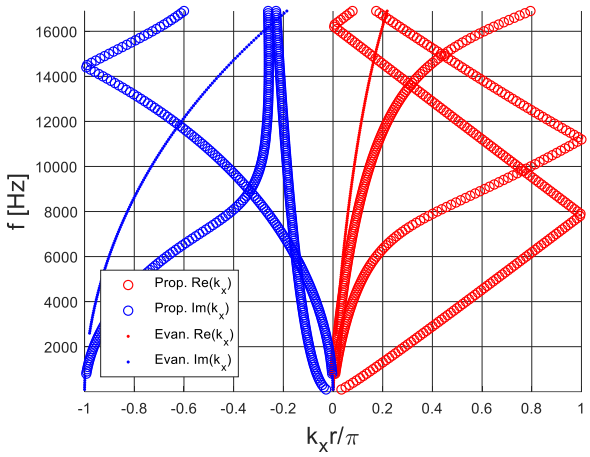

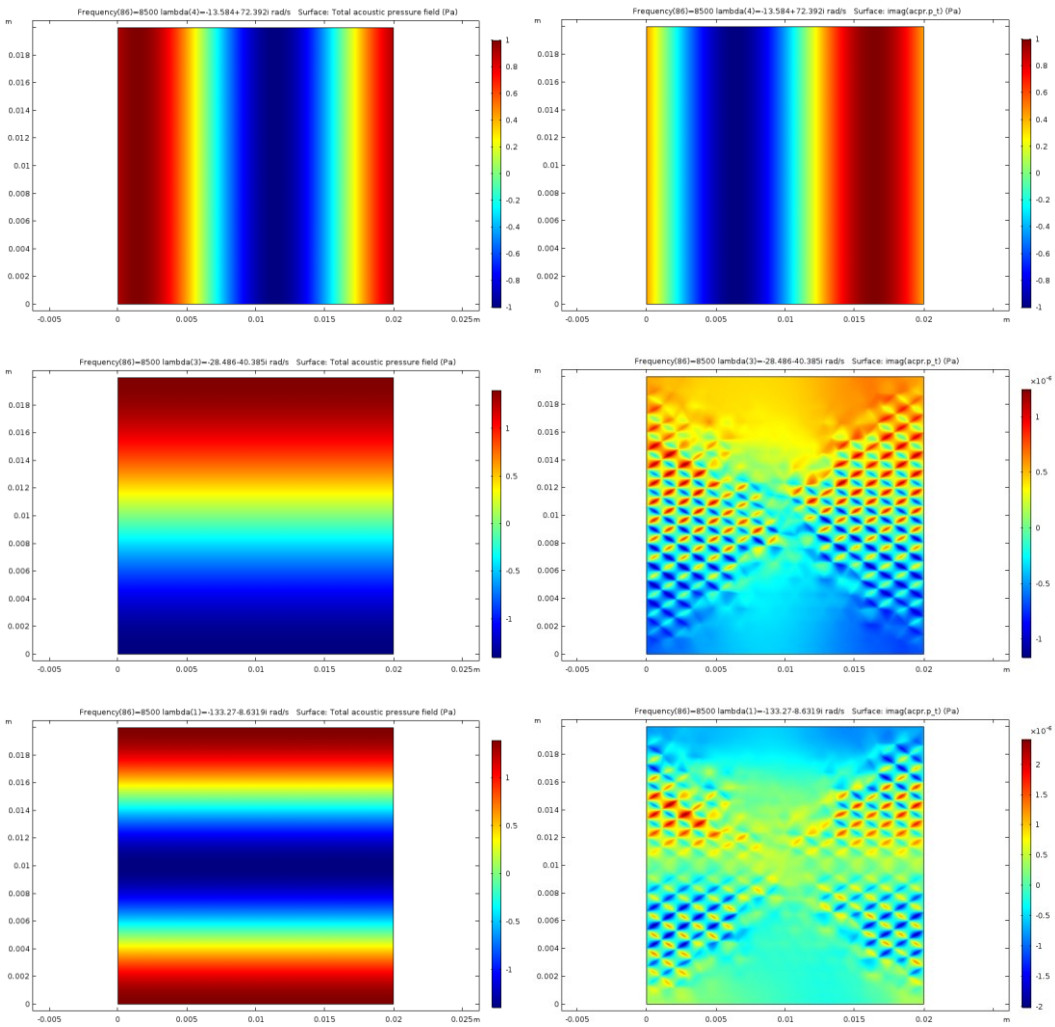

Figure 93: Dispersion curves for a homogeneous DB-modeled melamine 2D unit cell; from top to bottom, the 1st, 2nd and 3rd branch eigenvectors are shown in terms of real (on the left) and imaginary (on the right) parts.

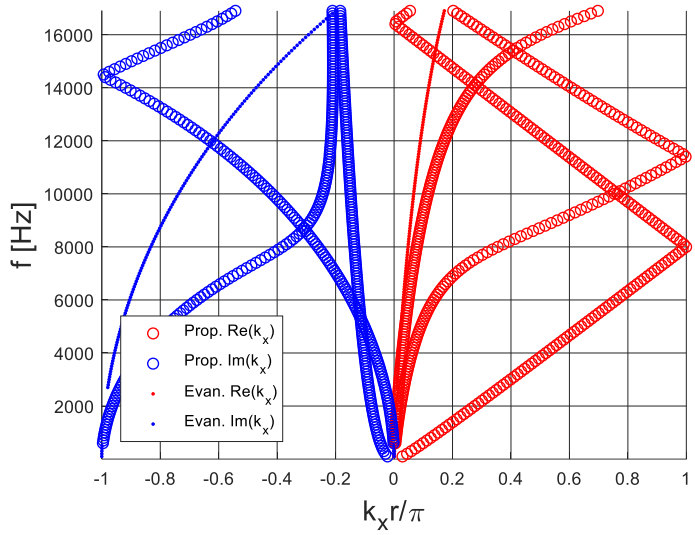

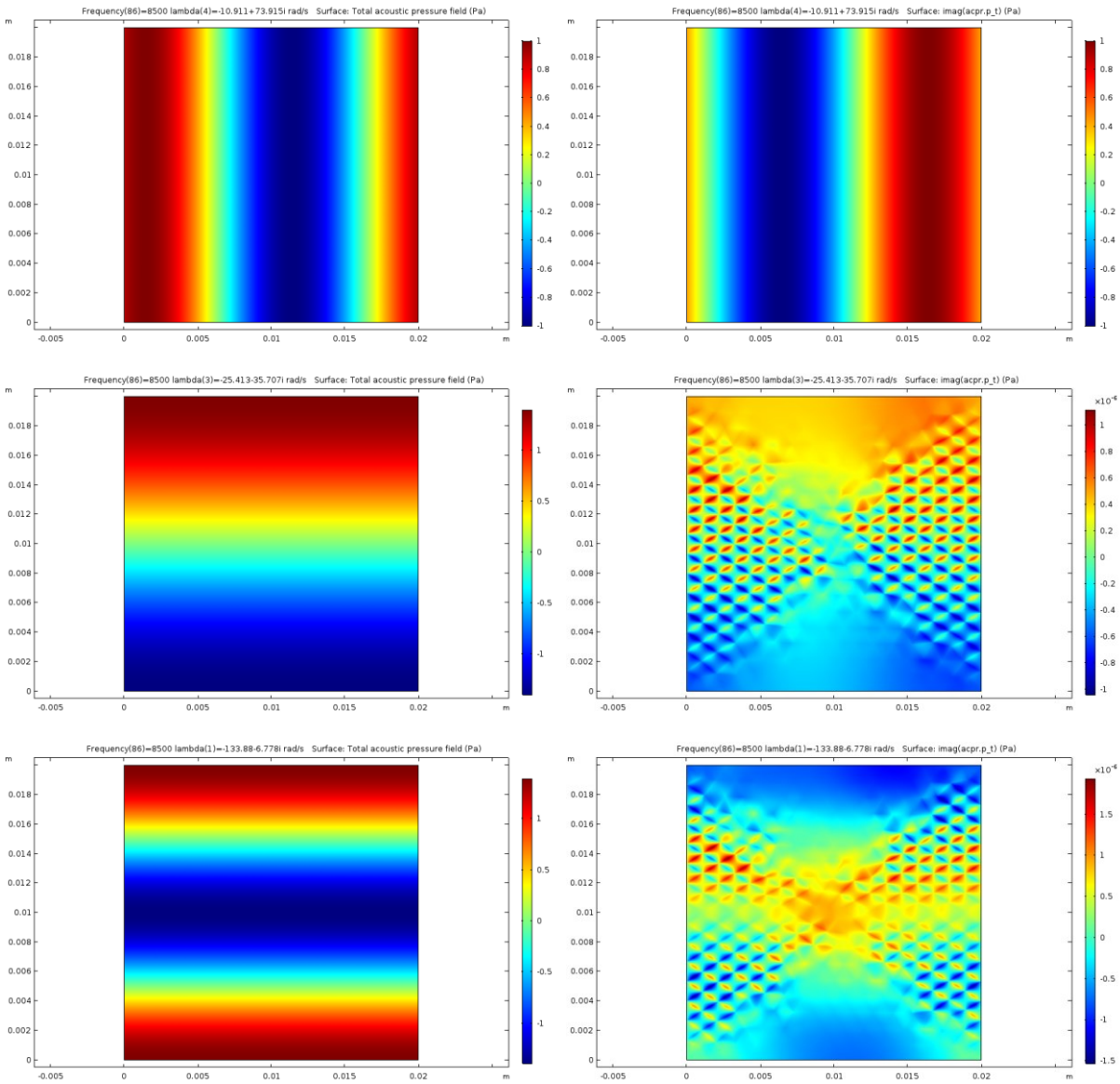

Figure 94: Dispersion curves for a homogeneous DB-modeled black PU 2D unit cell; from top to bottom, the 1st, 2nd and 3rd branch eigenvectors are shown in terms of real (on the left) and imaginary (on the right) parts.

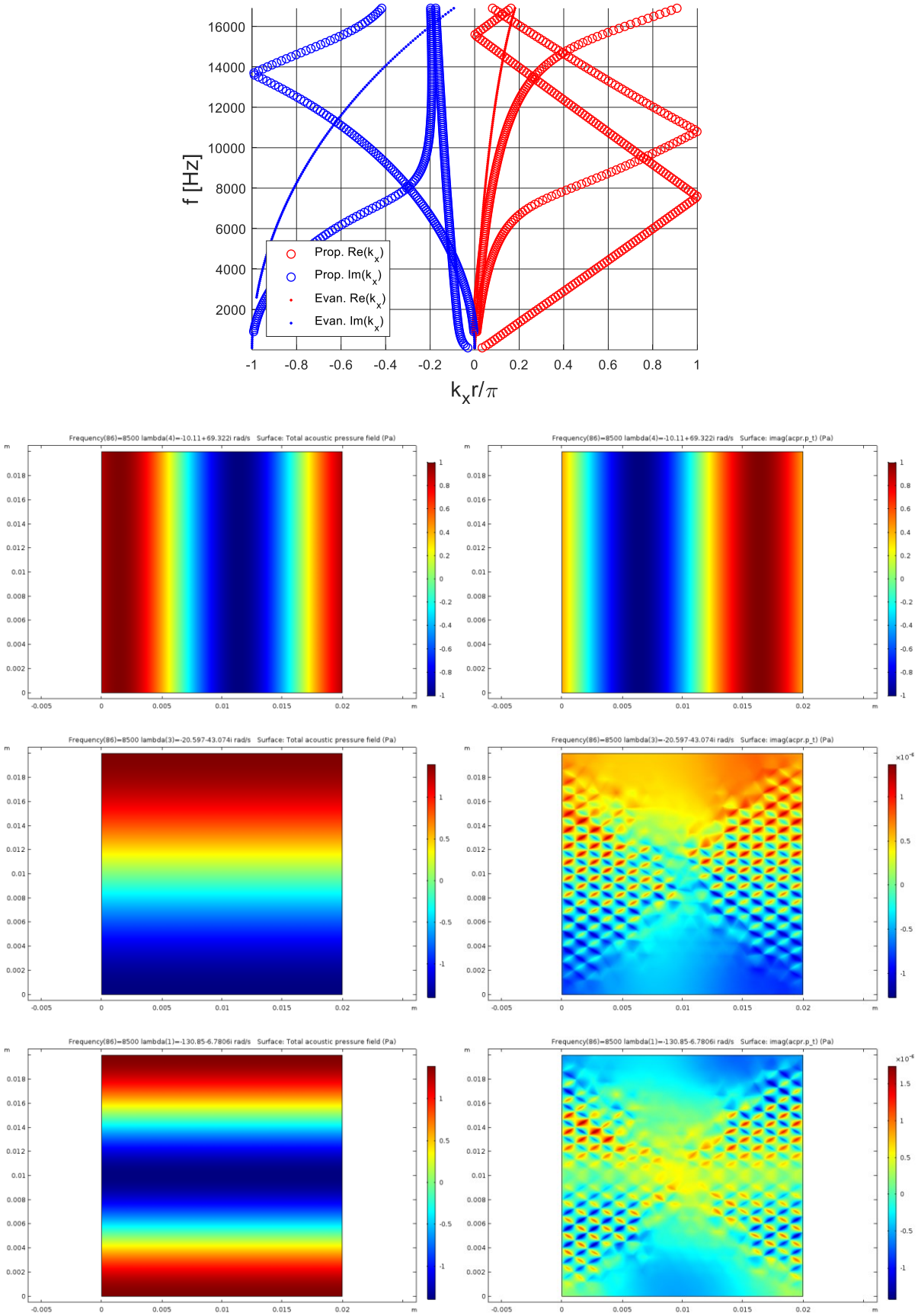

Figure 95: Dispersion curves for a homogeneous JCA-modeled melamine 2D unit cell; from top to bottom, the 1st, 2nd and 3rd branch eigenvectors are shown in terms of real (on the left) and imaginary (on the right) parts.

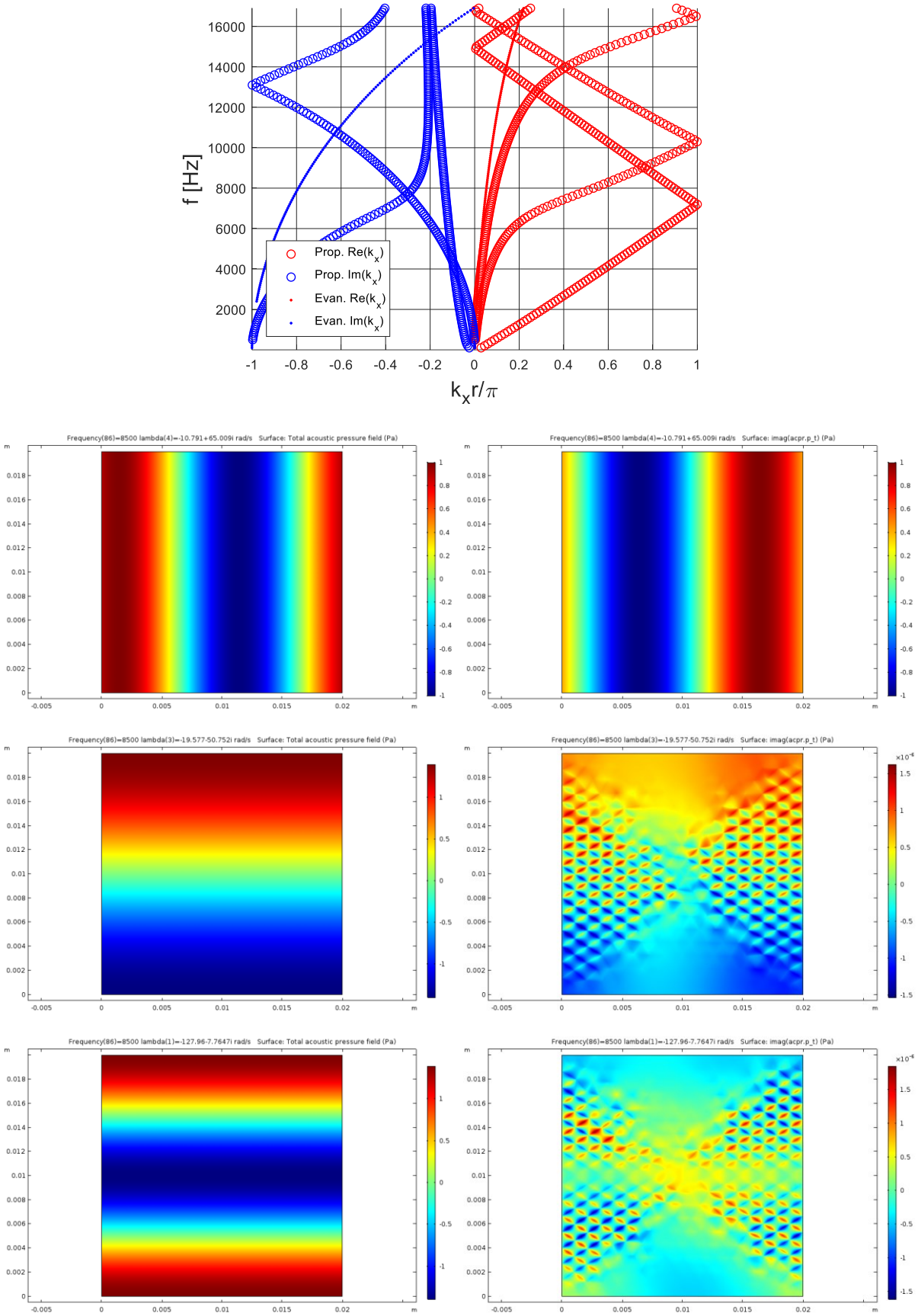

Figure 96: Dispersion curves for a homogeneous JCA-modeled black PU 2D unit cell; from top to bottom, the 1st, 2nd and 3rd branch eigenvectors are shown in terms of real (on the left) and imaginary (on the right) parts.

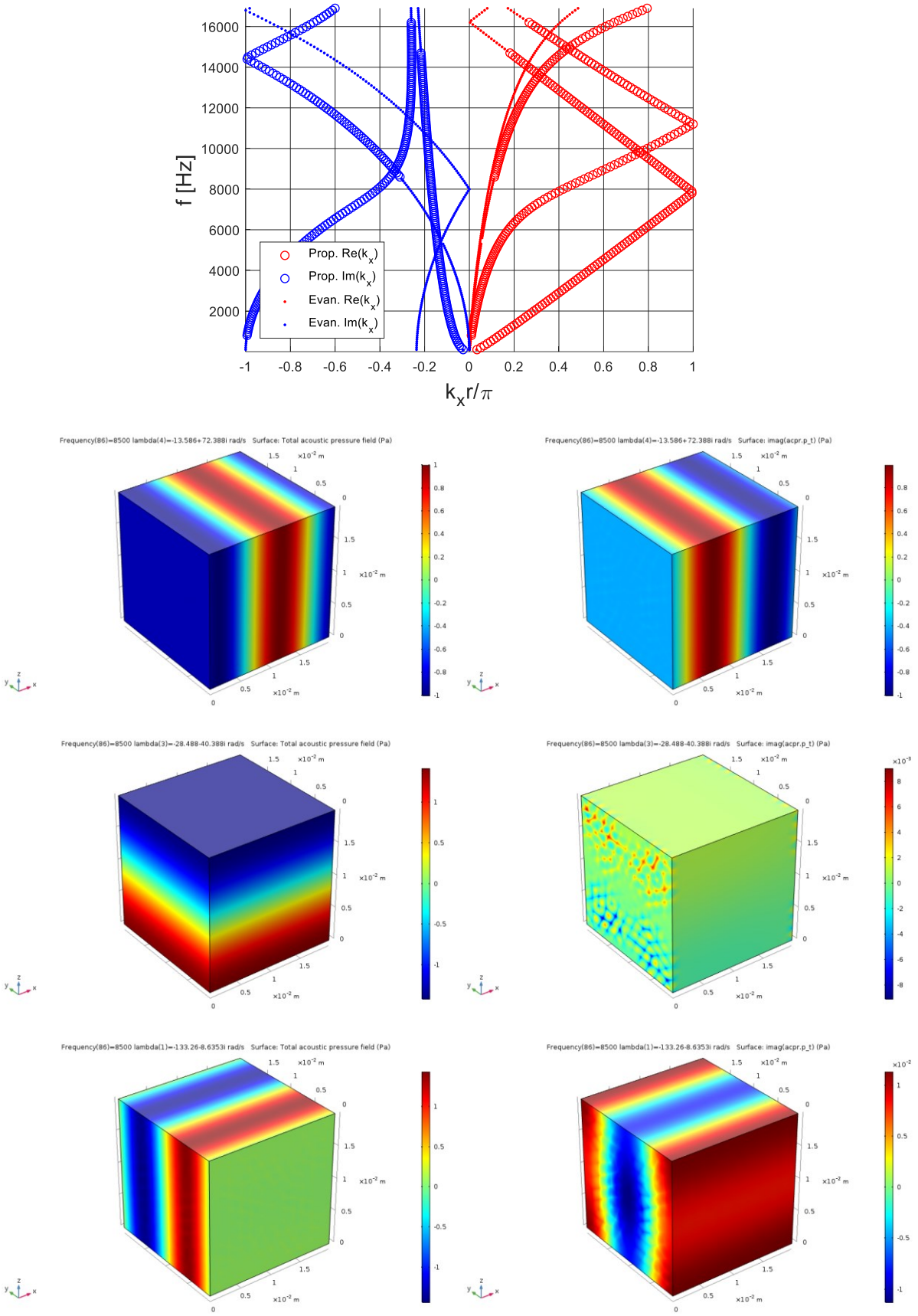

Figure 97: Dispersion curves for a homogeneous DB-modeled melamine 3D unit cell; from top to bottom, the 1st, 2nd and 3rd branch eigenvectors are shown in terms of real (on the left) and imaginary (on the right) parts.

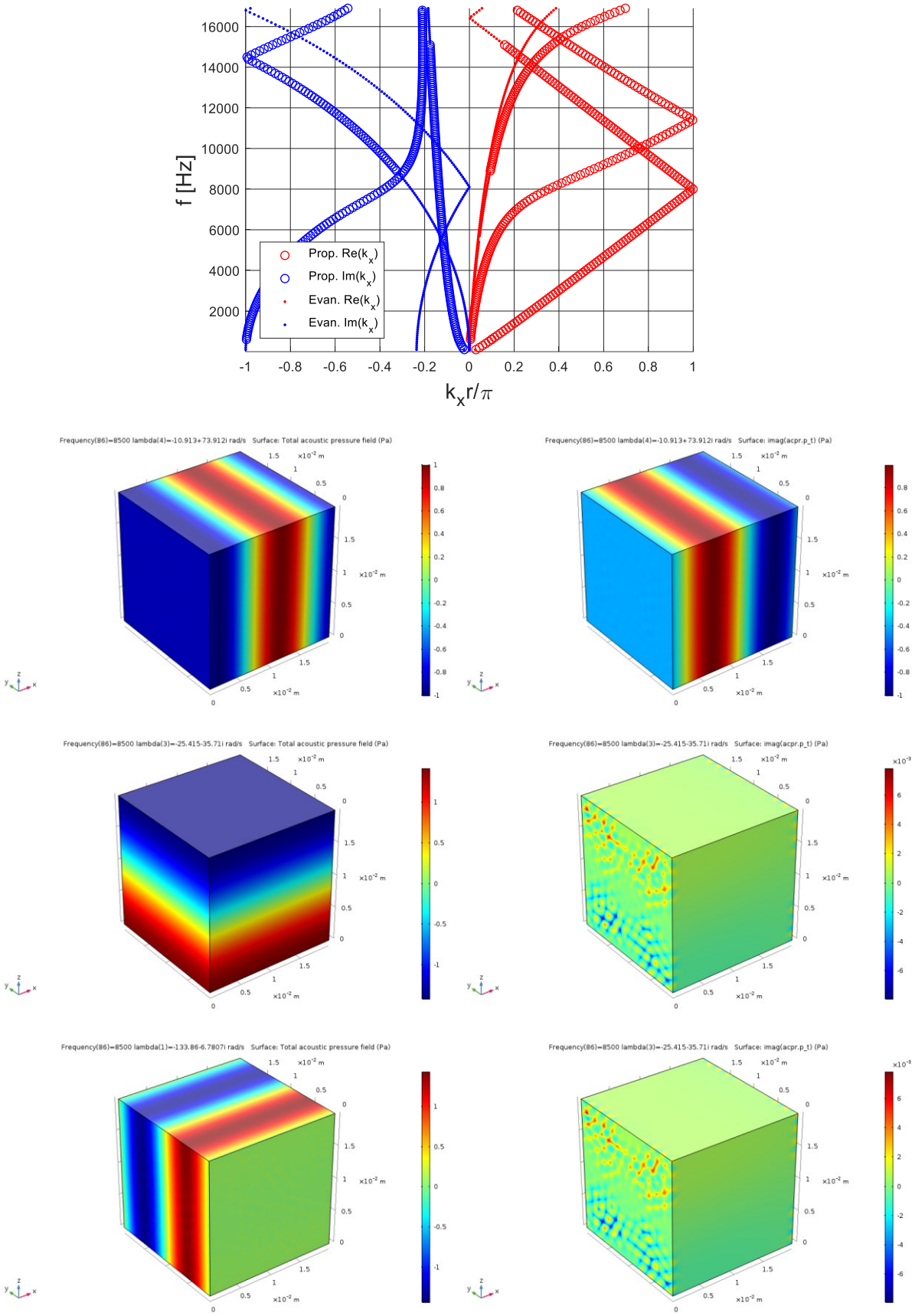

Figure 98: Dispersion curves for a homogeneous DB-modeled black PU 3D unit cell; from top to bottom, the 1st, 2nd and 3rd branch eigenvectors are shown in terms of real (on the left) and imaginary (on the right) parts.

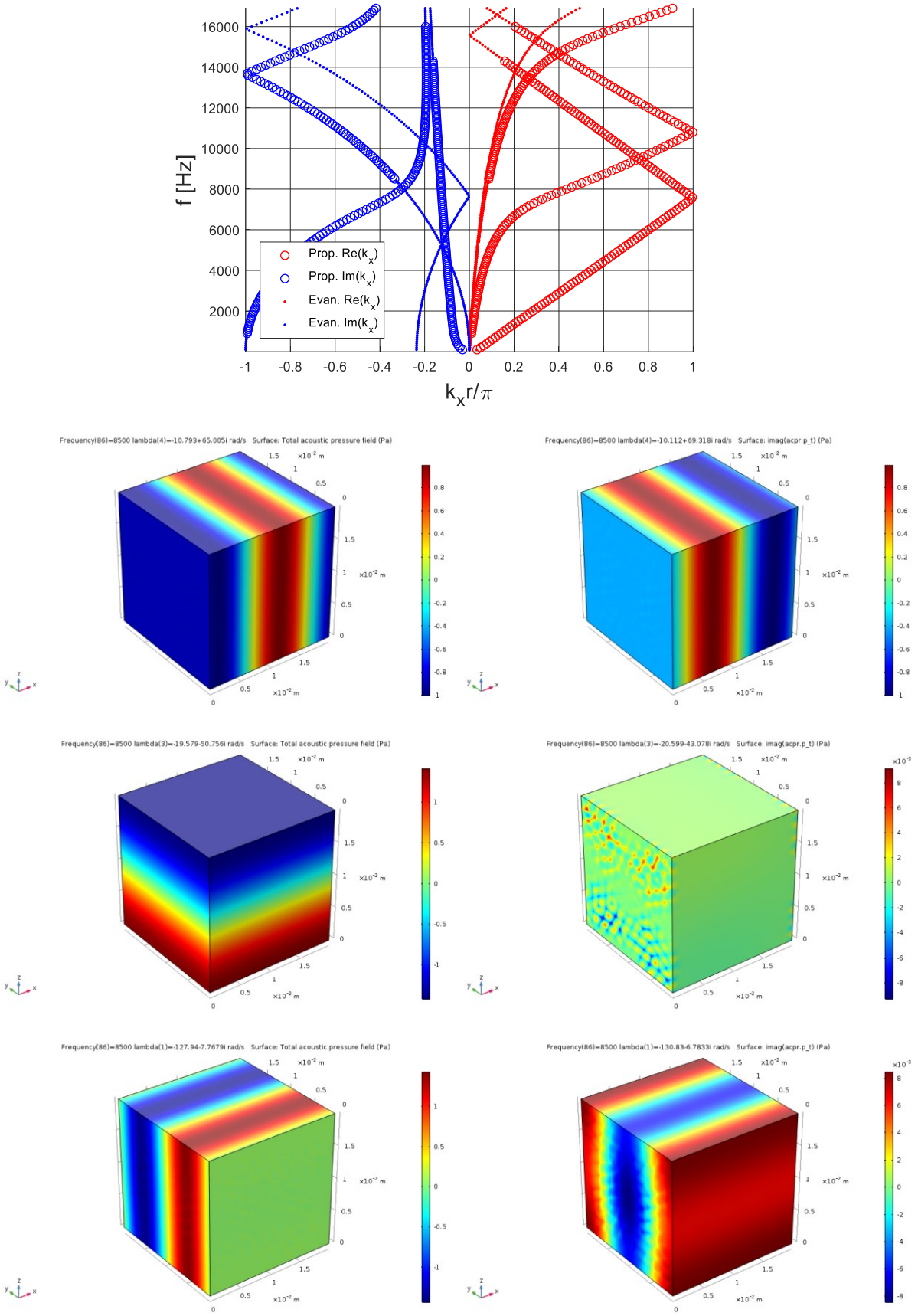

Figure 99: Dispersion curves for a homogeneous JCA-modeled melamine 3D unit cell; from top to bottom, the 1st, 2nd and 3rd branch eigenvectors are shown in terms of real (on the left) and imaginary (on the right) parts.

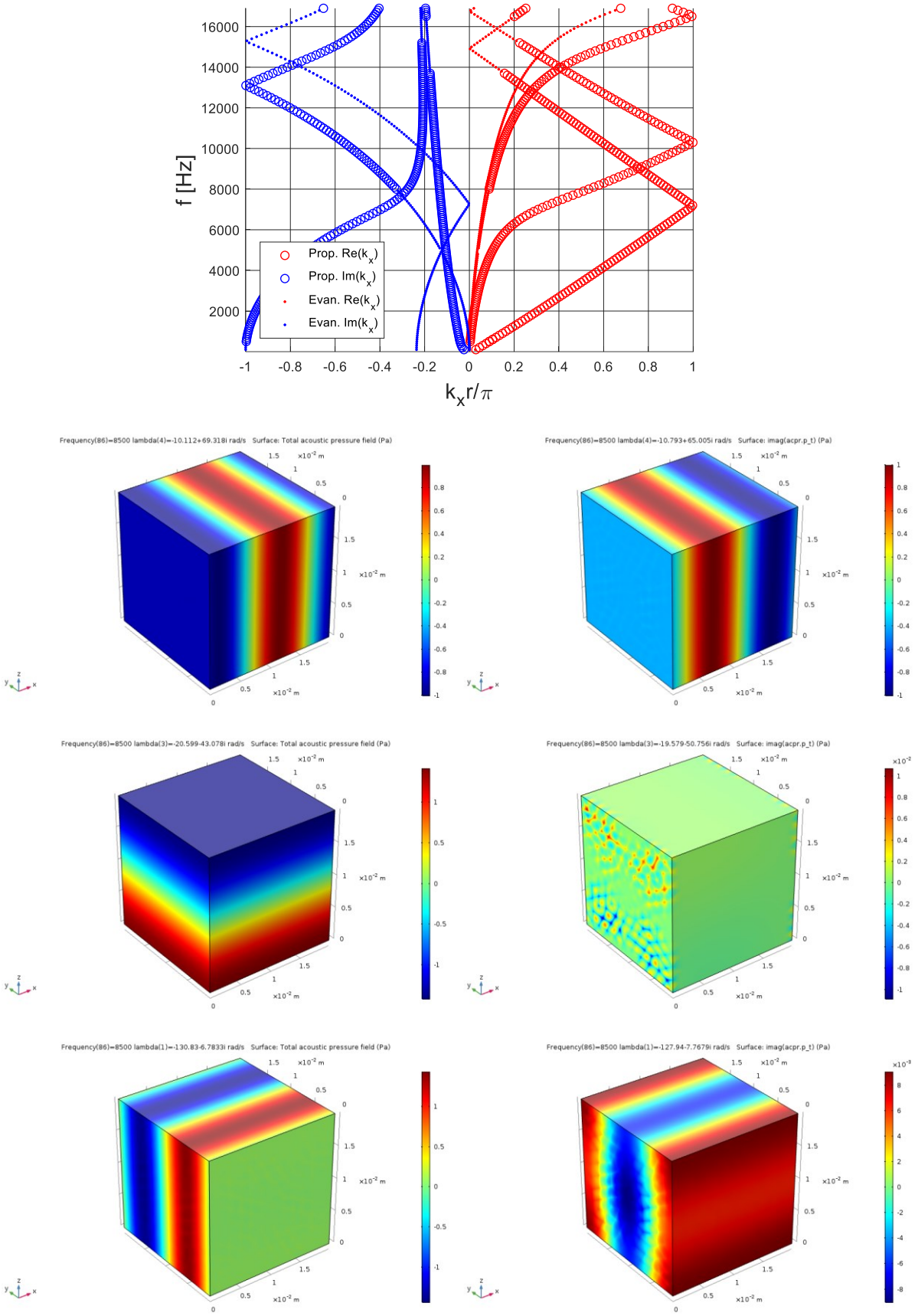

Figure 100: Dispersion curves for a homogeneous JCA-modeled black PU 3D unit cell; from top to bottom, the 1st, 2nd and 3rd branch eigenvectors are shown in terms of real (on the left) and imaginary (on the right) parts.

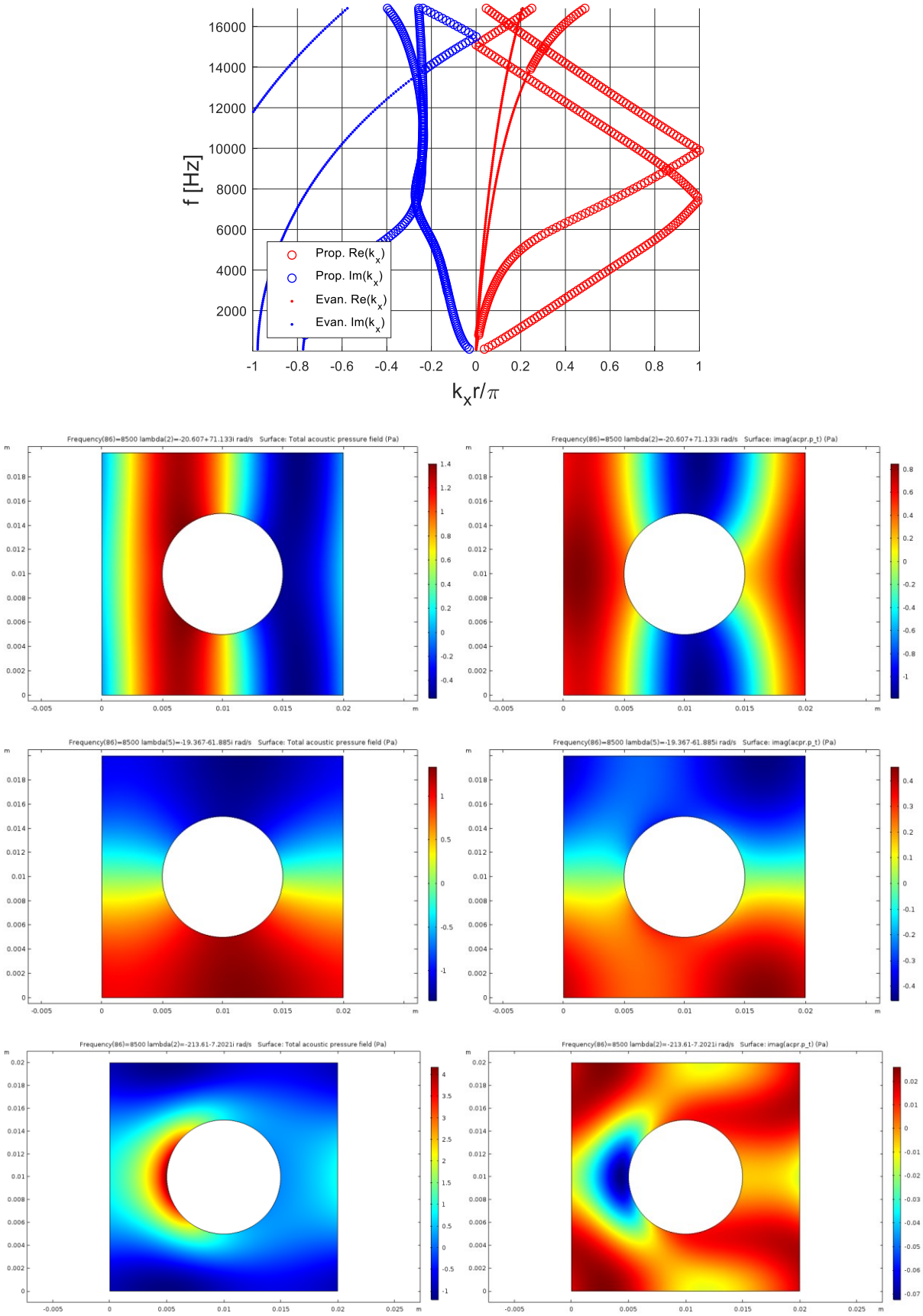

Figure 101: Dispersion curves for a DB-modeled melamine 2D unit cell with a perfectly rigid inclusion; from top to bottom, the 1st, 2nd and 3rd branch eigenvectors are shown in terms of real (on the left) and imaginary (on the right) parts.

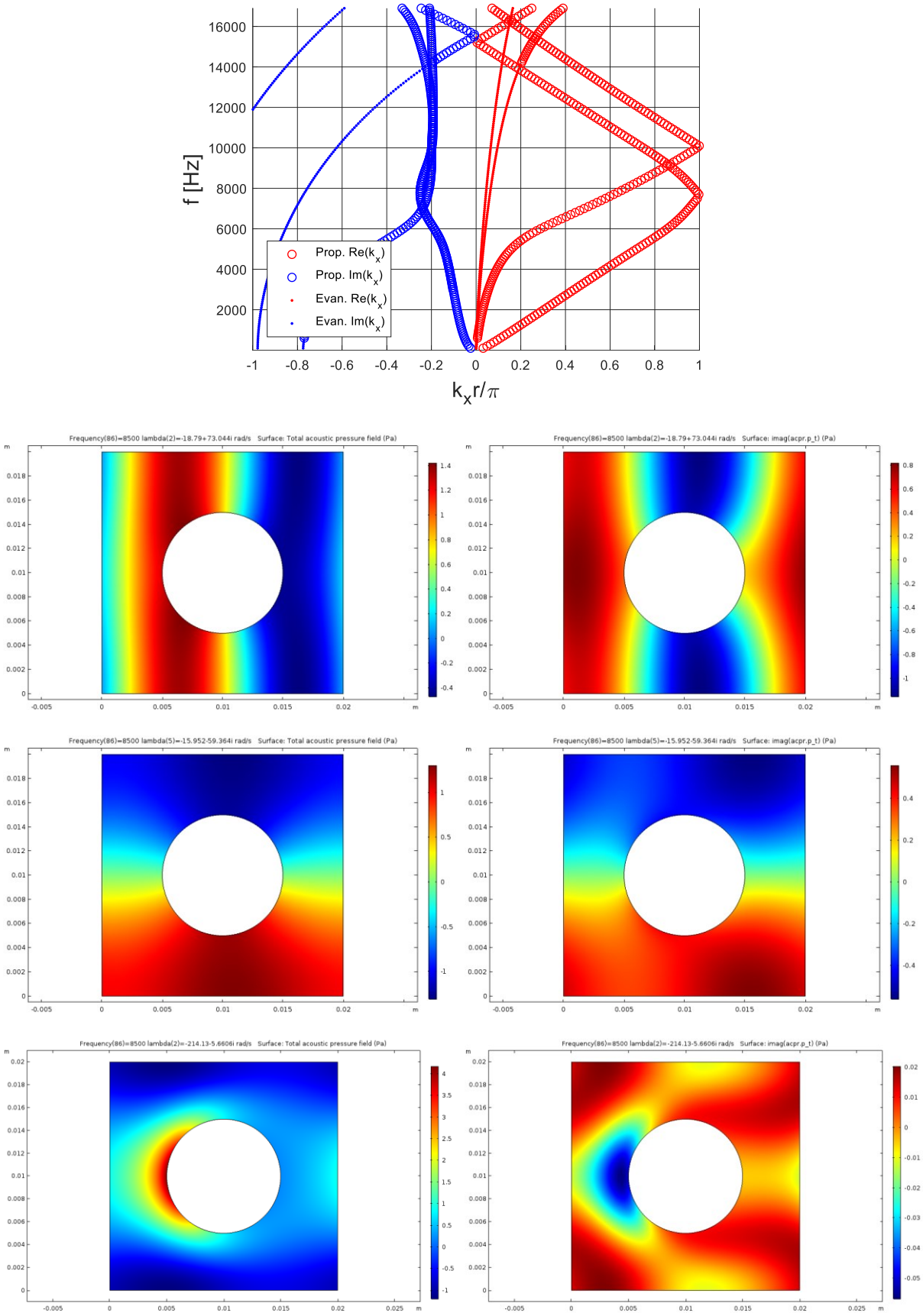

Figure 102: Dispersion curves for a DB-modeled black PU 2D unit cell with a perfectly rigid inclusion; from top to bottom, the 1st, 2nd and 3rd branch eigenvectors are shown in terms of real (on the left) and imaginary (on the right) parts.

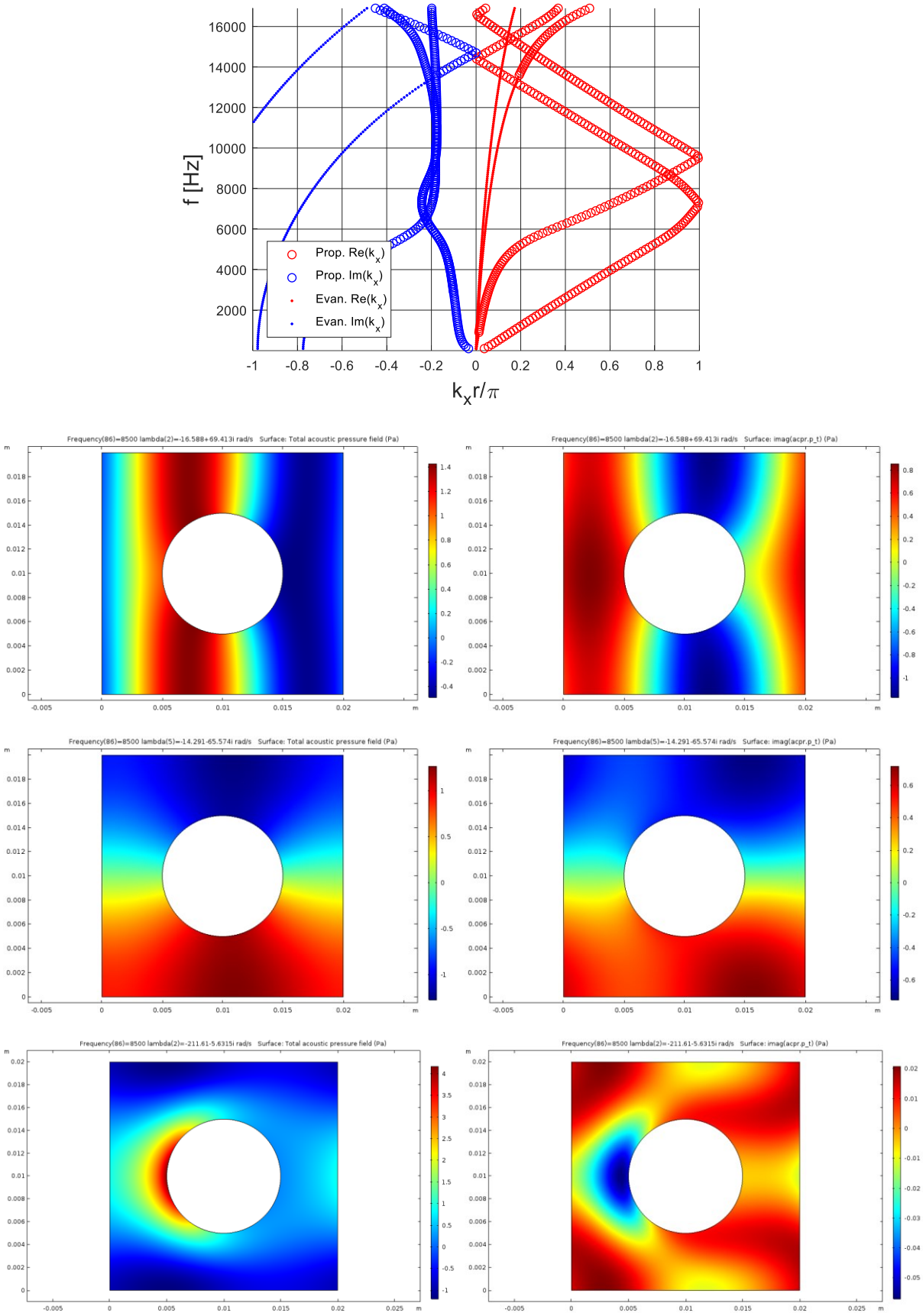

Figure 103: Dispersion curves for a JCA-modeled melamine 2D unit cell with a perfectly rigid inclusion; from top to bottom, the 1st, 2nd and 3rd branch eigenvectors are shown in terms of real (on the left) and imaginary (on the right) parts.

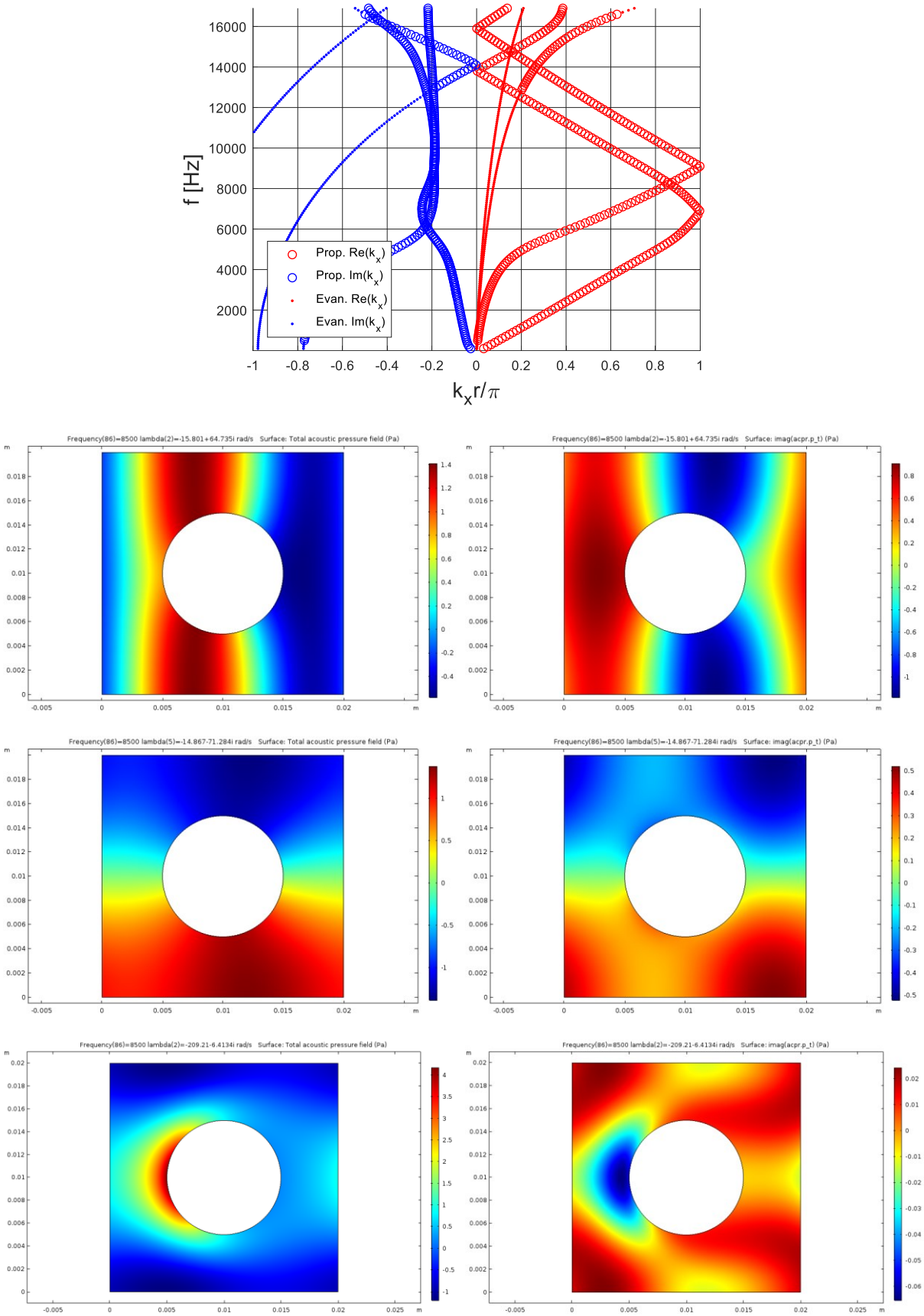

Figure 104: Dispersion curves for a JCA-modeled black PU 2D unit cell with a perfectly rigid inclusion; from top to bottom, the 1st, 2nd and 3rd branch eigenvectors are shown in terms of real (on the left) and imaginary (on the right) parts.

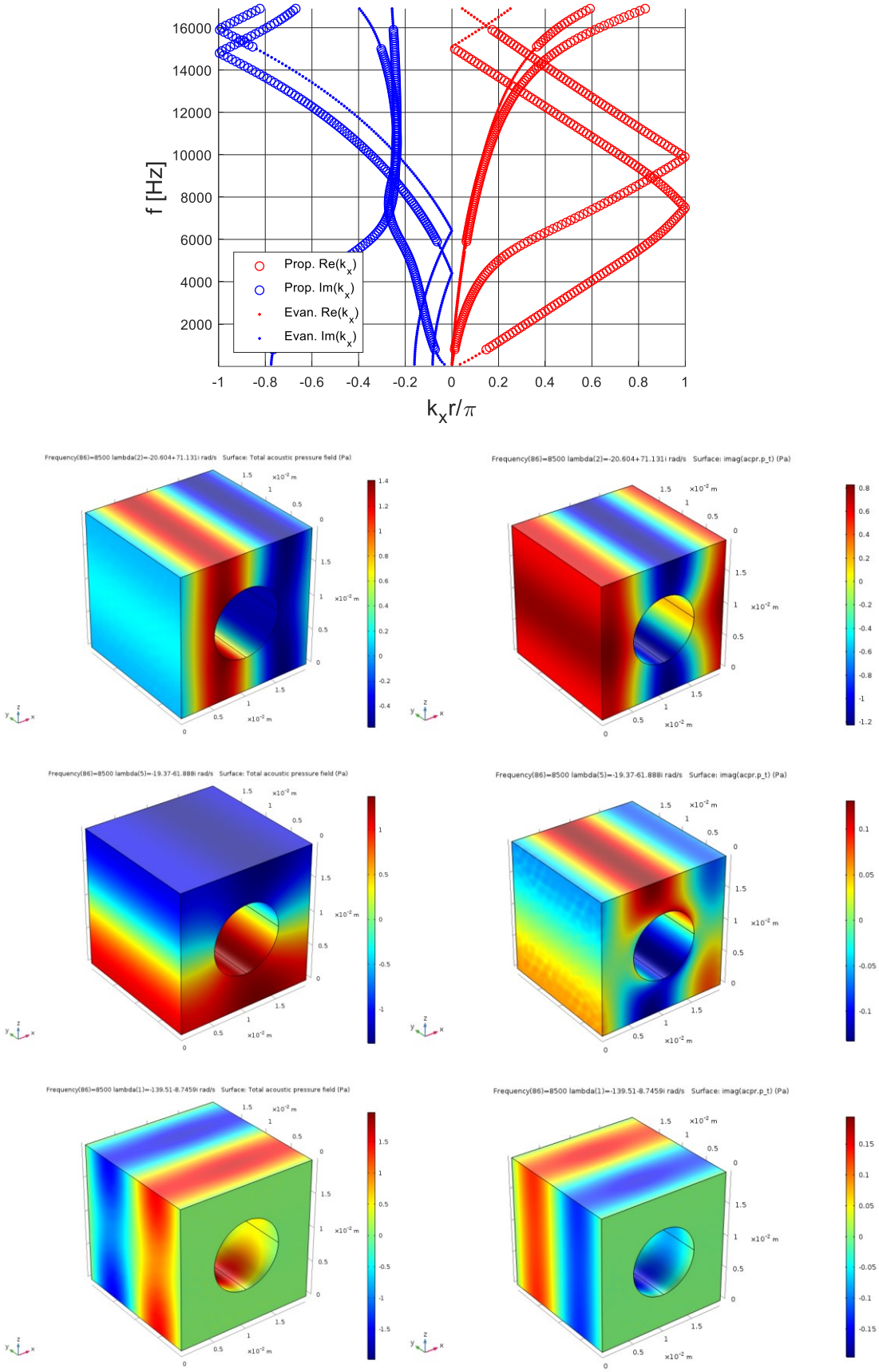

Figure 105: Dispersion curves for a DB-modeled melamine 3D unit cell with a perfectly rigid inclusion; from top to bottom, the 1st, 2nd and 3rd branch eigenvectors are shown in terms of real (on the left) and imaginary (on the right) parts.

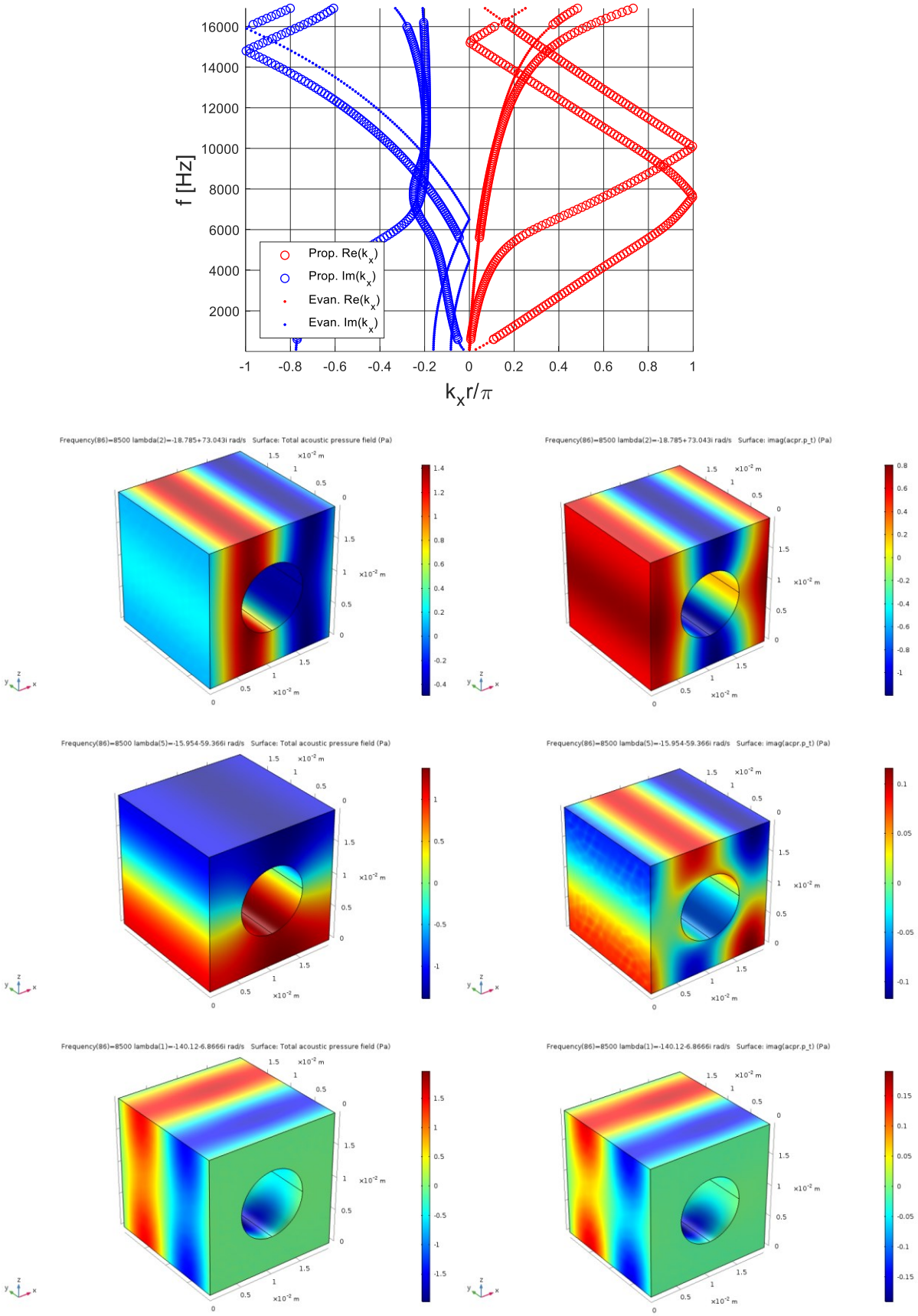

Figure 106: Dispersion curves for a DB-modeled black PU 3D unit cell with a perfectly rigid inclusion; from top to bottom, the 1st, 2nd and 3rd branch eigenvectors are shown in terms of real (on the left) and imaginary (on the right) parts.

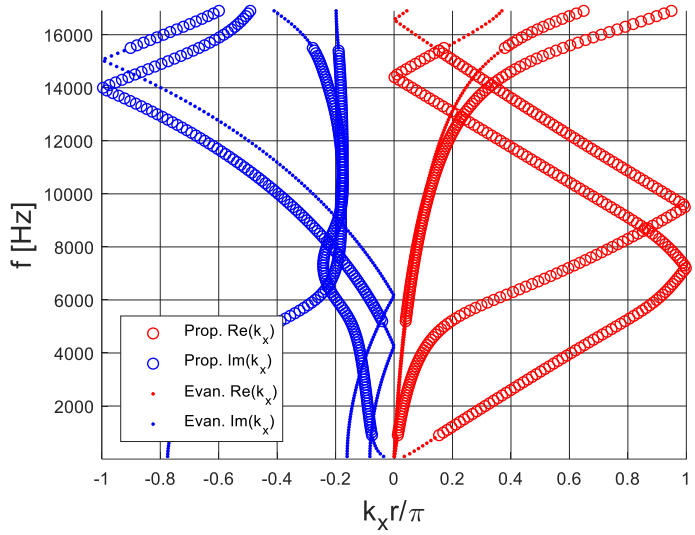

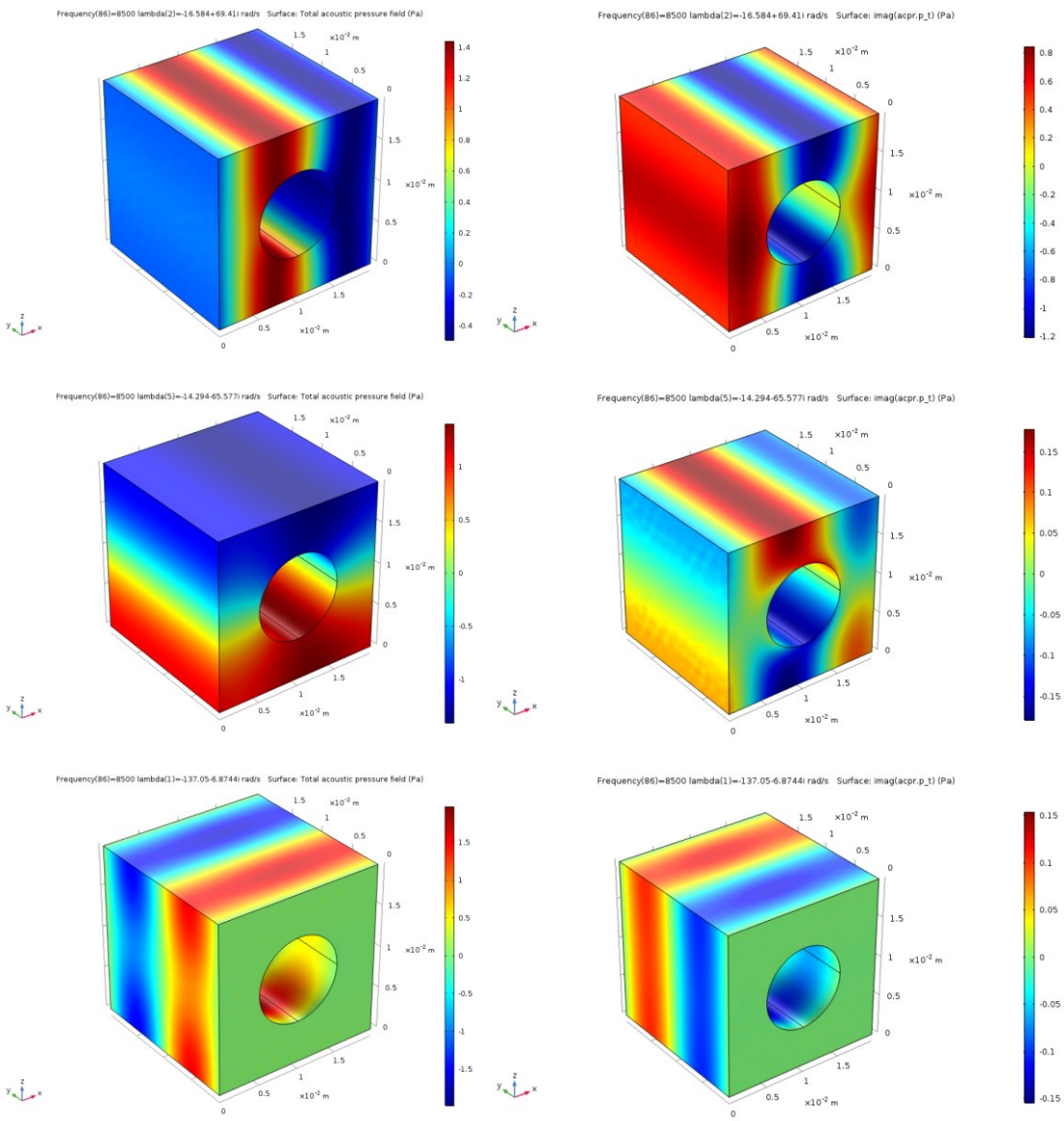

Figure 107: Dispersion curves for a JCA-modeled melamine 3D unit cell with a perfectly rigid inclusion; from top to bottom, the 1st, 2nd and 3rd branch eigenvectors are shown in terms of real (on the left) and imaginary (on the right) parts.

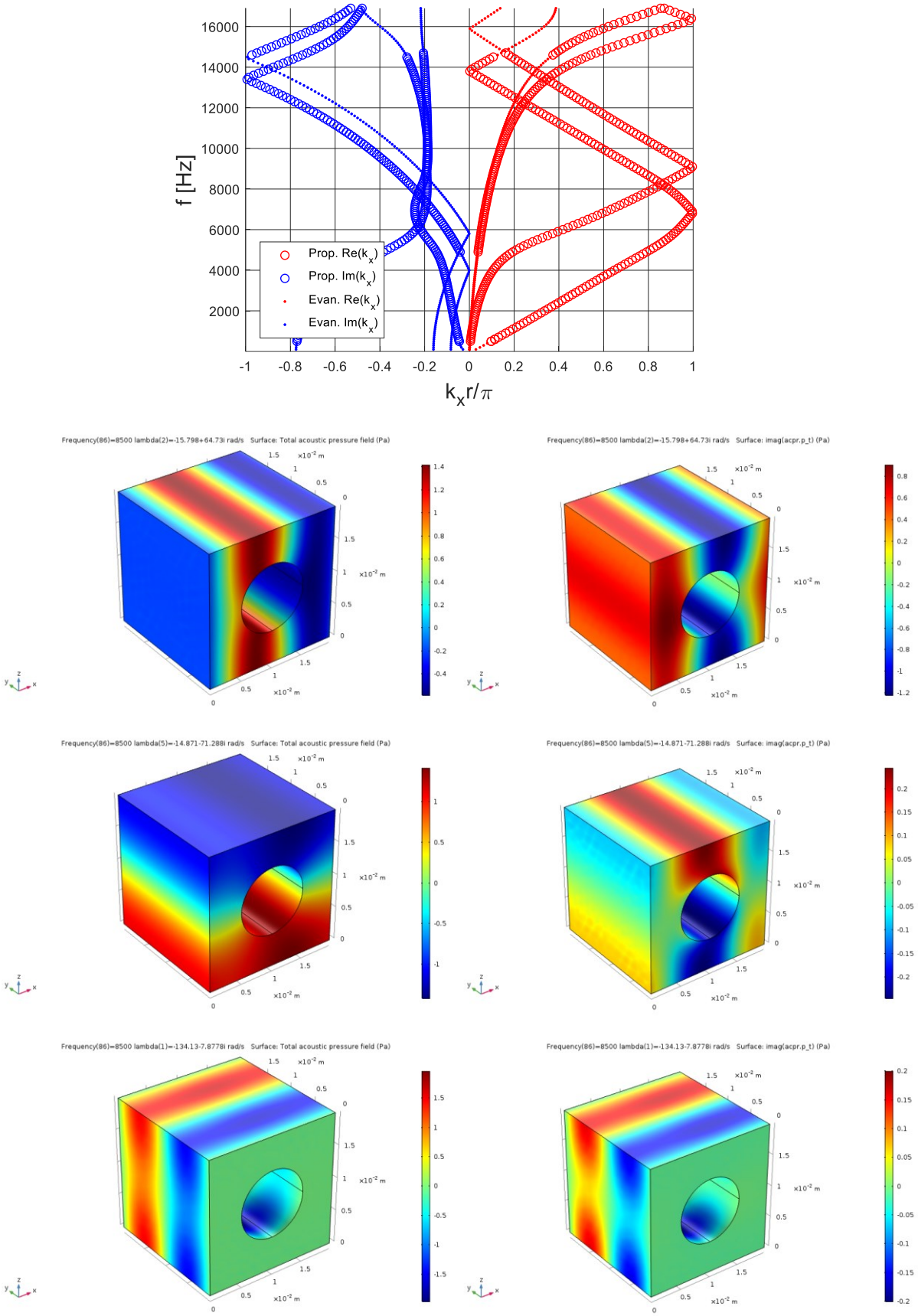

Figure 108: Dispersion curves for a JCA-modeled black PU 3D unit cell with a perfectly rigid inclusion; from top to bottom, the 1st, 2nd and 3rd branch eigenvectors are shown in terms of real (on the left) and imaginary (on the right) parts.

A.1.1. Non-rigid inclusions

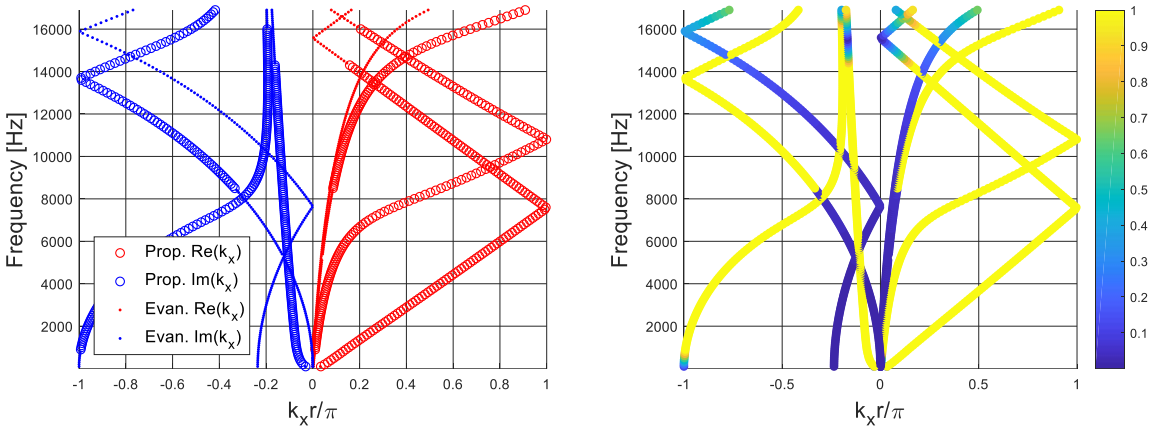

Figure 109: Dispersion curves computed for configuration 1 of Table 4.

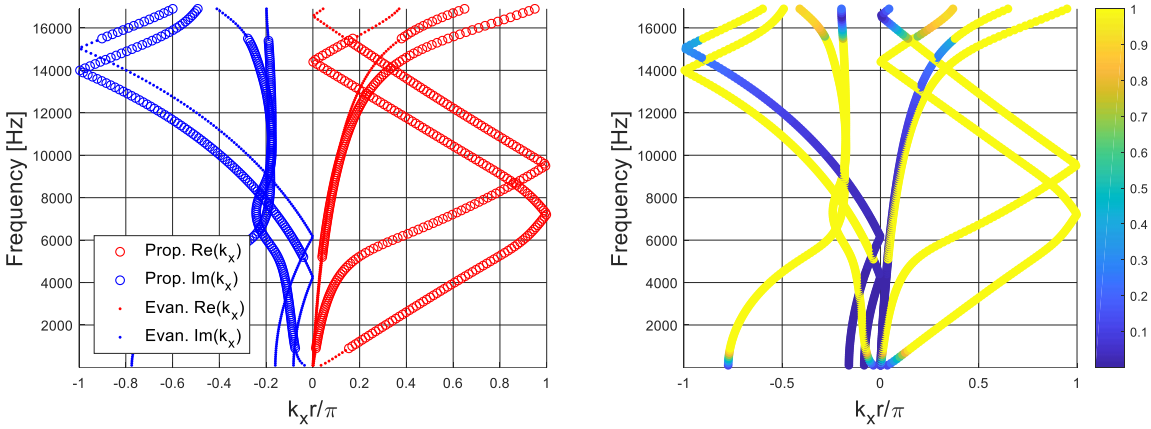

Figure 110: Dispersion curves computed for configuration 2 of Table 4.

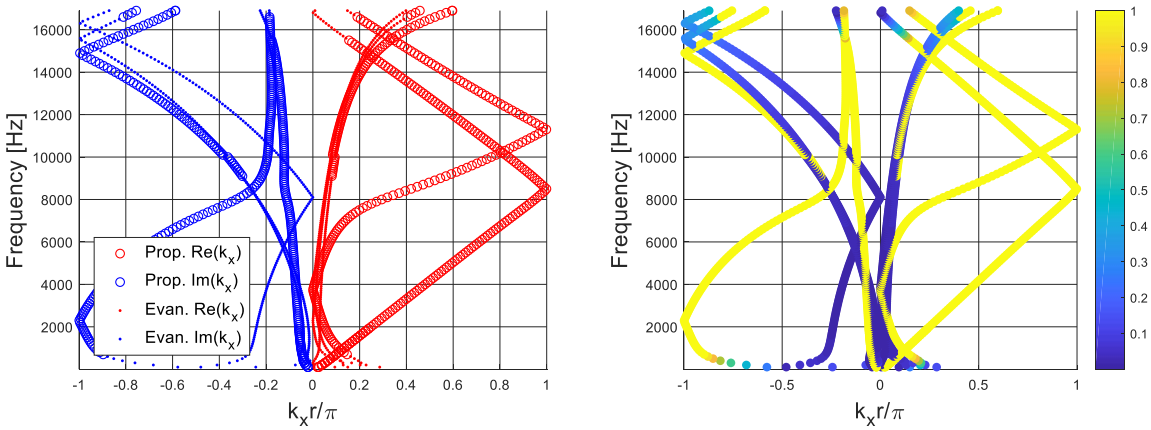

Figure 111: Dispersion curves computed for configuration 3 of Table 4.

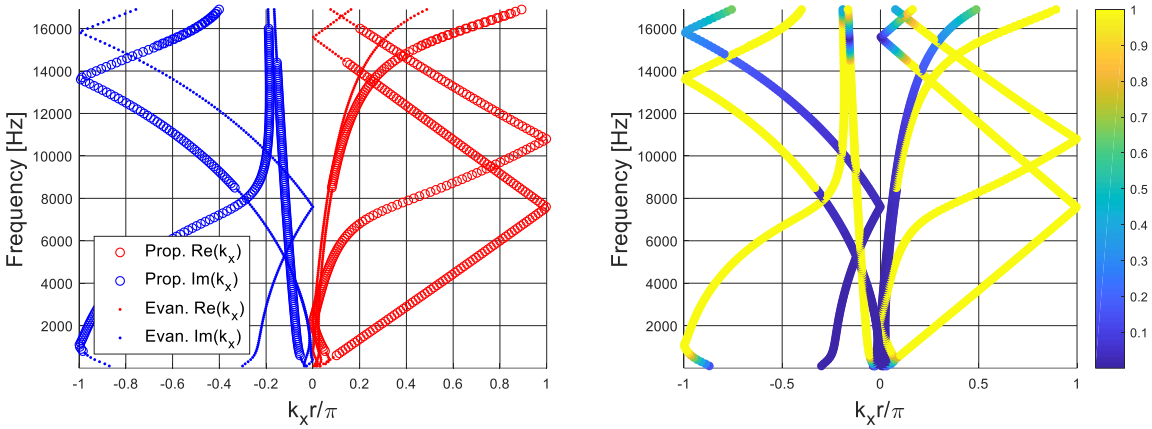

Figure 112: Dispersion curves computed for configuration 4 of Table 4.

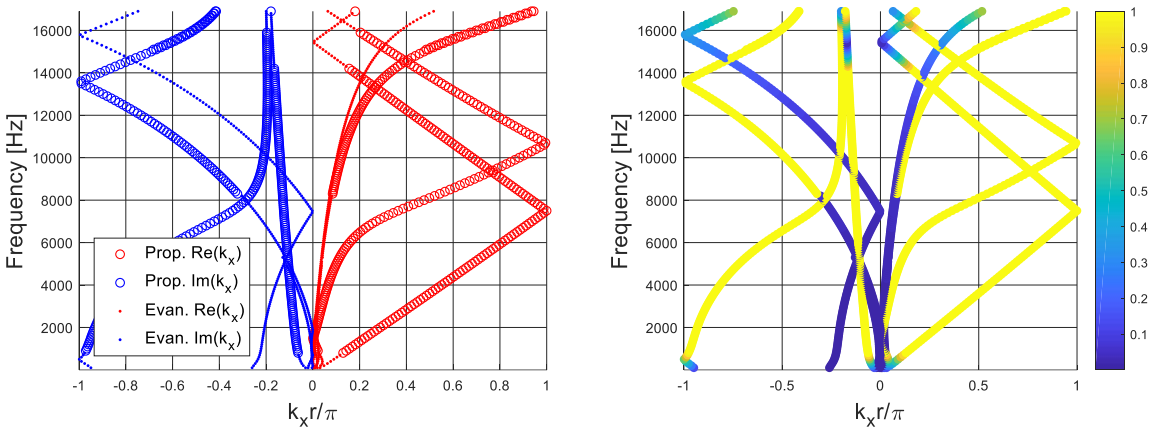

Figure 113: Dispersion curves computed for configuration 5 of Table 4.

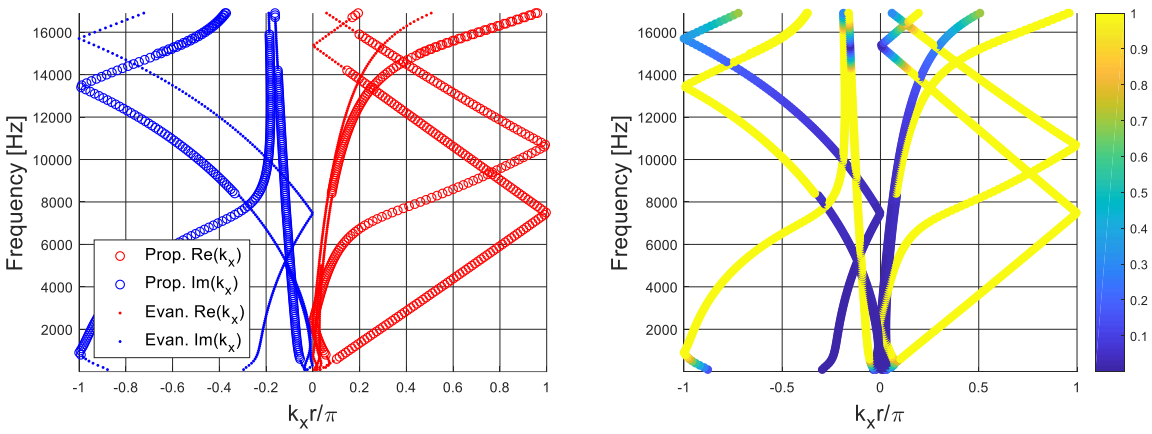

Figure 114: Dispersion curves computed for configuration 6 of Table 4.

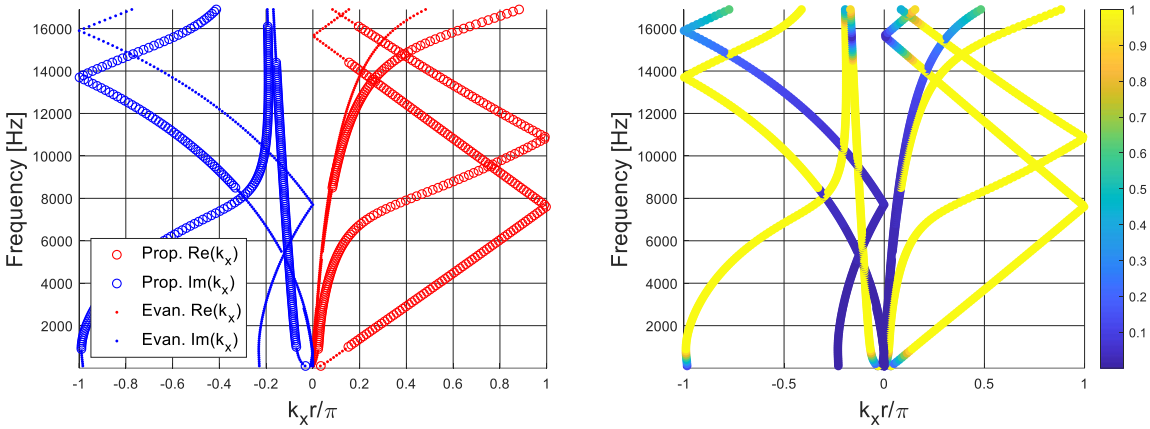

Figure 115: Dispersion curves computed for configuration 7 of Table 4.

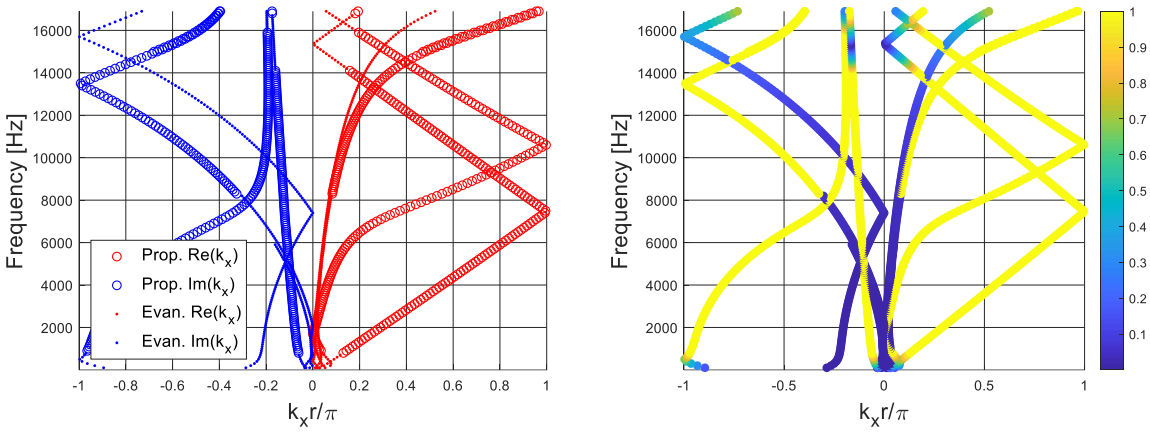

Figure 116: Dispersion curves computed for configuration 8 of Table 4.

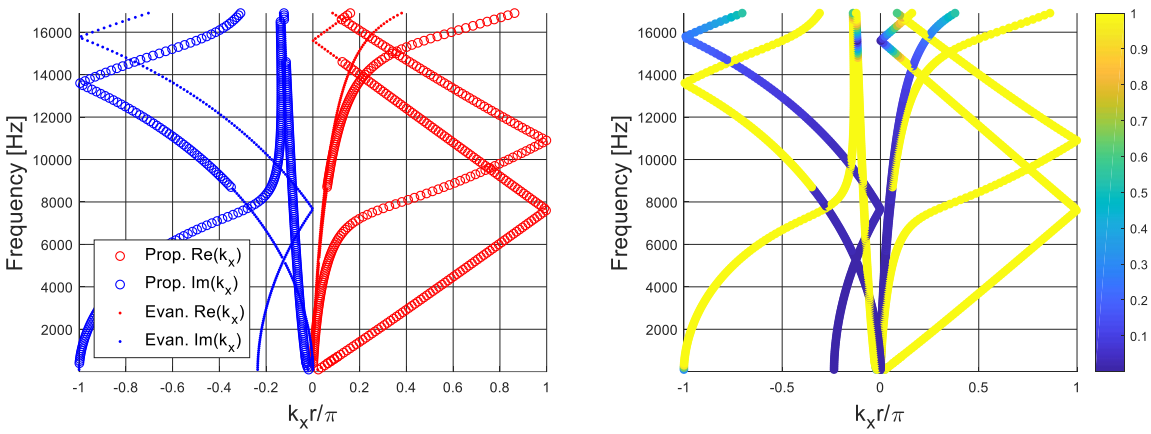

Figure 117: Dispersion curves computed for configuration 9 of Table 4.

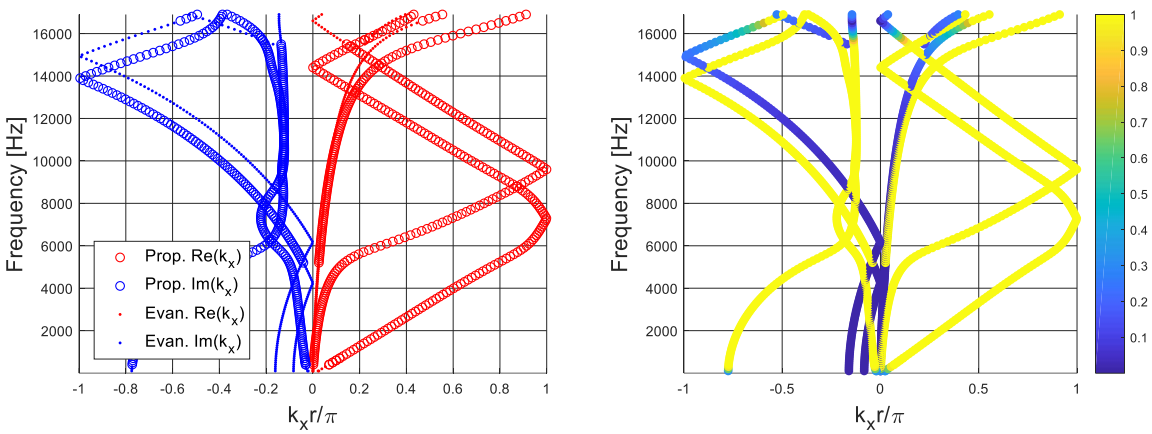

Figure 118: Dispersion curves computed for configuration 10 of Table 4.

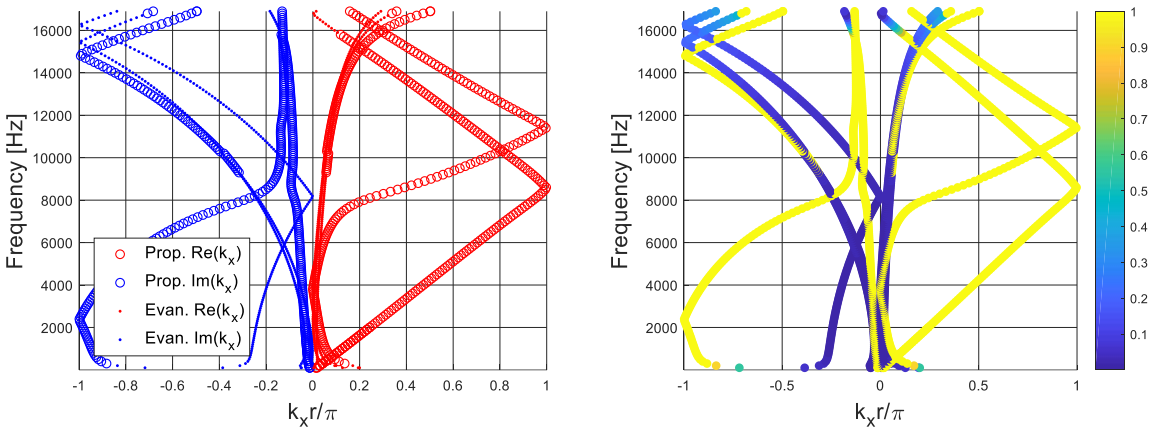

Figure 119: Dispersion curves computed for configuration 11 of Table 4.

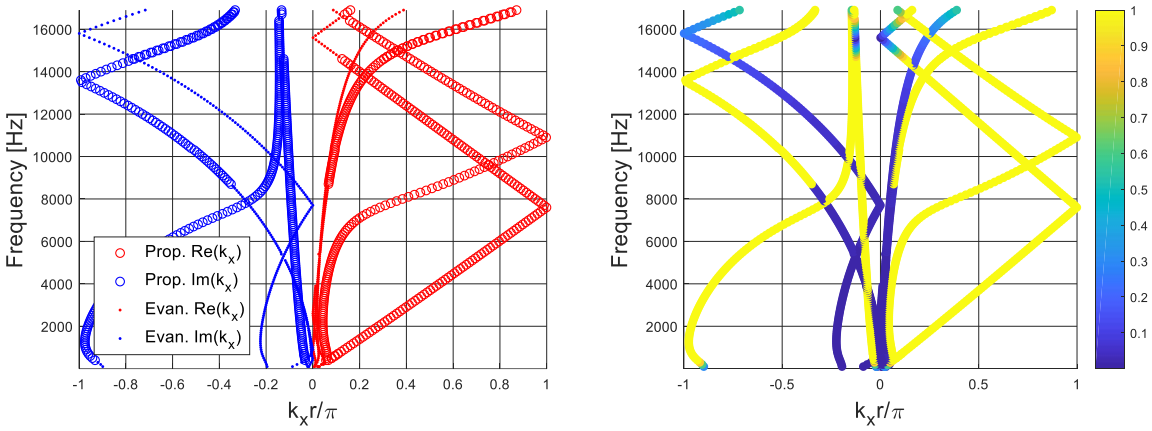

Figure 120: Dispersion curves computed for configuration 12 of Table 4.

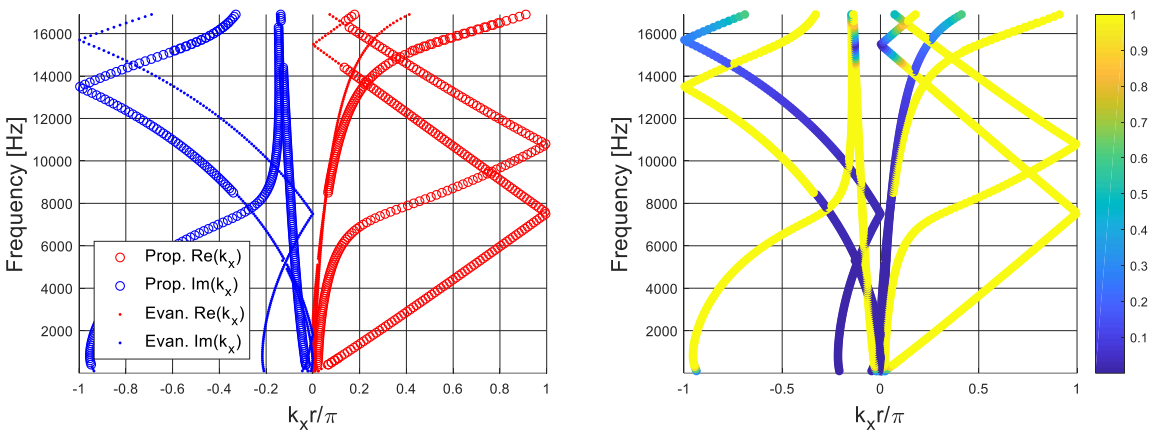

Figure 121: Dispersion curves computed for configuration 13 of Table 4.

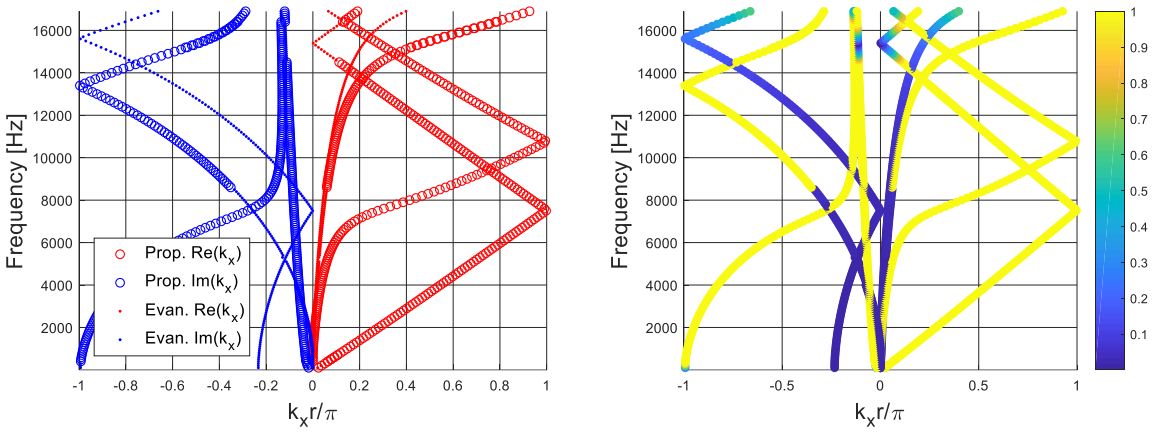

Figure 122: Dispersion curves computed for configuration 14 of Table 4.

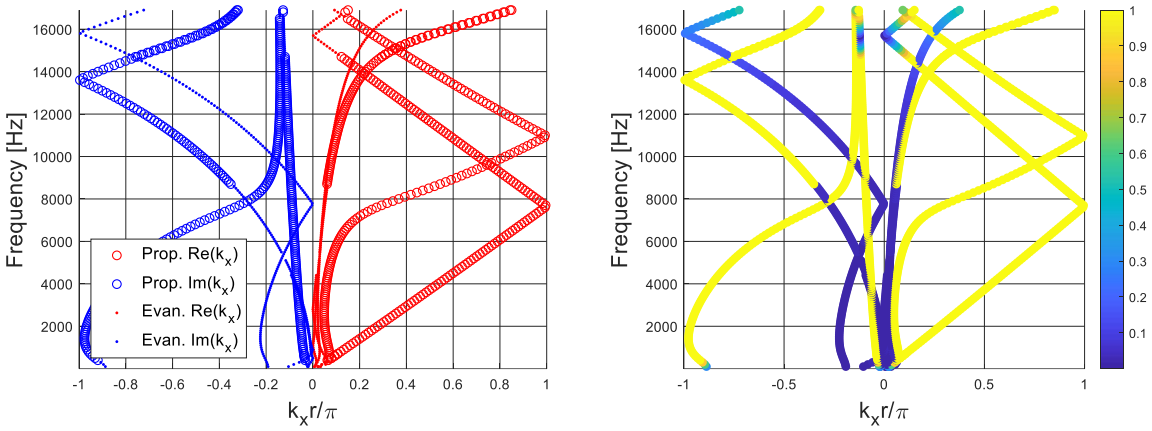

Figure 123: Dispersion curves computed for configuration 15 of Table 4.

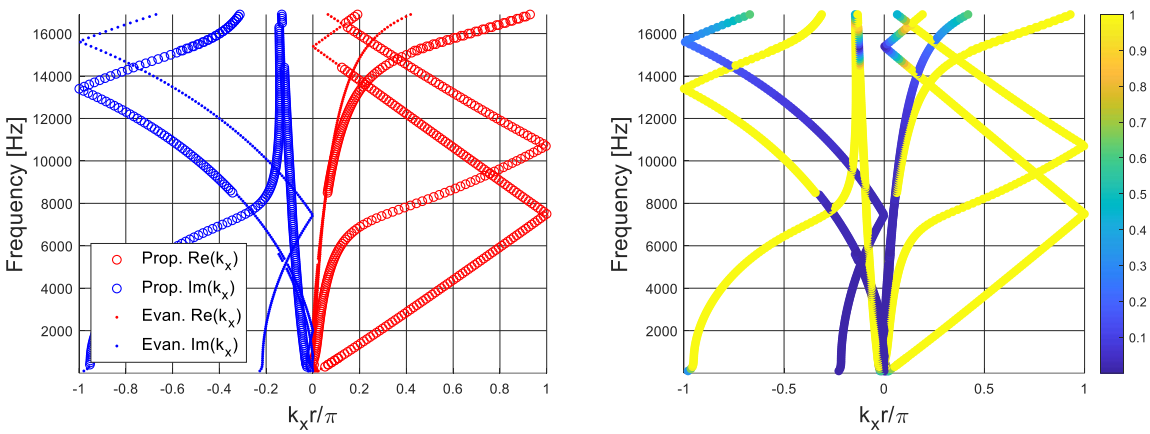

Figure 124: Dispersion curves computed for configuration 16 of Table 4.

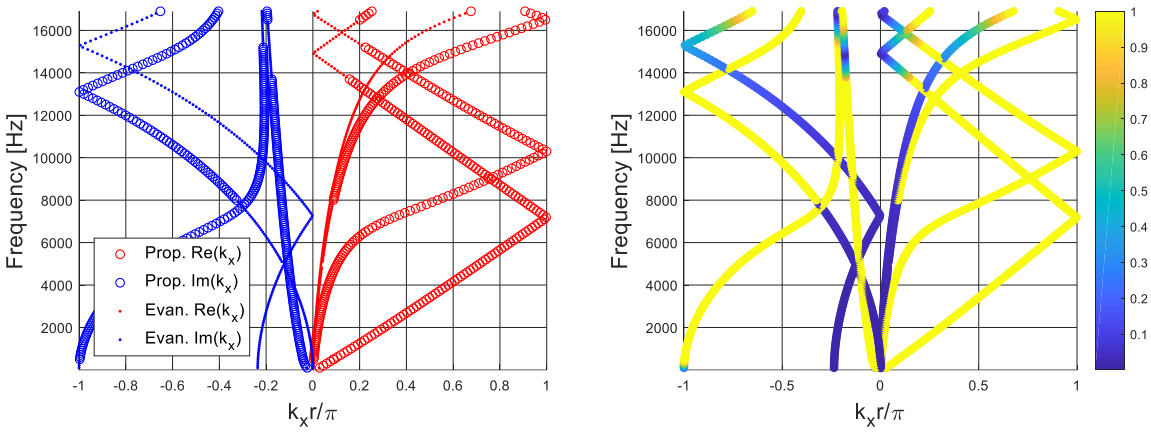

Figure 125: Dispersion curves computed for configuration 17 of Table 4.

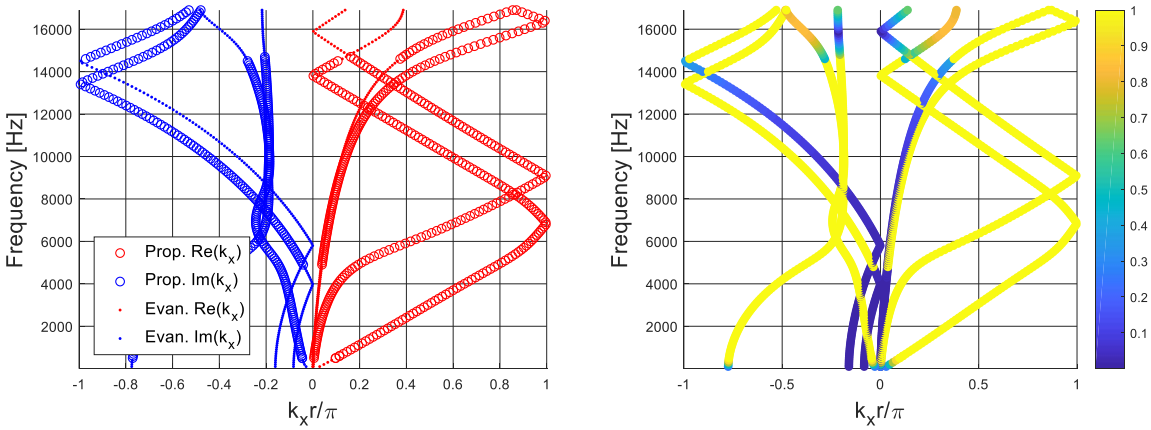

Figure 126: Dispersion curves computed for configuration 18 of Table 4.

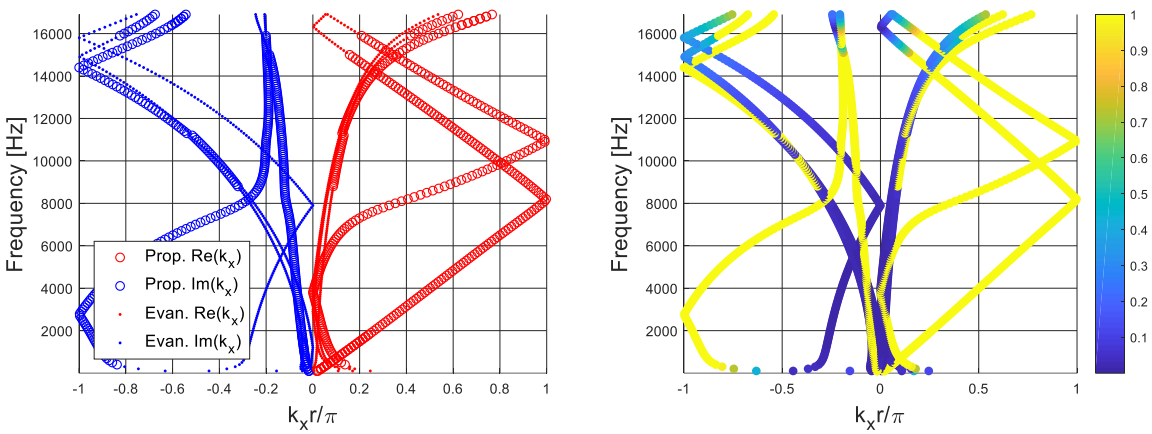

Figure 127: Dispersion curves computed for configuration 19 of Table 4.

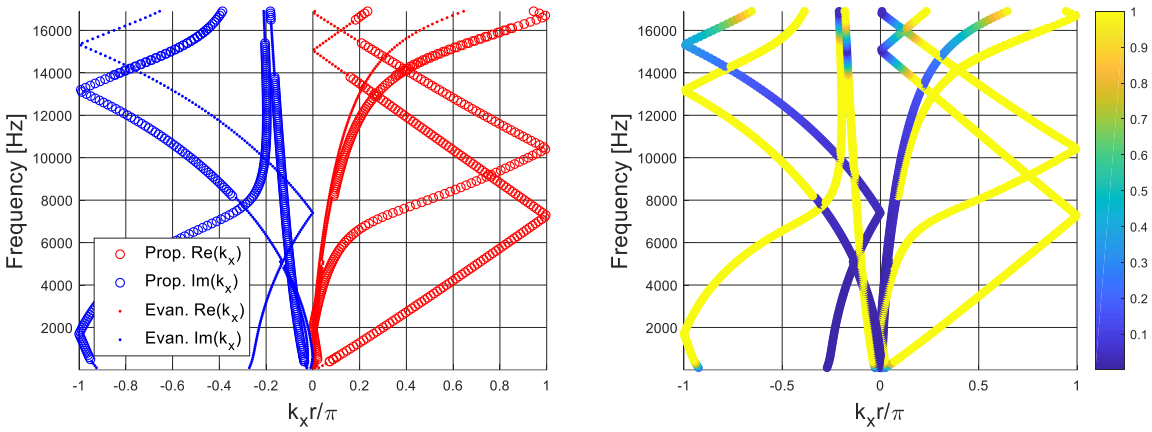

Figure 128: Dispersion curves computed for configuration 20 of Table 4.

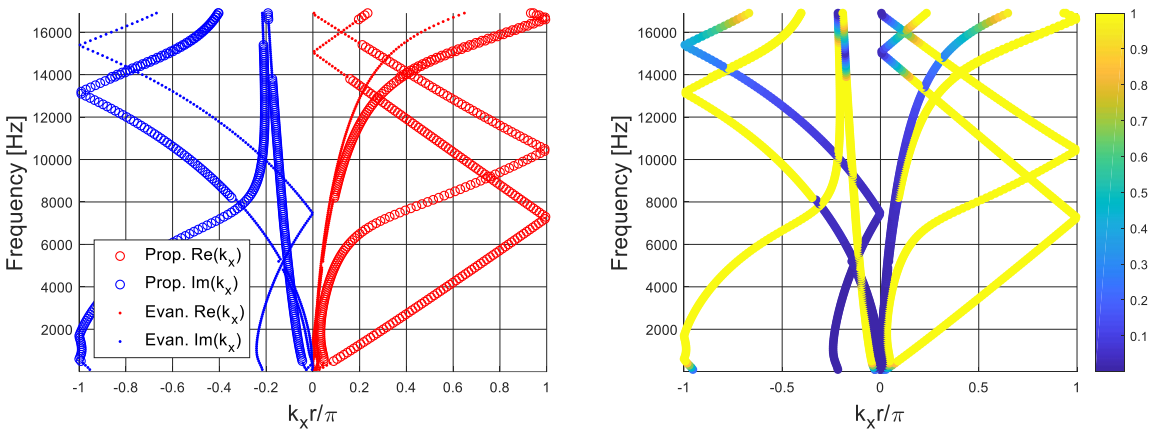

Figure 129: Dispersion curves computed for configuration 21 of Table 4.

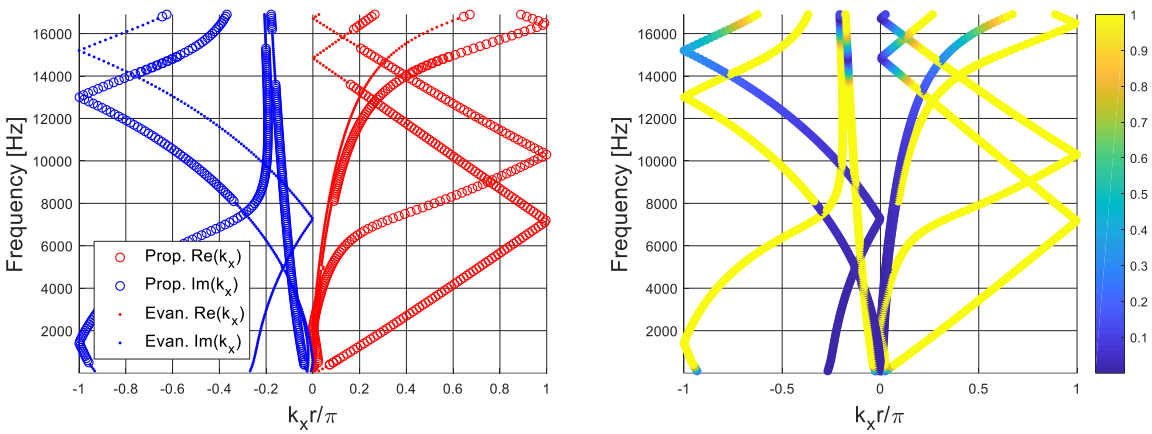

Figure 130: Dispersion curves computed for configuration 22 of Table 4.

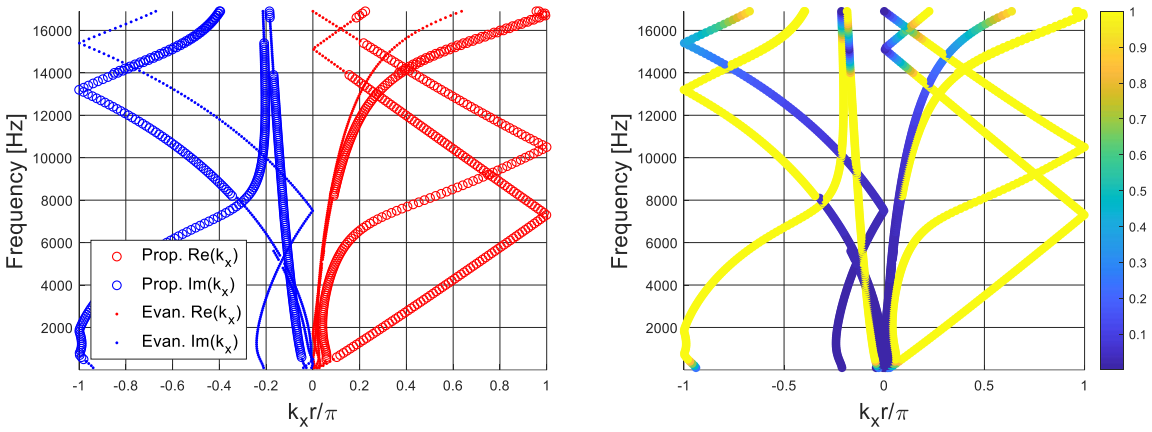

Figure 131: Dispersion curves computed for configuration 23 of Table 4.

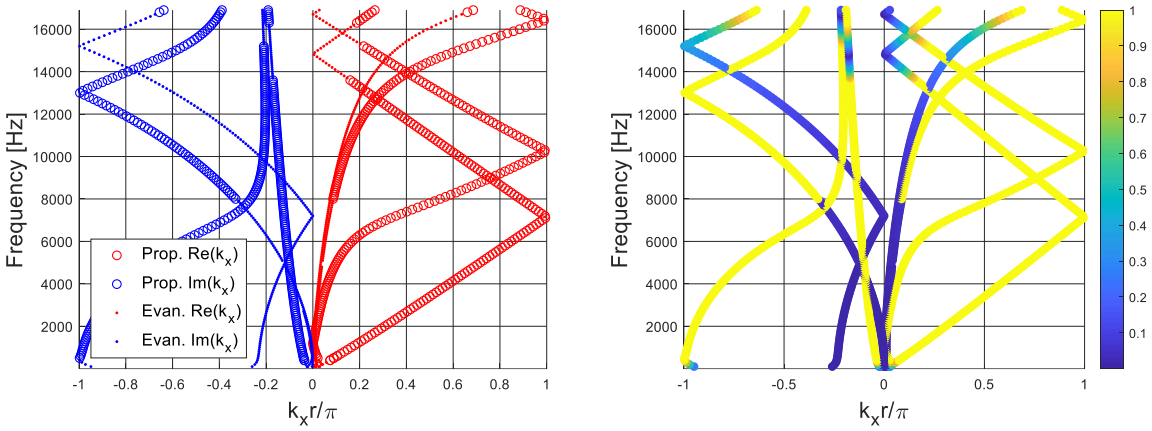

Figure 132: Dispersion curves computed for configuration 24 of Table 4.

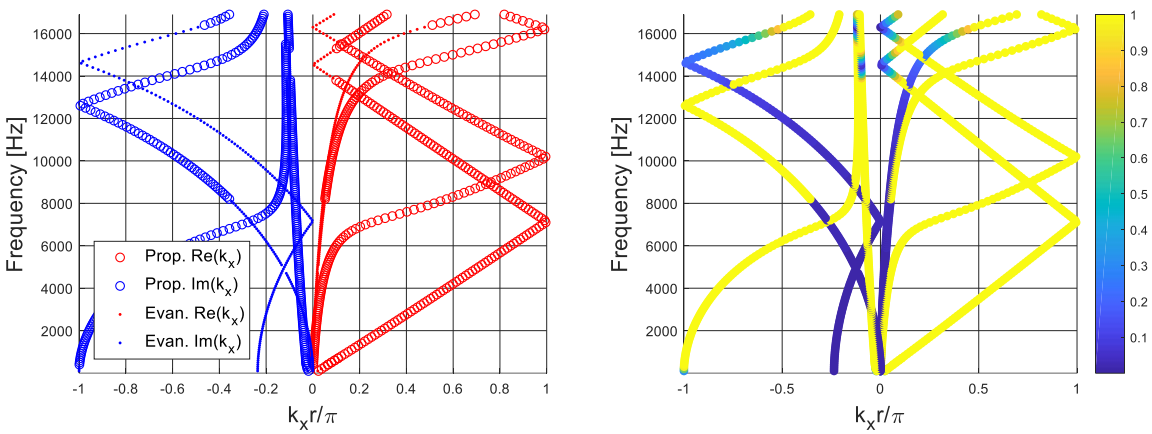

Figure 133: Dispersion curves computed for configuration 25 of Table 4.

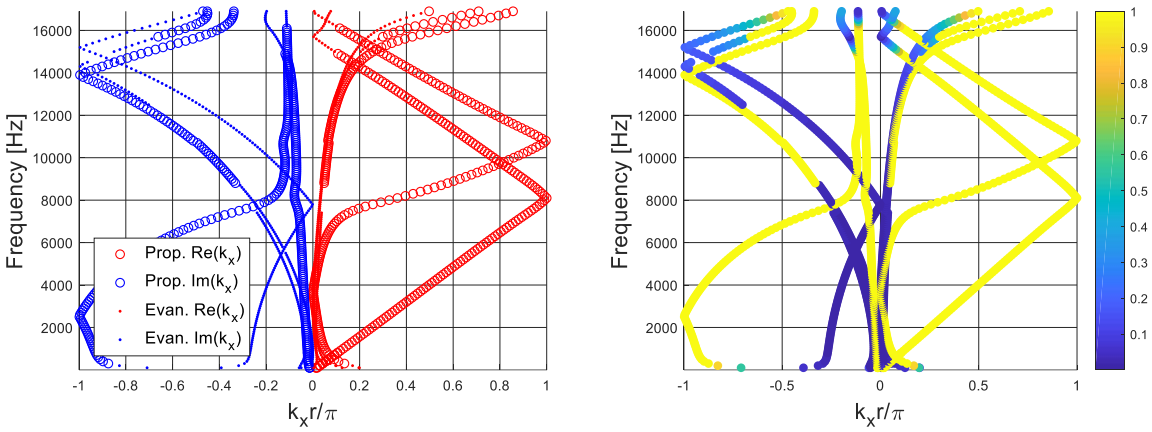

Figure 134: Dispersion curves computed for configuration 26 of Table 4.

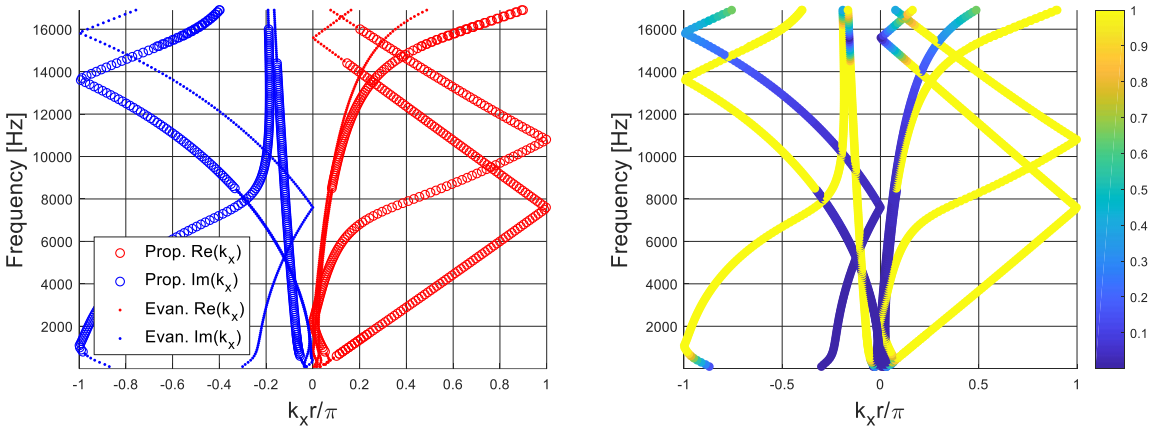

Figure 135: Dispersion curves computed for configuration 27 of Table 4.

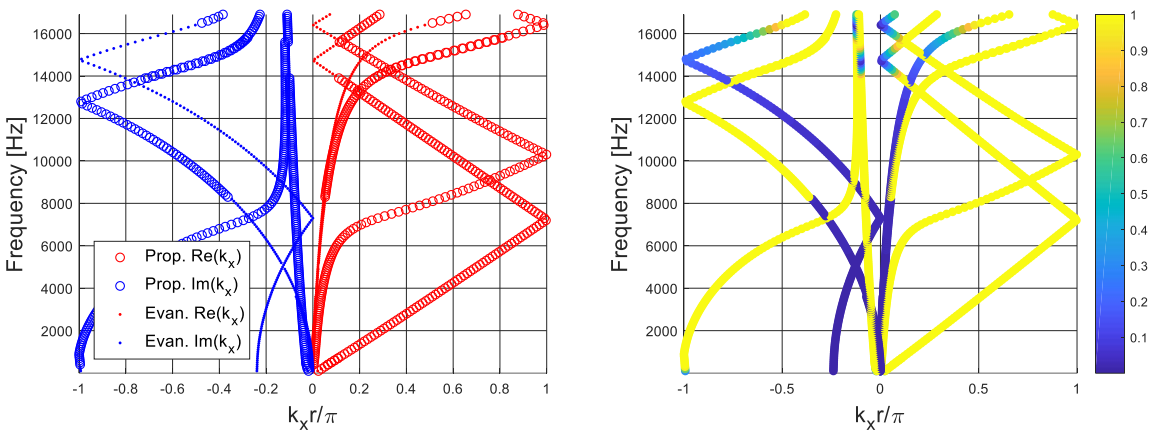

Figure 136: Dispersion curves computed for configuration 28 of Table 4.

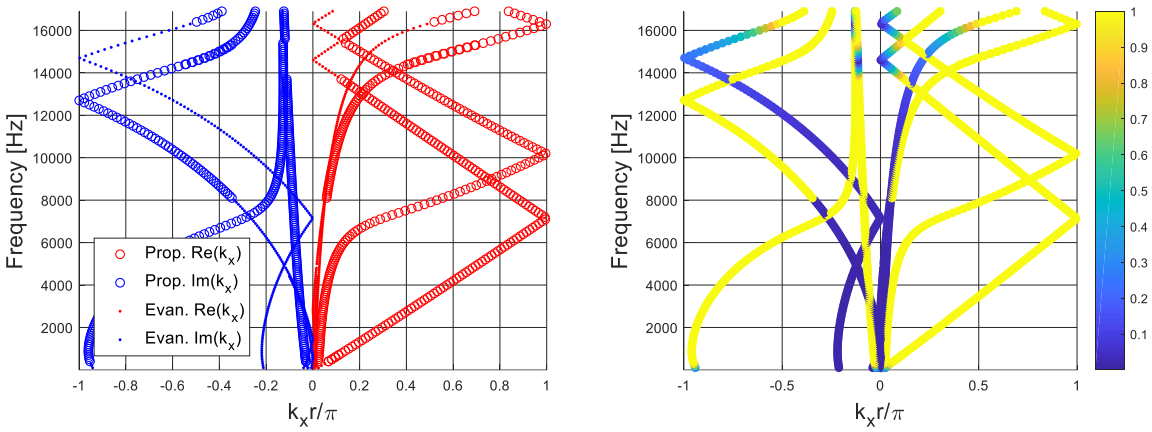

Figure 137: Dispersion curves computed for configuration 29 of Table 4.

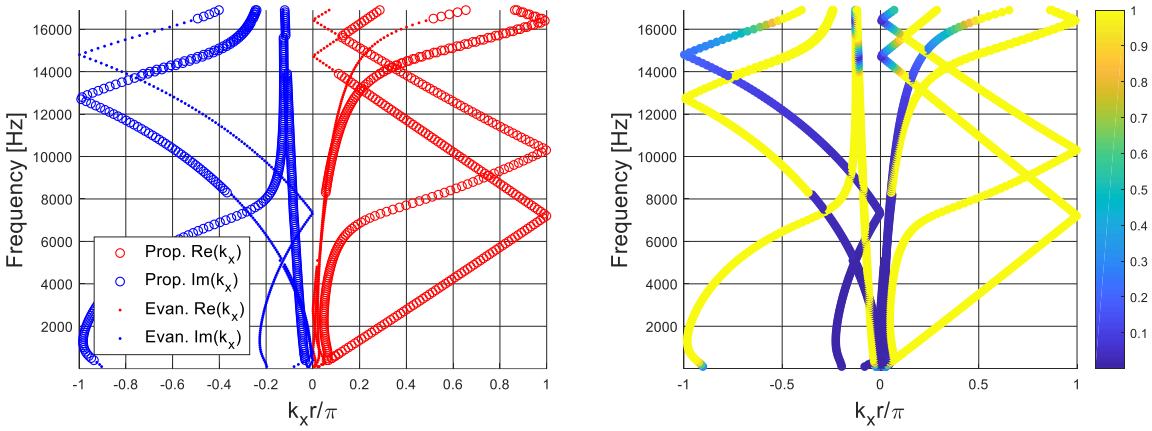

Figure 138: Dispersion curves computed for configuration 30 of Table 4.

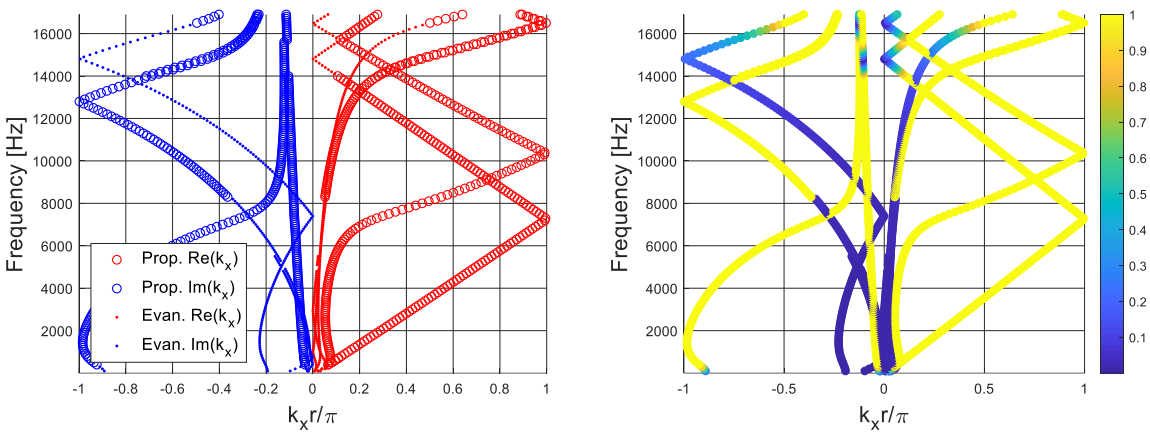

Figure 139: Dispersion curves computed for configuration 31 of Table 4.

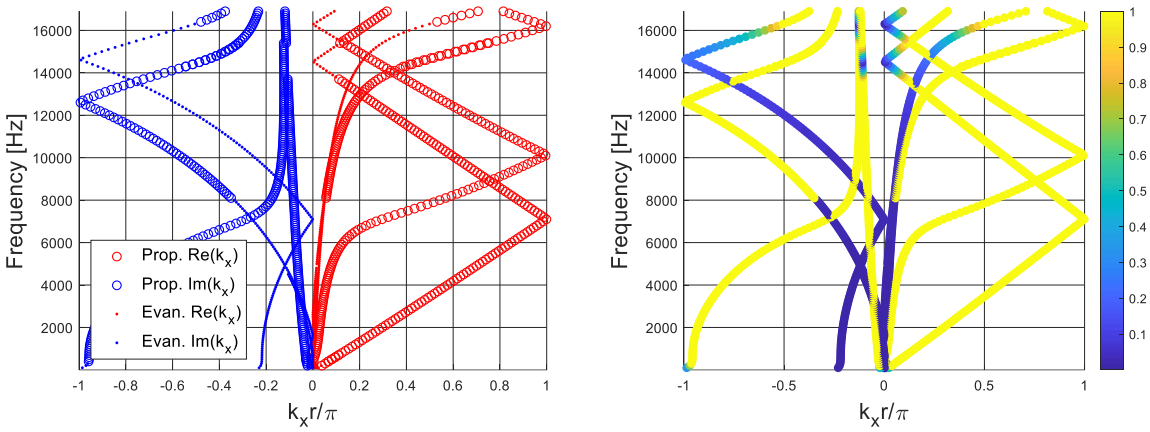

Figure 140: Dispersion curves computed for configuration 32 of Table 4.

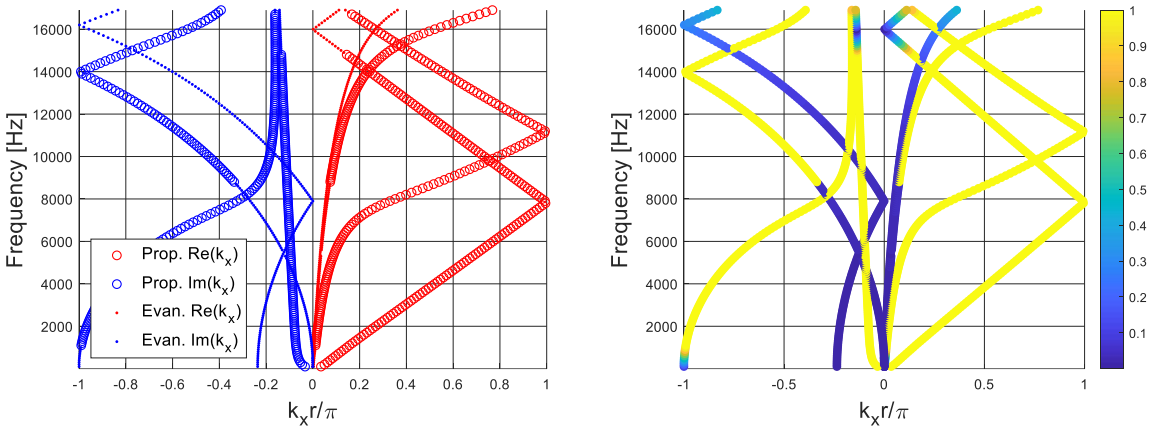

Figure 141: Dispersion curves computed for configuration 33 of Table 4.

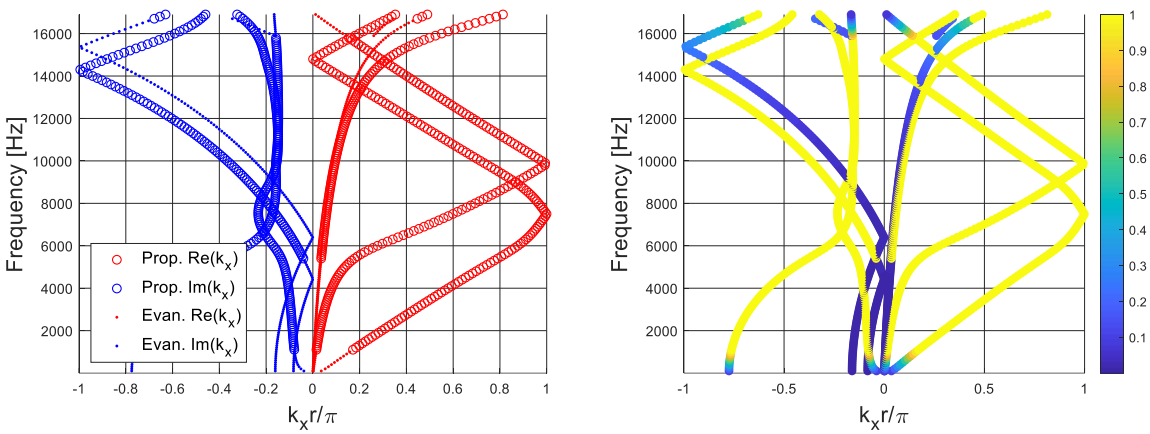

Figure 142: Dispersion curves computed for configuration 34 of Table 4.

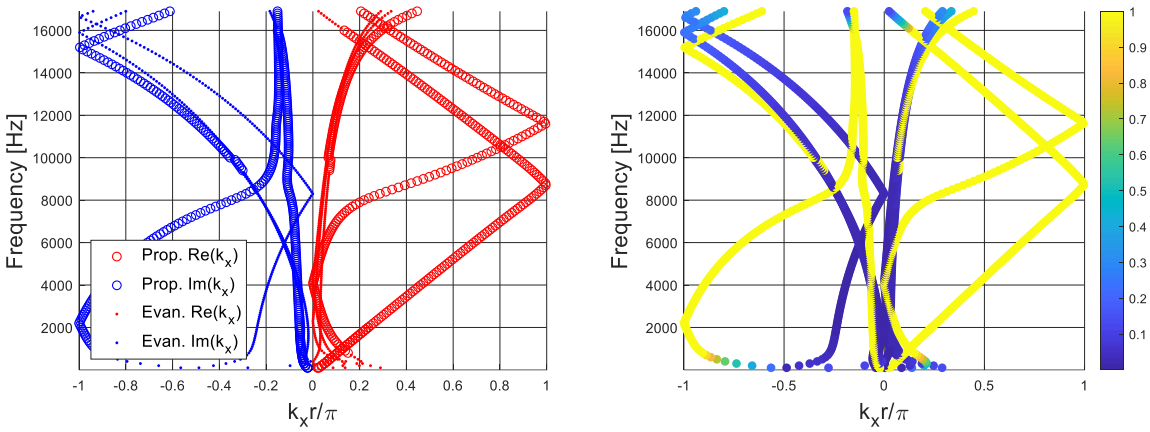

Figure 143: Dispersion curves computed for configuration 35 of Table 4.

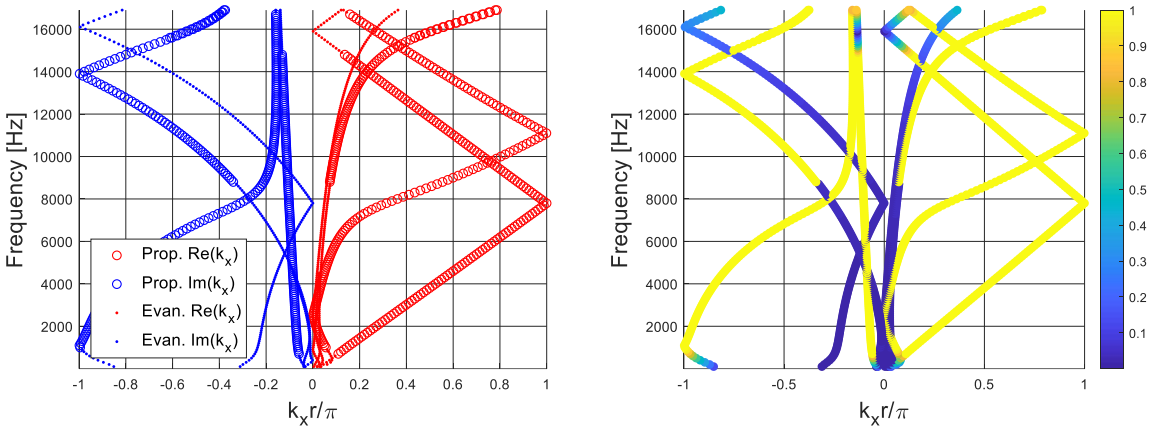

Figure 144: Dispersion curves computed for configuration 36 of Table 4.

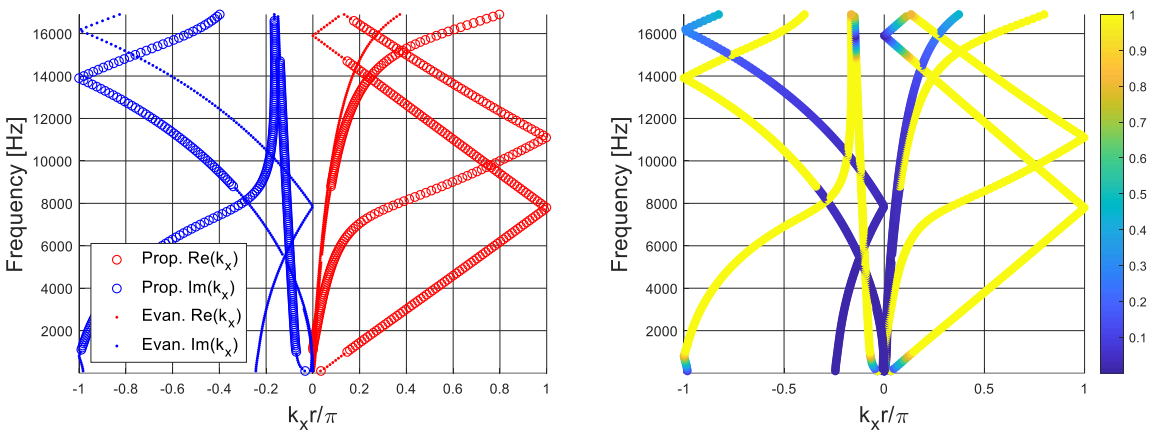

Figure 145: Dispersion curves computed for configuration 37 of Table 4.

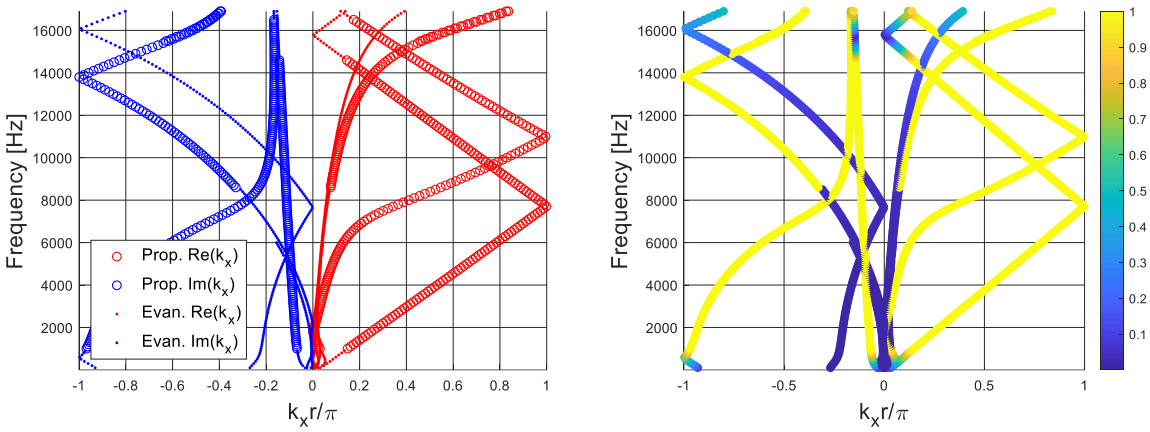

Figure 146: Dispersion curves computed for configuration 38 of Table 4.

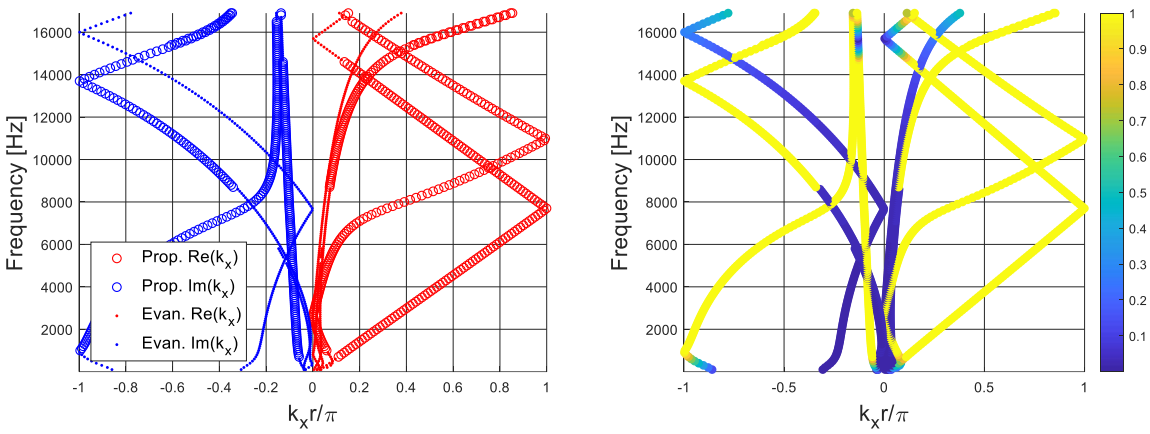

Figure 147: Dispersion curves computed for configuration 39 of Table 4.

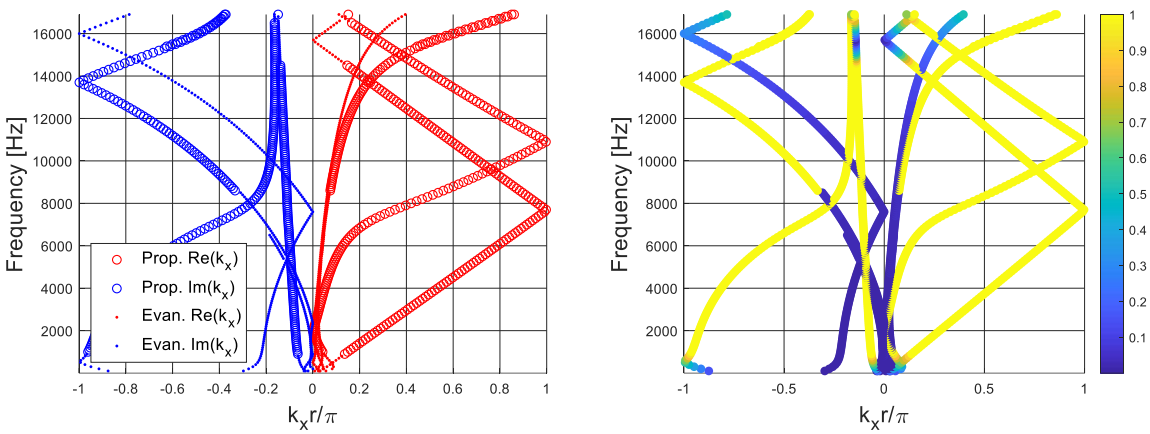

Figure 148: Dispersion curves computed for configuration 40 of Table 4.

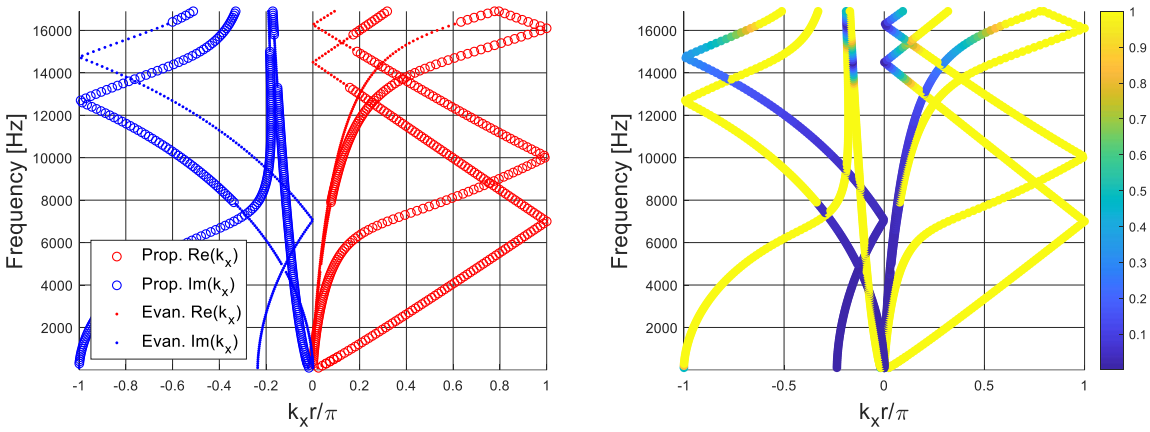

Figure 149: Dispersion curves computed for configuration 41 of Table 4.

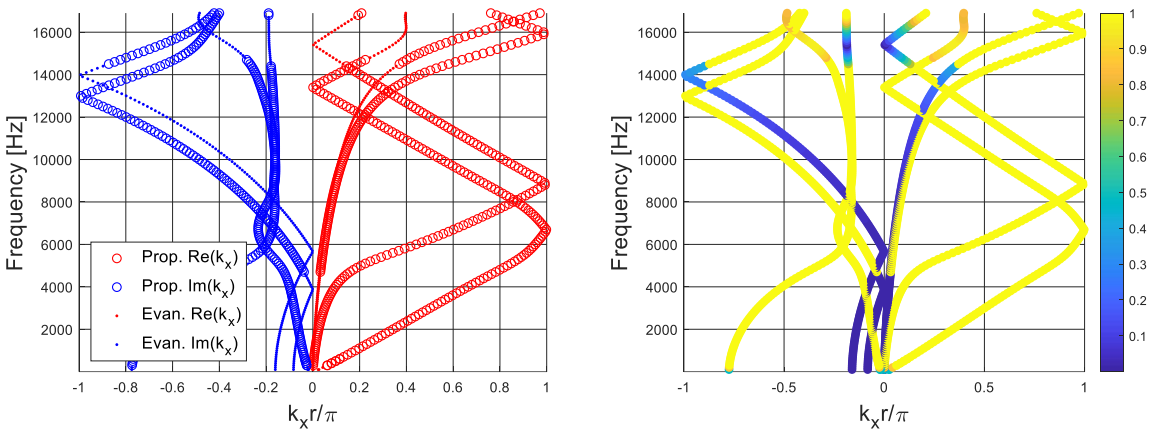

Figure 150: Dispersion curves computed for configuration 42 of Table 4.

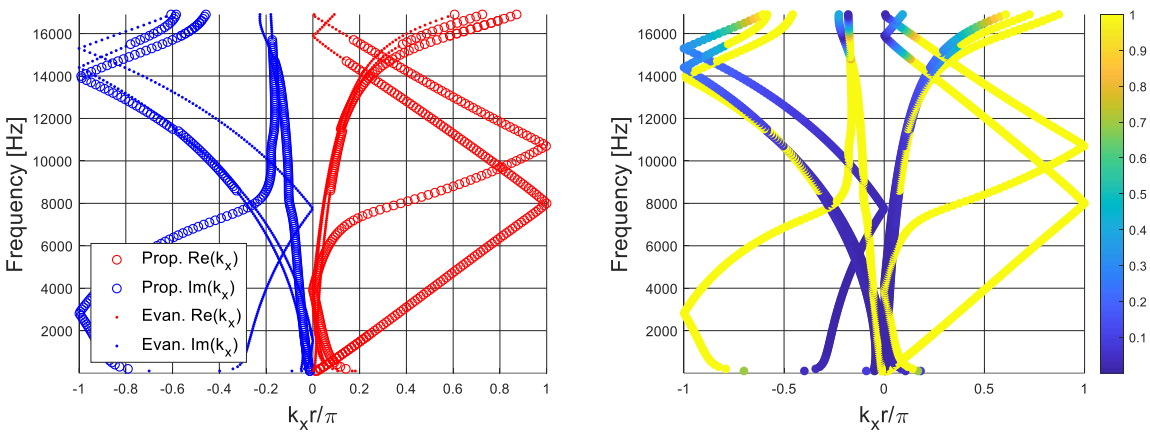

Figure 151: Dispersion curves computed for configuration 43 of Table 4.

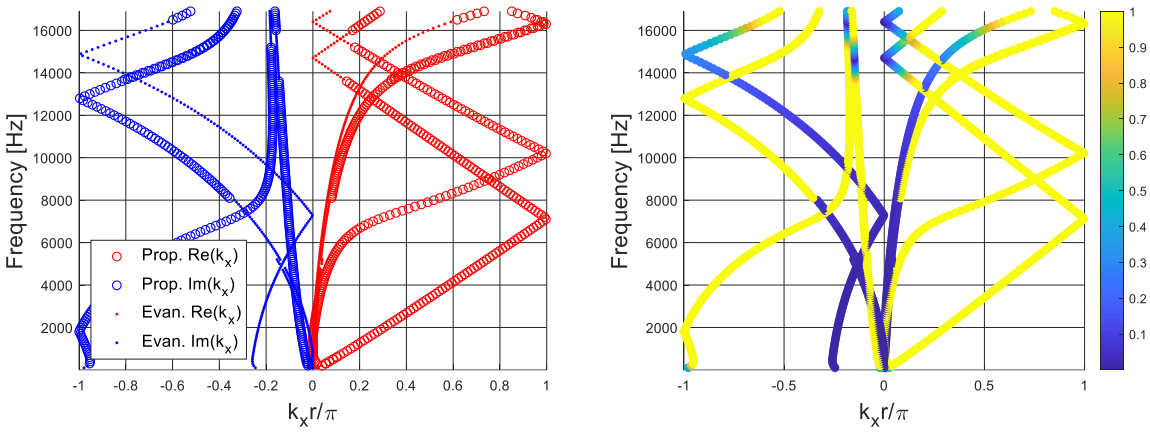

Figure 152: Dispersion curves computed for configuration 44 of Table 4.

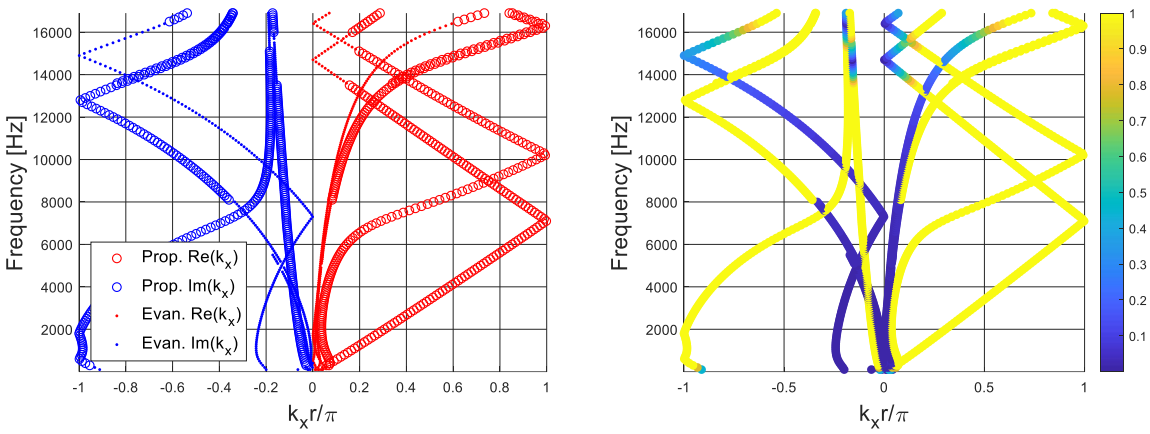

Figure 153: Dispersion curves computed for configuration 45 of Table 4.

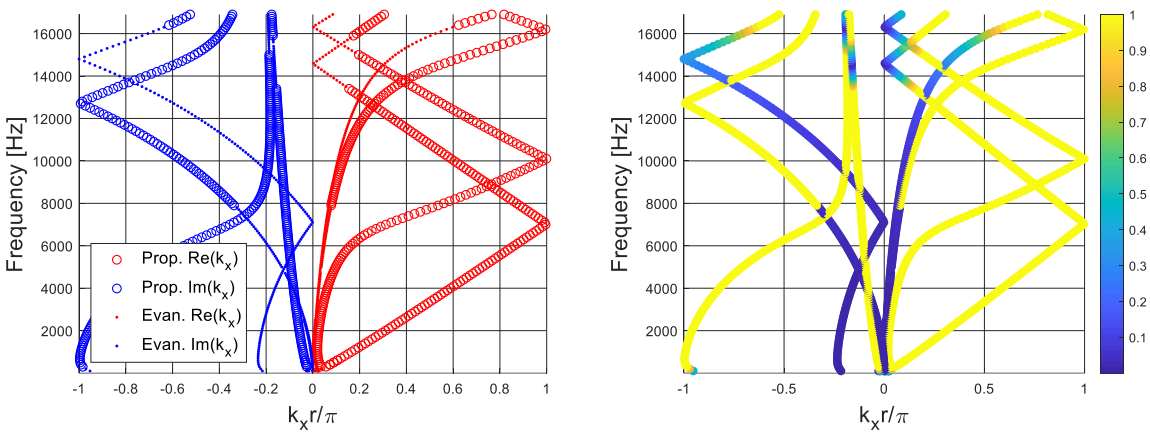

Figure 154: Dispersion curves computed for configuration 46 of Table 4.

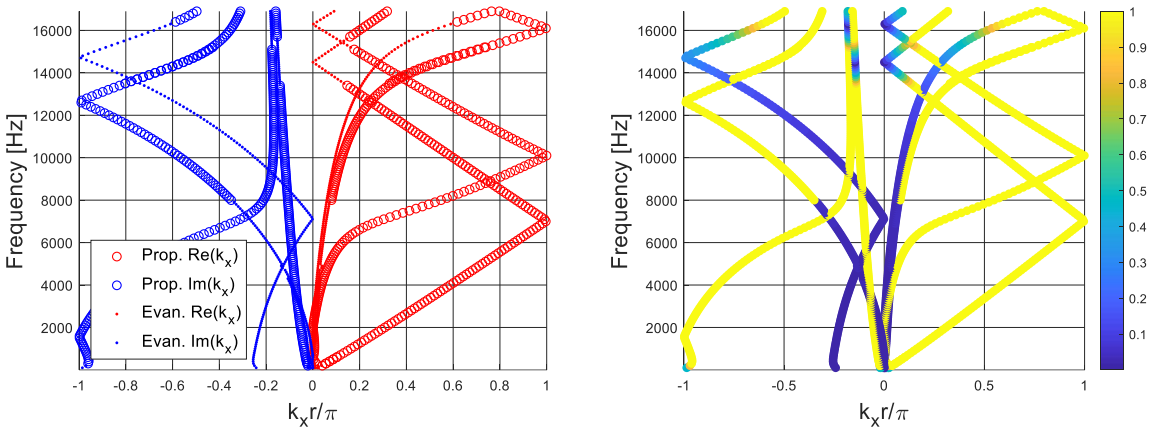

Figure 155: Dispersion curves computed for configuration 47 of Table 4.

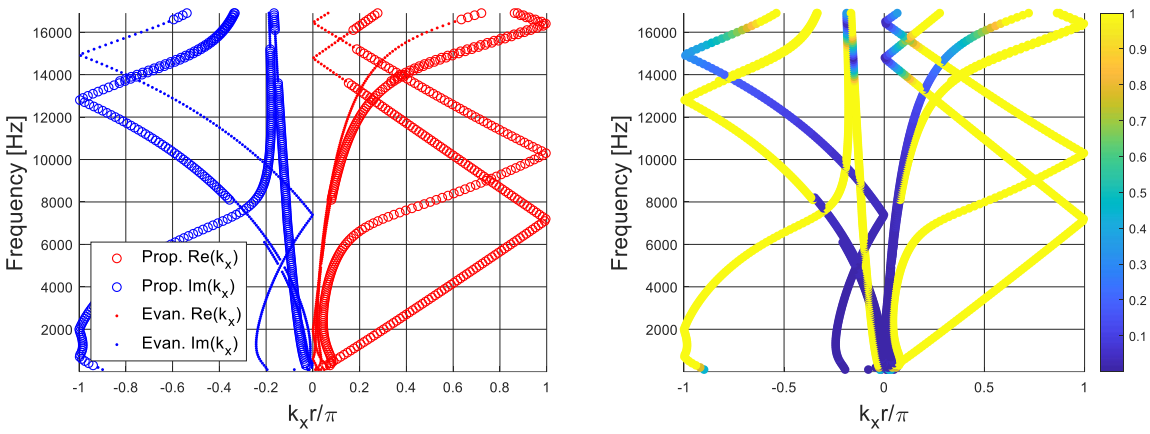

Figure 156: Dispersion curves computed for configuration 48 of Table 4.

A.2. Absorption coefficient

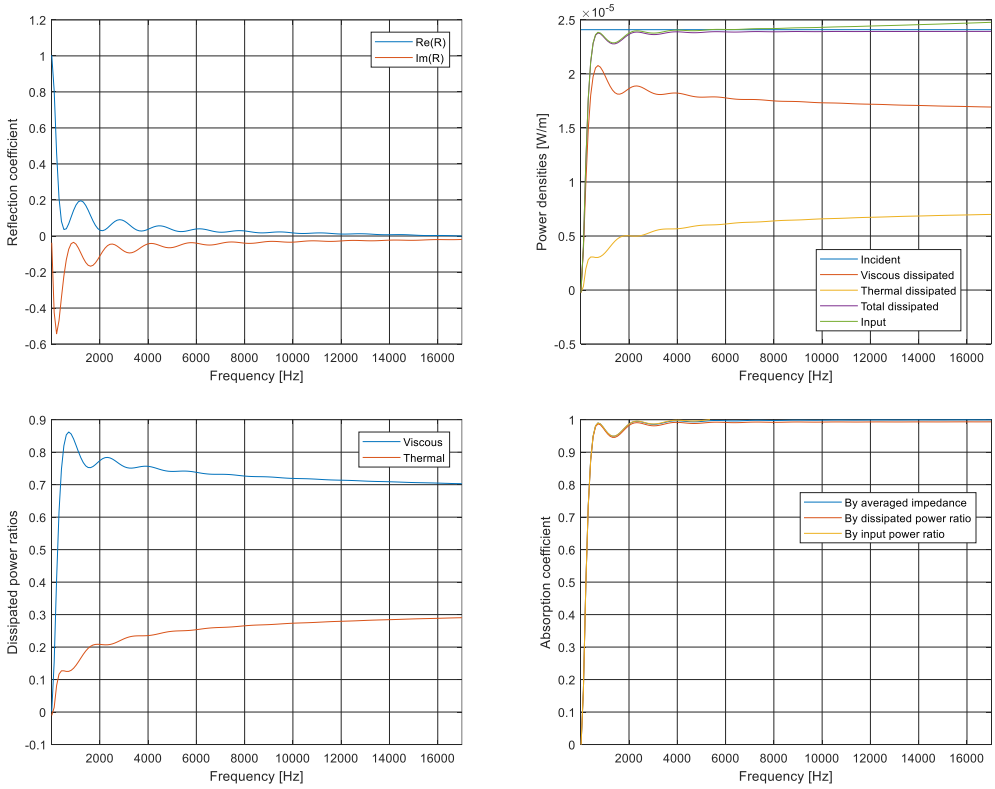

Figure 157: Reflection coefficient, power densities, dissipated power ratios and absorption coefficient computed for a homogeneous DB-modeled melamine 2D unit cell.

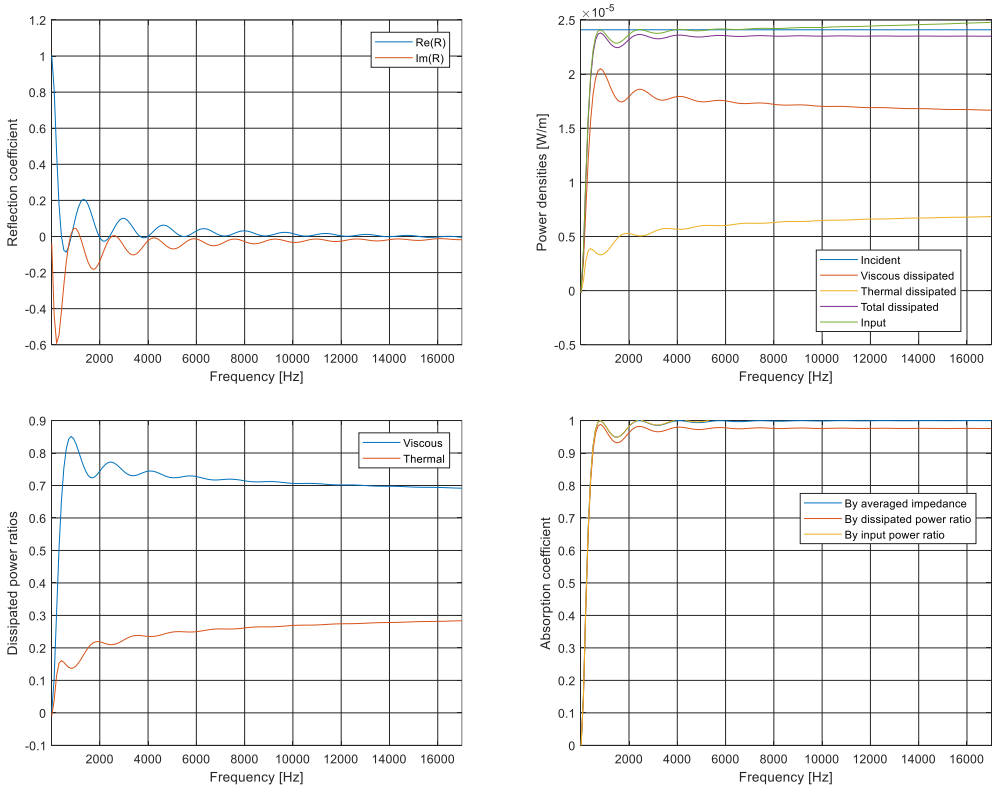

Figure 158: Reflection coefficient, power densities, dissipated power ratios and absorption coefficient computed for a homogeneous DB-modeled black PU 2D unit cell.

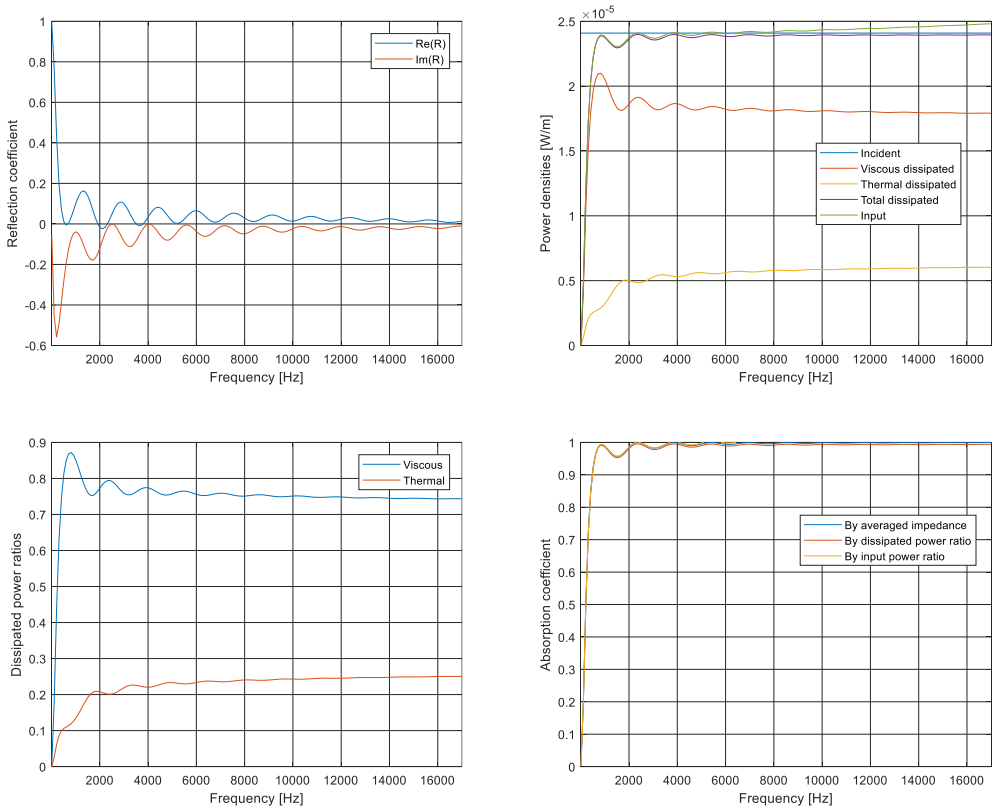

Figure 159: Reflection coefficient, power densities, dissipated power ratios and absorption coefficient computed for a homogeneous JCA-modeled melamine 2D unit cell.

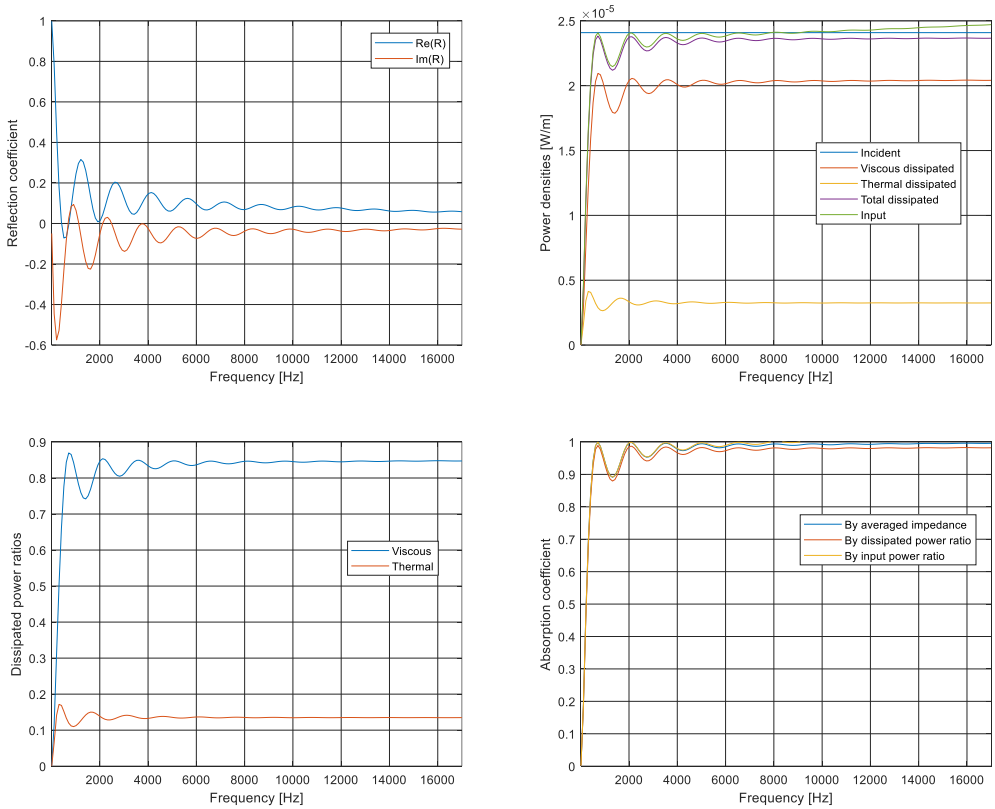

Figure 160: Reflection coefficient, power densities, dissipated power ratios and absorption coefficient computed for a homogeneous JCA-modeled black PU 2D unit cell.

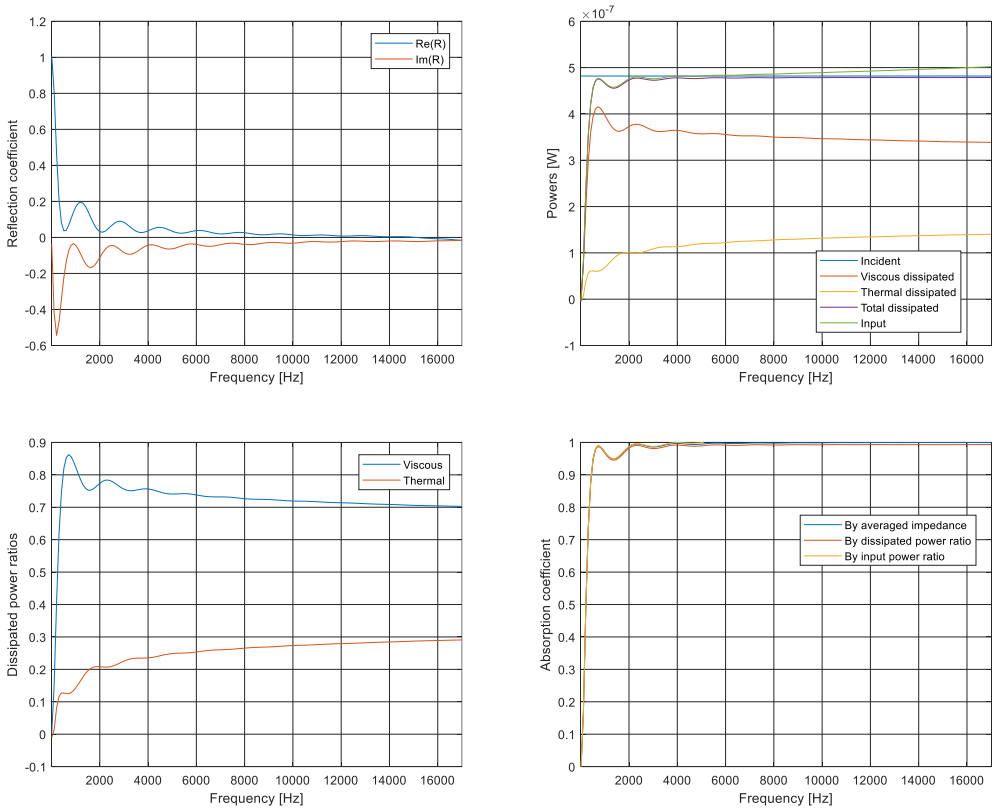

Figure 161: Reflection coefficient, powers, dissipated power ratios and absorption coefficient computed for a homogeneous DB-modeled melamine 3D unit cell.

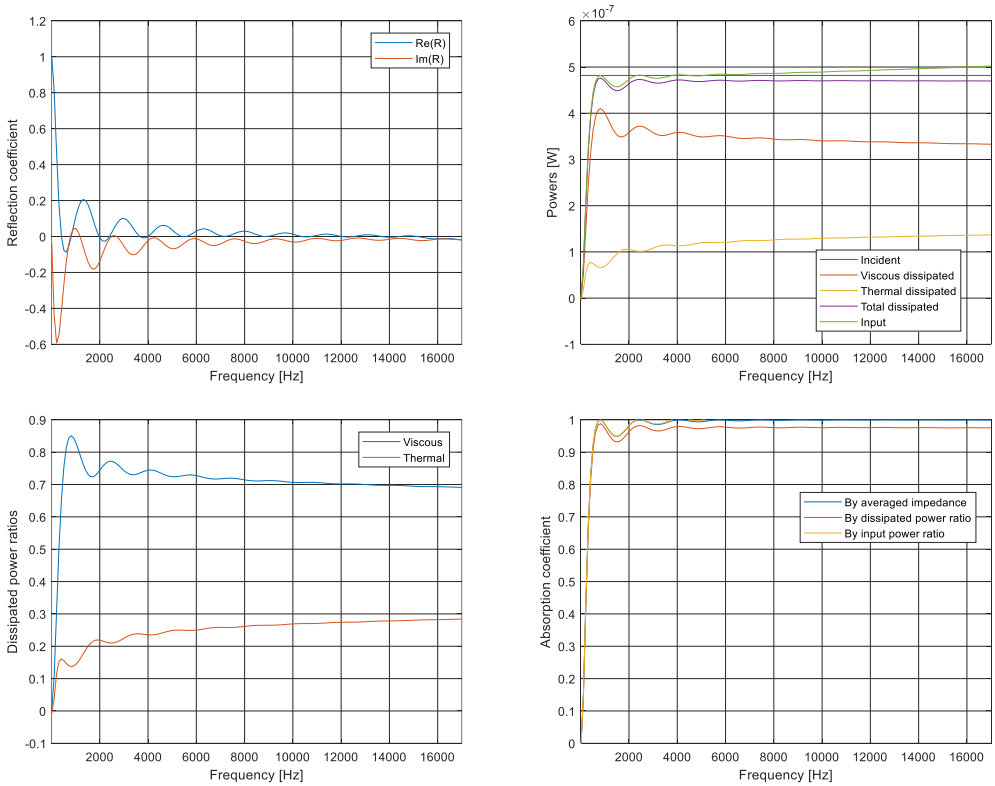

Figure 162: Reflection coefficient, powers, dissipated power ratios and absorption coefficient computed for a homogeneous DB-modeled black PU 3D unit cell.

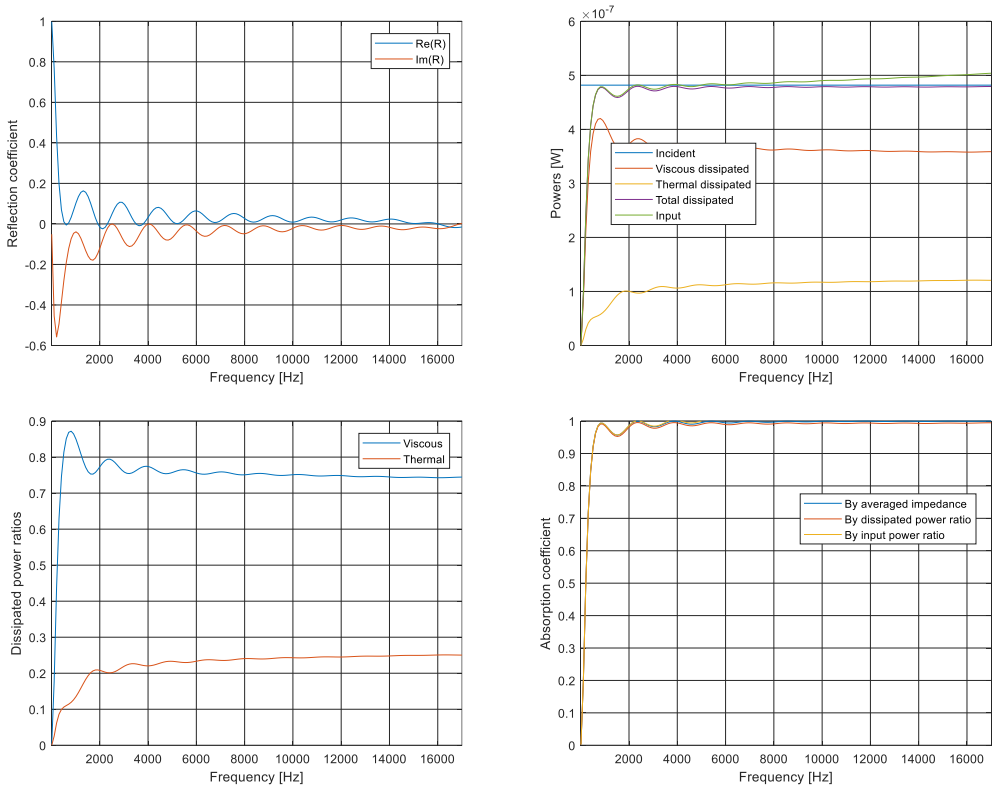

Figure 163: Reflection coefficient, powers, dissipated power ratios and absorption coefficient computed for a homogeneous JCA-modeled melamine 3D unit cell.

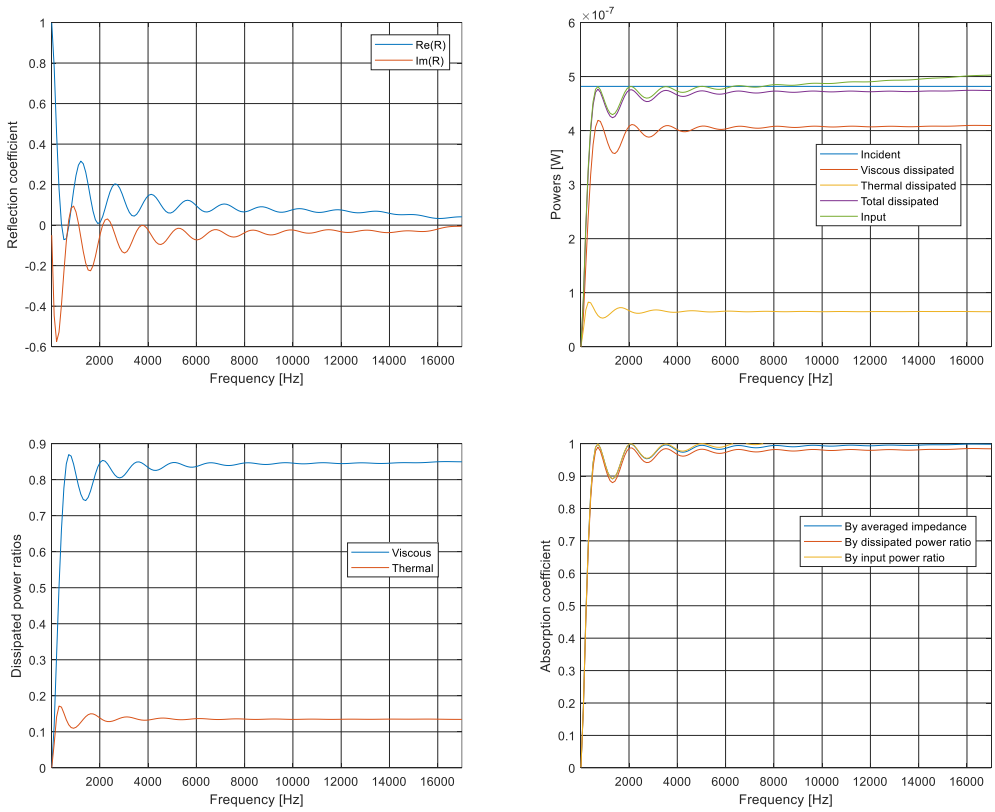

Figure 164: Reflection coefficient, powers, dissipated power ratios and absorption coefficient computed for a homogeneous JCA-modeled black PU 3D unit cell.

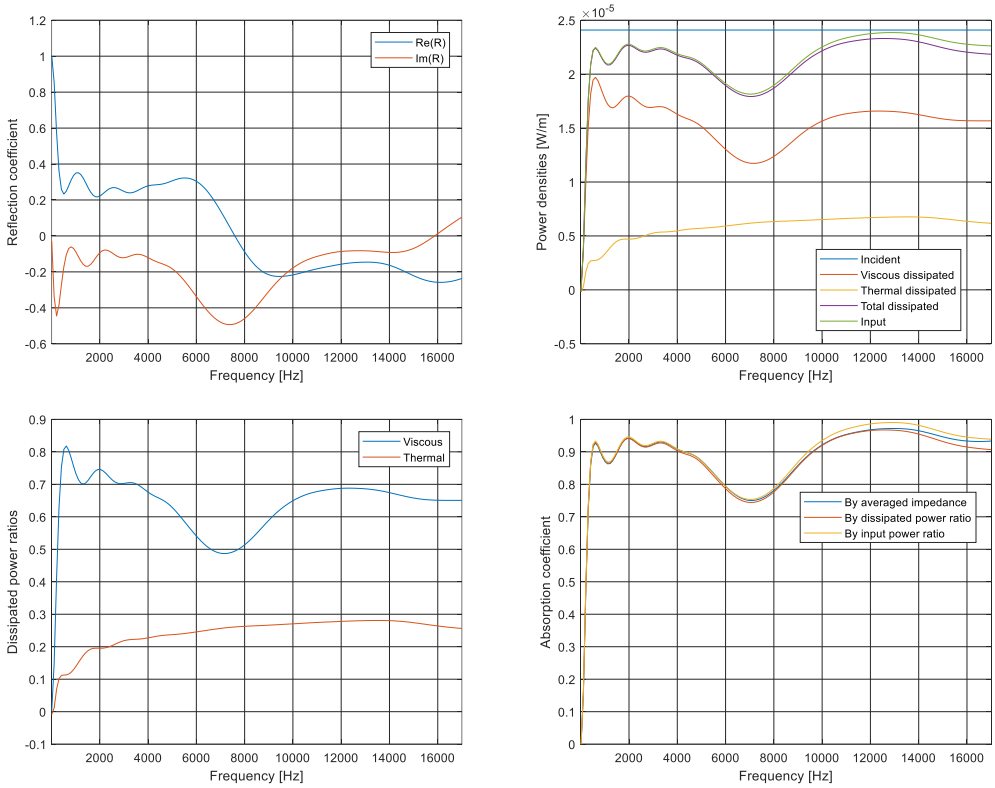

Figure 165: Reflection coefficient, power densities, dissipated power ratios and absorption coefficient computed for a DB-modeled melamine 2D unit cell with a perfectly rigid inclusion.

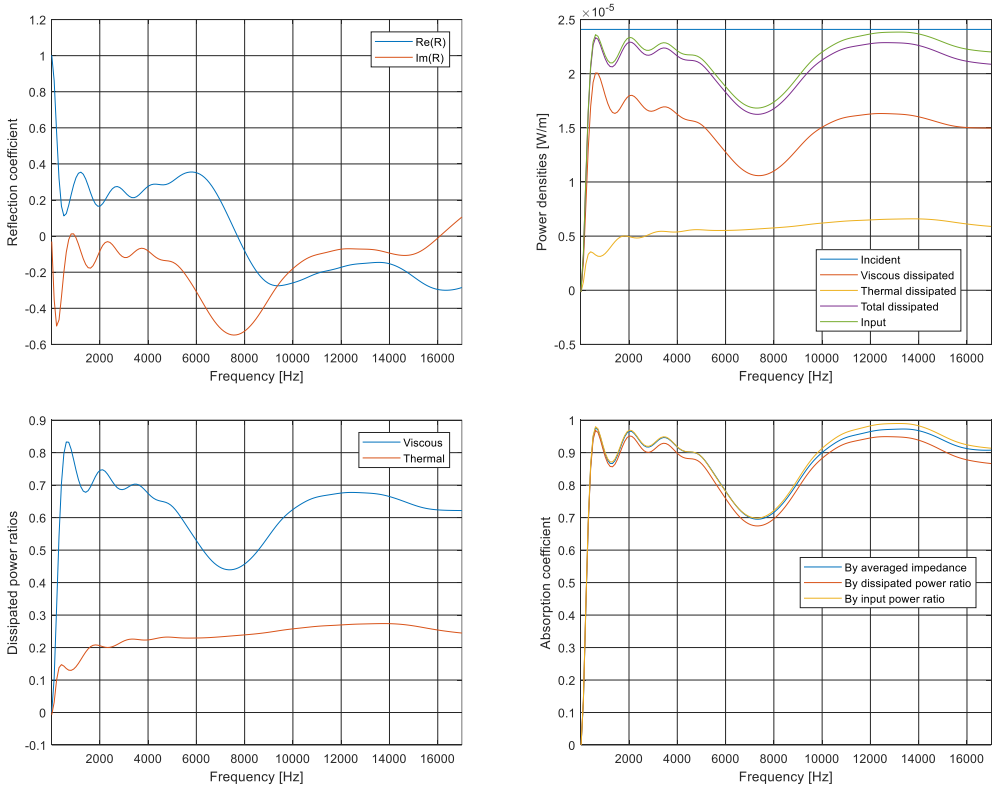

Figure 166: Reflection coefficient, power densities, dissipated power ratios and absorption coefficient computed for a DB-modeled black PU 2D unit cell with a perfectly rigid inclusion.

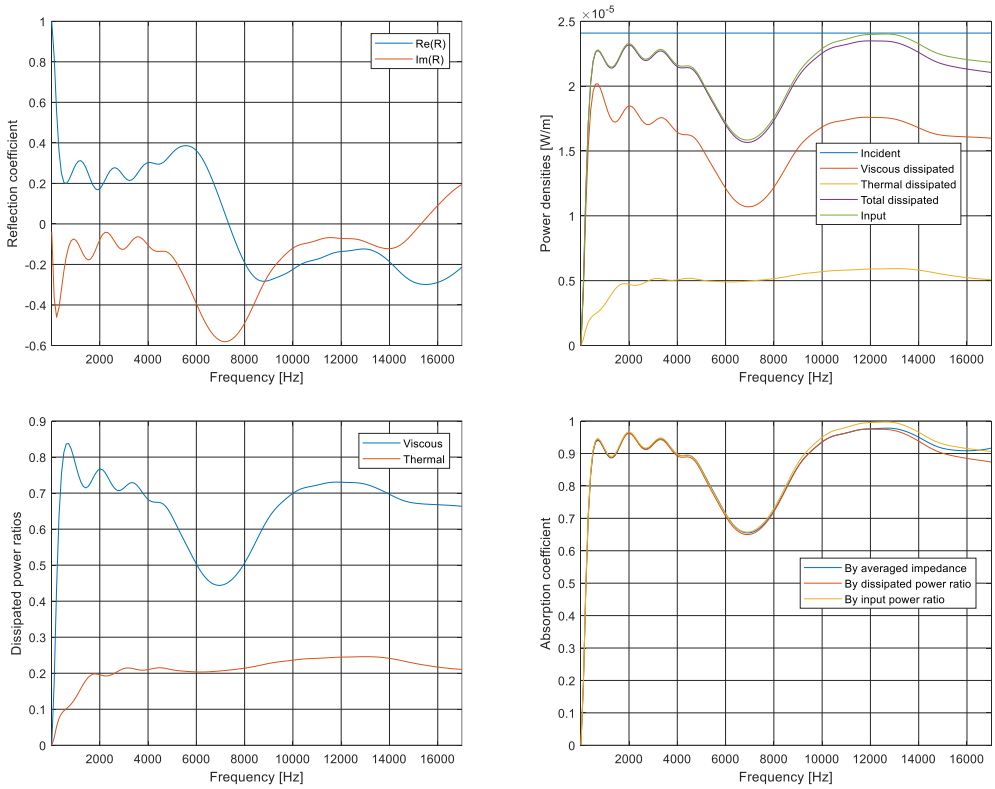

Figure 167: Reflection coefficient, power densities, dissipated power ratios and absorption coefficient computed for a JCA-modeled melamine 2D unit cell with a perfectly rigid inclusion.

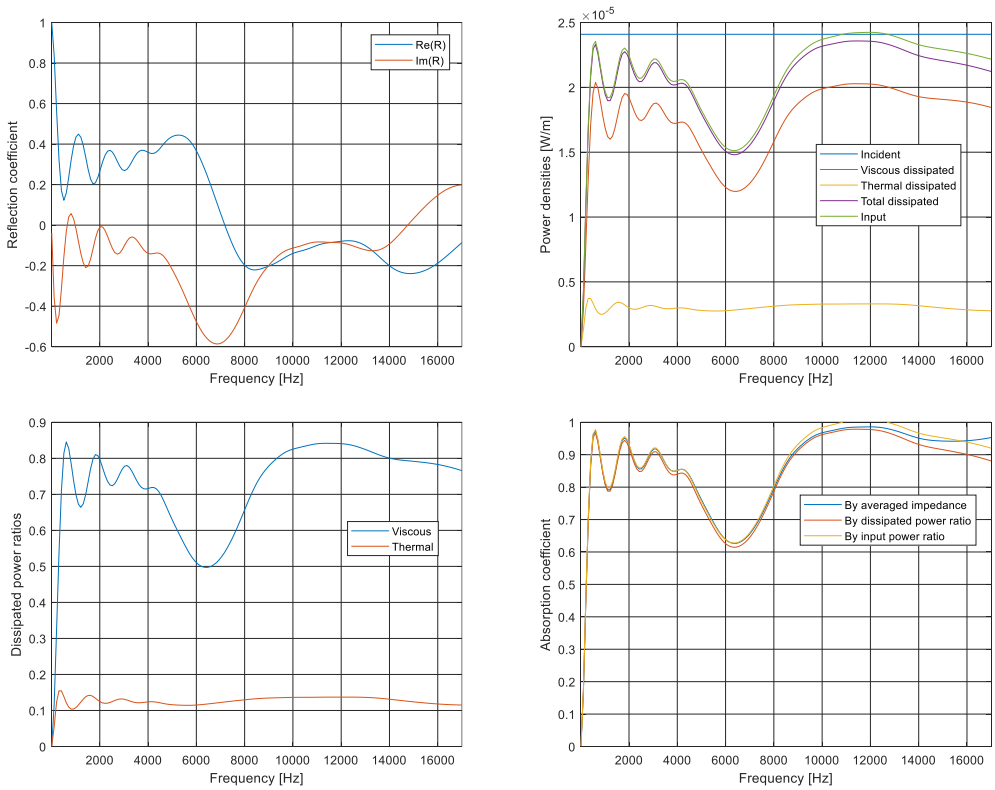

Figure 168: Reflection coefficient, power densities, dissipated power ratios and absorption coefficient computed for a JCA-modeled black PU 2D unit cell with a perfectly rigid inclusion.

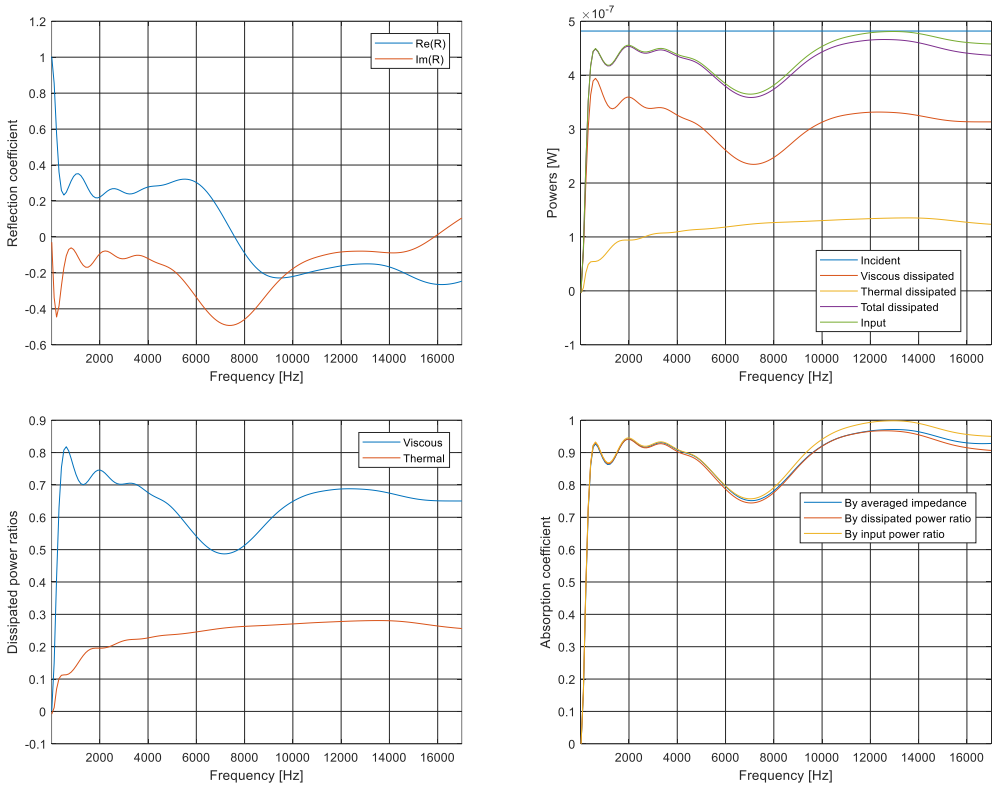

Figure 169: Reflection coefficient, powers, dissipated power ratios and absorption coefficient computed for a DB-modeled melamine 3D unit cell with a perfectly rigid inclusion.

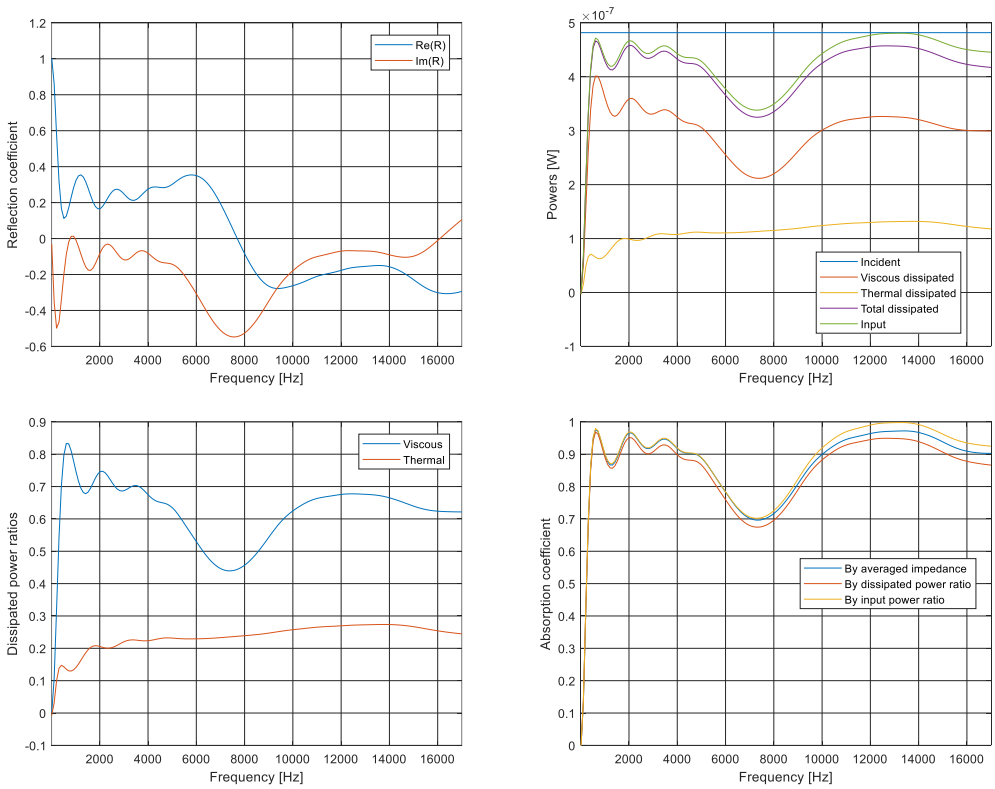

Figure 170: Reflection coefficient, powers, dissipated power ratios and absorption coefficient computed for a DB-modeled black PU 3D unit cell with a perfectly rigid inclusion.

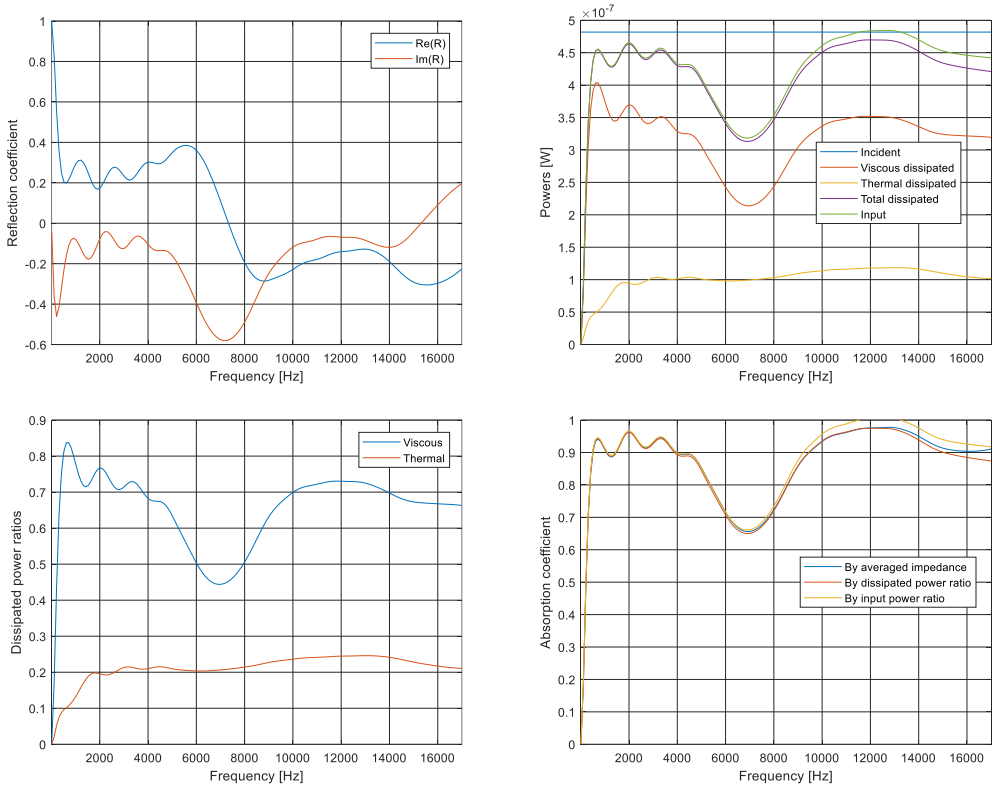

Figure 171: Reflection coefficient, powers, dissipated power ratios and absorption coefficient computed for a JCA-modeled melamine 3D unit cell with a perfectly rigid inclusion.

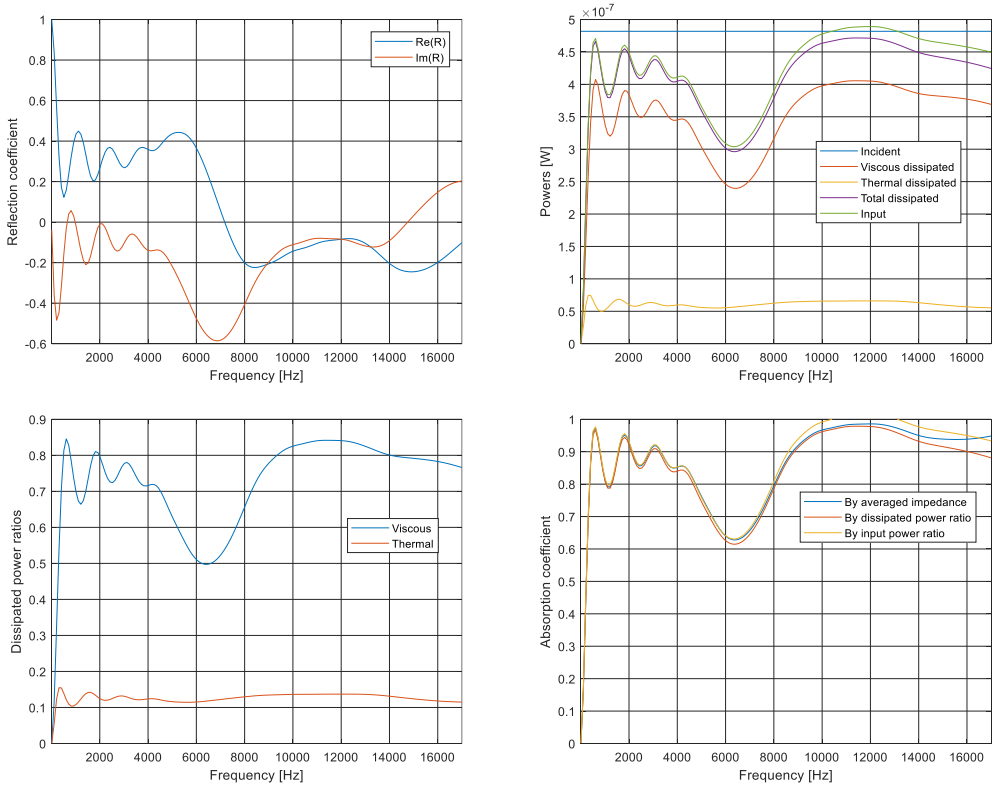

Figure 172: Reflection coefficient, powers, dissipated power ratios and absorption coefficient computed for a JCA-modeled black PU 3D unit cell with a perfectly rigid inclusion.

A.2.1. Unit cell dimensions design guidelines

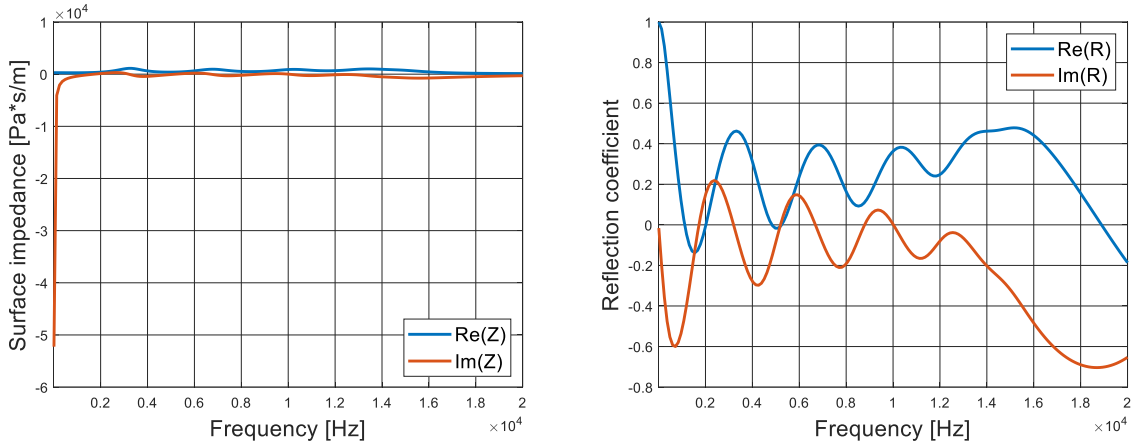

Figure 173: Surface impedance (on the left) and reflection coefficient (on the right) computed for a JCA-modeled melamine 3D unit cell with a perfectly rigid inclusion; dimension $= 0.008\ m$.

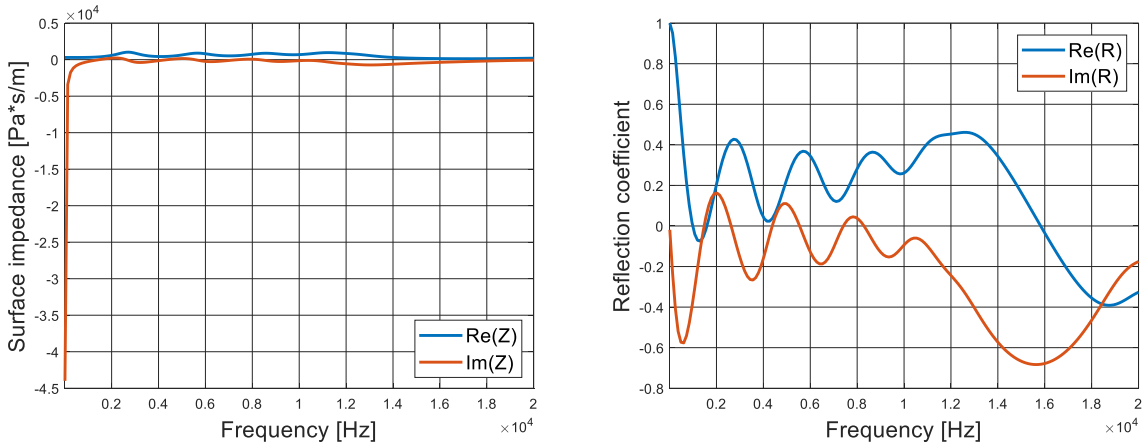

Figure 174: Surface impedance (on the left) and reflection coefficient (on the right) computed for a JCA-modeled melamine 3D unit cell with a perfectly rigid inclusion; dimension $= 0.0095\ m$.

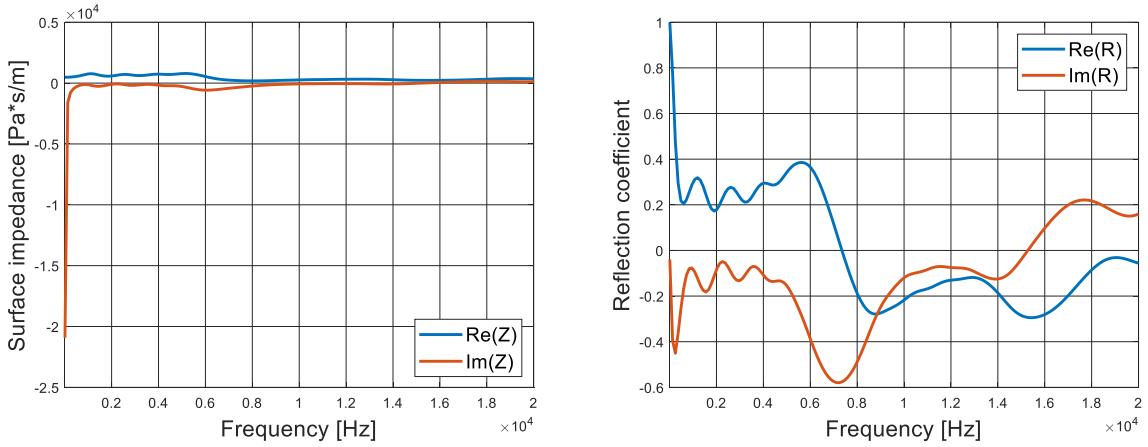

Figure 175: Surface impedance (on the left) and reflection coefficient (on the right) computed for a JCA-modeled melamine 3D unit cell with a perfectly rigid inclusion; dimension $= 0.02\ m$.

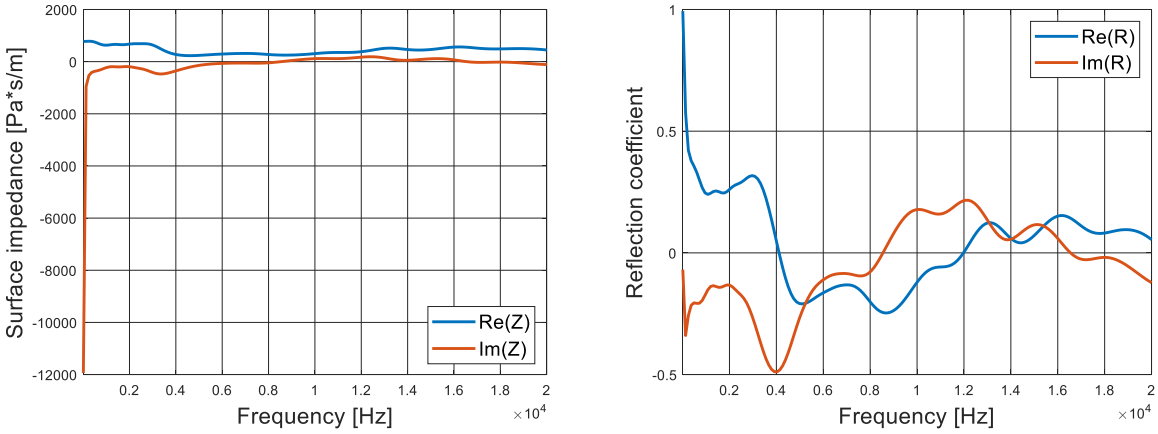

Figure 176: Surface impedance (on the left) and reflection coefficient (on the right) computed for a JCA-modeled melamine 3D unit cell with a perfectly rigid inclusion; dimension $= 0.035\ m$.

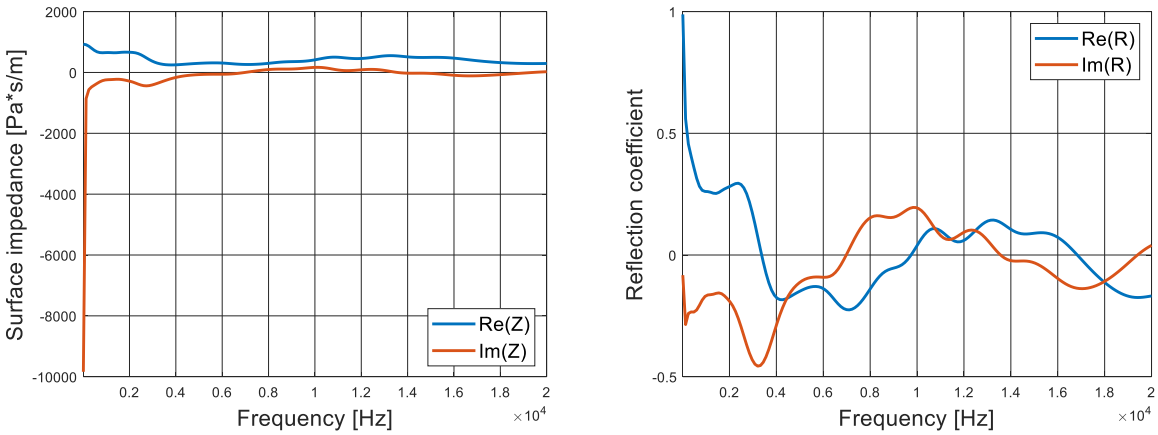

Figure 177: Surface impedance (on the left) and reflection coefficient (on the right) computed for a JCA-modeled melamine 3D unit cell with a perfectly rigid inclusion; dimension $= 0.0425\ m$.

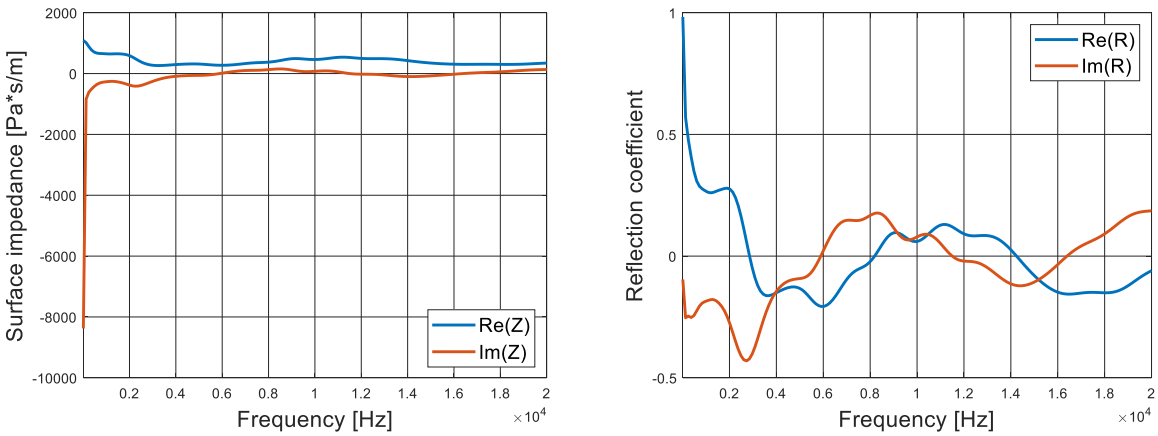

Figure 178: Surface impedance (on the left) and reflection coefficient (on the right) computed for a JCA-modeled melamine 3D unit cell with a perfectly rigid inclusion; dimension $= 0.05\ m$.

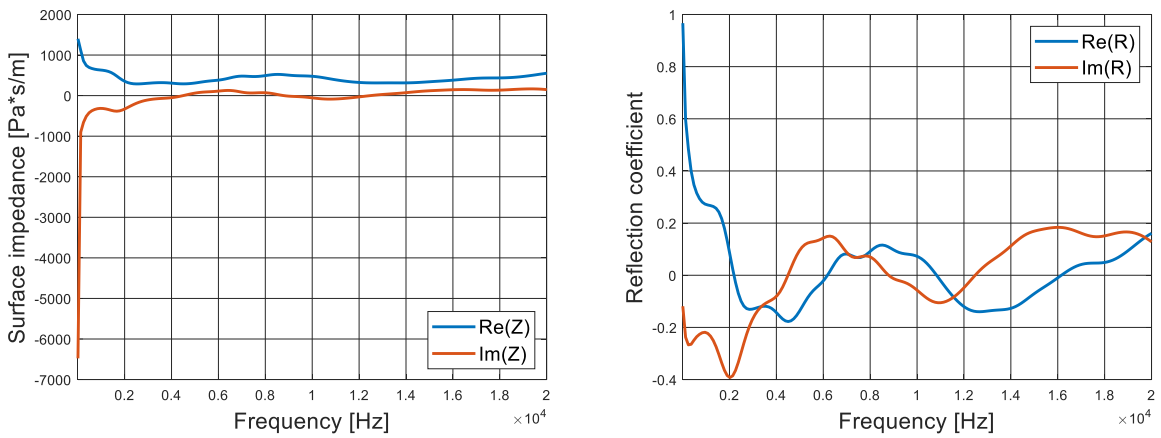

Figure 179: Surface impedance (on the left) and reflection coefficient (on the right) computed for a JCA-modeled melamine 3D unit cell with a perfectly rigid inclusion; dimension $= 0.065\ m$.

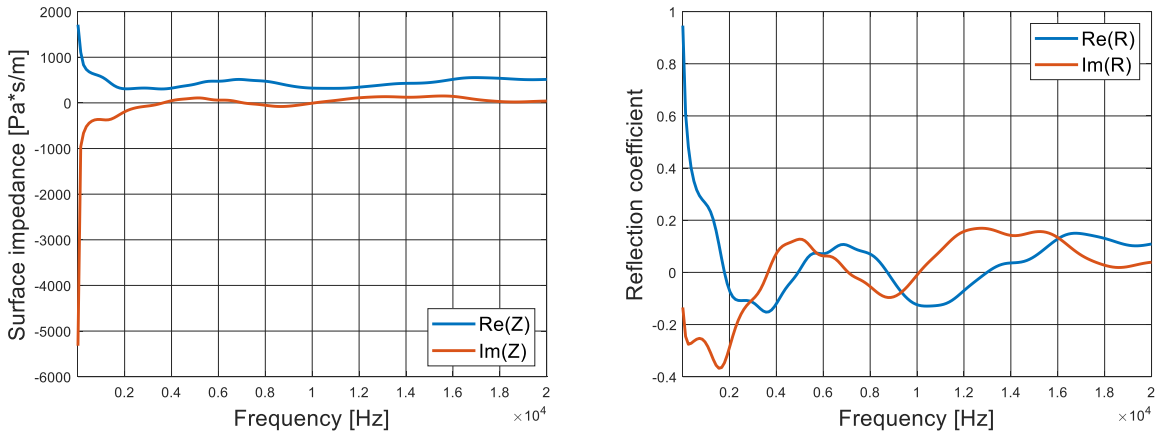

Figure 180: Surface impedance (on the left) and reflection coefficient (on the right) computed for a JCA-modeled melamine 3D unit cell with a perfectly rigid inclusion; dimension $= 0.08\ m$.

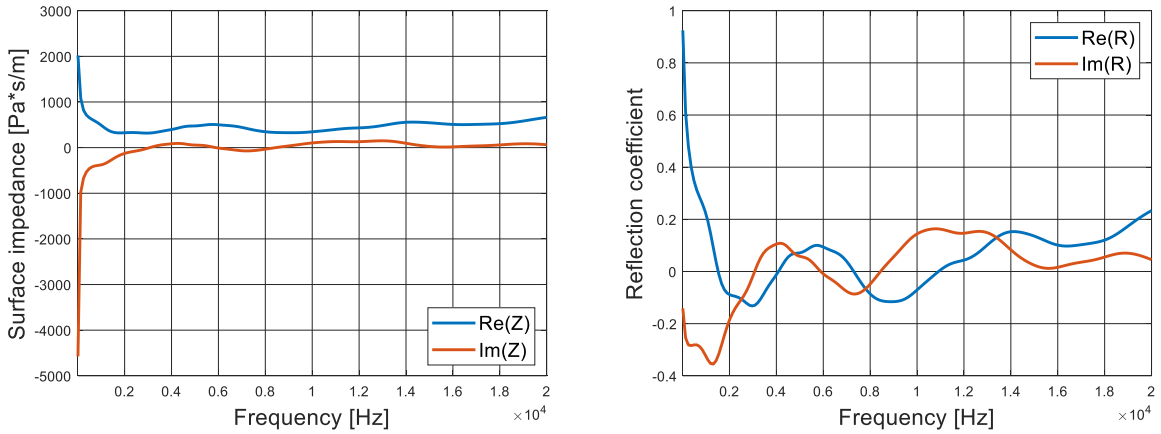

Figure 181: Surface impedance (on the left) and reflection coefficient (on the right) computed for a JCA-modeled melamine 3D unit cell with a perfectly rigid inclusion; dimension $= 0.095\ m$.

A.2.2. Foam airflow resistivity design guidelines

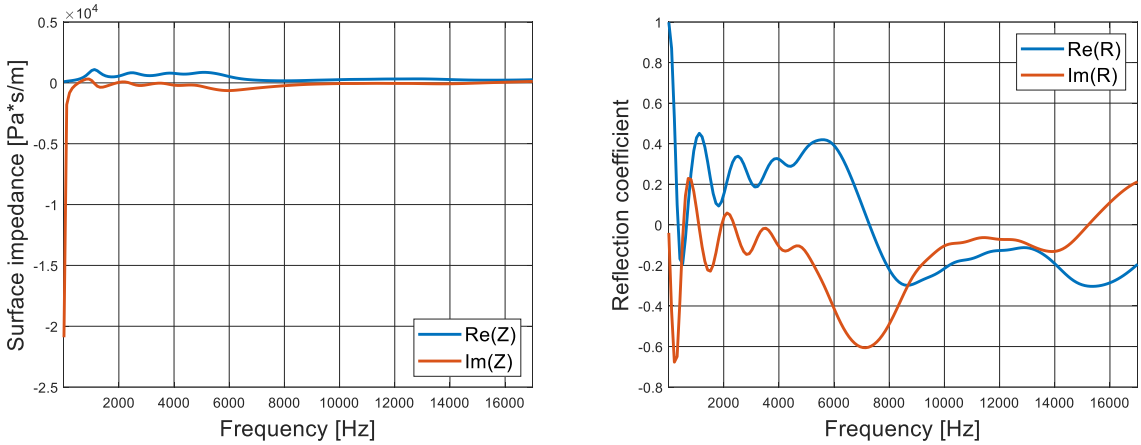

Figure 182: Surface impedance (on the left) and reflection coefficient (on the right) computed for a JCA-modeled melamine 3D unit cell with a perfectly rigid inclusion; $\sigma = 1000\ \frac{Pa*s}{m^2}$.

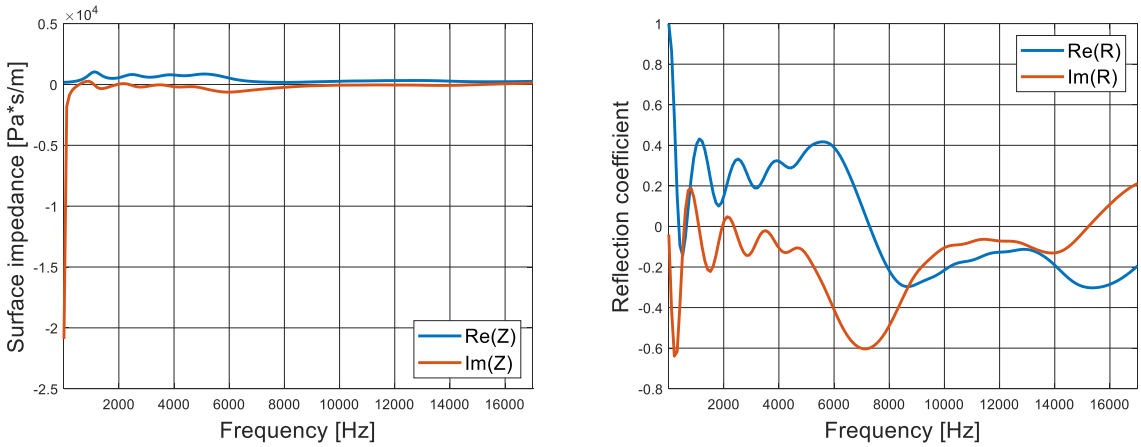

Figure 183: Surface impedance (on the left) and reflection coefficient (on the right) computed for a JCA-modeled melamine 3D unit cell with a perfectly rigid inclusion; $\sigma = 2500\ \frac{Pa*s}{m^2}$.

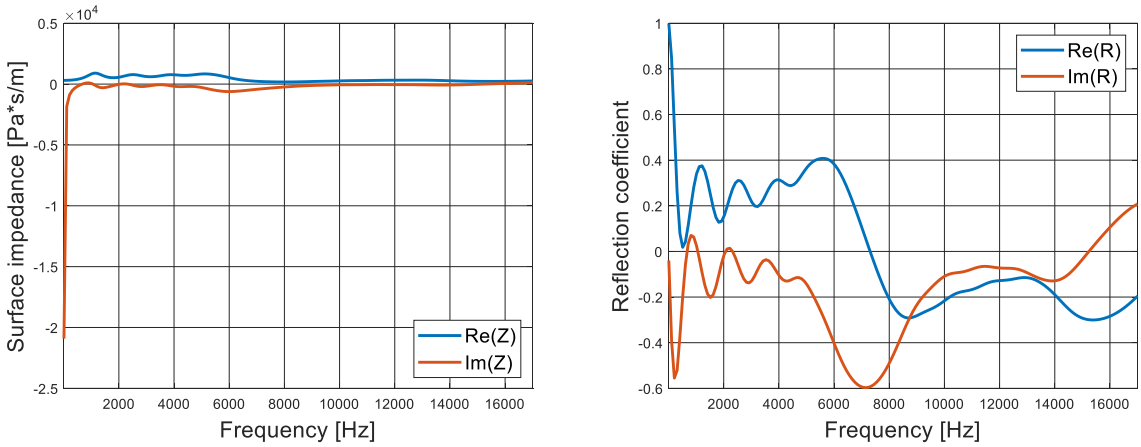

Figure 184: Surface impedance (on the left) and reflection coefficient (on the right) computed for a JCA-modeled melamine 3D unit cell with a perfectly rigid inclusion; $\sigma = 5000\ \frac{Pa*s}{m^2}$.

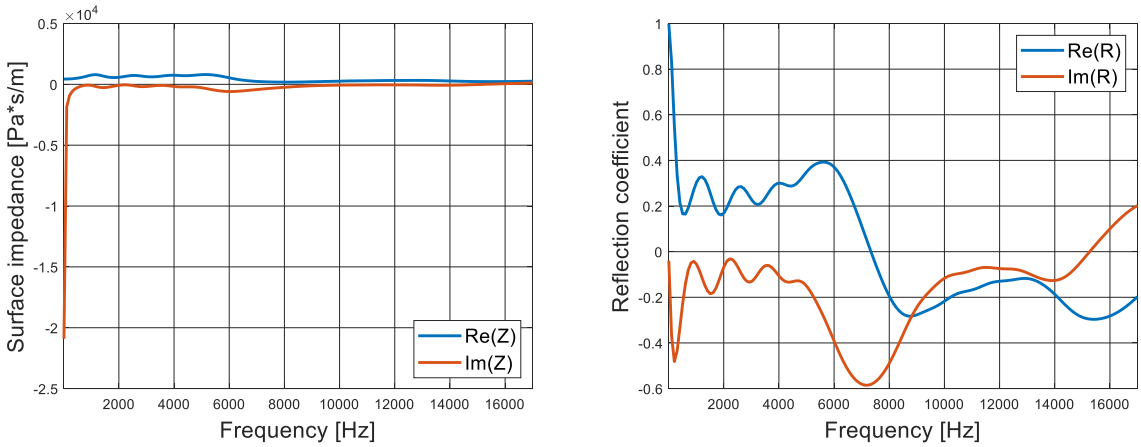

Figure 185: Surface impedance (on the left) and reflection coefficient (on the right) computed for a JCA-modeled melamine 3D unit cell with a perfectly rigid inclusion; $\sigma = 7500\ \frac{Pa*s}{m^2}$.

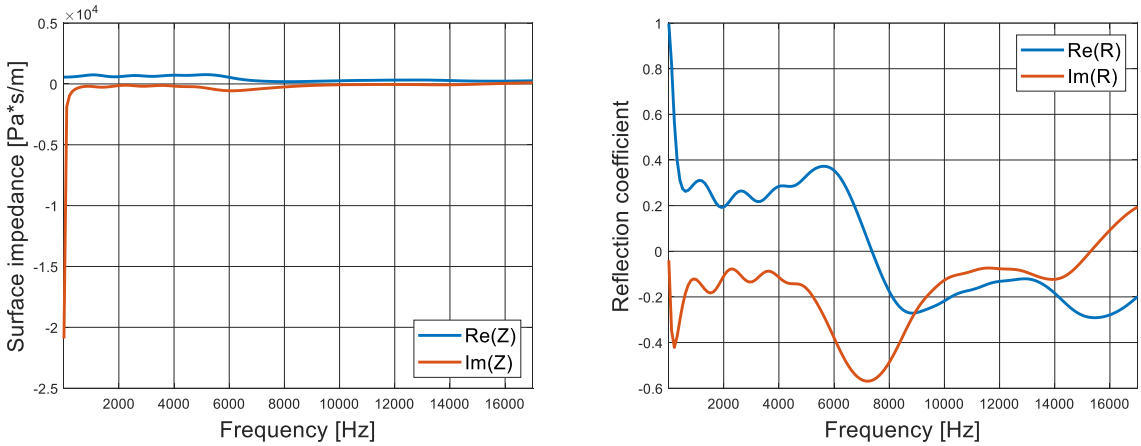

Figure 186: Surface impedance (on the left) and reflection coefficient (on the right) computed for a JCA-modeled melamine 3D unit cell with a perfectly rigid inclusion; $\sigma = 10000\ \frac{Pa*s}{m^2}$.

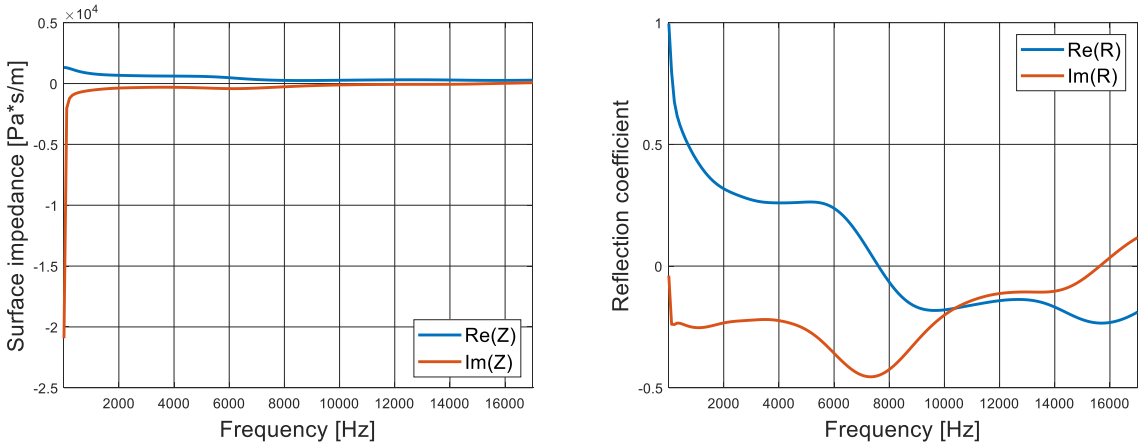

Figure 187: Surface impedance (on the left) and reflection coefficient (on the right) computed for a JCA-modeled melamine 3D unit cell with a perfectly rigid inclusion; $\sigma = 25000\ \frac{Pa*s}{m^2}$.

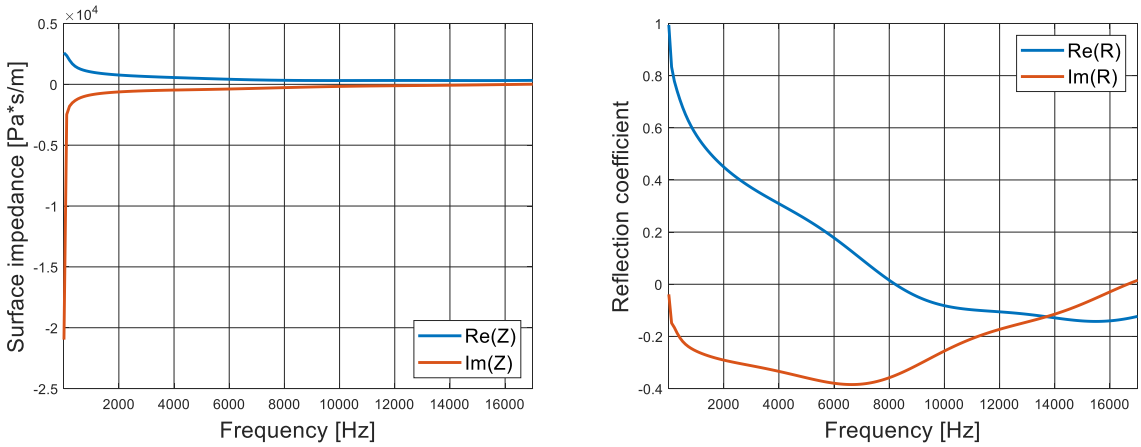

Figure 188: Surface impedance (on the left) and reflection coefficient (on the right) computed for a JCA-modeled melamine 3D unit cell with a perfectly rigid inclusion; $\sigma = 50000\ \frac{Pa*s}{m^2}$.

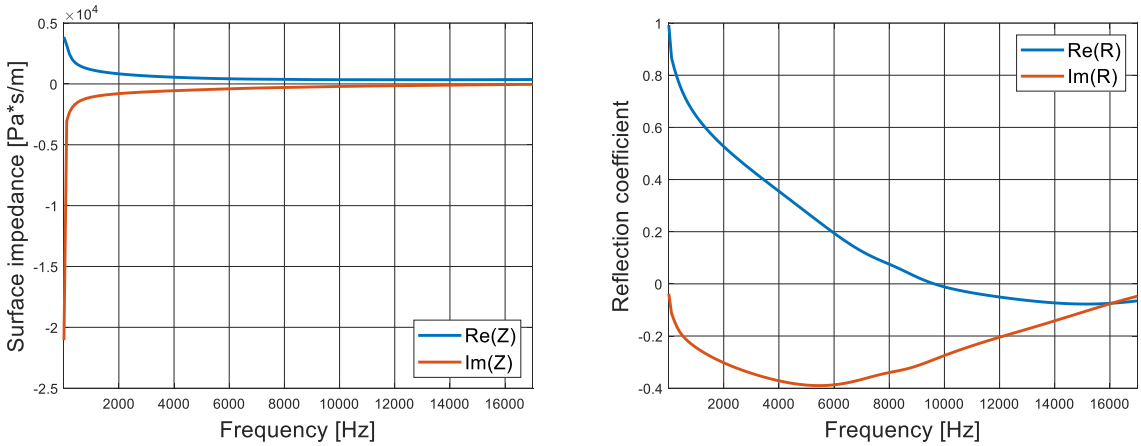

Figure 189: Surface impedance (on the left) and reflection coefficient (on the right) computed for a JCA-modeled melamine 3D unit cell with a perfectly rigid inclusion; $\sigma = 75000\ \frac{Pa*s}{m^2}$.

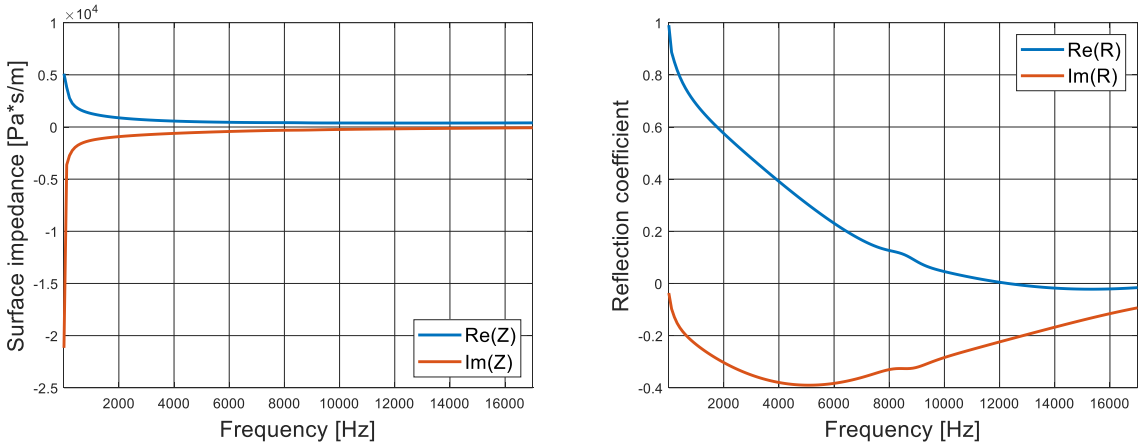

Figure 190: Surface impedance (on the left) and reflection coefficient (on the right) computed for a JCA-modeled melamine 3D unit cell with a perfectly rigid inclusion; $\sigma = 100000\ \frac{Pa*s}{m^2}$.

A.3. Transmission loss

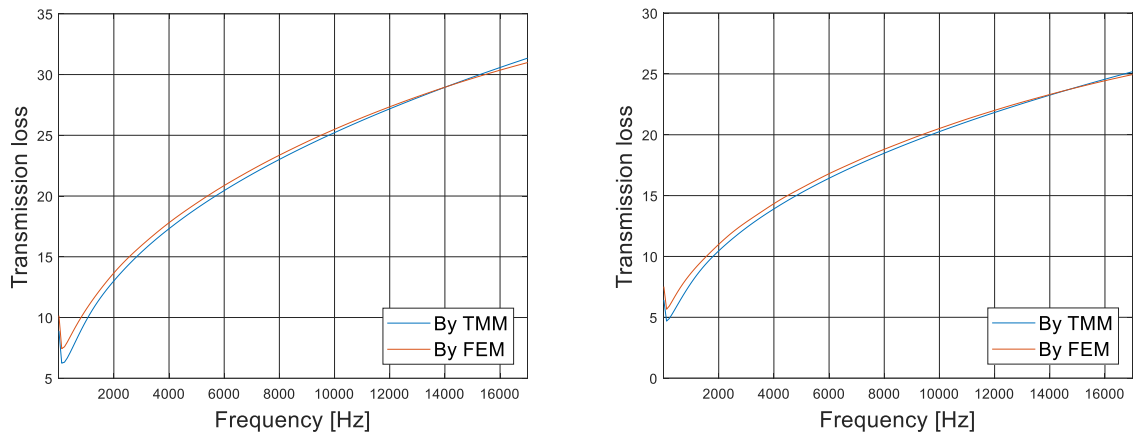

Figure 191: Transmission loss computed for a homogeneous DB-modeled melamine (on the left) and black PU (on the right) 2D unit cell.

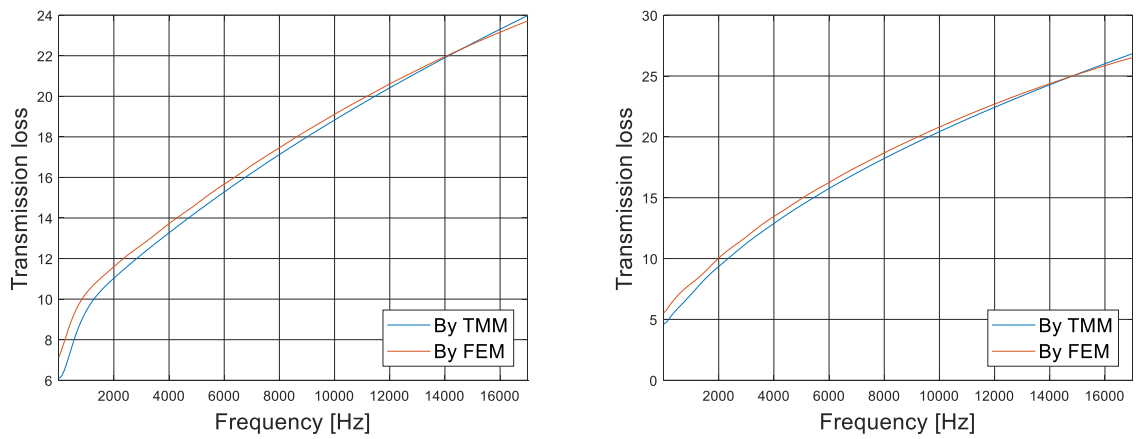

Figure 192: Transmission loss computed for a homogeneous JCA-modeled melamine (on the left) and black PU (on the right) 2D unit cell.

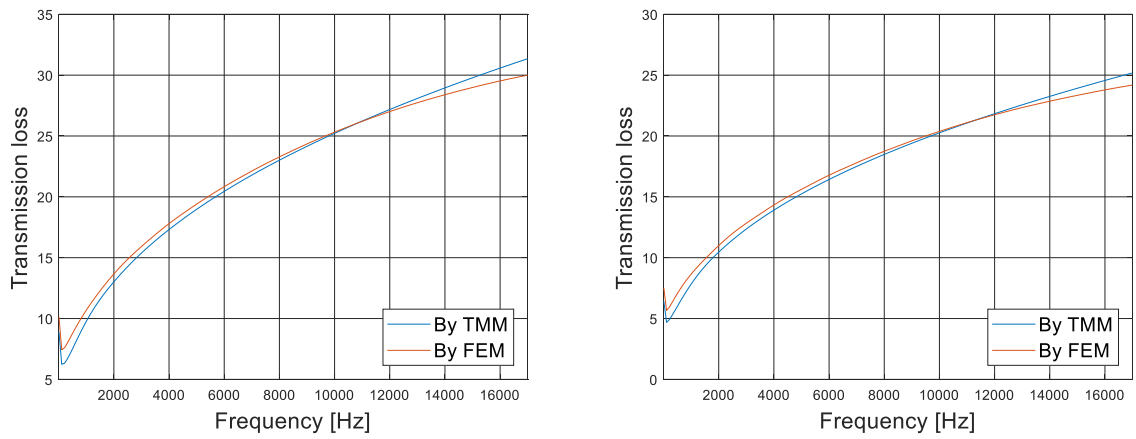

Figure 193: Transmission loss computed for a homogeneous DB-modeled melamine (on the left) and black PU (on the right) 3D unit cell.

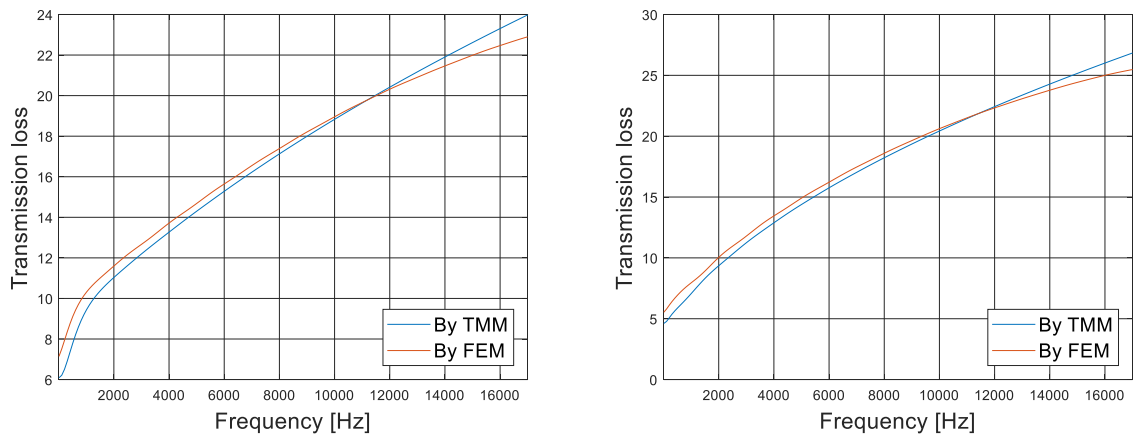

Figure 194: Transmission loss computed for a homogeneous JCA-modeled melamine (on the left) and black PU (on the right) 3D unit cell.

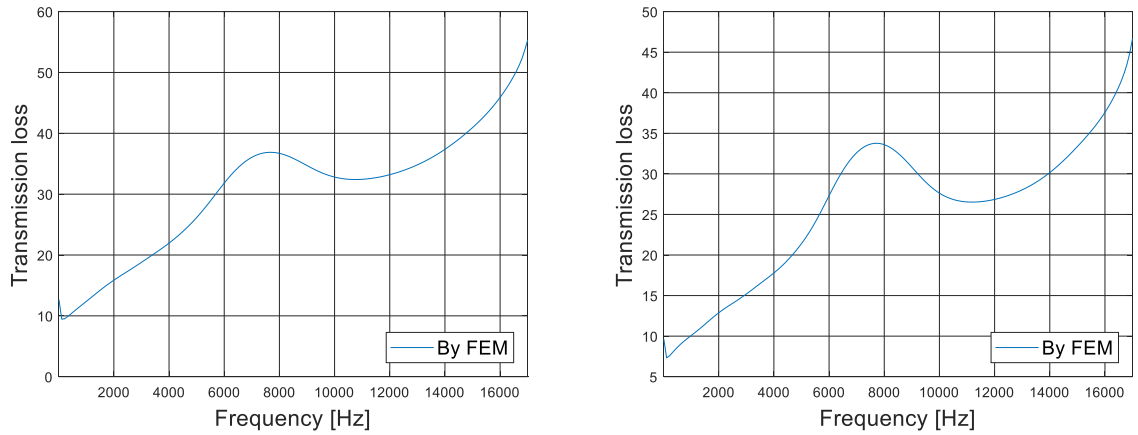

Figure 195: Transmission loss computed for a DB-modeled melamine (on the left) and black PU (on the right) 2D unit cell with a perfectly rigid inclusion.

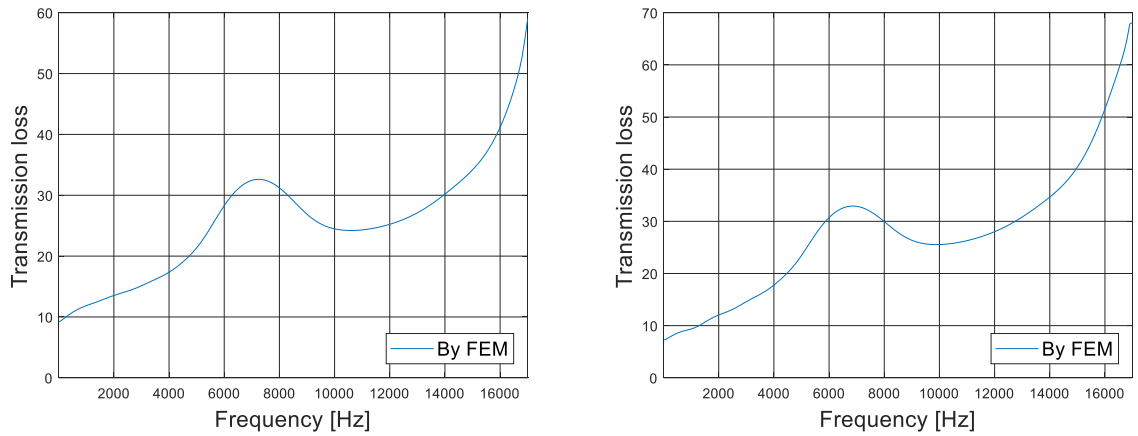

Figure 196: Transmission loss computed for a JCA-modeled melamine (on the left) and black PU (on the right) 2D unit cell with a perfectly rigid inclusion.

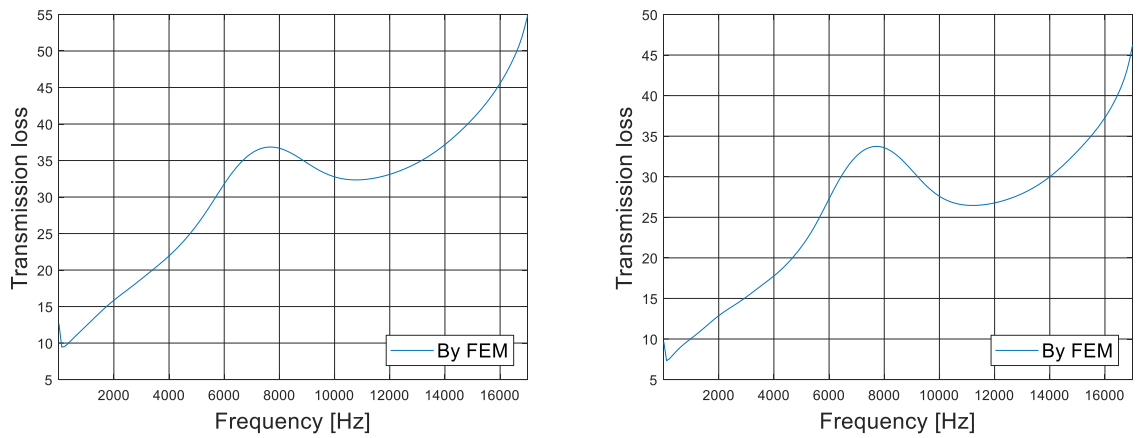

Figure 197: Transmission loss computed for a DB-modeled melamine (on the left) and black PU (on the right) 3D unit cell with a perfectly rigid inclusion.

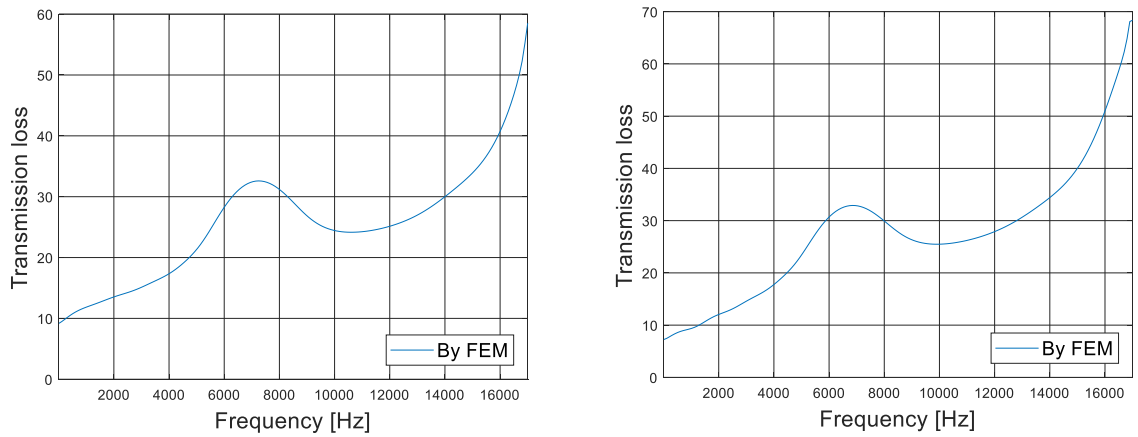

Figure 198: Transmission loss computed for a JCA-modeled melamine (on the left) and black PU (on the right) 3D unit cell with a perfectly rigid inclusion.

BIBLIOGRAPHY

[1] R. Liu, C. Ji, Z. Zhao, and T. Zhou, “Metamaterials: Reshape and Rethink,” *Engineering*, vol. 1, no. 2, pp. 179–184, 2015, doi: 10.15302/J-ENG-2015036.

[2] MarketsandMarkets, “Metamaterial Market: Analysis by Size, Growth, Trend and Forecast to 2025,” 2017.

[3] L. Cao, Q. Fu, Y. Si, B. Ding, and J. Yu, “Porous materials for sound absorption,” *Compos. Commun.*, vol. 10, pp. 25–35, 2018, doi: 10.1016/j.coco.2018.05.001.

[4] X. D. Zhao, Y. J. Yu, and Y. J. Wu, “Improving low-frequency sound absorption of micro-perforated panel absorbers by using mechanical impedance plate combined with Helmholtz resonators,” *Appl. Acoust.*, vol. 114, pp. 92–98, 2016, doi: 10.1016/j.apacoust.2016.07.013.

[5] C. Cai and C. M. Mak, “Noise attenuation capacity of a Helmholtz resonator,” *Adv. Eng. Softw.*, vol. 116, pp. 60–66, 2018, doi: 10.1016/j.advengsoft.2017.12.003.

[6] F. Yildiz, A. G. Parlar, Z. Parlar, and M. Bakkal, “Properties of sound panels made from recycled footwear treads,” *Acta Phys. Pol. A*, vol. 132, no. 3, pp. 936–940, 2017, doi: 10.12693/APhysPolA.132.936.

[7] L. Lv, J. Bi, C. Wei, X. Wang, Y. Cui, and H. Liu, “Effect of micro-slit plate structure on the sound absorption properties of discarded corn cob husk fiber,” *Fibers Polym.*, vol. 16, no. 7, pp. 1562–1567, 2015, doi: 10.1007/s12221-015-5002-x.

[8] U. Berardi and G. Iannace, “Acoustic characterization of natural fibers for sound absorption applications,” *Build. Environ.*, vol. 94, pp. 840–852, 2015, doi: 10.1016/j.buildenv.2015.05.029.

[9] X. Xinzhao, L. Guoming, L. Dongyan, S. Guoxin, and Y. Rui, “Electrically conductive graphene-coated polyurethane foam and its epoxy composites,” *Compos. Commun.*, vol. 7, pp. 1–6, 2018, doi: 10.1016/j.coco.2017.11.003.

[10] J. F. Allard and N. Atalla, *Propagation of Sound in Porous Media: Modelling Sound Absorbing Materials*, 2nd ed. Wiley, 2009.

[11] C. Boutin, “Acoustics of porous media with inner resonators,” *J. Acoust. Soc. Am.*, vol. 134, no. December 2013, pp. 4717–4729, 2015, doi: 10.1121/1.4824965.

[12] R. Rumpler, J.-F. Deü, and P. Göransson, “A modal-based reduction method for sound absorbing porous materials in poro-acoustic finite element models,” *J. Acoust. Soc. Am.*, vol. 132, no. 5, pp. 3162–3179, 2012, doi: 10.1121/1.4750496.

[13] R. Rumpler, P. Göransson, and J.-F. Deü, “A residue-based mode selection and sorting procedure for efficient poroelastic modeling in acoustic finite element applications,” *J. Acoust. Soc. Am.*, vol. 134, no. 6, pp. 4730–4741, 2013, doi: 10.1121/1.4824966.

[14] Z. Liu, R. Rumpler, and L. Feng, “Broadband locally resonant metamaterial sandwich plate for improved noise insulation in the coincidence region,” *Compos. Struct.*, vol. 200, no. May, pp. 165–172, 2018, doi: 10.1016/j.compstruct.2018.05.033.

[15] Z. Liu, R. Rumpler, and L. Feng, “Investigation of the sound transmission through a locally resonant metamaterial cylindrical shell in the ring frequency region,” *J. Appl. Phys.*, vol. 125, no. 11, 2019, doi: 10.1063/1.5081134.

[16] A. Khelif, P. A. Deymier, B. Djafari-Rouhani, J. O. Vasseur, and L. Dobrzynski, “Two-dimensional

phononic crystal with tunable narrow pass band: Application to a waveguide with selective frequency," *J. Appl. Phys.*, vol. 94, no. 3, pp. 1308–1311, 2003, doi: 10.1063/1.1557776.

[17] G. Palma, H. Mao, L. Burghignoli, P. Göransson, and U. Iemma, "Acoustic Metamaterials in Aeronautics," *Appl. Sci.*, vol. 8, no. 6, p. 971, 2018, doi: 10.3390/app8060971.

[18] M. Cinefra and G. Petrone, "SEA analysis in the cabin of a regional turboprop with metamaterial lining panels," in *AIAA SciTech Forum*, 2019, doi: 10.2514/6.2019-1806.

[19] I. Lopez Arteaga, R. E. A. Blom, N. B. Roozen, and H. Nijmeijer, "Modelling vibrations on deformed rolling tyres-a modal approach," *J. Sound Vib.*, vol. 307, no. 3–5, pp. 481–494, 2007, doi: 10.1016/j.jsv.2007.05.056.

[20] J. Carpentier, J. H. Thomas, C. Pézerat, C. Bailly, and A. Berry, "Comprehension of phenomena generating acoustic noise inside the passenger compartment of cars. Sources identification and simulation," in *ICSV 2016 - 23rd International Congress on Sound and Vibration: From Ancient to Modern Acoustics*, 2016.

[21] H. Hamdad, C. Pézerat, B. Gauvreau, C. Locqueteau, and P. De Gaillon, "Sensitivity analysis of model output for the prediction of vehicle pass-by noise," in *Automotive NVH Comfort*, 2016.

[22] H. Hamdad, C. Pézerat, B. Gauvreau, C. Locqueteau, and Y. Denoual, "Sensitivity analysis and propagation of uncertainty for the simulation of vehicle pass-by noise," *Appl. Acoust.*, vol. 149, pp. 85–98, 2019, doi: 10.1016/j.apacoust.2019.01.026.

[23] M. I. Fesina, A. V. Krasnov, and L. N. Gorina, "The Effectiveness of the Suppression of Low Frequency Acoustic Resonances with Porous Sound Absorbing Structures of Multifunctional Upholstery Materials of Car Body Interior," *Procedia Eng.*, vol. 176, pp. 159–168, 2017, doi: 10.1016/j.proeng.2017.02.284.

[24] Y. I. Bobrovnitskiĭ, K. D. Morozov, and T. M. Tomilina, "A periodic surface structure with extreme acoustic properties," *Acoust. Phys.*, vol. 56, no. 2, pp. 127–131, 2010, doi: 10.1134/S1063771010020016.

[25] K. V. Horoshenkov, "Innovative applications of materials for acoustic purposes," *Appl. Acoust.*, vol. 66, no. 6, pp. 603–605, 2005, doi: 10.1016/j.apacoust.2004.10.001.

[26] L. De Ryck *et al.*, "Acoustic wave propagation in a macroscopically inhomogeneous porous medium saturated by a fluid," *Appl. Phys. Lett.*, vol. 90, no. 18, pp. 2005–2008, 2007, doi: 10.1063/1.2431570.

[27] G. Pispola, K. V. Horoshenkov, and A. Khan, "Comparison of two modeling approaches for highly heterogeneous porous media," *J. Acoust. Soc. Am.*, vol. 121, no. 2, pp. 961–966, 2007, doi: 10.1121/1.2427114.

[28] N. ATALLA *et al.*, "Acoustic Absorption of Macro-Perforated Porous Materials," *J. Sound Vib.*, vol. 243, no. 4, pp. 659–678, 2001, doi: 10.1006/jsvi.2000.3435.

[29] C. Boutin, P. Royer, and J. L. Auriault, "Acoustic absorption of porous surfacing with dual porosity," *Int. J. Solids Struct.*, vol. 35, no. 34–35, pp. 4709–4737, 1998, doi: 10.1016/S0020-7683(98)00091-2.

[30] X. Olny and C. Boutin, "Acoustic wave propagation in double porosity media," *J. Acoust. Soc. Am.*, vol. 114, no. 1, pp. 73–89, 2003, doi: 10.1121/1.1534607.

[31] F. C. Sgard, X. Olny, N. Atalla, and F. Castel, "On the use of perforations to improve the sound absorption of porous materials," *Appl. Acoust.*, vol. 66, no. 6, pp. 625–651, 2005, doi: 10.1016/j.apacoust.2004.09.008.

[32] M. Seppi, “Numerical and analytical vibro-acoustic modelling of porous materials: the Cell Method for poroelasticity and the case of inclusions,” Università di Bologna (Italy), 2009.

[33] C. W. Zhou, J. P. Lainé, M. N. Ichchou, and A. M. Zine, “Wave finite element method based on reduced model for one-dimensional periodic structures,” *Int. J. Appl. Mech.*, vol. 7, no. 2, pp. 1–22, 2015, doi: 10.1142/S1758825115500180.

[34] J. M. Mencik and D. Duhamel, “A wave finite element-based approach for the modeling of periodic structures with local perturbations,” *Finite Elem. Anal. Des.*, vol. 121, pp. 40–51, 2016, doi: 10.1016/j.finel.2016.07.010.

[35] S. Ham and K. J. Bathe, “A finite element method enriched for wave propagation problems,” *Comput. Struct.*, vol. 94–95, pp. 1–12, 2012, doi: 10.1016/j.compstruc.2012.01.001.

[36] Q. Serra, M. N. Ichchou, and J. Deü, “Wave properties in poroelastic media using a Wave Finite Element Method,” *J. Sound Vib.*, vol. 335, pp. 125–146, 2015, doi: 10.1016/j.jsv.2014.09.022.

[37] Y. Fan, M. Collet, M. Ichchou, L. Li, O. Bareille, and Z. Dimitrijevic, “Enhanced wave and finite element method for wave propagation and forced response prediction in periodic piezoelectric structures,” *Chinese J. Aeronaut.*, vol. 30, no. 1, pp. 75–87, 2017, doi: 10.1016/j.cja.2016.12.011.

[38] J. M. Maeder and R. B. McQuistan, “Nearest neighbor lattice statistics on semi-infinite two-dimensional rectangular lattices of various widths,” *J. Math. Phys.*, vol. 30, no. 6, pp. 1380–1384, 1989, doi: 10.1063/1.528319.

[39] R. B. McQuistan and J. L. Hock, “Exact Composite Shift Operator Matrices for Two Dimensional Ising Lattices,” *Prog. Theor. Phys.*, vol. 81, no. 1, pp. 78–92, 1989.

[40] J. Li and R. B. McQuistan, “Thermodynamic properties of a two-dimensional nearest-neighbor interacting lattice gas,” *Physica A*, vol. 171, pp. 325–336, 1991.

[41] R. B. McQuistan and J. L. Hock, “The density of occupied nearest neighbor pairs on a rectangular 2× *N* lattice space,” *J. Math. Phys.*, vol. 27, no. 2, pp. 599–602, 1986, doi: 10.1063/1.527212.

[42] R. B. McQuistan and J. L. Hock, “Shift cell operator matrices for three-dimensional cubic-cell lattices,” *Physica A*, vol. 169, pp. 337–341, 1990.

[43] R. B. McQuistan and J. L. Hock, “The shift cell operator matrix method applied to the two-dimensional nearest and next nearest neighbor problem,” *J. Math. Chem.*, vol. 2, pp. 49–68, 1988.

[44] M. Collet, M. Ouisse, M. Ruzzene, and M. N. Ichchou, “Floquet-Bloch decomposition for the computation of dispersion of two-dimensional periodic, damped mechanical systems,” *Int. J. Solids Struct.*, vol. 48, no. 20, pp. 2837–2848, 2011, doi: 10.1016/j.ijsolstr.2011.06.002.

[45] A. Tayeb, M. Arfaoui, A. Zine, E. C. De Lyon, and A. Hamdi, “Modelling and identification of a class of hyperviscoelastic matherial behaviour,” in *DYNCOMP’2015*, 2015.

[46] T. Adel, M. Arfaoui, A. Zine, and E. C. De Lyon, “Identification of nonlinear viscoelastic model,” in *ATAVI, International Conference on Acoustics and Vibration*, 2016, doi: 10.13140/RG.2.1.3184.5529.

[47] N. Jridi *et al.*, “Separable finite viscoelasticity: integral-based models vs. experiments,” *Mech. Time-Dependent Mater.*, vol. 19, pp. 1–31, 2018, doi: 10.1007/s11043-018-9383-2.

[48] K. Billon *et al.*, “Design and experimental validation of a temperature-driven adaptive phononic crystal slab,” *Smart Mater. Struct.*, vol. 28, no. 3, pp. 1–23, 2019.

[49] M. Collet, “Adaptive Metacomposites : Material Programming for vibroacoustic control,” *1st Jt. Int. Symp. Syst. Intell. 2012*, pp. 179–182, 2012.

[50] M. I. Hussein, M. J. Leamy, and M. Ruzzene, “Dynamics of Phononic Materials and Structures: Historical Origins, Recent Progress, and Future Outlook,” *Appl. Mech.*, vol. 66, no. 4, 2014, doi: 10.1115/1.4026911.

[51] C. C. Claeys, P. Sas, and W. Desmet, “On the acoustic radiation efficiency of local resonance based stop band materials,” *J. Sound Vib.*, vol. 333, no. 14, pp. 3203–3213, 2014, doi: 10.1016/j.jsv.2014.03.019.

[52] C. Lagarrigue, J. P. Groby, V. Tournat, and O. Dazel, “Absorption of sound by porous layers with embedded periodic arrays of resonant inclusions,” *Acoust. Soc. Am. Artic.*, vol. 134, no. 4670, 2013, doi: 10.1121/1.4824843.

[53] M. A. Lewińska, J. A. W. van Dommelen, V. G. Kouznetsova, and M. G. D. Geers, “Towards acoustic metafoams: the enhanced performance of a poroelastic material with local resonators,” *J. Mech. Phys. Solids*, 2018, doi: 10.1016/j.jmps.2018.10.006.

[54] Y. F. Wang, J. W. Liang, A. L. Chen, Y. S. Wang, and V. Laude, “Wave propagation in one-dimensional fluid-saturated porous metamaterials,” *Phys. Rev. B*, vol. 99, no. 13, pp. 1–9, 2019, doi: 10.1103/PhysRevB.99.134304.

[55] Y. F. Wang, Y. S. Wang, and V. Laude, “Wave propagation in two-dimensional viscoelastic metamaterials,” *Phys. Rev. B - Condens. Matter Mater. Phys.*, vol. 92, no. 10, pp. 1–14, 2015, doi: 10.1103/PhysRevB.92.104110.

[56] B.-L. Su, C. Sanchez, and X.-Y. Yang, *Hierarchically Structured Porous Materials: From Nanoscience to Catalysis, Separation, Optics, Energy, and Life Science*. 2011.

[57] V. M. Starov and V. G. Zhdanov, “Effective viscosity and permeability of porous media,” *Colloids Surfaces A Physicochem. Eng. Asp.*, vol. 192, pp. 363–375, 2001.

[58] N. Gao and H. Hou, “Low frequency acoustic properties of a honeycomb-silicone rubber acoustic metamaterial,” *Mod. Phys. Lett. B*, vol. 31, no. 11, p. 1750118, 2017, doi: 10.1142/S0217984917501184.

[59] O. Doutres, N. Atalla, and K. Dong, “Effect of the microstructure closed pore content on the acoustic behavior of polyurethane foams,” *J. Appl. Phys.*, vol. 110, no. 6, 2011, doi: 10.1063/1.3631021.

[60] I. Chekkal, M. Bianchi, C. Remillat, F. X. Bécot, L. Jaouen, and F. Scarpa, “Vibro-acoustic properties of auxetic open Cell foam: Model and experimental results,” *Acta Acust. united with Acust.*, vol. 96, no. 2, pp. 266–274, 2010, doi: 10.3813/AAA.918276.

[61] I. Chekkal, C. Remillat, and F. Scarpa, “Acoustic properties of auxetic foams,” *WIT Trans. Built Environ.*, vol. 124, pp. 119–129, 2012, doi: 10.2495/HPSM120111.

[62] E. Deckers, S. Jonckheere, and D. Vandepitte, “Modelling Techniques for Vibro-Acoustic Dynamics of Poroelastic Materials,” *Arch Comput. Methods Eng*, no. 22, pp. 183–236, 2015, doi: 10.1007/s11831-014-9121-0.

[63] F.-X. Bécot and L. Jaouen, “An alternative Biot’s formulation for dissipative porous media with skeleton deformation,” *J. Acoust. Soc. Am.*, vol. 134, no. 6, pp. 4801–4807, 2013, doi: 10.1121/1.4826175.

[64] M. a Biot, “Mechanics of Deformation and Acoustic Propagation in Porous Media,” *J. Appl. Physiscs*, vol. 33, no. 4, pp. 1482–1498, 1962, doi: 10.1063/1.1728759.

[65] E. Detournay and A. H.-D. Cheng, “Fundamentals of Poroelasticity,” in *Comprehensive Rock Engineering: Principles, Practice and Projects*, vol. II, 1993, pp. 113–171.

[66] G. Ma *et al.*, “Polarization bandgaps and fluid-like elasticity in fully solid elastic metamaterials,” *Nat. Commun.*, vol. 7, 2016, doi: 10.1038/ncomms13536.

[67] C. Perrot, F. Chevillotte, L. Jaouen, and M. T. Hoang, “Acoustics properties and applications, in Metallic Foams: Fundamentals and Applications,” in *NEW BOOK ON METAL FOAM*, 2013, pp. 285–316.

[68] M. R. Stinson, “The propagation of plane sound waves in narrow and wide circular tubes, and generalization to uniform tubes of arbitrary cross-sectional shape,” *J. Acoust. Soc. Am.*, vol. 89, no. 2, pp. 550–558, 1991.

[69] M. E. Delany and E. N. Bazley, “Acoustical properties o f fibrous absorbent materials,” *Appl. Acoust.*, no. 3, 1969.

[70] Y. Miki, “Acoustical properties of porous materials-Modifications of Delany-Bazley models,” *J. Acoust. Soc. Jpn.(E)*, vol. 11, no. 1, pp. 19–24, 1990, doi: 10.1250/ast.11.19.

[71] D. L. Johnson, J. Koplik, and R. Dashen, “Theory of dynamic permeability and tortuosity in fluid-saturated porous media,” *J. Fluid Mech.*, vol. 176, no. 1, p. 379, 1987, doi: 10.1017/S0022112087000727.

[72] Y. Champoux and J. F. Allard, “Dynamic tortuosity and bulk modulus in air-saturated porous media,” *J. Appl. Phys.*, vol. 70, no. 4, pp. 1975–1979, 1991, doi: 10.1063/1.349482.

[73] D. Lafarge, P. Lemarinier, J. F. Allard, and V. Tarnow, “Dynamic compressibility of air in porous structures at audible frequencies,” *J. Acoust. Soc. Am.*, vol. 102, no. 4, pp. 1995–2006, 1997, doi: 10.1121/1.419690.

[74] D. J. Mead and S. Parthan, “Free Wave Propagation in Two-Dimensional Plates,” *J. Sound Vib.*, vol. 64, no. 3, pp. 325–348, 1979.

[75] N. Atalla, R. Panneton, and P. Debergue, “A mixed displacement-pressure formulation for poroelastic materials,” *J. Acoust. Soc. Am.*, vol. 104, no. 3, pp. 1444–1452, 2002, doi: 10.1121/1.424355.

[76] G. Gosse, C. Pezerat, and F. Bessac, “Periodic assembly of multi-coupled parallel plates: vibration propagation and acoustic radiation,” in *16th International Congress on Sound and Vibration 2009, ICSV 2009*, 2009, vol. 5, pp. 3019–3026.

[77] Y. Yang, B. R. Mace, and M. J. Kingan, “Wave and finite element method for predicting sound transmission through finite multi-layered structures with fluid layers,” *Comput. Struct.*, vol. 204, pp. 20–30, 2018, doi: 10.1016/j.compstruc.2018.04.003.

[78] T. Weisser *et al.*, “Acoustic behavior of a rigidly backed poroelastic layer with periodic resonant inclusions by a multiple scattering approach,” *J. Acoust. Soc. Am.*, vol. 139, no. 2, pp. 617–629, 2016, doi: 10.1121/1.4940669.

[79] M. Gaborit, O. Dazel, and P. Göransson, “A simplified model for thin acoustic screens,” *J. Acoust. Soc. Am.*, vol. 144, no. 1, pp. 76–81, 2018, doi: 10.1121/1.5047929.

[80] J.-P. Groby, A. Wirgin, L. De Ryck, W. Lauriks, R. P. Gilbert, and Y. S. Xu, “Acoustic response of a rigid-frame porous medium plate with a periodic set of inclusions,” *J. Acoust. Soc. Am.*, vol.

126, no. 2, pp. 685–693, 2009, doi: 10.1121/1.3158936.

[81] L. Xiong, B. Nennig, Y. Aurégan, and W. Bi, “Sound attenuation optimization using metaporous materials tuned on exceptional points,” *J. Acoust. Soc. Am.*, vol. 142, no. 4, pp. 2288–2297, 2017, doi: 10.1121/1.5007851.

[82] R. W. Wood, “A suspected case of the electrical resonance of minute metal particles for light-waves. A new type of absorption,” *Proc. Phys. Soc. London*, vol. 18, no. 1, pp. 166–182, 1901, doi: 10.1088/1478-7814/18/1/313.

[83] B. Budiansky, “On the elastic moduli of some heterogeneous materials,” *J. Mech. Phys. Solids*, vol. 13, no. 4, pp. 223–227, 1965, doi: 10.1016/0022-5096(65)90011-6.

[84] Z. Hashin and S. Shtrikman, “A variational approach to the theory of the elastic behaviour of multiphase materials,” *J. Mech. Phys. Solids*, vol. 11, no. 2, pp. 127–140, 1963, doi: 10.1016/0022-5096(63)90060-7.

[85] J. J. Cuomo, J. F. Ziegler, and J. M. Woodall, “A new concept for solar energy thermal conversion,” *Appl. Phys. Lett.*, vol. 26, no. 10, pp. 557–559, 1975, doi: 10.1063/1.87990.

[86] C. M. Horwitz, “Solar-Selective Globular Metal Films.,” *J Opt Soc Am*, vol. 68, no. 8, pp. 1032–1038, 1978, doi: 10.1364/JOSA.68.001032.

[87] J. P. Groby and A. Wirgin, “Seismic motion in urban sites consisting of blocks in welded contact with a soft layer overlying a hard half-space,” *Geophys. J. Int.*, vol. 172, no. 2, pp. 725–758, 2008, doi: 10.1111/j.1365-246X.2007.03678.x.

[88] A. Khelif, B. Djafari-Rouhani, V. Laude, and M. Solal, “Coupling characteristics of localized phonons in photonic crystal fibers,” *J. Appl. Phys.*, vol. 94, no. 12, pp. 7944–7946, 2003, doi: 10.1063/1.1627946.

[89] V. Laude, M. Wilm, S. Benchabane, and A. Khelif, “Full band gap for surface acoustic waves in a piezoelectric phononic crystal,” *Phys. Rev. E - Stat. Nonlinear, Soft Matter Phys.*, vol. 71, no. 3, pp. 1–7, 2005, doi: 10.1103/PhysRevE.71.036607.

[90] C. Kittel and H. Y. Fan, *Introduction to Solid State Physics*. 1956.

[91] F. Farzbod, “Analysis of Bloch Formalism In Undamped And Damped Periodic Structures,” Georgia Institute of Technology, 2010.

[92] Floquet and Gaston, “Sur les équations différentielles linéaires à coefficients périodiques,” *Ann. Sci. l’École Norm. Supérieure*, vol. 12, no. 2, pp. 47–88, 1883.

[93] N. Bombace, “Dynamic Adaptive Concurrent Multi-Scale Simulation of Wave Propagation in 3D Media,” University of Oxford A, 2018.

[94] P. G. García and J.-P. Fernández-Álvarez, “Floquet-Bloch Theory and Its Application to the Dispersion Curves of Nonperiodic Layered Systems,” *Math. Probl. Eng.*, vol. 2015, 2015, doi: 10.1155/2015/475364, 10.1155/2015/475364.

[95] V. Laude, J. M. Escalante, and A. Martínez, “Effect of loss on the dispersion relation of photonic and phononic crystals,” *Phys. Rev. B - Condens. Matter Mater. Phys.*, vol. 88, no. 22, pp. 1–8, 2013, doi: 10.1103/PhysRevB.88.224302.

[96] A. Vaziri Astaneh and M. N. Guddati, “Dispersion analysis of composite acousto-elastic waveguides,” *Compos. Part B Eng.*, vol. 130, pp. 200–216, 2017, doi: 10.1016/j.compositesb.2017.07.040.

[97] A. Bensoussan, J. L. Lions, and G. Papanicolaou, “Asymptotic Analysis of Periodic Structures,”

Stud. Math. its Appl., vol. 5, 1978.

[98] L. Gavric, “Computation of Propagative Waves,” *J. Sound Vib.*, vol. 185, no. 3, pp. 531–543, 1995.

[99] T. Hayashi, W. J. Song, and J. L. Rose, “Guided wave dispersion curves for a bar with an arbitrary cross-section, a rod and rail example,” *Ultrasonics*, vol. 41, no. 3, pp. 175–183, 2003, doi: 10.1016/S0041-624X(03)00097-0.

[100] V. Damljanović and R. L. Weaver, “Propagating and evanescent elastic waves in cylindrical waveguides of arbitrary cross section,” *J. Acoust. Soc. Am.*, vol. 115, no. 4, pp. 1572–1581, 2004, doi: 10.1121/1.1687424.

[101] I. Bartoli, A. Marzani, F. Lanza di Scalea, and E. Viola, “Modeling wave propagation in damped waveguides of arbitrary cross-section,” *J. Sound Vib.*, vol. 295, no. 3–5, pp. 685–707, 2006, doi: 10.1016/j.jsv.2006.01.021.

[102] S. Finnveden, “Evaluation of modal density and group velocity by a finite element method,” *J. Sound Vib.*, vol. 273, no. 1–2, pp. 51–75, 2004, doi: 10.1016/j.jsv.2003.04.004.

[103] D. Duhamel, “Finite element computation of Green’s functions,” *Eng. Anal. Bound. Elem.*, vol. 31, no. 11, pp. 919–930, 2007, doi: 10.1016/j.enganabound.2007.04.002.

[104] B. R. Mace and E. Manconi, “Modelling wave propagation in two-dimensional structures using finite element analysis,” *J. Sound Vib.*, vol. 318, no. 4–5, pp. 884–902, 2008, doi: 10.1016/j.jsv.2008.04.039.

[105] K. Billon, “Composites périodiques fonctionnels pour l’absorption vibroacoustique large bande,” Université de Franche-Comté (France), 2017.

[106] A. Salih, “Weighted Residual Methods,” in *Handbook of Differential Equations*, 2016, pp. 699–702.

[107] R. P. Moiseyenko and V. Laude, “Material loss influence on the complex band structure and group velocity in phononic crystals,” *Phys. Rev. B - Condens. Matter Mater. Phys.*, vol. 83, no. 6, pp. 1–6, 2011, doi: 10.1103/PhysRevB.83.064301.

[108] O. Umnova, K. Attenborough, and C. M. Linton, “Effects of porous covering on sound attenuation by periodic arrays of cylinders,” *J. Acoust. Soc. Am.*, vol. 119, no. 1, pp. 278–284, 2006, doi: 10.1121/1.2133715.

[109] O. Robin, A. Berry, O. Doutres, and N. Atalla, “Measurement of the absorption coefficient of sound absorbing materials under a synthesized diffuse acoustic field,” *J. Acoust. Soc. Am.*, vol. 136, no. 1, pp. 13–19, 2014, doi: 10.1121/1.4881321.

[110] J.-P. Groby, A. Duclos, O. Dazel, L. Boeckx, and W. Lauriks, “Absorption of a rigid frame porous layer with periodic circular inclusions backed by a periodic grating,” *J. Acoust. Soc. Am.*, vol. 129, no. 5, pp. 3035–3046, 2011, doi: 10.1121/1.3561664.

[111] T. Frenzel, M. Kadic, and M. Wegener, “Three-dimensional mechanical metamaterials with a twist,” *Science (80-.).*, vol. 358, no. 6366, pp. 1072–1074, 2017, doi: 10.1126/science.aao4640.

[112] M. Ouisse, M. Ichchou, S. Chedly, and M. Collet, “On the sensitivity analysis of porous material models,” *J. Sound Vib.*, vol. 331, no. 24, pp. 5292–5308, 2012, doi: 10.1016/j.jsv.2012.07.018.

[113] J.-P. Groby, W. Lauriks, and T. E. Vigran, “Total absorption peak by use of a rigid frame porous layer backed by a rigid multi-irregularities grating.,” *J. Acoust. Soc. Am.*, vol. 127, no. 5, pp.

2865–2874, 2010, doi: 10.1121/1.3508576.

[114] O. Dazel, F. Sgard, F.-X. Becot, and N. Atalla, “Expressions of dissipated powers and stored energies in poroelastic media modeled by {u,U} and {u,P} formulations,” *J. Acoust. Soc. Am.*, vol. 123, no. 4, pp. 2054–2063, 2008, doi: 10.1121/1.2874520.

[115] F. Sgard, F. Castel, and N. Atalla, “Use of a hybrid adaptive finite element/modal approach to assess the sound absorption of porous materials with meso-heterogeneities,” *Appl. Acoust.*, vol. 72, no. 4, pp. 157–168, 2011, doi: 10.1016/j.apacoust.2010.10.011.

[116] K. Kosała, “Calculation models for analysing the sound insulating properties of homogeneous single baffles used in vibroacoustic protection,” *Appl. Acoust.*, vol. 146, pp. 108–117, 2019, doi: 10.1016/j.apacoust.2018.11.012.

[117] K. Verdiere, R. Panneton, S. Elkoun, T. Dupont, and P. Leclaire, “Transfer matrix method applied to the parallel assembly of sound absorbing materials,” *J. Acoust. Soc. Am.*, vol. 134, no. 6, pp. 4648–4658, 2013, doi: 10.1121/1.4824839.

[118] O. Doutres, Y. Salissou, N. Atalla, and R. Panneton, “Evaluation of the acoustic and non-acoustic properties of sound absorbing materials using a three-microphone impedance tube,” *Appl. Acoust.*, vol. 71, no. 6, pp. 506–509, 2010, doi: 10.1016/j.apacoust.2010.01.007.

[119] Z. Liu, R. Rumpler, and L. Feng, “Locally resonant metamaterial curved double wall to improve sound insulation at the ring frequency and mass-spring-mass resonance,” *J. Sound Vib.*, 2019.

[120] A. Madeo, M. Collet, M. Miniaci, K. Billon, M. Ouisse, and P. Neff, “Modeling phononic crystals via theweighted relaxed micromorphic model with free and gradient micro-inertia,” *J. Elast.*, vol. 130, no. 1, pp. 59–83, 2018, doi: 10.1007/s10659-017-9633-6.

[121] C. Boutin, S. Hans, and A. Rallu, “On inner resonance in elastic composites Design of media with negative mass or stiffness.”

[122] C. Goffaux and J. Vigneron, “Theoretical study of a tunable phononic band gap system,” *Phys. Rev. B*, vol. 64, 2001, doi: 10.1103/PhysRevB.64.075118.

[123] N. Atalla, *NOVAFEM User’s guide*. Sherbrooke (QC, Canada): Université de Sherbrooke, 2017.

[124] E. Gourdon and M. Seppi, “On the use of porous inclusions to improve the acoustical response of porous materials: Analytical model and experimental verification,” *Appl. Acoust.*, vol. 71, no. 4, pp. 283–298, 2010, doi: 10.1016/j.apacoust.2009.11.004.

[125] O. Doutres, M. Ouisse, N. Atalla, and M. Ichchou, “Impact of the irregular microgeometry of polyurethane foam on the macroscopic acoustic behavior predicted by a unit-cell model,” *J. Acoust. Soc. Am.*, vol. 136, no. 4, pp. 1666–1681, 2014, doi: 10.1121/1.4895695.

[126] A. Peiffer, “Full frequency vibro-acoustic simulation in the aeronautics industry,” in *Isma2016*, 2016.

[127] A. Mohanty and S. Fatima, “An overview of automobile noise and vibration control,” *Noise Notes*, vol. 13, no. 1, pp. 43–56, 2014, doi: 10.1260/1475-4738.13.1.43.

[128] K. Idrisi, M. E. Johnson, D. Theurich, and J. P. Carneal, “A study on the characteristic behavior of mass inclusions added to a poro-elastic layer,” *J. Sound Vib.*, vol. 329, no. 20, pp. 4136–4148, 2010, doi: 10.1016/j.jsv.2010.04.001.

[129] C. Lagarrigue, J. P. Groby, O. Dazel, and V. Tournat, “Design of metaporous supercells by genetic algorithm for absorption optimization on a wide frequency band,” *Appl. Acoust.*, vol. 102, pp. 49–54, 2016, doi: 10.1016/j.apacoust.2015.09.011.

[130] R. Al Jahdali, Y. Wu, R. Al Jahdali, and Y. Wu, “Coupled Resonators for Sound Trapping and Absorption,” *Sci. Rep.*, vol. 8, no. 1, pp. 1–8, 2018, doi: 10.1038/s41598-018-32135-5.

[131] A. Alevizaki, R. Sainidou, P. Rembert, B. Morvan, and N. Stefanou, “Phononic crystals of poroelastic spheres,” *Phys. Rev. B - Condens. Matter Mater. Phys.*, vol. 94, no. 17, 2016, doi: 10.1103/PhysRevB.94.174306.

[132] X. An, H. Fan, and C. Zhang, “Elastic wave and vibration bandgaps in two-dimensional acoustic metamaterials with resonators and disorders,” *Wave Motion*, vol. 80, no. April, pp. 69–81, 2018, doi: 10.1016/j.wavemoti.2018.04.002.

[133] J.-P. Groby, O. Dazel, A. Duclos, L. Boeckx, and L. Kelders, “Enhancing the absorption coefficient of a backed rigid frame porous layer by embedding circular periodic inclusions,” *J. Acoust. Soc. Am.*, vol. 130, no. 6, pp. 3771–3780, 2011, doi: 10.1121/1.3652865.

[134] J.-P. Groby *et al.*, “Using simple shape three-dimensional inclusions to enhance porous layer absorption,” *J. Acoust. Soc. Am.*, vol. 136, no. 3, pp. 1139–1148, 2014, doi: 10.1121/1.4892760.

[135] H. G. Kim, S. Goo, J. Jung, and S. Wang, “Design optimization of a cellular-type noise insulation panel to improve transmission loss at low frequency,” *J. Sound Vib.*, vol. 447, pp. 105–119, 2019, doi: 10.1016/j.jsv.2019.01.046.

[136] N. Atalla, M. A. Hamdi, and R. Panneton, “Enhanced weak integral formulation for the mixed (u,p) poroelastic equations,” *J. Acoust. Soc. Am.*, vol. 109, no. 6, pp. 3065–3068, 2002, doi: 10.1121/1.1365423.

[137] W. X. Zhong and F. W. Williams, “On the Direct Solution of Wave Propagation for Repetitive Structures,” *J. Sound Vib.*, vol. 181, no. 3, pp. 485–501, 1995.

[138] N. Dauchez, S. Sahraoui, and N. Atalla, “Convergence of poroelastic finite elements based on Biot displacement formulation,” *J. Acoust. Soc. Am.*, vol. 109, pp. 33–40, 2001, doi: 10.1121/1.1289924.

LIST OF FIGURES

Figure 1: Comparison between the surface impedance predicted from the new model and that from the original model with $\sigma = 100{,}000$ N*s*m^{-4} and $d = 10$ mm [70]. 12
Figure 2: Comparison between measured and predicted surface impedance. Dots are the measured data by Nakajima et al.. Thick curves and thin curves show the predictions from the new model and the original, respectively, with $\sigma = 41{,}000$ N*S*M^{-4} and (a) $d = 50$ mm, (b) $d = 100$ mm [70]..... 13
Figure 3: Dynamic tortuosity of air for a porous ceramic media: (a) real part, (b) imaginary part. Solid line and dots respectively represent theoretical prediction and experimental results [72]. 14
Figure 4: Dynamic bulk modulus (in units of $P0$) of air for a porous ceramic: (a) real part, (b) imaginary part. Solid line and dots respectively represent theoretical prediction and experimental results [72]. 14
Figure 5: A layer of porous material bonded on to a rigid wall, in a normal acoustic field [10]..... 16
Figure 6: A thin layer of air and porous material including the boundary [10]..... 18
Figure 7: The reciprocal lattices (dots) and corresponding first Brillouin zones of (a) square lattice and (b) hexagonal lattice. 21
Figure 8: 2D and 3D unit cells used in COMSOL implementation of shift cell technique. The 2D geometry (on the left) is a 2 cm square with a 5 mm radius circular hole, while the 3D one (on the right) is a 2 cm cube with a 5 mm radius cylindrical hole. 27
Figure 9: Reciprocal lattice vector in a 3D unitary cell [105]..... 28
Figure 10: Comparison between dispersion curves obtained with classical Floquet-Bloch and shift cell techniques on a 2D (on the left) and 3D (on the right) unit cell made of air. 33
Figure 11: Dispersion curves for a 2D cell made of air, with increasing inclusion radius (from top to bottom: $s/32$, $s/4$ and $s/2.1$, with adiabatic (left column) and complex (right column) bulk modulus. 34
Figure 12: Computational times [s] in the 2D (left) and 3D (right) cases, for increasing number of elements. 35
Figure 13: Computational time percentage in the 2D (left) and 3D (right) cases, for increasing number of elements. 35
Figure 14: Dispersion curves for a JCA-modeled melamine 2D unit cell with a perfectly rigid inclusion; from top to bottom, the 1st, 2nd and 3rd branch eigenvectors are shown in terms of real (on the left) and imaginary (on the right) parts. 37
Figure 15: Dispersion curves for a JCA-modeled melamine 3D unit cell with a perfectly rigid inclusion; from top to bottom, the 1st, 2nd and 3rd branch eigenvectors are shown in terms of real (on the left) and imaginary (on the right) parts. 38
Figure 16: Reflection coefficient, power densities, dissipated power ratios and absorption coefficient computed for a 2D JCA-modeled melamine foam with a perfectly rigid inclusion. 40
Figure 17: Reflection coefficient, powers, dissipated power ratios and absorption coefficient computed for a 3D JCA-modeled melamine foam with a perfectly rigid inclusion. 40
Figure 18: Transmission loss computed for a 2D JCA-modeled melamine foam; homogeneous (on the left) and with a perfectly rigid inclusion (on the right). 41
Figure 19: Transmission loss computed for a 3D JCA-modeled melamine foam; homogeneous (on the left) and with a perfectly rigid inclusion (on the right). 41
Figure 20: Evanescent and propagative parts of dispersion curves computed for a 3D JCA-modeled melamine unit cell; homogeneous case. The color scale (on the right) indicates the level of propagativeness. 45

Figure 21: Evanescent and propagative parts of group velocities computed for a 3D JCA-modeled melamine unit cell; homogeneous case. The color scale (on the right) indicates the level of propagativeness. 45
Figure 22: Branch-tracked dispersion curves (on the left) and group velocities (on the right) computed for a 3D JCA-modeled melamine unit cell; homogeneous case. 45
Figure 23: Comparison of absorption coefficient between the equivalent curve and those previously obtained for wave incidence angles $\phi = 0°, \theta = 0°$ (on the left) and $\phi = 45°, \theta = 45°$ (on the right), computed for a 3D JCA-modeled melamine foam; homogeneous case. 46
Figure 24: Comparison of transmission loss between the equivalent curve and those previously obtained for wave incidence angles $\phi = 0°, \theta = 0°$ (on the left) and $\phi = 45°, \theta = 45°$ (on the right), computed for a 3D JCA-modeled melamine foam; homogeneous case. 46
Figure 25: Evanescent and propagative parts of dispersion curves computed for a 3D JCA-modeled melamine unit cell; case with inclusion. The color scale (on the right) indicates the level of propagativeness. 46
Figure 26: Evanescent and propagative parts of group velocities computed for a 3D JCA-modeled melamine unit cell; case with inclusion. The color scale (on the right) indicates the level of propagativeness. 47
Figure 27: Branch-tracked dispersion curves (on the left) and group velocities (on the right) computed for a 3D JCA-modeled melamine unit cell; case with inclusion. 47
Figure 28: Comparison of transmission loss between the equivalent curve and those previously obtained for wave incidence angles $\phi = 0°, \theta = 0°$ (on the left) and $\phi = 45°, \theta = 45°$ (on the right), computed for a 3D JCA-modeled melamine foam; case with inclusion. 47
Figure 29: Comparison between the absorption coefficient curves for cases 1-8 of Table 4. 49
Figure 30: Comparison between the transmission loss curves for cases 1-8 of Table 4. 49
Figure 31: Comparison between the absorption coefficient curves for cases 9-16 of Table 4. 50
Figure 32: Comparison between the transmission loss curves for cases 9-16 of Table 4. 50
Figure 33: Comparison between the absorption coefficient curves for cases 17-24 of Table 4. 50
Figure 34: Comparison between the transmission loss curves for cases 17-24 of Table 4. 51
Figure 35: Comparison between the absorption coefficient curves for cases 25-32 of Table 4. 51
Figure 36: Comparison between the transmission loss curves for cases 25-32 of Table 4. 51
Figure 37: Comparison between the absorption coefficient curves for cases 33-40 of Table 4. 52
Figure 38: Comparison between the transmission loss curves for cases 33-40 of Table 4. 52
Figure 39: Comparison between the absorption coefficient curves for cases 41-48 of Table 4. 52
Figure 40: Comparison between the transmission loss curves for cases 41-48 of Table 4. 53
Figure 41: Absorption coefficient design curves as functions of the unit cell dimension (on the left) and the frequency of the 1st peak (on the right), in the case of a 3D JCA-modeled melamine foam. 54
Figure 42: Transmission loss design curves as functions of the unit cell dimension (on the left) and the frequency of the 1st peak (on the right), in the case of a 3D JCA-modeled melamine foam. 54
Figure 43: Absorption coefficient (on the left) and transmission loss (on the right) design curves as functions of the foam airflow resistivity, in the case of a 3D JCA-modeled melamine foam. 55
Figure 44: Absorption coefficient value as a function of frequency and foam airflow resistivity; homogeneous case (on the left) and case with a cylindrical perfectly rigid inclusion (on the right), computed for a 3D JCA-modeled melamine foam. 55
Figure 45: Transmission loss value as a function of frequency and foam airflow resistivity; homogeneous case (on the left) and case with a cylindrical perfectly rigid inclusion (on the right), computed for a 3D JCA-modeled melamine foam. 55

Figure 46: Comparison of absorption coefficient curves between the homogeneous case, the case with inclusion with fixed dimensions and the case with inclusion with fixed mass, computed for a 3D JCA-modeled melamine foam. 57
Figure 47: Comparison of transmission loss curves between the homogeneous case, the case with inclusion with fixed dimensions, the case with inclusion with fixed mass and the homogeneous case with fixed performance in the 6000-8000 Hz frequency range, computed for a 3D JCA-modeled melamine foam. 57
Figure 48: Unit cell with Helmholtz resonators [129]. 58
Figure 49: Acoustic characteristics of the unit cell with Helmholtz resonators. 59
Figure 50: Comparison of absorption coefficient curves with the reference one for the unit cell with Helmholtz resonators. 59
Figure 51: Transmission loss curve for the unit cell with Helmholtz resonators. 60
Figure 52: Dispersion curves for the unit cell with Helmholtz resonators. 60
Figure 53: Dispersion curves for a 3D Biot-modeled unit cell, validation with Serra plots [36]; real (left) and imaginary (right) parts. 71
Figure 54: Ratios of the fluid over the solid velocities of the different wave types for a 3D Biot-modeled unit cell. 71
Figure 55: Dispersion curves validation with JCA plots; here, the Biot curves are computed for a 3D homogeneous PU 60 unit cell, with $E = 1015\ Pa$ and structural loss factor $= 0$. 72
Figure 56: Dispersion curves validation with JCA plots; here, the Biot curves are computed for a 3D PU 60 unit cell with a perfectly rigid cylindrical inclusion, with $E = 1015\ Pa$ and structural loss factor $= 0$. 72
Figure 57: Real (left) and imaginary (right) parts of analytically estimated dispersion curves for a 3D Biot-modeled homogeneous PU 60 foam. 73
Figure 58: Ratios of the fluid over the solid velocities of the different wave types in a 3D Biot-modeled homogeneous PU 60 foam. 73
Figure 59: Evanescent and propagative parts of dispersion curves for a 3D Biot-modeled PU 60 unit cell, with a perfectly rigid cylindrical inclusion. The color scale (on the right) indicates the level of propagativeness. 73
Figure 60: Branch-tracked dispersion curves for a 3D Biot-modeled PU 60 unit cell, with a perfectly rigid cylindrical inclusion. 74
Figure 61: Absorption coefficient comparisons between JCA and Biot models for PU 60 foam. 75
Figure 62: Transmission loss comparisons between JCA and Biot models for PU 60 foam. 75
Figure 63: Absorption coefficient comparisons between JCA and Biot models for Test foam 1. 75
Figure 64: Transmission loss comparisons between JCA and Biot models for Test foam 1. 76
Figure 65: Absorption coefficient comparisons between JCA and Biot models for Test foam 2. 76
Figure 66: Transmission loss comparisons between JCA and Biot models for Test foam 2. 76
Figure 67: Computational times [s] for a single value of absorption coefficient (left) and transmission loss (right), for increasing number of elements. 77
Figure 68: Computational time percentage for a single value of absorption coefficient (left) and transmission loss (right), for increasing number of elements. 77
Figure 69: Absorption coefficient computations for Configurations 1, 2 and 6. 78
Figure 70: Transmission loss computations for Configurations 1, 2 and 6. 78
Figure 71: Non-rigid inclusion test campaign for Test foam 1 absorption coefficient. 79
Figure 72: Non-rigid inclusion test campaign for Test foam 1 transmission loss. 79
Figure 73: Non-rigid inclusion test campaign for Test foam 2 absorption coefficient. 80
Figure 74: Non-rigid inclusion test campaign for Test foam 2 transmission loss. 80

Figure 75: Absorption coefficient low frequency improvement for a repetition of five 3D PU 60 unit cells. 81
Figure 76: Absorption coefficient design curves as a function of the unit cell dimension (on the left) and the frequency of the 1st peak (on the right). 82
Figure 77: Transmission loss design curves as a function of the unit cell dimension (on the left) and the frequency of the 1st peak (on the right). 82
Figure 78: Absorption coefficient (on the left) and transmission loss (on the right) design curves as functions of the foam airflow resistivity. 83
Figure 79: Absorption coefficient value as a function of frequency and foam airflow resistivity; homogeneous case (on the left) and case with a cylindrical perfectly rigid inclusion (on the right). .. 83
Figure 80: Transmission loss value as a function of frequency and foam airflow resistivity; homogeneous case (on the left) and case with a cylindrical perfectly rigid inclusion (on the right). .. 83
Figure 81: Absorption coefficient (on the left) and transmission loss (on the right) design curves as functions of the foam tortuosity. 84
Figure 82: Absorption coefficient value as a function of frequency and foam tortuosity; homogeneous case (on the left) and case with a cylindrical perfectly rigid inclusion (on the right). 84
Figure 83: Transmission loss value as a function of frequency and foam tortuosity; homogeneous case (on the left) and case with a cylindrical perfectly rigid inclusion (on the right). 84
Figure 84: Absorption coefficient (on the left) and transmission loss (on the right) design curves as functions of the foam viscous characteristic length. 85
Figure 85: Absorption coefficient value as a function of frequency and foam viscous characteristic length; homogeneous case (on the left) and case with a cylindrical perfectly rigid inclusion (on the right). 85
Figure 86: Transmission loss value as a function of frequency and foam viscous characteristic length; homogeneous case (on the left) and case with a cylindrical perfectly rigid inclusion (on the right). .. 85
Figure 87: Absorption coefficient (on the left) and transmission loss (on the right) design curves as functions of the foam thermal characteristic length. 86
Figure 88: Absorption coefficient value as a function of frequency and foam thermal characteristic length; homogeneous case (on the left) and case with a cylindrical perfectly rigid inclusion (on the right). 86
Figure 89: Transmission loss value as a function of frequency and foam thermal characteristic length; homogeneous case (on the left) and case with a cylindrical perfectly rigid inclusion (on the right). .. 86
Figure 90: Absorption coefficient (on the left) and transmission loss (on the right) design curves as functions of the foam skeleton density. 87
Figure 91: Absorption coefficient (on the left) and transmission loss (on the right) design curves as functions of the foam Young modulus. 87
Figure 92: Absorption coefficient (on the left) and transmission loss (on the right) design curves as functions of the foam loss factor. 87
Figure 93: Dispersion curves for a homogeneous DB-modeled melamine 2D unit cell; from top to bottom, the 1st, 2nd and 3rd branch eigenvectors are shown in terms of real (on the left) and imaginary (on the right) parts. 92
Figure 94: Dispersion curves for a homogeneous DB-modeled black PU 2D unit cell; from top to bottom, the 1st, 2nd and 3rd branch eigenvectors are shown in terms of real (on the left) and imaginary (on the right) parts. 93
Figure 95: Dispersion curves for a homogeneous JCA-modeled melamine 2D unit cell; from top to bottom, the 1st, 2nd and 3rd branch eigenvectors are shown in terms of real (on the left) and imaginary (on the right) parts. 94

Figure 96: Dispersion curves for a homogeneous JCA-modeled black PU 2D unit cell; from top to bottom, the 1st, 2nd and 3rd branch eigenvectors are shown in terms of real (on the left) and imaginary (on the right) parts. 95
Figure 97: Dispersion curves for a homogeneous DB-modeled melamine 3D unit cell; from top to bottom, the 1st, 2nd and 3rd branch eigenvectors are shown in terms of real (on the left) and imaginary (on the right) parts. 96
Figure 98: Dispersion curves for a homogeneous DB-modeled black PU 3D unit cell; from top to bottom, the 1st, 2nd and 3rd branch eigenvectors are shown in terms of real (on the left) and imaginary (on the right) parts. 97
Figure 99: Dispersion curves for a homogeneous JCA-modeled melamine 3D unit cell; from top to bottom, the 1st, 2nd and 3rd branch eigenvectors are shown in terms of real (on the left) and imaginary (on the right) parts. 98
Figure 100: Dispersion curves for a homogeneous JCA-modeled black PU 3D unit cell; from top to bottom, the 1st, 2nd and 3rd branch eigenvectors are shown in terms of real (on the left) and imaginary (on the right) parts. 99
Figure 101: Dispersion curves for a DB-modeled melamine 2D unit cell with a perfectly rigid inclusion; from top to bottom, the 1st, 2nd and 3rd branch eigenvectors are shown in terms of real (on the left) and imaginary (on the right) parts. 100
Figure 102: Dispersion curves for a DB-modeled black PU 2D unit cell with a perfectly rigid inclusion; from top to bottom, the 1st, 2nd and 3rd branch eigenvectors are shown in terms of real (on the left) and imaginary (on the right) parts. 101
Figure 103: Dispersion curves for a JCA-modeled melamine 2D unit cell with a perfectly rigid inclusion; from top to bottom, the 1st, 2nd and 3rd branch eigenvectors are shown in terms of real (on the left) and imaginary (on the right) parts. 102
Figure 104: Dispersion curves for a JCA-modeled black PU 2D unit cell with a perfectly rigid inclusion; from top to bottom, the 1st, 2nd and 3rd branch eigenvectors are shown in terms of real (on the left) and imaginary (on the right) parts. 103
Figure 105: Dispersion curves for a DB-modeled melamine 3D unit cell with a perfectly rigid inclusion; from top to bottom, the 1st, 2nd and 3rd branch eigenvectors are shown in terms of real (on the left) and imaginary (on the right) parts. 104
Figure 106: Dispersion curves for a DB-modeled black PU 3D unit cell with a perfectly rigid inclusion; from top to bottom, the 1st, 2nd and 3rd branch eigenvectors are shown in terms of real (on the left) and imaginary (on the right) parts. 105
Figure 107: Dispersion curves for a JCA-modeled melamine 3D unit cell with a perfectly rigid inclusion; from top to bottom, the 1st, 2nd and 3rd branch eigenvectors are shown in terms of real (on the left) and imaginary (on the right) parts. 106
Figure 108: Dispersion curves for a JCA-modeled black PU 3D unit cell with a perfectly rigid inclusion; from top to bottom, the 1st, 2nd and 3rd branch eigenvectors are shown in terms of real (on the left) and imaginary (on the right) parts. 107
Figure 109: Dispersion curves computed for configuration 1 of Table 4. 108
Figure 110: Dispersion curves computed for configuration 2 of Table 4. 108
Figure 111: Dispersion curves computed for configuration 3 of Table 4. 108
Figure 112: Dispersion curves computed for configuration 4 of Table 4. 109
Figure 113: Dispersion curves computed for configuration 5 of Table 4. 109
Figure 114: Dispersion curves computed for configuration 6 of Table 4. 109
Figure 115: Dispersion curves computed for configuration 7 of Table 4. 110
Figure 116: Dispersion curves computed for configuration 8 of Table 4. 110
Figure 117: Dispersion curves computed for configuration 9 of Table 4. 110

Figure 118: Dispersion curves computed for configuration 10 of Table 4. 111
Figure 119: Dispersion curves computed for configuration 11 of Table 4. 111
Figure 120: Dispersion curves computed for configuration 12 of Table 4. 111
Figure 121: Dispersion curves computed for configuration 13 of Table 4. 112
Figure 122: Dispersion curves computed for configuration 14 of Table 4. 112
Figure 123: Dispersion curves computed for configuration 15 of Table 4. 112
Figure 124: Dispersion curves computed for configuration 16 of Table 4. 113
Figure 125: Dispersion curves computed for configuration 17 of Table 4. 113
Figure 126: Dispersion curves computed for configuration 18 of Table 4. 113
Figure 127: Dispersion curves computed for configuration 19 of Table 4. 114
Figure 128: Dispersion curves computed for configuration 20 of Table 4. 114
Figure 129: Dispersion curves computed for configuration 21 of Table 4. 114
Figure 130: Dispersion curves computed for configuration 22 of Table 4. 115
Figure 131: Dispersion curves computed for configuration 23 of Table 4. 115
Figure 132: Dispersion curves computed for configuration 24 of Table 4. 115
Figure 133: Dispersion curves computed for configuration 25 of Table 4. 116
Figure 134: Dispersion curves computed for configuration 26 of Table 4. 116
Figure 135: Dispersion curves computed for configuration 27 of Table 4. 116
Figure 136: Dispersion curves computed for configuration 28 of Table 4. 117
Figure 137: Dispersion curves computed for configuration 29 of Table 4. 117
Figure 138: Dispersion curves computed for configuration 30 of Table 4. 117
Figure 139: Dispersion curves computed for configuration 31 of Table 4. 118
Figure 140: Dispersion curves computed for configuration 32 of Table 4. 118
Figure 141: Dispersion curves computed for configuration 33 of Table 4. 118
Figure 142: Dispersion curves computed for configuration 34 of Table 4. 119
Figure 143: Dispersion curves computed for configuration 35 of Table 4. 119
Figure 144: Dispersion curves computed for configuration 36 of Table 4. 119
Figure 145: Dispersion curves computed for configuration 37 of Table 4. 120
Figure 146: Dispersion curves computed for configuration 38 of Table 4. 120
Figure 147: Dispersion curves computed for configuration 39 of Table 4. 120
Figure 148: Dispersion curves computed for configuration 40 of Table 4. 121
Figure 149: Dispersion curves computed for configuration 41 of Table 4. 121
Figure 150: Dispersion curves computed for configuration 42 of Table 4. 121
Figure 151: Dispersion curves computed for configuration 43 of Table 4. 122
Figure 152: Dispersion curves computed for configuration 44 of Table 4. 122
Figure 153: Dispersion curves computed for configuration 45 of Table 4. 122
Figure 154: Dispersion curves computed for configuration 46 of Table 4. 123
Figure 155: Dispersion curves computed for configuration 47 of Table 4. 123
Figure 156: Dispersion curves computed for configuration 48 of Table 4. 123
Figure 157: Reflection coefficient, power densities, dissipated power ratios and absorption coefficient computed for a homogeneous DB-modeled melamine 2D unit cell. 124
Figure 158: Reflection coefficient, power densities, dissipated power ratios and absorption coefficient computed for a homogeneous DB-modeled black PU 2D unit cell. 124
Figure 159: Reflection coefficient, power densities, dissipated power ratios and absorption coefficient computed for a homogeneous JCA-modeled melamine 2D unit cell. 125
Figure 160: Reflection coefficient, power densities, dissipated power ratios and absorption coefficient computed for a homogeneous JCA-modeled black PU 2D unit cell. 125

Figure 161: Reflection coefficient, powers, dissipated power ratios and absorption coefficient computed for a homogeneous DB-modeled melamine 3D unit cell. 126
Figure 162: Reflection coefficient, powers, dissipated power ratios and absorption coefficient computed for a homogeneous DB-modeled black PU 3D unit cell. 126
Figure 163: Reflection coefficient, powers, dissipated power ratios and absorption coefficient computed for a homogeneous JCA-modeled melamine 3D unit cell. 127
Figure 164: Reflection coefficient, powers, dissipated power ratios and absorption coefficient computed for a homogeneous JCA-modeled black PU 3D unit cell. 127
Figure 165: Reflection coefficient, power densities, dissipated power ratios and absorption coefficient computed for a DB-modeled melamine 2D unit cell with a perfectly rigid inclusion. 128
Figure 166: Reflection coefficient, power densities, dissipated power ratios and absorption coefficient computed for a DB-modeled black PU 2D unit cell with a perfectly rigid inclusion. 128
Figure 167: Reflection coefficient, power densities, dissipated power ratios and absorption coefficient computed for a JCA-modeled melamine 2D unit cell with a perfectly rigid inclusion. 129
Figure 168: Reflection coefficient, power densities, dissipated power ratios and absorption coefficient computed for a JCA-modeled black PU 2D unit cell with a perfectly rigid inclusion. 129
Figure 169: Reflection coefficient, powers, dissipated power ratios and absorption coefficient computed for a DB-modeled melamine 3D unit cell with a perfectly rigid inclusion. 130
Figure 170: Reflection coefficient, powers, dissipated power ratios and absorption coefficient computed for a DB-modeled black PU 3D unit cell with a perfectly rigid inclusion. 130
Figure 171: Reflection coefficient, powers, dissipated power ratios and absorption coefficient computed for a JCA-modeled melamine 3D unit cell with a perfectly rigid inclusion. 131
Figure 172: Reflection coefficient, powers, dissipated power ratios and absorption coefficient computed for a JCA-modeled black PU 3D unit cell with a perfectly rigid inclusion. 131
Figure 173: Surface impedance (on the left) and reflection coefficient (on the right) computed for a JCA-modeled melamine 3D unit cell with a perfectly rigid inclusion; dimension $= 0.008\ m.$ 132
Figure 174: Surface impedance (on the left) and reflection coefficient (on the right) computed for a JCA-modeled melamine 3D unit cell with a perfectly rigid inclusion; dimension $= 0.0095\ m.$ 132
Figure 175: Surface impedance (on the left) and reflection coefficient (on the right) computed for a JCA-modeled melamine 3D unit cell with a perfectly rigid inclusion; dimension $= 0.02\ m.$ 132
Figure 176: Surface impedance (on the left) and reflection coefficient (on the right) computed for a JCA-modeled melamine 3D unit cell with a perfectly rigid inclusion; dimension $= 0.035\ m.$ 133
Figure 177: Surface impedance (on the left) and reflection coefficient (on the right) computed for a JCA-modeled melamine 3D unit cell with a perfectly rigid inclusion; dimension $= 0.0425\ m.$ 133
Figure 178: Surface impedance (on the left) and reflection coefficient (on the right) computed for a JCA-modeled melamine 3D unit cell with a perfectly rigid inclusion; dimension $= 0.05\ m.$ 133
Figure 179: Surface impedance (on the left) and reflection coefficient (on the right) computed for a JCA-modeled melamine 3D unit cell with a perfectly rigid inclusion; dimension $= 0.065\ m.$ 134
Figure 180: Surface impedance (on the left) and reflection coefficient (on the right) computed for a JCA-modeled melamine 3D unit cell with a perfectly rigid inclusion; dimension $= 0.08\ m.$ 134
Figure 181: Surface impedance (on the left) and reflection coefficient (on the right) computed for a JCA-modeled melamine 3D unit cell with a perfectly rigid inclusion; dimension $= 0.095\ m.$ 134
Figure 182: Surface impedance (on the left) and reflection coefficient (on the right) computed for a JCA-modeled melamine 3D unit cell with a perfectly rigid inclusion; $\sigma = 1000\ Pa * sm2$ 135
Figure 183: Surface impedance (on the left) and reflection coefficient (on the right) computed for a JCA-modeled melamine 3D unit cell with a perfectly rigid inclusion; $\sigma = 2500\ Pa * sm2$ 135
Figure 184: Surface impedance (on the left) and reflection coefficient (on the right) computed for a JCA-modeled melamine 3D unit cell with a perfectly rigid inclusion; $\sigma = 5000\ Pa * sm2$ 135

Figure 185: Surface impedance (on the left) and reflection coefficient (on the right) computed for a JCA-modeled melamine 3D unit cell with a perfectly rigid inclusion; $\sigma = 7500\ Pa * sm2$..... 136
Figure 186: Surface impedance (on the left) and reflection coefficient (on the right) computed for a JCA-modeled melamine 3D unit cell with a perfectly rigid inclusion; $\sigma = 10000\ Pa * sm2$. 136
Figure 187: Surface impedance (on the left) and reflection coefficient (on the right) computed for a JCA-modeled melamine 3D unit cell with a perfectly rigid inclusion; $\sigma = 25000\ Pa * sm2$. 136
Figure 188: Surface impedance (on the left) and reflection coefficient (on the right) computed for a JCA-modeled melamine 3D unit cell with a perfectly rigid inclusion; $\sigma = 50000\ Pa * sm2$. 137
Figure 189: Surface impedance (on the left) and reflection coefficient (on the right) computed for a JCA-modeled melamine 3D unit cell with a perfectly rigid inclusion; $\sigma = 75000\ Pa * sm2$. 137
Figure 190: Surface impedance (on the left) and reflection coefficient (on the right) computed for a JCA-modeled melamine 3D unit cell with a perfectly rigid inclusion; $\sigma = 100000\ Pa * sm2$. 137
Figure 191: Transmission loss computed for a homogeneous DB-modeled melamine (on the left) and black PU (on the right) 2D unit cell. 138
Figure 192: Transmission loss computed for a homogeneous JCA-modeled melamine (on the left) and black PU (on the right) 2D unit cell. 138
Figure 193: Transmission loss computed for a homogeneous DB-modeled melamine (on the left) and black PU (on the right) 3D unit cell. 138
Figure 194: Transmission loss computed for a homogeneous JCA-modeled melamine (on the left) and black PU (on the right) 3D unit cell. 139
Figure 195: Transmission loss computed for a DB-modeled melamine (on the left) and black PU (on the right) 2D unit cell with a perfectly rigid inclusion. 139
Figure 196: Transmission loss computed for a JCA-modeled melamine (on the left) and black PU (on the right) 2D unit cell with a perfectly rigid inclusion. 139
Figure 197: Transmission loss computed for a DB-modeled melamine (on the left) and black PU (on the right) 3D unit cell with a perfectly rigid inclusion. 140
Figure 198: Transmission loss computed for a JCA-modeled melamine (on the left) and black PU (on the right) 3D unit cell with a perfectly rigid inclusion. 140

LIST OF TABLES

Table 1: Acoustical parameters for two porous materials modeled as equivalent fluids: black PU and melamine. 36
Table 2: Techniques used to estimate the transmission loss, according to the angles of incidence.... 44
Table 3: Techniques used to estimate the absorption coefficient, according to the angles of incidence. 44
Table 4: Combinations of foams and inclusions used for the non-rigid inclusion test campaign, performed on a 3D JCA-modeled unit cell. 48
Table 5: Non-acoustic parameters of the foams used for the non-rigid inclusion test campaign, performed on a 3D JCA-modeled unit cell. 49
Table 6: Air properties. 49
Table 7: Raw data for unit cell dimension design guidelines, in the case of a 3D JCA-modeled melamine unit cell. 54
Table 8: Raw data for airflow resistivity design guidelines, in the case of a 3D JCA-modeled melamine unit cell. 56
Table 9: Acoustical parameters of the reference porous material used in the study of an Helmholtz resonating system. 58
Table 10: Poro-elastic properties of the tested foams. 74
Table 11: Elastic properties of the materials used in the non-rigid inclusions test campaign, with a Biot-modeled PU 60 foam. 78
Table 12: Combinations of inclusions used in the non-rigid inclusions test campaign, with a Biot-modeled PU 60 foam, and mass variations respect to the homogeneous case. 79

LIST OF PUBLICATIONS

This PhD manuscript is based on the following publications and/or part of them.

International journals (peer-reviewed)

- D. Magliacano, M. Ouisse, A. Khelif, S. De Rosa, F. Franco, N. Atalla and M. Collet, *Computation of dispersion diagrams for periodic porous materials modeled as equivalent fluids*, Mech. Syst. Signal Process., vol. 130 (second issue under review), pp. 692–706, 2019. **Sections 2.1, 2.2 and 2.3 of the present manuscript are based on this journal paper.**
- D. Magliacano, S. Ashani, M. Ouisse, E. Deckers, G. Petrone, W. Desmet and S. De Rosa, *Formulation and validation of the shift cell technique for acoustic applications of poro-elastic materials described by the Biot theory*, submitted to Mech. Syst. Signal Process. on 21/01/2020. **Section 3.1 of the present manuscript is based on this journal paper.**
- D. Magliacano, M. Ouisse, S. De Rosa, F. Franco and A. Khelif, *Computation of acoustic properties and design guidelines of periodic Biot-modeled foams*, in submission to Applied Acoustics. **Sections 3.3 and 3.4 of the present manuscript are based on this journal paper.**

International conferences

- D. Magliacano, M. Ouisse, A. Khelif, S. De Rosa and F. Franco, *A literature review for the analysis of vibroacoustic properties of periodic inclusions in porous materials*, 2nd Euro-Mediterranean Conference on Structural Dynamics and Vibroacoustics, Sevilla (Spain), 2017.
- D. Magliacano, M. Ouisse, A. Khelif, S. De Rosa and F. Franco, *The shifted cell operator technique applied to equivalent fluids models for the computation of dispersion diagrams of periodic porous materials*, 5th Symposium on the Acoustics of Poro-Elastic Materials, Le Mans (France), 2017.
- D. Magliacano, M. Ouisse, A. Khelif, S. De Rosa, F. Franco and N. Atalla, *Validation of shift cell approach for the modelling of acoustic properties of porous materials embedding periodic inclusions*, 6th Noise and Vibration Emerging Methods Conference, Ibiza (Spain), 2018.
- D. Magliacano, M. Ouisse, A. Khelif, S. De Rosa, F. Franco and N. Atalla, *Computation of wave dispersion characteristics in periodic porous materials modeled as equivalent fluids*, 29th International Conference on Noise and Vibration Engineering, Leuven (Belgium), 2018.
- D. Magliacano, M. Ouisse, S. De Rosa, F. Franco and A. Khelif, *Investigations about the modelling of acoustic properties of periodic porous materials with the shift cell approach*, 9th ECCOMAS Thematic Conference on Smart Structures and Materials, Paris (France), 2019. **Sections 2.4 and 2.6 of the present manuscript are based on this conference paper.**
- D. Magliacano, M. Ouisse, S. De Rosa, F. Franco and A. Khelif, *Design guidelines for the acoustic performance improvement of a periodic porous material*, 3rd Euro-Mediterranean Conference on Structural Dynamics and Vibroacoustics, Napoli (Italy), 2020. **Section 2.5 of the present manuscript is based on this conference paper.**